Biomimetic articulated appendages for small unmanned aerial vehicles

by

Titilayo Tolulope Ogunwa

A thesis presented for the degree of

Doctor of Philosophy in Engineering

(Mechanical and Manufacturing)

UniSA STEM



University of
South Australia

2023

Abstract

Insect-inspired unmanned aerial vehicles (UAVs) continue to be an active research area as some insects demonstrate flight capabilities required for complex military and civil operations, beyond what the prevalent fixed and rotary wing UAVs can provide. They can hover, glide, manoeuvre and switch between all three modes of flight while exhibiting high manoeuvrability. However, our understanding of insect flight is still limited as the flight capability of even the most modest and occasional flyers far exceed that of current insect-inspired biomimetic drones. Research into insect flight has primarily focused on the role of wings, especially in hover. However, evidence from observational studies suggests that some insects dynamically alter their body posture in flight by exploiting the movement of body appendages such as the legs and abdomen, adjusting their centre of mass, and changing moments of inertia. Yet, these behaviours have not been well captured in a flight dynamics framework. In addition, with more focus being placed on the wings and hover, very little is understood about the effects appendage motions have on insect forward flight. In this thesis, the subject is investigated by exploring the effects the motions of the appendages have on insect forward flight, using a combination of mathematical modelling, flight testing and supplementary observational studies.

Taking inspiration from dragonflies, nonlinear multibody equations of motion were derived with the Newton-Euler method, for a dragonfly-inspired straight-wing aircraft (DISWA) with an articulated abdomen, and implemented in the MATLAB/Simulink environment. As opposed to the conventional Newton-Euler method that used vector formulation, the formulation in this thesis is tensor-based, and includes the dynamic effects of time-varying mass and inertia properties associated with appendage motions observed in dragonflies. The tensor flight dynamics models of the multibody aircraft that were developed allow unified dynamic and aerodynamic simulation and control of biomimetic aircraft with wings and any number of idealised appendage masses. To ensure relative dynamic and aerodynamic effects can be determined, the aerodynamic contribution of the appendage was modelled as an additive component. Since the flight of some insects consists of both flapping and fixed-wing episodes, and this was an isolated study of the effects of appendage motion, the approach used will provide insight into the effects of appendage motions on insect forward flight. The aircraft configuration gives rise to three possible control effector solutions: (1) Aerodynamic control surfaces (aerosurface) (2) Articulated mass (AM), and (3) Combination or hybrid of aerosurface and articulated mass.

Two sets of equations of motion were developed to validate the formulation and perform simulations that represent two modes of appendage mass articulation: translational and

rotational modes. Relevant performance indicators for various forward flight conditions and scenarios were considered to investigate some functionalities of abdomen movements, and the benefits they might provide due to only dynamic/inertial effects (due to mass and inertia) or in addition to aerodynamic (shape) effects. Results from the research indicate that both abdominal articulation modes due to only dynamic effects, are beneficial for balancing steady cruise flight against trim changes at different cruise speeds, and improving the performance (power required) in the process. Meanwhile, compared to the aerosurface controlled (A-C) option and considering only dynamic effects, trimming for steady cruise at different cruise speeds with the combined controlled (C-C) aircraft achieves better performance with the translational actuation mode, with the same combined trimmability range, and worse with the rotational actuation mode, with no extended combined trimmability range benefit. However, when both dynamic and aerodynamic effects were considered for the rotational actuation mode, the performance worsened with increased area. In addition, compared to the A-C solution for initiating a pull up manoeuvre from steady cruise flight, both articulated mass solutions resulted in increased manoeuvre advantage due to purely inertial and also added aerodynamic effects. The effect of rotational abdominal motion on lateral-directional trimmability over the feasible speed range for steady turning flight was then explored. The results demonstrate the potential benefits of a C–C aircraft with yaw abdominal articulation, compared to an A-C aircraft, in terms of increased combined trimmability range, however, the C-C aircraft required more power. The results also indicate that the conventional turn using aerosurfaces only, would be more useful during a fast, forward flight but would experience sideslip. On the other hand, yaw turns using an articulated abdomen were revealed to be more effective in slow flight and eliminated sideslip.

Subsequently, simulations were carried out to investigate the use of appendage mass rotation/deflection for manoeuvring and the effect of area and rotational rate on manoeuvre effectiveness. Upward and rightward deflection of the abdomen of the DISWA initiated diving and right turning manoeuvres, respectively, using dynamic as well as combined dynamic and aerodynamic effects. For the diving manoeuvre, the results obtained show that compared to when only the dynamic effects are in play, the inclusion of the aerodynamic effects decreases the manoeuvre effectiveness, which worsens with increasing area. In the case of the turning manoeuvre, the inclusion of the aerodynamic effects increases effectiveness, which further increases with the area. However, effectiveness increased with deflection rate for both diving and turning manoeuvres and considering both inertial and aerodynamic effects.

The stabilising and controlling effect of a rotational articulated appendage was also investigated. The analysis was based on the linearised model of the multibody model of the DISWA about stable equilibrium (level cruising flight). Once controllability was verified, a quadratic integral regulator (LQR) was designed for stabilisation, while a linear quadratic integral controller (LQI) was designed and implemented to optimally track the attitude (pitch and yaw) of the DISWA. In both controller designs, the three above mentioned control actuation options (aerosurface, AM and hybrid), were investigated. The stabilising and control effect of the articulated abdomen were comparable to the control surfaces, with lateral abdominal motion substituting for an aerodynamic rudder to achieve coordinated turns. Vertical motion achieved the same effect as an elevator, and included potentially useful transient torque reactions both up and down. The best performance was achieved when both moving masses and control surfaces were employed in the control solution.

Finally, this study also involved the design and demonstration of a practical and controllable appendage system with readily available components. A Phantom FX-61 flying wing UAV with a wingspan of 1.55 m, modified to include an externally articulated mass, was flight tested in an open loop as a proof-of-concept. The articulated mass was able to rotate longitudinally and laterally. The developed nonlinear model implemented in Simulink was used to simulate the aircraft flight for comparison. The simulation results are in good agreement with the experimental data, demonstrating the feasibility of flying the airplane with an airframe-based control mechanism.

The implications of the research presented in this thesis will provide a foundation for further advancing the development of insect-inspired biomimetic aircraft based on a better understanding of the effects of appendage movements in insect forward flight.

Declaration

I declare that this thesis does not incorporate, without acknowledgement, any material previously submitted for a degree or diploma in any university, and that to the best of my knowledge does not contain any materials previously published or written by another person except where due reference is made in the text; and all other substantive contributions by others to the work presented, including jointly authored publications, are clearly acknowledged.

Signed: Titilayo Tolulope Ogunwa

_____

Date: March 2023

_____

Dedication

To my parents Engr. and Mrs Ogunwa who have always supported me.

Acknowledgements

I thankfully acknowledge the Australian Government for the Research Training Program international (RTPi) Scholarship received to fund my PhD, through the University of South Australia.

I would like to express my special gratitude to Professor Javaan Singh Chahl, my project supervisor. I count myself truly blessed for having you as my supervisor. Your support, patience and motivation helped me through this phase of my life. To Dr. Ermira Junita Abdullah my external supervisor, your belief in me set this plan in motion six years ago during my final year project. I am truly grateful.

I would like to express my gratitude to Prof. Jonas Addai-Mensah for this guidance, support, and encouragement throughout my studies.

To Engr. Omoniyi and Mrs Aribike Ogunwa, my parents, who gave me the opportunity to pursue my dreams, I appreciate you. You have supported me in every aspect throughout my studies and I must say I am blessed to have you as my parents. To Laolu and Precious my darling sisters, and my brother-in-law, Steve, thank you for always being there. To Ellie my niece, you have been a sure source of light and happiness, especially on days when I struggled. You are forever cherished and loved.

My family in Australia; Dr. Emmanuel Baawuah and Dr. Mathias Aakyiir, thank you so much. Having you in my corner was truly a blessing and I am very grateful. I could not have done this without your help and continual support. To the rest of my Adelaide family, Dr. Jumal Ibrahim, Dr. Mustafa Adam, Dr. and Mrs George Abaka-Wood, Philip Forson, Kwaku Owusu,

Amankwaa-Kyeremeh Bismark, Derrick Aikins, James Dankwah, Dan Bonsu, Evelyn and Eugene Uroro, thanks for always encouraging and supporting me. You all made this journey worth it.

My friends abroad, Glory Iserhienrhien, Titiloye Bolaji, Joke Smith, Tope Taiwo, Ese Udeh and Feyi Omoya. Your belief in me and prayers inspired and got me through the tough days. Thank you all so much.

To my research group members, Yiting Tao, Asanka Perera, Tim McIntyre, Sam Teague, John Mcguire, Blake McIvor and Fatema Khanam, I could not imagine going through this with any other research group. Thanks so much for all your help and encouragement.

Most of all, I will like to thank Eledumare for the gift of life, wisdom and understanding to undertake this research. To God be the glory.

Contents

Abstract **i**

Declaration **v**

Dedication **vii**

Acknowledgements **ix**

Contents **x**

List of Figures **xvii**

List of Tables **xxiv**

List of Abbreviations **xxvii**

List of Symbols **xxx**

List of Publications **xxxv**

1 Introduction **1**

1.1 Background 1

1.2 Motivation 3

1.3 Aim and Objectives 4

1.4 Research Questions 5

1.5 Thesis Structure 5

2 Literature Review **7**

2.1 The Forces of Flight in Aerospace Vehicles 7

2.2 Moving Mass Control Effectors in Aerospace Vehicles 9

2.3 Control of Aircraft with Multiple Control Effectors 12

2.4 Insect Flight and Biomimetic Vehicles 13

2.4.1 Aerodynamics Modelling 13

2.4.2 Flight Dynamics Modelling 17

2.4.3 Stability Studies 22

2.4.4 Control Studies 25

2.5 Conclusion 27

3 Research Methodology **29**

3.1 Introduction 29

3.2 A Dragonfly Biomimetic Aircraft Model 31

3.3 Modelling, Simulation and Control 34

3.3.1 Equations of Motion 34

3.3.2 Aerodynamic Model 35

3.3.3 Design Tools 36

3.3.4 Performance Characterisation 37

3.4 Experimental Works 38

3.4.1 Flight Data Logger 38

3.4.2 Ground Control Station 39

3.4.3 Post-flight Data Analysis 39

3.5 Chapter Summary 40

4 Multibody Dynamics for Bioinspired Vehicles **41**

4.1 Introduction 41

4.2 Development of the Multibody Equations of Motion 43

4.2.1 Preliminaries 46

4.2.2 Reference Frames and Coordinate Systems 48

4.2.3 Reference Points 48
4.2.4 Orientation and Transformation Matrices 49
4.2.5 Kinematics 50
4.2.5.1 Model 1 Abdominal Kinematic Equations 51
4.2.5.2 Model 2 Abdominal Kinematic Equations 51
4.3 Multibody Equations of Motion 53
4.3.1 Model 1: Multibody Equations of Motion 53
4.3.1.1 Translational Dynamics 53
4.3.1.2 Rotational Dynamics 55
4.3.2 Model 2: Multibody Equations of Motion 58
4.3.2.1 Translational Dynamics 58
4.3.2.2 Rotational Dynamics 61
4.4 Chapter Summary 64

5 Performance Analysis of Bioinspired Vehicle Motion 65
5.1 Introduction 65
5.2 Longitudinal Flight 66
5.2.1 Dynamic Equations of Motion 67
5.2.1.1 Model 1: Aircraft Dynamics 67
5.2.1.2 Model 2: Aircraft Dynamics 68
5.2.2 Forces and Moments 69
5.2.3 Control Effectors 70
5.2.4 Aircraft Model Specifications 71
5.2.5 Simulation Environment 73
5.2.6 Aerodynamic Model for Simulation 74
5.2.7 Analyses and Results 75
5.2.7.1 Trim for Steady Cruise Flight 75
5.2.7.2 Steady Cruise Trim Analyses 76
5.2.7.3 Correction of Imbalance in Cruise Flight 79

5.2.7.4 Steady Pull up Manoeuvre 84
5.3 Lateral-directional Flight 90
5.3.1 Steady Turn Trim Analyses 91
5.3.2 Discussion 93
5.4 Summary 94

6 Multibody Control System Design **97**
6.1 Introduction 97
6.2 Explicit Equations of Motion 98
6.2.1 Abdominal Motion 100
6.3 Linearisation of Equations of Motion 101
6.4 Stability 102
6.5 Controllability and Observability 102
6.6 Control System Design 103
6.6.1 Linear Quadratic Regulator Control Theory 103
6.6.2 Linear Quadratic Integral (LQI) Control 104
6.7 Simulation and Results 105
6.7.1 Model Validation 105
6.7.2 Aircraft Linearisation 107
6.7.2.1 Aircraft in Trimmed Steady Cruise Flight 108
6.7.2.2 Linear State Space Model 108
6.7.3 Validation of Linearised Aircraft Model 110
6.7.3.1 Stability 110
6.7.3.2 Longitudinal Perturbation Response 110
6.7.3.3 Lateral-Directional Perturbation Response 112
6.7.4 Effect of Abdomen Mass on Longitudinal Stability 114
6.7.5 Aircraft Stabilisation and Control 115
6.7.5.1 Longitudinal Motion Regulator 116
6.7.5.2 Lateral-Directional Motion Regulator 119

6.7.5.3 Pitch Attitude Control . . . 121
6.7.5.4 Yaw Attitude Control . . . 125
6.7.6 Discussion . . . 129
6.7.6.1 Effect of Abdominal Mass on Longitudinal Stability . . . 129
6.7.6.2 Longitudinal Motion Regulator . . . 129
6.7.6.3 Lateral-Directional Motion Regulator . . . 131
6.7.6.4 Pitch Attitude Control . . . 132
6.7.6.5 Yaw Attitude Control . . . 133
6.8 Summary . . . 135

7 Articulated Appendage Test Bed **137**
7.1 Introduction . . . 137
7.2 Overview of Experimental Aircraft . . . 138
7.2.1 Hardware Description . . . 138
7.2.1.1 Flight Controller . . . 139
7.2.1.2 Global Positioning System . . . 140
7.2.1.3 Airspeed Sensor . . . 140
7.2.1.4 Wireless Telemetry . . . 140
7.2.1.5 Power Module . . . 140
7.2.1.6 Propulsion System . . . 140
7.2.1.7 Battery . . . 141
7.2.1.8 Control Surface Servos . . . 141
7.2.1.9 Mechanical Design of Articulated Mass . . . 141
7.2.2 Software Description . . . 142
7.2.2.1 Flight Controller Software . . . 143
7.2.2.2 Ground Station Software . . . 143
7.3 Theoretical Model . . . 143
7.3.1 Aerodynamic Model . . . 143
7.3.2 Actuator Model . . . 144

7.3.3 Control Effector Deflection Angles Calibration 145
7.4 Flight Testing Procedure 147
7.5 Model Comparison with Flight Data 148
7.5.1 Flight 1 – Articulated Mass in Longitudinal Flight 149
7.5.2 Flight 2 – Articulated Mass in Lateral-directional Flight 150
7.6 Discussion 150
7.7 Summary 152

8 Aerodynamic Loading Effects on the Appendage 155
8.1 Introduction 155
8.2 Aerodynamic Loading of Abdomen 156
8.3 Performance Analysis 159
8.3.1 Steady Cruise Flight 159
8.3.2 Quasi-steady Pull Up Manoeuvre 161
8.3.3 Discussion 162
8.4 Manoeuvring Using Abdominal Deflection 164
8.4.1 Manoeuvring Using Longitudinal Abdominal Deflection 165
8.4.1.1 Effect of Increased Abdominal Area on Longitudinal Manoeuvring 165
8.4.1.2 Effect of Abdominal Angular Speed on Longitudinal Manoeuvring 168
8.4.1.3 Discussion 170
8.4.2 Manoeuvring Using Lateral Abdominal Deflection 170
8.4.2.1 Effect of Increased Abdominal Area on Lateral Manoeuvring 170
8.4.2.2 Effect of Abdominal Angular Speed on Lateral Manoeuvring 174
8.4.2.3 Discussion 177
8.5 Summary 177

9 Conclusion and Future Work 179
9.1 Summary of Findings and Contributions 179

9.2 Future Work 183

A Athena Vortex Lattice Aerodynamic Models **185**

A.1 Input Geometry File 185

A.1.1 DISWA 185

A.1.2 Phantom FX-61 188

A.2 Output of Aerodynamic Data 191

A.2.1 DISWA 191

A.2.2 Phantom FX-61 193

B Articulated Mass Mechanism **197**

C Leg Movement in Hoverfly Flight **199**

C.1 Introduction 199

C.2 Observation Methods 201

C.3 Mass Estimation 203

C.4 Feasibility of Balance Based Hover Control 203

C.5 Discussion 208

C.6 Summary 209

Bibliography **211**

List of Figures

2.1 The forces on an aircraft in flight. 8
2.2 Fixed wing aircraft aerodynamic control effectors: (**a**) Conventional fixed wing aircraft. (**b**) Flying wing aircraft. 9
2.3 Lateral view of stroke plane of insect flight showing figure eight motion of the left wing tip. 14

3.1 Templates and anchor concepts for task-level behaviour in cockroach locomotion. 30
3.2 Outlines of representative dragonflies from different families. (**a**) Aeshnidae, *Epiaeschna heros*. (**b**) Libellulidae, *Libellula croceipennis* Selys. (**c**) Gomphidae, *Erpetogomphus designatus* Hagen. (**d**) Petaluridae, *Petalura ingentissima* 32
3.3 Comparison of a mosquito to a dragonfly: (**a**) Outline of a Culex mosquito, *Culex quinquefasciatus*. (**b**) Outline of an Australian Emerald dragonfly, *Hemicordulia australiae*. 32
3.4 The relationship between engineering and biology is a fundamental part of this thesis. 33
3.5 Screenshot of Mission Planner user interface. 39

4.1 Free flying dragonfly (Video taken from [214]). 43
4.2 Dragonfly in diving manoeuvre (Video taken from [215]). 44
4.3 Dragonfly (*Plathemis lydia*) in turning flight for prey capture (Video taken from [216]). 45

4.4 Description of the DISWA: (**a**) Photograph of an Australian emerald dragonfly, *Hemicordulia australiae*. (**b**) Reference points and coordinate systems of the dragonfly-inspired straight-wing aircraft (DISWA). 49

5.1 Dragonfly side view showing longitudinal tail actuation modes. (**a**) Tail contraction and extension. (**b**) Tail up down wag movement. 67

5.2 Phoenix airfoil. 72

5.3 Phoenix airfoil characteristics. (**a**) Lift curve. (**b**) Drag polar. 72

5.4 Aircraft model in Simulink. 73

5.5 Aircraft model with no abdominal deflection. (**a**) AVL model. (**b**) Mass distribution in XFLR5. 75

5.6 Trimmed steady cruise flight performance using Model 1. 77

5.7 Trimmed steady cruise flight performance using Model 2. 78

5.8 Model 1 trim in steady level powered flight for a range of airspeed. (**a**) Elevator deflection. (**b**) Power required. 82

5.9 Model 2 trim in steady level powered flight for a range of airspeeds. (**a**) Elevator deflection vs. airspeed. (**b**) Power required vs. airspeed. 83

5.10 Forces acting on the aircraft model in flight. 85

5.11 Model 1 aircraft pull up manoeuvre time response. (**a**) Airspeed. (**b**) Height. 88

5.12 Model 1 aircraft pull up manoeuvre time response. (**a**) Specific excess power. (**b**) Specific energy. 88

5.13 Model 2 aircraft pull up manoeuvre time response. (**a**) Airspeed. (**b**) Height. 89

5.14 Model 2 aircraft pull up manoeuvre time response. (**a**) Specific excess power. (**b**) Specific energy. 89

5.15 Plan view of showing abdominal articulation in turning flight. 91

5.16 Sideslip β and abdominal yaw ψ_T variation with airspeed for $\dot{\psi} = 1°/s$ in steady turn. 92

5.17 Sideslip β and abdominal yaw ψ_T variation with airspeed for $\dot{\psi} = 5°/s$ in steady turn. 93

5.18 Power required variation with airspeed. (**a**) $\dot{\psi} = 1°/s$. (**b**) $\dot{\psi} = 5°/s$. 93

6.1 Simulink diagram for actuator dynamics. 101

6.2 Linear quadratic regulator (LQR) control system block diagram. 104

6.3 Linear quadratic integral (LQI) control system block diagram. 105

6.4 Time response at trimmed steady cruise flight: (a) Flight trajectory. (b) Attitudes (ϕ, θ, ψ). (c) Linear velocities (u, v, w). (d) Angular velocities (p, q, r). (e) Control inputs $(\delta_e, \delta_a, T_n, \theta_T, \psi_T)$. 109

6.5 Response of longitudinal states due to elevator doublet input: (a) Forward velocity (u). (b) Vertical velocity (w). (c) Pitch rate (q). (d) Pitch angle (θ). (e) Height (H). (f) Control input perturbations $(\Delta\delta_e, \Delta\theta_T)$. 111

6.6 Response of longitudinal states due to abdominal pitch doublet input: (a) Forward velocity (u). (b) Vertical velocity (w). (c) Pitch rate (q). (d) Pitch angle (θ). (e) Height (H). (f) Control input perturbations $(\Delta\delta_e, \Delta\theta_T)$. . . . 112

6.7 Response of lateral-directional states due to aileron doublet input: (a) Sideway velocity (v). (b) Roll rate (p). (c) Yaw rate (r). (d) Roll angle (ϕ). (e) Yaw angle (ψ). (f) Control inputs $(\Delta\delta_a, \Delta\psi_T)$. 113

6.8 Response of lateral-directional states due to abdominal yaw doublet input: (a) Sideway velocity (v). (b) Roll rate (p). (c) Yaw rate (r). (d) Roll angle (ϕ). (e) Yaw angle (ψ). (f) Control inputs $(\Delta\delta_a, \Delta\psi_T)$. 114

6.9 Time histories of the longitudinal states: (**a**) angle of attack (α). (**b**) pitch rate (q). (**c**) pitch angle (θ). 119

6.10 Time histories of the longitudinal control inputs: (**a**) elevator deflection (δ_e). (**b**) abdominal pitch angle (θ_T). 120

6.11 Time response of the lateral states: (**a**) sideslip (β). (**b**) roll angle (ϕ). (**c**) roll rate (p). (**d**) yaw rate (r). (**e**) yaw angle (ψ). 123

6.12 Time histories of the lateral control inputs: (**a**) aileron deflection (δ_a). (**b**) abdominal yaw angle (ψ_T). 124

6.13 Time histories of the longitudinal states: (**a**) angle of attack (α). (**b**) pitch rate (q). (**c**) pitch angle (θ). 127
6.14 Time histories of the longitudinal control inputs: (**a**) elevator deflection (δ_e). (**b**) abdominal pitch angle (θ_T). 128
6.15 Time response of the lateral states: (**a**) sideslip (β). (**b**) roll angle (ϕ). (**c**) roll rate (p). (**d**) yaw rate (r). (**e**) yaw angle (ψ). 131
6.16 Time histories of the lateral control inputs: (**a**) aileron deflection (δ_a). (**b**) abdominal yaw angle (ψ_T). 132

7.1 Modified Phantom FX-61 flying wing aircraft. 138
7.2 Aircraft hardware components: 139
7.3 Articulated mass bob. 142
7.4 S5010 airfoil. 144
7.5 Aircraft model: (**a**) In AVL. (**b**) In XFLR5. 144
7.6 Set-up for left elevon calibration: (**a**) Upward deflection (**b**) Deflection angle estimation. 145
7.7 Articulated mass positions in longitudinal flight: (**a**) Neutral. (**b**) Intermediate. (**c**) Maximum. 146
7.8 Articulated mass positions in lateral-directional flight: (**a**) Neutral (**b**) Left. (**c**) Right. 147
7.9 Flight data signal processing showing the raw flight data and smoothed data. 148
7.10 Comparison of simulation and flight log data of the elevator δ_e, articulated mass pitch angle θ_T, pitch rate q 149
7.11 Comparison of simulation and flight log data of the aileron δ_a, articulated mass yaw angle ψ_T, roll rate p, and yaw rate r 150

8.1 Inclined cylindrical bar in a flow. 157
8.2 Variation of cylinder drag coefficient with Reynolds number [257]. 158
8.3 Variation of drag load functions with inclination angle. 159

8.4 Steady cruise flight performance parameters variation with abdominal pitch angle. The black, blue and red lines represent results for V=5, 10 and 15 m/s, respectively. 160
8.5 Pull up manoeuvre states time response. (**a**) Airspeed. (**b**) Height. 161
8.6 Pull up manoeuvre longitudinal control inputs time response. (**a**) Elevator deflection. (**b**) Abdominal pitch angle. 162
8.7 Pull up manoeuvre energy state and rate time response. (**a**) Specific excess power. (**b**) Specific energy. 162
8.8 Linear segment with parabolic blend (LSPB): (**a**) Angular deflection. (**b**) Angular velocity. (**b**) Angular acceleration. 165
8.9 Time history comparing the longitudinal states: (**a**) Velocity. (**b**) Height. (**c**) Pitch rate. 166
8.10 Time history of control inputs for longitudinal manoeuvre: Abdominal pitch angle, abdominal pitch rate and abdominal pitch acceleration. 167
8.11 Time history comparison of the longitudinal states due to abdominal pitch rate: (**a**) Velocity. (**b**) Height. (**c**) Pitch rate. 168
8.12 The forces on an aircraft in flight. 169
8.13 Time history of control inputs for longitudinal manoeuvre: Abdominal pitch angle, abdominal pitch rate and abdominal pitch acceleration. 169
8.14 Flight trajectories. 171
8.15 Time response comparison of the lateral-directional states: Velocity and height, roll angle and roll rate, pitch angle and pitch rate, yaw angle and yaw rate. 172
8.16 Time history of control inputs for lateral-directional manoeuvre: Abdominal yaw angle, abdominal yaw rate, abdominal yaw acceleration. 173
8.17 Flight trajectory due to rightward abdominal deflection. 174
8.18 Time response comparison of the lateral-directional states: Velocity and height, roll angle and roll rate, pitch angle and pitch rate, yaw angle and yaw rate. 175

8.19 Time history of control inputs for lateral-directional manoeuvre: Abdominal yaw angle, abdominal yaw rate, abdominal yaw acceleration. 176

B.1 Articulated mass mechanism components in openSCAD: (**a**) First half of the bob mass. (**b**) Second half of the bob mass. (**c**) Mechanism for mounting mass longitudinally. (**d**) Mechanism for mounting mass laterally. 197

C.1 Individual hoverfly of the the species *Melangyna viridiceps*: (a) in flight. (b) at rest. 201

C.2 First sequence extracted from mobile telephone video of hoverfly leg lowering and raising in flight. 202

C.3 Second sequence extracted from mobile telephone video of hoverfly leg lowering and raising in flight. 203

C.4 Outlines of dorsal and lateral views of a hoverfly: (a) scanned outline [268]. (b) approximated outline. 204

C.5 The configuration of a hoverfly in flight: (a) with raised legs, cg to rear. (b) with lowered legs, cg to front. 205

C.6 (a) Centre of gravity shift geometry when legs are lowered. (b) abstraction of forces (c) abstraction of angles 205

C.7 Morphological parameters definition. 207

List of Tables

5.1 Aircraft model (DISWA) physical properties. 73

5.2 Parameter constraints. 74

5.3 Physical constraints of longitudinal control inputs. 74

5.4 Steady level trim flight condition for Model 1 and Model 2 76

5.5 Disturbed DISWA mass properties without the tail. 81

5.6 Model 1 cases for correction of imbalance. 81

5.7 Trimmed steady cruise elevator deflection and power required for Model 1 cases. 82

5.8 Model 2 cases for correction of imbalance. 83

5.9 Trimmed steady cruise elevator deflection and power required for Model 2 cases. 83

5.10 Aircraft Model 1 pull up manoeuvre control effector comparison using $\Delta\delta_e$ or Δs_{tb_x}. 87

5.11 Aircraft Model 2 trim condition before pull up. 88

5.12 Aircraft Model 2 pull up manoeuvre control effector comparison using $\Delta\delta_e$ or $\Delta\theta_T$. 89

5.13 Physical constraints of lateral-directional control inputs. 92

6.1 Abdomen servo mechanism parameters. 107

6.2 Single-body vs multibody trim results at steady cruise trim condition. . . . 107

6.3 Aircraft initial state and control inputs at steady cruise trim condition. . . . 108

6.4 Effect of abdominal mass as a percentage of central body mass on longitudinal stability. 115

6.5 Simulation parameters for longitudinal motion stabilisation cases. 117

6.6 Comparison of settling times for the different longitudinal motion stabilisation cases. 118
6.7 Comparison of steady state error for the different longitudinal motion stabilisation cases. 118
6.8 Simulation parameters for lateral-directional motion stabilisation cases. . . 121
6.9 Comparison of settling times for the different lateral-directional motion stabilisation cases. 122
6.10 Comparison of steady state error for the different lateral-directional motion stabilisation cases. 122
6.11 Simulation parameters for pitch control (PC) cases. 125
6.12 Comparison of performance characteristics for the different pitch control (PC) cases. 126
6.13 Simulation parameters for yaw control (YC) cases. 129
6.14 Comparison of performance characteristics for the different yaw control (YC) cases. 130

7.1 Summary of important aircraft geometry 138
7.2 Turnigy 3300mAh 3S 30C lipo battery technical specifications. Source: Hobbyking.com 141
7.3 Hextronik HXT900 servo technical specifications. Source: Hobbyking.com 141
7.4 Turnigy TGY-4409MD servo technical specifications. Source: Hobbyking.com 142
7.5 Physical constraints of control effectors. 147
7.6 Physical properties of physical model for simulation. 149

8.1 Percentage average variation of steady cruise flight performance parameters compared to the simplified/inertial model 161
8.2 Energy manoeuvrability comparison using $\Delta\delta_e$ or $\Delta\theta_T$. 162
8.3 Percentage average variation compared to the simplified model with nominal abdominal area 166

C.1 Hoverfly parameters. 207

C.2 Initial centre of gravity locations in hover. 208

List of Abbreviations

AoA	Angle of Attack
APM	ArduPilot Mega
ARE	Algebraic Riccati Equation
ARP	Aerodynamic Reference Point
AM	Articulated mass
AVL	Athena Vortex Lattice
BET	Blade Element Theory
BID	Biologically Inspired Design
CA	Control Allocation
CoM	Center of Mass
CFD	Computational Fluid Dynamics
cg	Center of Gravity
DAE	Differential Algebraic Equation
DARPA	Defense Advanced Research Projects Agency
DISWA	Dragonfly-Inspired Straight-Wing Aircraft
DoF	Degree of Freedom
EoM	Equation of Motion
GPS	Global Positioning Unit
LHS	Left-hand Side
LQI	Linear Quadratic Integral
LQR	Linear Quadratic Regulator
LSPD	Linear segment with parabolic blend
LTI	Linear Time Invariant

MAV	Micro Aerial Vehicle
MIMO	Multiple-input Multiple-output
MMC	Moving Mass Control
MPC	Model Predictive Control
NAV	Nano Aerial Vehicle
NLTI	Nonlinear Time Invariant
NLTP	Nonlinear Time Periodic
NP	Neutral Point
PC	Pitch Control
PID	Proportional Integral Derivative
PIV	Particle Image Velocimetry
PWM	Pulse Width Modulation
RC	Radio Control
Re	Reynold's number
RHS	Right-Hand Side
SM	Static Margin
SMC	Sliding Mode Control
SPC	Stroke-Plane-Change
SUAV	Small Unmanned Aerial Vehicle
TEC	Trailing-Edge-Change
UAV	Unmanned Aerial Vehicle
VTOL	Vertical take-off and landing
wrt	with respect to
YC	Yaw Control

List of Symbols

A,O	Arbitrary rigid bodies A and O (Central body (B), abdomen (T) or aircraft (C),
	Body-fixed frames associated with rigid bodies A and O
a,o	First-order tensors (equivalent to a vector) associated with frames A and O
m^A, m^O	Mass of rigid bodies A and O, respectively (kg)
m	Total mass (kg)
$[*]^A$	Vector or tensor expressed in reference frame A
s_{oa}	Displacement vector of point o relative to point a (m)
S_{oa}	Skew symmetric matrix of s_{oa} (m)
V_A^o	Velocity of rigid body A relative to point o (m/s)
ω^{OA}	Angular velocity of frame O relative to frame A (rad/s)
$\mathbf{\Omega}^{OA}$	Skew symmetric matrix of angular velocity ω^{OA} (rad/s)
I_a^A	Inertia tensor of rigid body A about at point a (kg·m^2)
$[R]^{OA}$	Transformation matrix from frame A to O
$D^A(*)$	Rotational time derivative of a vector or tensor $*$ with respect to frame A
$\frac{d(*)}{dt}$	Ordinary time derivative of $*$
e	Output error of additional integral state
f_N	Normal drag loading function for an inclined cylinder
f_T	Tangential drag loading function for an inclined cylinder
g	Acceleration due to gravity (m/s^2)
i	Imaginary unit
$\mathbb{I}$	Identity matrix
H	Altitude/height (m)

H_∞	H infinity
F	External force vector (N)
M	External moment vector (N·m)
V	Airspeed (m/s)
T_n	Propulsive thrust (N)
c_{ref}	Reference wing chord (m)
b_{ref}	Reference wing span (m)
S_{ref}	Reference wing area (m^2)
$C_{(x,y,z)}$	Dimensionless aerodynamic coefficients for axial, side and normal force, respectively
$C_{(l,m,n)}$	Dimensionless aerodynamic coefficients for roll, pitch and yaw moment, respectively
u, v, w	Velocity vector components (m/s)
p, q, r	Angular velocity vector components (rad/s)
X, Y, Z	Position vector components (m)
α, β	Angle of Attack and sideslip angle (rad)
δ_r	Elevator deflection angle (rad)
δ_e	Aileron deflection angle (rad)
η	Elevon deflection angle (rad)
Δ	Represents a change from nominal/trim value
κ	Damping constant (N·m·s)
ρ	Air density (kg/m^3)
τ_l	Load torque due to gravity (N·m)
τ_a	Actuator torque (N·m)
ϕ, θ, ψ	Roll, pitch and yaw Euler angles (rad)
$\mathbf{x}, \mathbf{u}, \mathbf{z}$	state, input, output vector
$\mathbf{r}, \mathbf{y}$	Reference input signal, output signal
$\mathbf{A}, \mathbf{B}, \mathbf{C}, \mathbf{D}$	System state, control, output and feedforward matrices
$\mathbf{K}$	Optimal gain matrix

Q	State-weighting matrix
R	Control weighting matrix
J	Cost function
P	Algebraic Riccati Equation solution

Subscripts

act	Actuator
0	Initial/nominal value
i	Additional integral states
k	k_{th} rigid body
B, L, T	Central body, legs, abdomen
I, B, T	Inertial, central body and abdominal reference frames systems
l, r	left, right
lat	Lateral–directional motion
long	Longitudinal motion
max	Maximum value

Superscripts

$\dot{}$	First-order time derivative
$\ddot{}$	Second-order time derivative
$\hat{}$	Augmented matrix
$'$	Transpose of parameter
$^{-1}$	Inverse of parameter

List of Publications

Topical journal papers

[I] **Ogunwa, T.**, Abdullah, E., & Chahl, J. (2022). Modeling and Control of an Articulated Multibody Aircraft. Applied Sciences, 12(3), 1162.

[II] Chahl, J., Chitsaz, N., McIvor, B., **Ogunwa, T.**, Kok, J. M., McIntyre, T., & Abdullah, E. (2021). Biomimetic Drones Inspired by Dragonflies Will Require a Systems Based Approach and Insights from Biology. Drones, 5(2), 24.

[III] **Ogunwa, T.**, McIvor, B., Jumat, N. A., Abdullah, E., & Chahl, J. (2020). Longitudinal Actuated Abdomen Control for Energy Efficient Flight of Insects. Energies, 13(20), 5480.

Topical conference publications

[IV] **Ogunwa, T.**, & Chahl, J. (2020). The Role of Posture in Dragonfly-like Air Vehicles in Turning Flight. In AIAC19: 19th Australian International Aerospace Congress.

Other publications 2018–2022

Awang Jumat, N., **Ogunwa, T.**, Abdullah, E. J., Chahl, J., Romli, F. I., & Abdul Majid, D. L. (2021). Flapping Actuation using Temperature Feedback Control of Coated Shape Memory Alloy Actuators. Microsystem Technologies, 27(9), 3299-3311.

Tarr, A. A., Perera, A. G., Chahl, J., Chell, C., **Ogunwa, T.**, & Paynter, K. (2021). Drones: healthcare, Humanitarian Efforts and Recreational use. In Drone Law and Policy (pp. 35-54). Routledge.

Khanam, F.T.Z., Chahl, L.A., Chahl, J.S., Al-Naji, A., Perera, A.G., Wang, D., Lee, Y.H., **Ogunwa, T.**, Teague, S., Nguyen, T.X.B. & McIntyre, T.D., 2021. Noncontact Sensing of Contagion. Journal of Imaging, 7(2), p.28.

McIvor, B. A., **Ogunwa, T.**, & Chahl, J. S. (2020). Geometry of Efficient Electromagnetic Linear Actuators for Flapping Wing MAVs. Engineering Research Express, 2(4), 045027.

Perera, A. G., Law, Y. W., **Ogunwa, T.**, & Chahl, J. (2020). A Multiviewpoint outdoor Dataset for Human Action Recognition. IEEE Transactions on Human-Machine Systems, 50(5), 405-413.

Chapter 1

Introduction

This chapter introduces the background and motivation for this research, the aims and objectives, key research questions to be addressed, and outlines the structure of the thesis.

1.1 Background

The potential applications of unmanned aerial vehicles (UAVs) for both civil and military operations have steadily increased over recent years. A UAV is a pilotless aircraft that is capable of flying without the need for a human operator onboard. They can perform operations without jeopardising human safety, and can often operate more cost effectively than comparable manned systems [1]. They can be remotely piloted, in which case, some control is carried out remotely from a ground control station, or they can be operated autonomously, in which case, the UAV is capable of completing all control actions onboard, utilising the autopilot and sensor suite [2], [3]. UAVs vary widely in size, configuration, and performance characteristics due to the diversity of applications such as reconnaissance, surveillance, search and rescue, precision agriculture, remote sensing, aerial photography, and delivery. Therefore, there have been different classifications of UAVs according to various parameters [1]. Ultimately weight, size and configuration classes are most useful. Going beyond these descriptions, for rigorous purposes, is equivalent to taxonomy in the absence of phylogeny.

Size is one of the most common metrics used to classify UAVs, of which there are four categories. Ultra-small UAVs include nano aerial vehicles (NAVs) with a maximum wingspan length of 75 mm, and micro aerial vehicles (MAVs) with lengths between 75 mm and 150 mm [4]. Small UAVs, also known as mini-UAVs, have a maximum dimension between 150 mm and 2 m [5]. Medium UAVs, are UAVs with a wingspan between 2 m and 10 m, while large UAVs have dimensions greater than 10 m. Another common classification is based on weight, where there are ten classes of UAVs. Nano UAVs weigh less than 200 g, micro UAVs weigh between 200 g and 2 kg, mini UAVs weigh between 2 kg and 20 kg, light UAVs weigh between 20 kg and 50 kg, small UAVs weigh between 50 kg and 150 kg, tactical UAVs weigh between 150 kg and 600 kg, medium-altitude long-endurance and high-altitude long-endurance UAVs weigh between 600 kg and 1000 kg, heavy UAVs weigh between 1000 kg and 2000 kg, and super heavy UAVs have the largest weight between 2000 kg and 24950 kg [6], [7].

In terms of configuration, there are four major UAV configurations: fixed wing, rotary wing, flapping wing (inspired by birds and insects), and hybrid UAVs. Fixed wing UAVs are only capable of horizontal take-off and landing, and are characterised by good forward speed, range and endurance but typically have the inability to hover for practical purposes. Rotary wing vehicles combine high and low speed characteristics, including hovering and vertical take-off and landing (VTOL) capabilities at a high price in range and endurance compared to fixed wing aircraft . Hybrid UAV configurations combine the benefits of fixed wing UAVs with VTOL abilities often by having both propulsion systems and using them at different stages of flight [8]. Flapping wing vehicles are a relatively new group of UAVs, inspired by birds and insects, that offer an alternative technology with both VTOL and fixed wing characteristics, without duplicating lifting systems.

1.2 Motivation

Since the Defense Advanced Research Projects Agency established a MAV and NAV program in 1997 [9], academic interest in the development of small autonomous flying air vehicles has increased greatly. Biologically inspired (bioinspired) or biomimetic design continues to attract interest because it provides access to a huge biological repository of proofs of enduring aeronautical solutions that can be used for developing innovative technological craft. Insects have evolved over millions of years, developing features for flight to allow for predation and evasion of predators. Some insects demonstrate supermanoeuvrability by their ability to operate beyond the flight envelope limits of conventional fixed or rotary wing aircraft in a controlled way [10]. They have the capability to hover, glide, manoeuvre and switch between all three modes of flight. All of these are desirable characteristics for small UAVs that might be expected to operate in cluttered environments [5].

Although nature provides many examples of efficient sustained controlled agile flapping wing insects, there is yet to exist any man-made flapping aircraft that can rival the performance of natural flyers. Flight dynamics and aerodynamics of bioinspired flapping wing systems are more complex (and scientifically contested) than for fixed and rotary wing aircraft [11], and the development of bio-inspired flapping wing MAVs is not as simple as copying the outer mold line of biological systems, requiring a systems based approach and insights from biology [12]. In addition, engineers are confronted with design challenges such as microfabrication, prediction of stability, and control design for highly coupled fluid-structure interactions. Another hindrance to the widespread adoption of biologically inspired design is the knowledge gap that exists between application engineers who understand how to design aircraft, and biologists who understand how biological organisms behave in their natural environments [13].

For instance, observational studies [14]–[16] have shown that during flight, some insects actively change their body posture by exploiting the movement of body appendages, and hence, mass distribution, to produce forces and moments for propulsion and control [17], [18]. In

fact, active manoeuvring relies on an ability to optimise the benefits of three main physical mechanisms to control posture: aerodynamic lift and drag on wings and body [19], [20], control of the centre of body mass and thus distance to aerodynamic force vectors [17], [21], and body moments of inertia quantities and rates through active changes in body shape [22]. Yet, the aerodynamics of the wings and wing movements have been an almost exclusive interest of most past and recent flight dynamics modelling studies on animal flight [23]–[27]. Existing formulations of flight dynamics models do not adequately capture the effect of relatively heavy articulated appendages observed in insect flight, and very little is understood about the mechanisms for using the appendages in flight. Therefore, this thesis attempts to address this research gap through the development of flight dynamic models that efficiently capture salient appendage movements observed in insect flight and some associated effects of these movements. Taking inspiration mainly from the Odonata infraorder Anisoptera (dragonflies), an increased understanding of the various moving anatomical masses and their importance for balance, manoeuvrability, stability and control in insect forward flight is explored.

1.3 Aim and Objectives

The aim of this research is to investigate the effects of moving appendages on the forward flight dynamics of insects, focusing on performance, manoeuvrability, stability and control.

The objectives are:

1. To derive the multibody flight dynamics model for a dragonfly-inspired straight-wing aircraft (DISWA) with articulated appendage using a tensor-based approach

2. To implement the flight dynamics model for the DISWA in the MATLAB/Simulink environment

3. To investigate the utility of an articulated appendage and benefits they might provide in forward flight through simulation

4. To design a modern flight control system for a DISWA with multiple control effectors

5. To establish feasibility and demonstrate the application of articulated appendage-based control of a small unmanned aerial vehicle (SUAV)

1.4 Research Questions

To achieve the stated objectives, the following questions will be answered:

1. Can an efficient matrix-based framework for mathematical modelling of appendage movements be developed for simulation and control system design?

2. What are the effects of appendage movements on forward flight, considering dynamic/inertial effects only, and considering the combined aerodynamic and dynamic/inertial effects?

3. Is the multibody dynamics model suitable for modern optimal control law development for stabilisation and control?

4. Is this biologically inspired appendage movement feasible for controlling the flight of a SUAV?

1.5 Thesis Structure

The remainder of this thesis is structured as follows.

Chapter 2 is dedicated to the review of the literature, reporting on studies regarding the basic flight principles of aerospace vehicles and control effectors, as well as dynamics, stability and control of insects and insect-inspired systems.

Chapter 3 outlines the methodology used to answer the research questions and achieve the objectives of this research.

Chapter 4 contains a detailed derivation of the DISWA multibody flight dynamics models. The equations of motion are developed using a tensor-based invariant formulation of the Newton-Euler method.

In **Chapter 5**, the DISWA multibody flight dynamics models are used to simulate the dynamic effects of articulated appendages on steady forward flight performance and manoeuvrability.

In **Chapter 6**, a control system for the DISWA with a deflectable abdomen is designed and simulated. This includes linearisation of the nonlinear model and implementation of optimal control strategies for stabilisation and attitude control.

Chapter 7 uses a physical model to demonstrate the practicality of using a controllable appendage on a flying system. A SUAV system with articulated appendage was built and flight tested to investigate its utilisation for control in open loop.

In **Chapter 8**, the DISWA model with the deflectable appendage is extended to include aerodynamic effects. Studies on the dynamic and aerodynamic effects of the deflectable appendage on forward flight performance and manoeuvrability were conducted. Furthermore, the relative effects of various properties of the appendage were explored, including area and deflection rate.

Chapter 9 summarises the major conclusions of the thesis and provides future recommendations for the research.

Chapter 2

Literature Review

This study draws together two specific parts of the literature. One part replicates mechanisms and control paradigms that have been observed in insects, that have an application to small aircraft. Another part involves developing flight dynamics and control models for such aircraft using conventional nomenclature and extensions of established techniques, aiming to apply modern control methods. Therefore, the literature review is divided into three parts. The first part of this chapter introduces the basic forces of flight in aerospace vehicles. The second part reviews unconventional control mechanisms that have been implemented in aerospace vehicles, analogous to those observed in insect flight. The third part of this chapter reviews studies related to insect flight and by extension, insect-inspired air vehicles, including significant works in the areas of dynamic modelling, stability and control.

2.1 The Forces of Flight in Aerospace Vehicles

Basic aerodynamic principles involve the interaction between a solid object and the air flowing around the object, maintaining contact at all points. The forces acting on an aerospace vehicle depend on the vehicle flight regime (endo-atmospheric, exo-atmospheric, or both) [28].

Considering an aircraft in flight, due to physical contact with the air, pressure changes along its constituent parts create aerodynamic forces acting through the centre of pressure [29]. This force can be decomposed into a component perpendicular to the direction of the airflow, called

lift, and a component along the direction of airflow, called drag. Lift is always an upward force perpendicular to the direction of flight and it depends on several variables. Likewise, drag is a backward force that is highly sensitive to many factors, the main source of which is the skin friction between the air and the surface of the aircraft [30].

There are two other forces that act on the aeroplane: thrust, which is the propulsive force to move the plane forward, and the gravitational force which always points towards the centre of the earth due to the weight of the aeroplane. So, the lift force is what makes an aeroplane overcome its weight in the air, and thrust is what makes it move forward to overcome drag. For cruise or steady level flight, the aircraft is in equilibrium, meaning it is in unaccelerated flight with all the net forces (*Lift=Weight, Thrust= Drag*) balanced as illustrated in Figure 2.1 [29]. The four forces that affect the flight of an aeroplane are vectors, thus they have both magnitude and direction.

For exo-atmospheric vehicles on the other hand, the forces acting on the vehicle are weight and thrust. Lift and drag, which are atmospheric forces, are all but absent in the near-vacuum of space. Motion in flight then depends entirely on the parameters of these force vectors and the relationships between them. To control the vehicle, these forces must be manipulated precisely. Therefore, to achieve precise control of attitude, it is necessary to understand their properties and have the means to adjust their direction and magnitude.

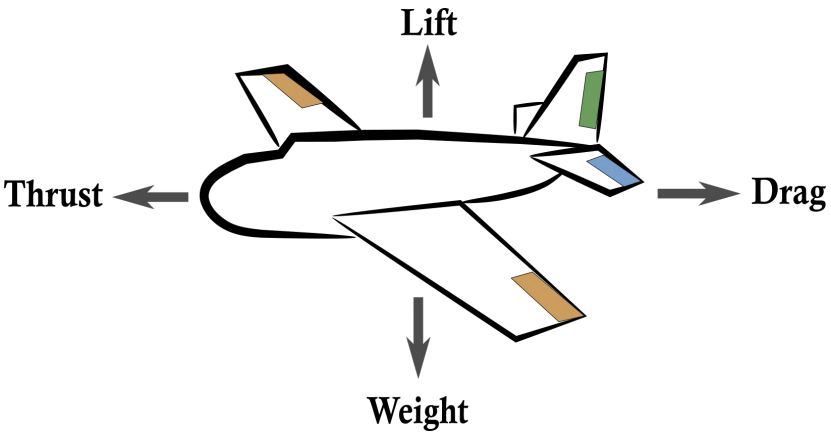


Figure 2.1: The forces on an aircraft in flight.

2.2 Moving Mass Control Effectors in Aerospace Vehicles

Aerospace vehicles may come in many configurations and sizes, but they all work on the same principle, which is to manipulate the forces of flight. The manipulation of the forces is accomplished through control effectors, which are used to change forces and moments acting on flight vehicles. The typical, or conventional control effector options are aerodynamic surfaces (aerosurfaces), propellers, thrust vector control, reaction control system, reaction wheels, control moment gyros , and torque rods, depending on the vehicle flight regime and mission requirements [28]. Figure 2.2 shows the conventional aerodynamic control surfaces used in some fixed wing aircraft.

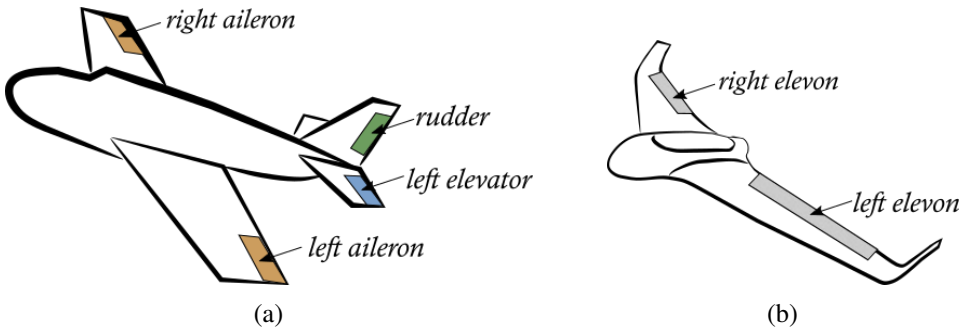


Figure 2.2: Fixed wing aircraft aerodynamic control effectors: (**a**) Conventional fixed wing aircraft. (**b**) Flying wing aircraft.

However, due to the nature of this study involving the application of biological observations to design, we focus on more unconventional aerospace vehicle control effectors in the literature, that have been implemented to complement or replace conventional control effectors, specifically the use of mass distribution variation or moving mass control in aerospace vehicles.

The use of a variation of mass distribution for flight control is not an entirely new concept. Mass distribution plays an important role in vehicle dynamics, and varying the vehicle's mass distribution affects the system's dynamics, stability and performance [31]–[33] , therefore, the variation of mass distribution for flight control has been adapted for various aerospace vehicles. Internally moving masses have been used in addition to or in replacement of traditional aerodynamic moment generating actuators for control. Moving masses generate

gravity induced moments and/or change the inertia properties to control the motion of the vehicle. Most efforts have focused on employing internal mass movement for trim, attitude, stability margin, detumbling of spinning spacecraft, trajectory, orbit, glide path and depth control.

In the early days of aviation, pilots would modify their body posture during flight, thus moving the aircraft's centre of mass to accomplish control or stability [34], [35]. The concept is of primary importance in the control of hang gliders [21]. In [36], Qin and Yang designed an attitude control system for a transatmospheric missile using three internal moving masses. Each mass was able to move along its respective axis to change the attitude of the missile. Simulation results showed the method was able to effectively control the missile, achieving static stability and attitude control.

Rogers and Mark [37]–[39] developed a seven degree of freedom (DoF) flight dynamics model for trajectory control of a projectile with an internal translating vibrating mass to study the potential of this control mechanism. Significant control authority was achieved with a mass of about 1% of the total projectile mass by vibrating the mass normal to the axis of symmetry and at the roll rate frequency. Nonlinear equations of a spinning vehicle with two internal moving elements were derived by Wang et al. [40] to investigate the use of linear moving-mass actuators for trajectory control. Results showed that the moving-mass controller was able to effectively control the vehicle's trajectory.

Chen et al. [41] investigated a stratospheric airship with various control systems, including traditional aerodynamic control surfaces, vector thrust, ballonet, and moving mass. One mass moved laterally, controlling roll angle, while the other moved longitudinally to regulate pitch angle. The results showed that moving mass control (MMC) outperformed control surfaces, since the moving masses had no effect on the drag of the airship.

The use of internal moving masses for flight control in SUAVs has also been demonstrated. Ertuk [42] was able to demonstrate the use of translational internal moving masses as a feasible alternative moment generation mechanism to conventional aerodynamic control

surfaces for SUAVs. Another study by Vengate [43], showed through flight tests that without ailerons, a small unmanned aircraft was able to control roll using two laterally moving internal masses.

MMC has been implemented in rotorcraft as well. For the control of a large quadrotor, Haus et al. [44], [45] implemented four translational movable masses in the quadrotor's four arms to change the centre of gravity and control the pitch and roll of the craft. Bouabdallah [46] used MMC for passive roll and pitch stabilisation of an indoor coaxial helicopter. The mechanism involved the use of two semi-circular guides for mass movement. A study presented by Bermes [47] successfully implemented a spherical moving-mass steering mechanism to improve the passive stability of a mini-coaxial helicopter in hover.

Moving masses are attractive for exo-atmospheric situations, where aerodynamic forces are not available. Spacecraft can also suffer from wobbling. A study carried out by Childs [48] identified the movement of astronauts (moving mass) inside a space station as the main source of wobbling motion. Accordingly, Childs designed and implemented a momentum exchange mechanism for attitude stabilisation with a single moving mass [49], [50]. The mechanism comprised two cylindrical rigid bodies axially connected by cables that was effective in generating torque to eliminate wobbling.

When angular velocity is high, docking and reentry of spaceships is unsafe for astronauts. Accidental collisions can cause dangerous uncontrolled tumbling. Edwards and Kaplan [51] using a MMC concept, designed a mechanism to convert tumbling motion into a simple spin and demonstrated it through simulation. Results from the study showed that a large space station tumbling after collision was able to stabilise using a movable mass of about 1% of its total mass.

Due to the low density of the upper atmosphere, aerodynamic controllers such as a rudder may be inadequate for reentry vehicles [52]. Because aerodynamic control surfaces are prone to ablation and degradation by hypersonic flow, internal moving mass actuation has been used to control reentry vehicles for decades [53]. Gao et al. [54] investigated the combined

use of moving mass and aileron control. Pitch and yaw were controlled by moving masses along two orthogonal rails, while roll was controlled by ailerons. The study demonstrated the benefits of combining these control methods. Su et al. [55] also demonstrated roll control for a non-axisymmetric reentry vehicle using a moving mass. The moving mass was able to provide robust stability throughout the flight without the need to modify controller gains. For other applications of moving mass in air and spacecraft, see [42]. Fluid transfer is another mass-shifting mechanism that has been used for control. For instance, because the Concorde could fly at supersonic speeds, changing the internal mass distribution by moving fuel helped with trimming the aircraft under transonic conditions [56]–[58].

2.3 Control of Aircraft with Multiple Control Effectors

One of the many attributes that emerged from the application of internal moving masses in vehicles is the concept of multiple effectors. The availability of multiple effectors with overlapping functions introduces the problem of control allocation in an overactuated system. Feedback control system theory forms the backbone to address the challenges associated with multiple-input-multiple-output (MIMO) systems. By comparing the reference signal to the actual response of the system, the controller calculates the control effort required [59], [60]. The response of an aircraft system can be represented by nonlinear equations of motion with six DoF , which can further be divided into longitudinal and lateral–directional parts respectively, describing pitching and rolling–yawing motions. Using the dynamics of each of these parts, individual flight controllers can be developed. Analysis of linear systems is performed using concepts and tools that facilitate control. Compared to nonlinear system control theory, linear system control theory presents a tractable solution and has been used extensively in aircraft flight control [59]. The Proportional Integral Derivative (PID) controller is the most widely used controller in real-world applications and has been used for flight control as in [61]–[66]. However, the gain of the controller needs to be iteratively tuned, which consumes time and effort. Of the more robust control methods, H_∞ control and sliding mode control (SMC) are some popular choices [67]–[71]. However, H_∞ control is conceptually

difficult and challenging to implement because it requires in-depth mathematical knowledge and model information. On the other hand, SMC is susceptible to chattering due to switching of the high-frequency control [72]. Dynamic inversion is another common control method used for flight control [61], [73]. Although this method is intended for nonlinear systems, estimation of the analytical inversion of nonlinear systems online is very difficult.

Optimal control is another control design approach, which has the advantage of being able to provide the best possible solution for a given cost function. Popular optimal control schemes include linear quadratic regulator (LQR), linear quadratic integrator (LQI), and model predictive control . Such schemes provide the optimal solution, and can also include multiple loop feedback at the same time [60], [65], [74], [75]. Control Allocation (CA) is another strategy that has been developed to handle overactuated systems, which answers the question of how to distribute control action among a redundant set of effectors to achieve a control design. In control allocation, actuator selection is separated from the controller task so that the controller only handles virtual control [76]. Common methods for solving the control allocation problem include optimisation-based CA [77]–[79], direct CA [80] and daisy chaining CA [81], [82]. A detailed description of these methods can be found in [76], [80], [83].

2.4 Insect Flight and Biomimetic Vehicles

The study of insect flight and insect-inspired air vehicles are inherently linked. This section reviews studies related to the aerodynamics, flight dynamics, stability and control of insect flight and by extension, insect-inspired air vehicles.

2.4.1 Aerodynamics Modelling

Insect flight comprises flapping flight and fixed wing (non-flapping) flight modes. Each wing of the insect is generally defined by three degrees of freedom with respect to (wrt) a stroke plane, with the wings able to actively pitch about the wing root and deviate from the stroke

plane. In hover, the three DoF of the wing can be defined such that the wing tip traces a figure eight pattern with respect to the wing root (see Figure 2.3). An insect's flapping cycle comprises of a moving forward (downward stroke) and a moving backward (upward stroke) motion, where the insect may flip its wing at the end of each stroke.

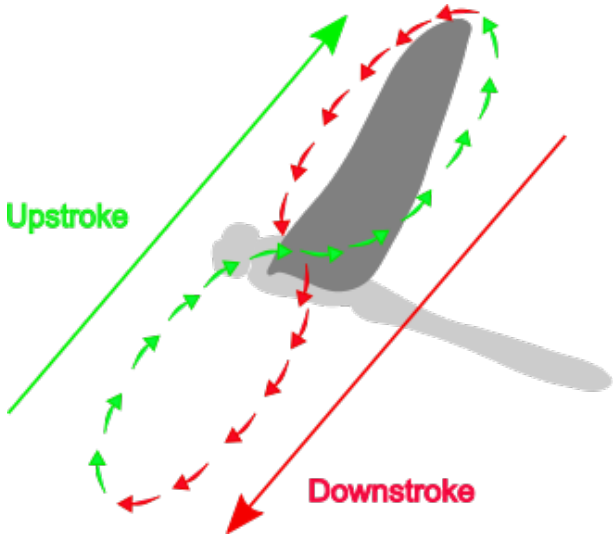


Figure 2.3: Lateral view of stroke plane of insect flight showing figure eight motion of the left wing tip.

The aerodynamics of flapping insects are significantly different from those of fixed and rotary wing flight vehicles due to their low Reynolds number. Over the past decade, the three major methods that have been used for studying low Reynolds number flow properties of flapping flight, and estimating aerodynamic forces: (1) computational simulations, (2) experimental studies, and (3) simplified flapping wing aerodynamic models. These methods will be discussed in the paragraphs that follow [84], [85] .

Initially, researchers attempted to evaluate insect flight properties and estimate aerodynamic forces using classical theories. They offered a variety of simple models based on momentum theory, blade element theory (BET), and vortex ring theory [86]–[90]. BET is by far the most popular theory employed for flapping wing aerodynamic analysis. Initially designed for propellers, the BET was modified by Osborne [91] for flapping wing flight. The first theoretical work on unsteady aerodynamics was performed by Theodorsen [92]. The theory used in the study was based on potential airflow around an airfoil or wing undergoing small amplitude

oscillations. The study was mainly concerned with the lift force produced. Garrick [93] subsequently extended the study to predict thrust using two different methods. The first method was based on energy and the second was based on pressure distribution around the airfoil. Garrick considered the wake vortices responsible for producing horizontal thrust, as identified by Von Karman [94]. Some studies have also applied a combination of the momentum and blade element theories. Willmott and Ellington [95], used the quasi-steady blade element momentum theory approach to develop and analyse the aerodynamics of insect flight. For every flapping cycle, the induced velocity was assumed to be constant and the instantaneous velocity could be determined for any location on the wing span. A number of studies have been carried out over the years as an extension of the works originally done by Theodorsen, Von Karman, and Garrick [92]–[94]. A theoretical model of insect flight was proposed by Żbikowski [96] based on velocity potential and the circulation method used by Von Karman [94]. Żbikowski focused on linear attached flow and the nonlinear leading-edge vortex and presented a linear theory with nonlinear corrections. A similar method was used by Pedersen [97] to predict the aerodynamic forces on the wings of an insect in hover. Minotti [98] also used an approach similar to Żbikowski's circulation approach. The study modelled the leading-edge vortex as a single discrete vortex shed from the leading edge. Although, initially for a 2D airfoil, Minotti extended the approach to a 3D wing using a factor of the square root of the non-dimensional second moment of wing area and the wing tip velocity. Ansari [99] developed a novel theoretical approach for modelling insect flight using a set of coupled nonlinear equations. The approach considered a flat plate wing section with leading and trailing edge separations and assumed potential flow. Ansari's approach was quasi-three-dimensional, as the two-dimensional approach was extended using BET. However, Ansari's method is limited by its inability to capture tip vortices Prosser [100].

For experimental studies, living insects and prototypes were used. Because of their small size and high flapping frequency, experiments with live insects are problematic. To examine the aerodynamic mechanisms, prototypes often use one or two wings with simplified kinematics. Experimental techniques that have been applied to study the aerodynamics of insects include

various flow visualisation techniques like slow motion filming, kinematic motion response monitoring using force transducers, Particle Image Velocimetry (PIV) and high-speed photography. Test areas where these techniques were applied include wind tunnels, water tunnels and open air. Weis-Fogh [101] captured the wing kinematics of small insects like the wasp, *Encarsia formosa*, in hover and proposed that insects use a "clap-and-fling" mechanism to possibly increase the forces produced in hover. However, Sane [102], observed that not all insects use the clap-and-fling mechanism. Sane and Dickinson in [103] and [104], used Digital Particle Image Velocimetry to measure the aerodynamic forces for a scaled mechanical wing model of a fruit fly, immersed in oil. The setup of the scaled-up wing used in the study made it easier to measure the forces. In another study, Willmott and Ellington [95], using smoke visualisation, observed the flight of *Manduca sexta* and a hawkmoth-inspired robotic wing. The study identified the leading-edge vortex and spanwise flow as essential mechanisms for insect flight. Using instantaneous force estimation together with flow visualisation, Lentink and Dickinson [105] attempted and failed to derive the relationship between forces involved in the flight of fruit flies (*Drosophila melanogaster*) due to the time delay experienced in obtaining force estimates. Nagai and Isogai [106] in a water tunnel, experimentally investigated the aerodynamic characteristics of a mechanical model mimicking the hovering and forward flight kinematics of a bumblebee. The flapping and feathering motions were independently driven using a controller and two stepping motors. The force and moments measured from the experiment demonstrated that the use of trapezoidal and sinusoidal motions to predict insect flight kinematics is acceptable to a reasonable extent. In an open circuit wind tunnel, Ren et al. [107] also used the PIV technique to visualise and characterise the near wake flow field associated with flapping flight.

Computational simulations, such as computational fluid dynamics (CFD) simulations, have become a viable tool for exploring flow mechanics and measuring aerodynamic forces since the introduction of computational methodologies. Many studies have analysed flapping flight aerodynamics using CFD simulations, with varying degrees of success [102], [104], [108]–[110]. Liu and Sun [111] applied CFD to simulate the kinematics of a single dronefly

wing in hover. In a similar study, Sun and Tang [112] adapted the same CFD code to simulate unsteady flow around the wing of a fruit fly model. For a hawkmoth wing in hover, Liu and Kawachi [113] applied CFD to study how the leading-edge vortex enhances lift production. Wu et al. [114] used a combination of CFD and equations of motion to simulate the hovering flight of two insects: the hawkmoth and the dronefly.

The ability to predict the aerodynamic performance of flapping wing micro air vehicles (FWMAVs) quickly is critical during the preliminary design, control, and optimisation phases. Experimentation and computational simulations, on the other hand, have time and resource constraints. As a result, simpler aerodynamic modelling approaches are more applicable [115]. Many researchers have made significant progress in establishing various aerodynamic modelling approaches for predicting flapping wing aerodynamics with differing fidelity levels. However, due to the complexity and specific unsteady flow characteristics of flapping wings, flapping wing aerodynamic modelling approaches continue to encounter significant difficulties and challenges. A more detailed review of aerodynamic modelling of flapping wing can be found in Ansari et al. [116], Taha et al. [117], Chin and Lentink [118], and Xuan et al. [119].

2.4.2 Flight Dynamics Modelling

The reproductive efficiency and survival of many animals depend on their locomotion ability during migration, territorial defence, foraging, predation and avoidance behaviours [120]. During aerial locomotion, controlling body posture is a necessary task as it is linked to the production and regulation of forces for propulsion, as well as the corresponding moments for control [17], [18]. Although for aerial locomotion, the moments are largely due to the control of the aerodynamics of the wings, an increasing number of studies show that the aerodynamics of body appendages such as the legs and abdomen are also important.

Prior research on the importance of body appendages for force and moment generation in actively flying animals was largely observational, done on insects, including fruit flies [14],

[121], [122], house flies [123], orchid bees [124], moths [125], [126], honeybees [127] and butterflies [15]. Several videos by Rüppell show dragonfly abdominal movements during flight [16]. The study conducted by Bode-Oke [128] also found some abdominal movement from the kinematic analysis of dragonfly flight. This theory was tested using visual stimulation that mimicked yaw rotations, in which flying tethered flies bent their rear legs and abdomen horizontally to the inside of the intended turn [121]–[123], [129]. In contrast, visual stimulation that mimicked body-pitching caused the abdomen to bend upward during the upward motion of the visual pattern [130]–[132]. Abdominal steering is adequate for the maintenance of body posture in the hawkmoth, according to mathematical models [125], [126], [130], [133]. Some insects, such as desert locusts, flex their abdomens in response to changing airflow conditions in addition to the visual stimulus [134]. This behaviour is said to resemble an aerodynamic rudder that aids the animal in orienting itself into the direction of the wind during flight [135], [136]. In the flight of monarch butterflies, abdomen undulation has been shown to improve stability, and reduce energy and power consumption [137], [138].

Establishing mathematical models for dynamic systems is important in areas such as control design and performance analysis. Flight dynamics of flapping wing systems is more complex than that of fixed and rotary wing aircraft, however, efforts have been made to develop flight dynamics models of insect-like MAVs for various flight conditions. The common approach in the literature involves using the conventional single-body equations of motion aircraft model, ignoring the effects of moving parts such as the wings on the entire system. Khan and Agrawal [139] used the standard aircraft model to demonstrate flapping wing micro air vehicles in hover. A quasi-steady aerodynamic model was used to estimate the forces generated by the wings, however, the inertial effects of the wings were neglected. The rigid body dynamic equations of motion for flapping flight were developed by Gebert et al. [140], however, according to Sun et al. [141], the reliability of the formulation used was limited by some errors. Sun et al. in [141] claimed that the equations developed by Gebert et al. in [140] lacked some expected terms given the assumptions made by Gebert et al. [140] and therefore, re-derived the equations of motion specified for hovering flight. Using averaging

theory, a time-averaged longitudinal model of an insect was developed, while neglecting the effects of the inertial and gravitational forces and moments of the wing. The application of averaging theory for insect inspired flapping wing air vehicles was introduced by Schenato et al. [142], [143]. In using this theory, for insects that have high flapping frequency, only the wingbeat-cycle-averaged aerodynamic forces and moments influence the body, therefore, a simplified time-averaging insect model can be developed and used for analysis and control design.

What has been observed in the literature is that for large aircraft, in almost all instances, the standard single rigid body flight dynamics modelling approach is used and the effects of the movement of individual parts are ignored. While large aircraft could be designed with dominant multibody characteristics, thus far, there is no indication of such vehicles in the literature. As the size of the aircraft decreases, however, these sub-component motions such as wing and abdominal motions can become larger and have larger effects, resulting in significant changes of the combined centre of gravity (cg) position and moment of inertia of the aircraft, and interactions between the various parts of the aircraft. To capture these effects, an insect inspired MAV is better modelled as a multibody dynamic system.

The formulations of EoMs for multibody dynamics are discussed in numerous works in the literature (e.g. [144], [145]). However, there are two basic principles for these methodologies: either they are founded on the principles of analytical mechanics and/or Newtonian mechanics (Newton's laws of motion) [145]. The application of Newton's Second Law lies at the heart of engineering mechanics, and it is the most fundamental and commonly used of all modelling techniques for formulating equations of motion for dynamical systems. This method, which is essentially a vectorial approach employing an inertial reference frame, analyses the motion of a system using concepts such as force and momentum [146]. All motion variables (displacements, velocities and accelerations) are expressed in this reference frame and forces are used to describe the interaction between bodies, including the effects of constraints. For simple systems with few degrees of freedom, this is a relatively straightforward task, however, for systems with higher degrees of freedom, the consideration of all constraint forces is

laborious and the resulting vectorial algebra is cumbersome [146].

While Newton's second Law uses vectorial mechanics to derive dynamical system equations of motion, the analytical/Lagrangian formulation uses Hamilton's principle to obtain scalar equations. Generalised coordinates are allowed instead of physical ones, making them more versatile. Kinetic energy, potential energy, and work are then expressed using these generalised coordinates. Lagrange's formulation only requires the computation of first order time derivatives (velocities) for each body, which are simpler and easier to compute than accelerations. In addition, the approach is invariant to the coordinate system and eliminates non-working constraint forces. Therefore, it can be an efficient way of deriving the equations of motion for systems with high degrees of freedom [146], [147]. However, there are some limitations associated with the use of Lagrangian formulation. First, the number of partial derivatives required increases significantly for systems with higher degrees of freedom. Furthermore, the Lagrangian formulation prohibits the routine incorporation of modifications to a system's mathematical model. The equations of motion must nearly always be completely rewritten for such an endeavour. Scalar and sophisticated algebraic formulations prevent analysts from making intuitive adjustments to motion equations. This labour-intensive re-formulating procedure hinders model fine-tuning. Furthermore, the acceleration terms in Lagrange-derived equations of motion tend to be strongly coupled, and integration and decoupling are needed to find a solution. In most cases, this involves matrix inversion, which is not always possible for systems with higher degrees of freedom, whereas, computationally intensive numerical inversion is necessary at each time step during integration, which slows down solution times and simulations. Kane's method incorporates the benefits of Newtonian and analytical mechanics. It applies virtual power theory and avoids calculating internal forcing and the differentiation of energy functions. However, it still necessitates a lengthy re-derivation of the EoMs whenever a new body with more DoFs is introduced to the system [145], [148].

Various methods/formulations have been utilised to derive multibody equations of motion for air vehicles including Newton–Euler, which uses Newtonian mechanics [42], [140], [149],

[150], Lagrange's energy-based methods [137], [138], [151], [152] and D'Alembert's principle [153], [154], which use analytical mechanics, and Kane's method [155], [156] which uses a combination of Newtonian and analytical principles. Although the application scope may vary depending on particular applications, all approaches for collecting the EoMs are essentially comparable.

Regarding insect-inspired aircraft, most of the multibody flight dynamics models in the literature focus on the degrees of freedom associated with wing motion. Lasek and Sibilski [157] developed one of the first multibody models for flapping wing flight. Gibbs-Appel equations were used to derive the equations of motion for simulation and the degrees of freedom of the wings were limited to two. In Jackson et al. [158], a trajectory optimisation problem was proposed for a FWMAV, modelled as a system of three bodies, where the inertial effects of the wings were included. Bolender used Kane's equation in [155] to derive the equations of motion for a FWMAV with four rigid bodies. The derivation of the inertial and active forces for the wings was limited and the degrees of freedom of the wings were also limited to two. In [140], Gebert et al. used the Newton-Euler method to derive the multibody equations of motion (EoMs) for a FWMAV. The inertial effects of the wings were included, however, simulations were not presented to validate the developed model. To investigate the use of articulated wings for control by controlling the dihedral angle of the wings, Paranjape in [159] developed multibody EoMs using the Newton-Euler method. The model incorporated dynamic centre of gravity variation using the combined centre of mass of the aircraft as the reference point. A tensor-based approach of the Newton-Euler method was used in [150] to derive a simulation model for a FWMAV and only the effects of the wings were considered. In [23] the equations of motion for flapping wing micro aerial vehicles were derived using D'Alembert's principle. The inertial effects of the wings were included as the developed model was used to analyse the importance of the mass of the wings to flight dynamics stability and control. Hassan and Taha in [24] also used D'Alembert's principle to derive the multibody flight dynamics equations of motion of FWMAVs, including the wing inertial effects. The equations were then used to analyse the longitudinal flight dynamics of FWMAVs near hover.

Fewer studies have considered the effect or role of abdominal articulation. A nonlinear model of a dragonfly-like flapping-wing MAV was developed by Du [160]. The study considered the effect of the head and abdomen in developing the equations of motion of a dragonfly-like MAV; however, their movements were not investigated with regard to their effects on flight, stabilisation or control of the model. Dhyr et al. [130] developed a model to examine the active role of the abdomen in the hawkmoth. However, the model was obtained using a phenomenological, system identification approach. Another study by Tejaswi et al. [137], [138] developed a model of the dynamics of a flapping-wing flyer, inspired by monarch butterflies. The model was, however, developed using Euler–Lagrange equations to examine the use of abdomen undulation to improve stability and reduce energy and power consumption.

2.4.3 Stability Studies

Stability describes the ability of an aircraft to return to its equilibrium position after being disturbed from it, without control intervention [161]. For stability analysis, two major approaches have been observed in the literature. The first approach involves averaging the dynamics of the system over one flapping cycle such that the nonlinear time-periodic (NLTP) system can be converted to a nonlinear time invariant (NLTI) system. The NLTI systems can then be linearised to a linear time invariant (LTI) system, where the eigenvalues can be used to check the matrix stability. The second approach involves the use of Floquet theory which is suitable for linearised time-periodic systems [117]. Details of the Floquet theory for stability analysis can be found in [162].

Initially, specific insects were studied for insight and understanding into flapping flight stability. Using the desert locust, *Schistocerca gregaria*, Taylor and Thomas [163] performed the first analysis of the dynamics stability of insects. Based on the assumption that the wing beat is not enough to cause excitement to the central body modes, the study ignored the wing mass and coupling terms associated with it. Experimental methods were used to estimate the stability derivatives, using the equations of motion for standard aircraft. Taylor and Żbikowski later on in [164], expanded the works by Taylor and Thomas [163] to a NLTP dynamics model, using

the same experimental methods and assumptions as before where the wing inertial effects were neglected. The same approach was used by Sun and Xiong [165] to analyse the stability of a bumblebee in hover. The averaged values of aerodynamic force and moments were used and stability derivatives were obtained using CFD. The results from the study showed that for a linearised system and for the longitudinal axis, the oscillatory mode of the bumblebee is unstable. Also, for the open loop system, destabilisation of the longitudinal axis was a pitching moment effect which is enhanced by improper phasing between flapping and pitching motions of the wings.

Sun and Wang [166] used the same methodology mentioned above to analyse the dynamic stability of four other insects (crane fly, dronefly, hawkmoth and housefly) in hover. The use of standard aircraft equations of motion was justified given two conditions: that the wing effects compared to the body are very small and that these effects for one flapping cycle are approximately zero. The values of the stability derivatives were also obtained using CFD and the resulting model was used to analyse the eigenvalue modes. The Eigenvalues indicated the presence of two stable modes and one unstable mode. The authors indicated that the rigid body assumption may not be suitable for analysis of the large insects studied and suggested the assumptions needs to be analysed further for validation.

Sun and Xiong [165] took the analysis of the bumblebee further for forward flight. Linear stability analysis was conducted using varying forward flight speeds from 0 to 4.5m/s. It was observed that for speed values less than 1.0m/s, the system presented two stable modes and one unstable mode but with a speed value of about 2.5m/s, the longitudinal dynamics was neutrally stable. The modal structure finally indicated two stable and two unstable modes. In a comparative study by Taylor and Thomas [163], different results were presented, where for faster forward flight speeds, the modal structure observed was similar to that in hover. It is important to note that two separate insects were used and the methods employed to determine the stability derivatives were also different. Another method which involved coupling between Navier-Stokes equations and equations of motion was used by Wu et al. [114] to derive the hover solution for a hawkmoth and a dronefly. The uniqueness of this study was in the fact

that body of the insect model was not fixed. Also, the focus was on longitudinal motion for hover and lateral motion was ignored. Results were similar to that from biological studies of hawkmoths and droneflies. The coupling wing effects were also neglected.

Zhang and Sun [167] evaluated the validity of the assumptions made in [165] for the hawkmoth and dronefly. The effects of disturbances were introduced and numerical simulations obtained. Results were similar for both insects for three flapping cycles. Because of the Hawkmoth's low flapping frequency, the conclusion validated the use of an approximate model for all insects. Using a quasi-steady aerodynamic model, Faruque and Humbert [168], [169] estimated the average forces and moment for a Hawkmoth based on the equations of motion for a standard aircraft. Frequency based system identification methods were employed to obtain the system and control input matrix for the hover flight condition. For longitudinal motion, one unstable oscillatory mode and two subsidence modes were observed for an open loop system. In the numerical analysis of a hawkmoth in hovering position carried out by Gao et al. [170], a stable modal structure was observed. This study did not use the popular sinusoidal assumption for wing stroke but used actual wing kinematics instead. The numerical analysis presented two subsidence modes and a stable oscillatory mode. The authors also analysed the coupled and decoupled closed loop lateral system and observed the system to be stable in both cases with one stable oscillatory mode and two subsidence modes. The difference between the coupled and decoupled systems was only in magnitude. Zhang and Sun [167] used a similar approach in the lateral motion analysis of a dronefly model and observed a stable oscillatory mode, one stable subsidence mode and one unstable subsidence mode. Bolender [171] also examined the open-loop stability of a flapping wing MAV in hover.

A two-dimensional quasi steady aerodynamic model was used and the Floquet theory [162] was adapted for stability analysis. Using a multibody model with a rigid central body, the body of the point mass as well as the multibody was observed to be unstable. Two insect-inspired FWMAVs with various methodologies for generating control moments (Stroke-Plane-Change (SPC) and the Trailing-Edge-Change (TEC)) for the longitudinal and lateral attitude controls were compared in terms of hovering stability by Nguyen et al. [172]. The results showed that

the SPC's rapid and slow subsidence modes in longitudinal and lateral motions stabilised faster than the TEC's, whereas, the SPC's lateral and longitudinal divergence modes were both more unstable than the TEC's. In [173], Hassan and Taha developed a reduced-order three DoF multibody longitudinal flight dynamics model to analyse the stability of a FWMAV near hover. The stability analysis using first order averaging yielded an unstable system at hover, while second order averaged system proved to be stable in hover.

2.4.4 Control Studies

Control strategies for FWMAVs in the literature span linear and nonlinear control. Doman et al. [174] designed a control system for the FWMAV developed by Wood [175]. The aerodynamic model used was based on that of Sane and Dickinson [103]. Using cycle-averaged values of aerodynamic forces and moments, a six DoF control method was presented. The method entailed the use of a bob-weight for pitch control and split-cycle frequency modulation for varying the frequency during downstroke or upstroke. The work was expanded when the authors developed a control system for a near hover condition using the nonlinear equations of motion for a standard aircraft. The mass of the wing and associated effects were neglected. Due to the flight condition considered in the study, each degree of freedom was reduced to a one-dimensional second order system such that every degree of freedom acted like a second order damped harmonic oscillator. Also, the pseudo-inverse method was used to estimate the control required by each degree of freedom, applied only at the end of a wing stroke. The command followed by the inner-loop controller was provided by an outer-loop controller which allowed the desired trajectories to be entered. This work was further expanded to consider wing bias, increasing the number of inputs to four. This new inclusion in the model made six degree of freedom control possible and also enabled asymmetric lateral forces to be generated.

In a bid to further understand six degree of freedom control, Serrani [176] presented a nonlinear robust control for a one DoF FWMAV. Augmentation of the system was achieved using a set-point error tracking method. The authors also designed robust control for a three

DoF FWMAV using the flight dynamics model developed by Bolender [171]. Control was achieved by varying the stroke plane angle and the wing beat frequency. Again, the set point tracking method was used to increase the vertical dynamic states, while other positions of the FWMAV were controlled directly. The results demonstrated the effectiveness of the control method as the set point tracking command was achieved in about 60s. Deng [142] designed a switch controller for a biomimetic insect using standard aircraft equations of motion and time averaged moments and forces. The controller was successfully able to control the insect-like air vehicle for hover. Although the wings were given three DoFs, it was represented as one DoF in the model. To enable proper stroke movements, a control strategy was devised with the use of averaging and linear quadratic regulator (LQR) theory.

Minglang et al. [177], [178] demonstrated the possibility of a six DoF control for the model developed in [142]. Four control inputs were used, parameterised and coupled. For the wing, the control was for delayed or advanced rotation and change in mid-stroke angle of attack. Results of the simulation showed the FWMAV was successfully controlled. The results were further expanded to use time-periodic feedback control for attitude stabilisation. Using time averaged moments, forces and dynamics and given that the number of inputs was the same as the degrees of freedom of the system, the controller was able to stabilise the system. Sun and Wang [166] used the analysis from a previous study to model an insect in hover, using a linear time-invariant model and four control inputs; a change in flap offset, a change in flap amplitude, a differential change in angle of attack (AoA) and an equal change in angle of attack. The aerodynamic forces were calculated using CFD. Xiong and Sun [179] also applied the linear time invariant technique to stabilise the bumblebee model previously developed. Forward flight and hover were considered in this study. The study concluded that the system was controllable for all forward flight speeds considered. With active control present using linear theory, the system was stable. The work on control for the study was taken further by Wu et al. [114] to include control input selection for transition from hover to slow forward flight.

Geder [180] included actuators and sensors in their model and achieved control for turning,

forward flight and hover control using Proportional Integral Derivative (PID) control and an extended Kalman filter. Fuzzy neural networks have also been applied for FWMAV control. For instance, Guo [181] developed a neural network controller based on the study by Hu [182], that could effectively stabilise the orientation and position of a biomimetic robot. Cheng and Deng [183] derived the linear dynamics and control of a fruit fly, Drosophila, in near hover. The body was modelled as three rigid body ellipsoids and the wings with two degrees of freedom with respect to the stroke plane. The model neglected the effects of change in the angle of attack on aerodynamic forces and also used the differential change in stroke plane angle, the equal change in mean position of the right and left wings and the differential change in stroke amplitudes as control inputs. Although the open loop system was initially unstable, it was stabilised using selected control input choices and proportional control. A bounded, nonlinear state feedback control was presented by Rifai et al. [184] for a FWMAV model. The model was based on the equations of motion of a standard aircraft and average moments, forces and dynamics were used. From an initial condition, the controller was able to bring the model to equilibrium even under the influence of disturbances. Faruque and Humbert [168], [169] were able to demonstrate controllability for a model from an earlier study by using two of the available control inputs (stroke plane change, flapping magnitude change, change in angle of attack between the downstroke and upstroke and flapping offset). The most effective control input choices from the literature include changes in the stroke plane and angle of attack changes between downstroke and upstroke.

2.5 Conclusion

Although significant progress has been made towards understanding the mechanics of insect flight, it is clear that our knowledge in this area is far from complete as the flight characteristics of biological flyers far exceed any available technological flyers on the same scale. A review of the literature identified some key knowledge gaps in the area of insect flight, which underpins the scope of this thesis.

The literature on formulating equations of motion for insect flight dynamics is abundant, with each study using a preferred method related to the specific problem at hand. As such, a variety of modelling fidelities have been presented showing their application for modelling the nonlinear dynamic responses of insects. It was seen in general that a single body approximation was used and in some other cases, the multibody approach was used. The classical/typical Newton-Euler formulation which uses a vectorial approach is one of the most intuitive and widely used formulation for systems with low degrees of freedom. However, the classical vector mechanics formulation results in a cumbersome derivation process. In addition, for computational simulation purposes, matrix instead of vector formulation is preferred and is necessary for modern control design. Furthermore, the direct experimental validation of these mathematical models has been relatively absent from the literature.

Most of the work on multibody formulation focused on the aerodynamic and inertial effects of the wings. However, other body parts contribute to flight control and manoeuvrability of insects such as the use of appendage movements to actively change their body configuration during flight. In addition, most of the literature mainly focuses on hover flight. Although hover is important, other modes of flight such as forward and manoeuvring flight which have received less attention, are also critical to understanding insect flight. The lack of quantitative studies on the role of appendage movement in insect forward flight represents a significant limitation in our understanding of the functional constraints driving the evolution of insect flight control systems.

As a result, the objectives of this thesis aim to address these research gaps by using systematic formulations in developing mathematical models that not only truly represent insect flight but support modern control techniques to explore the effects and functions of other morphological features like the articulated abdomen in insect flight.

Chapter 3

Research Methodology

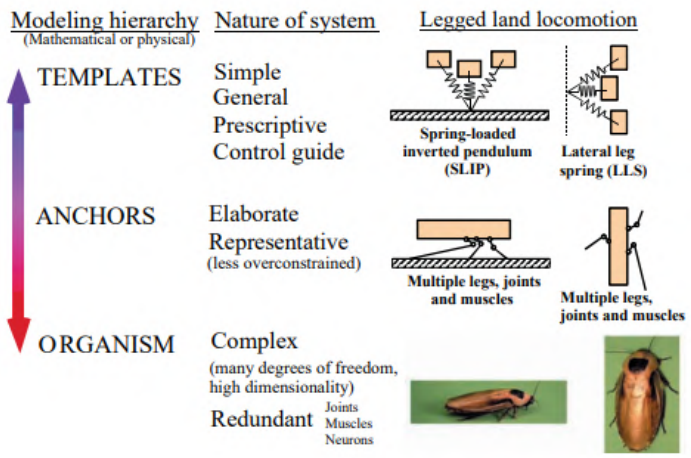
In this chapter, an overview of the methodology and tools used to accomplish the objectives of this thesis is presented, where the primary focus is on investigating the effects appendage movements have on insect forward flight, for insect inspired systems. The scope of this work is therefore not to replicate trajectories, but is driven by the hypothesis of what is possible with the movements which have been observed. The methodologies adopted were strongly influenced by the scope and the resources available.

3.1 Introduction

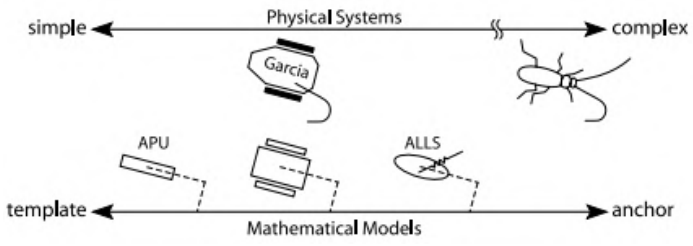
Biologically inspired design (BID) paradigms represent various approaches to overcoming the knowledge barrier for biological systems through problem solving, learning from nature, and mimicry. These paradigms, as discussed in detail by Lenau et al. [13], can be categorised as either problem-driven, solution-driven, sustainability-driven, bioreplication-driven, or a combination of two or more of them. The paradigm behind the development of methodology for the work done in this thesis takes the bioreplication or mimicry approach. Bioreplication is a solution-based BID that directly replicates biological structures to achieve a certain function. Sometimes called inspiration-driven biologically inspired design, solution-driven BID, starts with interesting biological occurrences and analyses them to establish essential principles and

find viable applications. Mimicry, analysis, and use of problems and biological phenomena, depend on the level of abstraction.

This approach seems appropriate for the objective of this study which involves investigating the effects of appendage motion in forward flight modes, particularly abdominal movements observed in dragonfly flight. It is well established that insect flight is complex, however, a reductionist approach was applied, where the approach uses the simplest mathematical model to introduce representations of specific biological details whose dynamics were of interest. This is similar to the concept of templates and anchors first proposed by Full and Koditschek [185]. Examples of the templates and anchors concept used for modelling locomotion of terrestrial animals and robotics are shown in Figure 3.1.



(a) The spring loaded inverted pendulum (SLIP) and lateral leg spring (LLS) templates. Image from [185]



(b) The antenna-based planar unicycle (APU) and antenna-based lateral leg spring (ALLS). Image from [186]

Figure 3.1: Templates and anchor concepts for task-level behaviour in cockroach locomotion.

3.2 A Dragonfly Biomimetic Aircraft Model

The conceptual small unmanned aerial vehicle developed in this study is inspired by the impressive flight characteristics of the dragonfly (of order Odonata, infraorder Anisoptera) [187]. Dragonflies can both hover and achieve high performance and efficiency in forward flight with cruise speeds of up to 54 km/h, with some species documented to migrate up to 800 km [188]. Compared to other insects, dragonflies have excellent glide properties, with lift-to-drag ratios ranging from 3.5 to over 10 [189]–[191]. The dragonfly body form is dominated by a long segmented abdomen (weighing 31–35% of the total body mass), two pairs of comparatively high aspect ratio wings (weighing less than 2% of the total body mass), a dense thorax and a large head dominated by large eyes [192]. The dragonfly abdomen is by no means a "tail" in the normal sense for terrestrial vertebrates, neither is it analogous to traditional aircraft empennage. Aircraft tails are generally rigid structures on which there are aerodynamic surfaces, both horizontal and vertical. In most species of dragonfly, there are no aerodynamic structures at the distal end of the abdomen. Figure 3.2a–d shows the typical abdomen shape of dragonfly families. Most dragonfly and damselfly abdomens are slender, as in Figure 3.2a showing the silhouette of a dragonfly from the family Aeshnidae. Variations exist, for example, some "chasers" of the family Libellulidae have a shorter thicker abdomen as shown in Figure 3.2b. Some "clubtails" of the family Gomphidae as shown in Figure 3.2c, have a pronounced club shaped structure terminating the abdomen, from which the family draws its name, strengthening a hypothesis of a predominantly inertial role in this case at least. Some "petaltails" of the family Petaluridae appear to have an aerodynamic structure terminating their abdomens, shown in Figure 3.2d. It might be relevant that the largest dragonfly species by some measures, *Petalura ingentissima*, carries such a structure.

The dragonfly can be considered a tailless aircraft due to the lack of conventionally arranged aileron/elevator/rudder aerodynamic control surfaces for roll/pitch/yaw control. Most tailless aircraft are swept, with some dihedral. Dragonflies in fixed wing flying mode, however, operate with a nearly straight-wing (zero quarter-chord sweep) configuration and are convenient insects

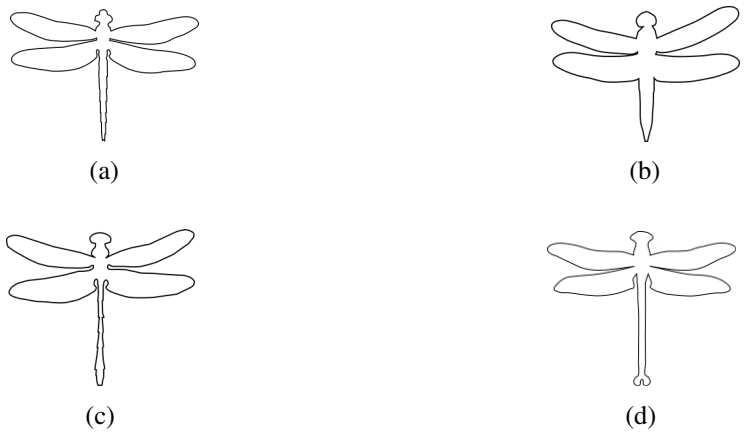


Figure 3.2: Outlines of representative dragonflies from different families. (**a**) Aeshnidae, *Epiaeschna heros*. (**b**) Libellulidae, *Libellula croceipennis* Selys. (**c**) Gomphidae, *Erpetogomphus designatus* Hagen. (**d**) Petaluridae, *Petalura ingentissima*

for this study because they arguably best represent conventional aircraft. In many ways, they have made the fewest concessions to terrestrial operation, with limbs so adapted to grappling that they can hardly be used for walking. Long, unencapsulated, permanently horizontal wings sprout from a heavily muscled thorax, with most weight concentrated close to the line of bilateral symmetry. This leads to an anatomical simplicity relative to other flying insects. Comparing a mosquito to a dragonfly in Figure 3.3, it is apparent that the number of appendages available for the control of a mosquito is high.

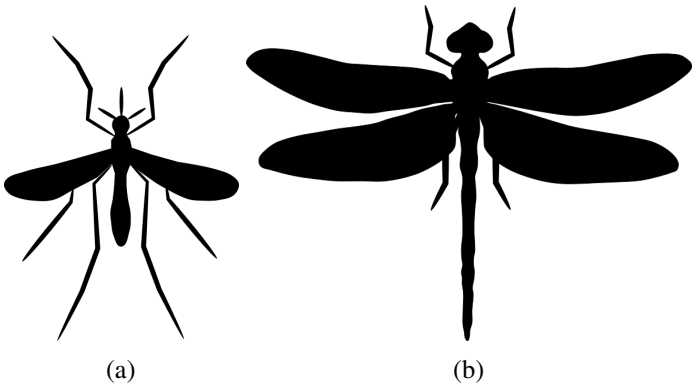


Figure 3.3: Comparison of a mosquito to a dragonfly: (**a**) Outline of a Culex mosquito, *Culex quinquefasciatus*. (**b**) Outline of an Australian Emerald dragonfly, *Hemicordulia australiae*.

Since this is an isolated study of the effects of appendage motion, and taking inspiration from the dragonfly, an articulated tail was placed in the analytical framework developed for small

fixed wing aircraft, birthing the conceptual dragonfly-inspired straight-wing aircraft (DISWA) template shown in Figure 3.4. The nature of this study enabled the investigation of the effects of appendage motion using different approaches, namely:

1. Mathematical modelling, simulation, and control design using the DISWA template
2. Experimental works using a physical model in form of a small fixed wing aircraft with appendage

The adopted approach benefits both fields of biology and engineering as depicted in Figure 3.4.

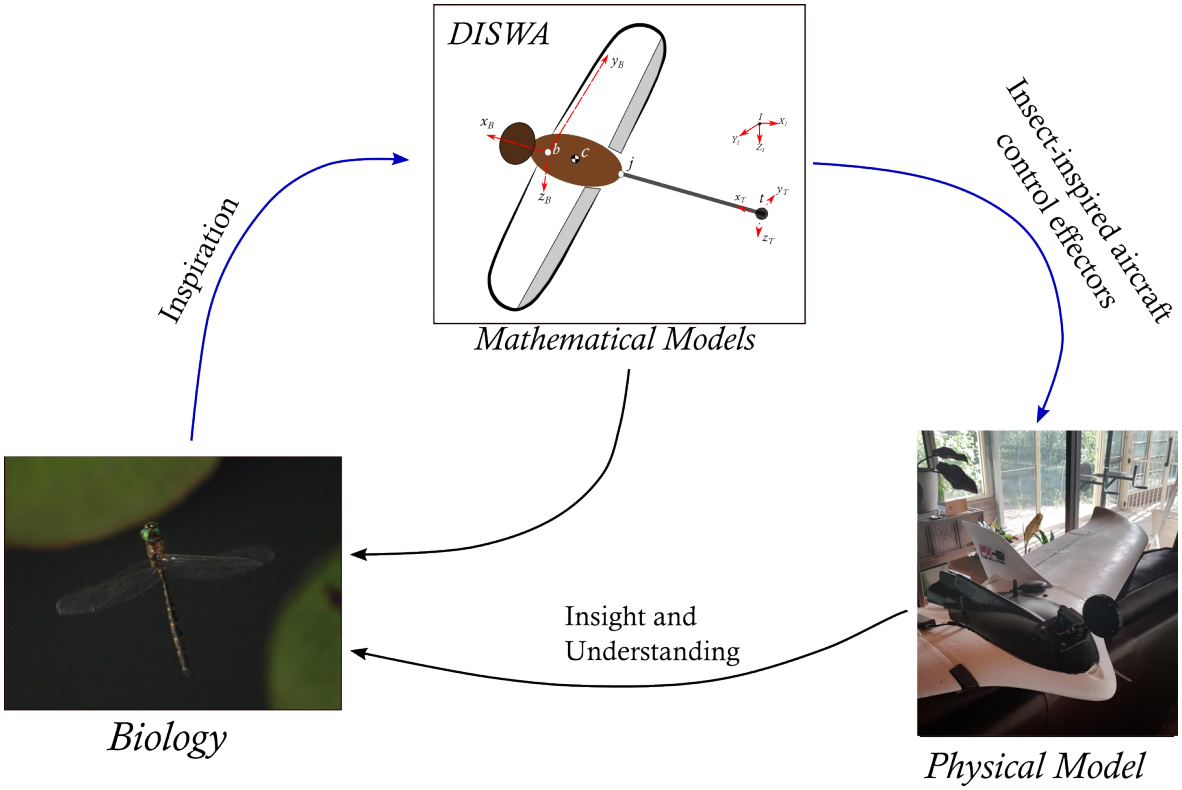


Figure 3.4: The relationship between engineering and biology is a fundamental part of this thesis.

The fixed wing template approach was adapted to this study for various reasons. In comparison with other insects, dragonfly wings demonstrate exceptional steady state aerodynamic properties credited by Wakeling, with glide slope of 6.3:1 [190]. Many documented observations of dragonflies engaging in extended periods of soaring and gliding exist [190], [193]–[195], so, fixed wing flight is an appropriate and accessible aspect of their flight for our analysis, with

direct analogies to technological fliers. Although the analysis for forward flight in this study focuses on fixed wing modes of flight, the qualities of the outcomes should apply to flapping wing flight. The assumption of the analysis is that the abdomen/tail is a mass that is already present and is required by insects, thus making additional functions an optimisation.

Moreover, fixed wing aircraft remain the most common configuration of drones with extended endurance and range, making their performance and agility of interest. Furthermore, the study included goals to undertake flight tests and given the absence of viable flapping wing aircraft that are mature enough to use for testing secondary systems, fixed wing was really the only option for testing. Finally, models for fixed wing flight dynamics and performance are well established, with accepted algebraic formulations that are not, for the most part, considered to be topics of scientific debate.

3.3 Modelling, Simulation and Control

This section presents an overview of the methods and tools used throughout this thesis for deriving the equations of motion and tools for simulation and control design.

3.3.1 Equations of Motion

Newton-Euler method is still considered one of the most intuitive for deriving equations of motion due to its collapsive and additive nature when modelling multibody systems. Flight dynamics involves the use of many reference frames and respective coordinate systems, and changing the reference frame, for example, from inertial to body frame, is sometimes advantageous. The change of frame is governed by Euler's generalised transformation. The typical/classical formulation of the Newton-Euler EoM is based on vector formulation, where the classical Euler transformation factors the change in reference frame using *ordinary time derivatives*, and additional terms appear in the equations of motion to account for the time-dependent coordinate transformations. Using this classical formulation results in non-tensor

expressions due to the extra terms from time-dependent changes in coordinates, leading to equations that are often described as complex and cumbersome [23], [154].

It was determined at the outset, in the absence of any constraint, that the entire system, including all coupling between axes should be expressible in the model. This excluded classical modelling techniques that rely on decoupled equations. In addition one of the objectives of this thesis is the implementation of the EoMs in a simulation environment, to which matrix equations are better suited. Whether intended or not, such a model is explicitly capable of representing almost any dynamics of an aircraft that can be expressed in state space. Furthermore, in control theory, state-space representation is the necessary form of system equations. Therefore, the modern approach of the Newton–Euler method was used to derive the multibody nonlinear equations of motion in this thesis. This adapted formulation was first introduced by Zipfel [196]. As opposed to the classical vector formulation using *ordinary time derivatives*, the modern approach preserves the tensor formulation using the *rotational time derivative* operator, offering a few major advantages. It is tensor-based, compact and is easily adapted to the desired matrix equation for simulation purposes. It is in an invariant tensor form, which is independent of any coordinate system and therefore, allows us to derive the mathematical model first without consideration of coordinate systems. Points and frames are used instead of classical radius vectors and coordinate systems.

3.3.2 Aerodynamic Model

The aerodynamics data for the fixed wing analogical aircraft were obtained using open source tools, Athena Vortex Lattice (AVL) and XFLR5 [197]–[199]. AVL, developed by Drela, uses an extended vortex-lattice method for lifting surfaces to generate aerodynamic derivatives data. AVL produces relatively accurate aerodynamic data for conceptual and preliminary design stages, and is widely used both in industry and academia [200], [201]. The tool takes an input file containing the aircraft geometric parameters defined in sections, and computes the static stability, dynamic stability, and control derivatives. More information on how to use the AVL tool can be found in [202].

The aerodynamic derivatives were generated for a range of angle of attack and sideslip angles, and implemented in the form of lookup tables, which were then used to find the corresponding force and moment coefficients for aircraft states. Outside of the data envelope, the values for the simulation were either set to the value of the last data point or extrapolated.

One limitation of AVL is that it does not capture viscous effects and can only predict lift induced drag. To account for viscous effects, a constant pressure drag was estimated using XFLR5, and included in the AVL input geometry file. These derivatives were calculated in the body-fixed frame and follow conventionally accepted standards with regard to nomenclature and non-dimensionality. The AVL input geometry file used for the DISWA in this study is shown in Appendix A.1. The generated body-fixed aerodynamic derivatives data at a sample angle of attack is shown in Appendix A.2.

XFLR5 extends the 2D solutions of XFOIL to 3D applications using analysis tools such as vortex lattice method, nonlinear lifting line theory and 3D panels. Viscous calculations can also be interpolated from XFOIL data [203]. XFLR5 software provides a graphical user interface for aircraft design, with mass and inertia estimation capabilities using component point masses. More information on how to use XFLR5 can be found in [204], [205].

Later in the thesis in Chapter 8, the aerodynamic effects of the abdomen appendage, which was assumed to be negligible in the analysis carried out in previous chapters was included. The analytical method based on the cross-flow principle proposed by Hoerner [206], was used in estimating the aerodynamic loading associated with the abdomen. This principle develops the relationship for the forces acting on a slender cylindrical body inclined with respect to the oncoming flow.

3.3.3 Design Tools

The numerical simulation framework was implemented in the MATLAB/Simulink environment. MATLAB is a high-level language software developed by MathWorks Inc., which allows for modelling, simulation and control of dynamic systems, while Simulink is the graphical

extension of MATLAB. Since Simulink is integrated with MATLAB, data can be easily transferred between the two programs. There are many different toolboxes that are available, that extend MATLAB's core functions into different application areas. The MATLAB function and tools that were used in this research included the Aerospace, Control Systems and Symbolic Math Toolboxes. Time-domain simulation, system linearisation, modal analysis, optimal controller placement, feedback signal selection, and control design are all possible with the application. In addition, MATLAB allows custom functions to be defined.

Furthermore, various explicit and implicit techniques are available for solving differential algebraic equations (DAEs). The $ode45$, $ode113$, $ode15s$, $ode23$, $ode23t$, $ode23tb$, and $ode23s$ solvers in MATLAB, are available to solve stiff and non-stiff DAEs. To overcome some numerical challenges in handling stiff problems, each solver has several configurable options. Other effective solvers for solving nonlinear algebraic equations in MATLAB include the $fsolve$ and $lsqnonlin$ functions, which can be used to solve the problem explicitly [207]. These functions include a number of important options that can be set for the solvers as well. MATLAB 2019b version [208] was used in this study.

3.3.4 Performance Characterisation

The term performance describes how well an aircraft performs against specified metrics. Aircraft control authority, stability, and manoeuvrability characteristics that determine vehicle performance, depend on the environment, vehicle configuration, and capabilities of the control effectors [209]. These determining factors of vehicle performance can be estimated using various metrics, depending on the nature of flight, be it static or dynamic. Steady or static flight performance measures an aircraft's ability to perform steady coordinated manoeuvres at various speeds and altitudes (e.g., its ability to maintain a straight and level flight; a steady level turn; climbing or gliding turns etc.). An aircraft's manoeuvrability, on the other hand, is defined as the ability to perform a change, or a combination of changes in, altitude, direction and airspeed, of which there are levels of manoeuvrability [209]. Hence, while steady state

performance metrics measure an aircraft's steady-state or point performance, manoeuvrability metrics measure the performance's time derivative [210].

To investigate the effects of appendage movements by insects on steady forward flight performance, metrics relating to static stability, power and energy requirements, as well as control efforts will be used for evaluation. For quasi-steady pull up manoeuvre performance, an energy-based metric that measures the energy manoeuvrability of an aircraft will be used. For dynamic flight conditions involving attitude stabilisation and control design, transient response characteristics for states and control effort will be used as evaluation metrics. Lastly, effects on manoeuvrability efficiency will measure changes in velocity and attitude over a specific time.

3.4 Experimental Works

A physical model of an aircraft with articulated appendages was developed for experimental purposes. This section presents an overview of the methods and tools used in Chapter 7. The aim of this research was not necessarily to create a new aircraft from scratch, but rather, to investigate the effects of moving appendages in flight, using already available technology if possible. Internal payload capacity for mounting autopilot avionics and structural integrity of the platform to handle the increased weight of the avionics and articulated mass were important factors considered in choosing an RC platform. Therefore, an already available remote control (RC) flying wing aircraft that met these considerations was retrofitted with an articulated mass.

3.4.1 Flight Data Logger

The flight data was recorded using a Pixhawk 1.2, a commercially available flight autopilot. Data from a three-axis accelerometer, three-axis gyroscope, three-axis magnetometer, a digital airspeed sensor, a global positioning unit (GPS) unit and a barometer, as well as the position of multiple servo commands, are all sensed and recorded by the Pixhawk. An attitude filter

also calculates roll, pitch, and yaw [211]. All of this information was stored on an SD card at a sample rate that ranged from 5 Hz for the GPS receiver, to 50 Hz for the inertial measurement unit (IMU) data and some external sensors.

3.4.2 Ground Control Station

A ground station is a software application that uses wireless telemetry to communicate with the flight controller, while running on a ground-based computer. It is first and foremost used to set up and configure the flight controller. Following that, it displays real-time data on the aircraft's performance and position and can be used as a "virtual cockpit", displaying many of the same instruments as a manned aircraft. A ground control station can also be used to control the aircraft while it is in flight, upload new mission commands, new parameter settings, and download and analyse the data collected. Mission Planner [212], an open source ground station software, developed by Michael Oborne for the open-source ArduPilot Mega (APM) autopilot project, was used in this research. A screenshot of the Mission Planner user interface is shown in Figure 3.5.

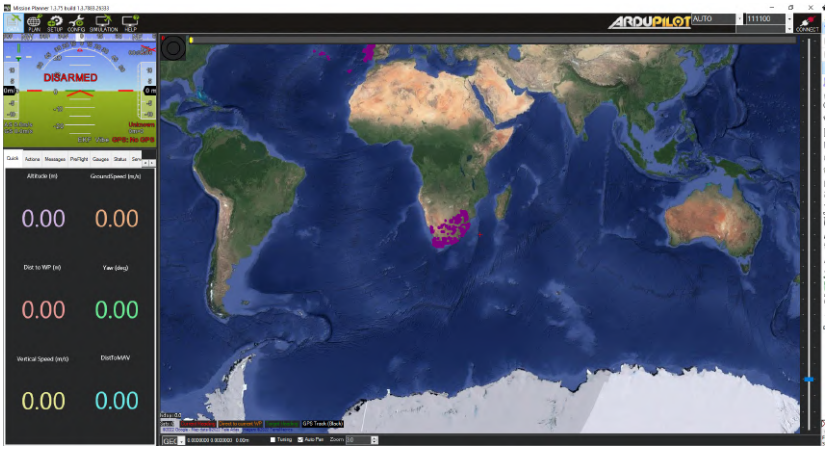


Figure 3.5: Screenshot of Mission Planner user interface.

3.4.3 Post-flight Data Analysis

Even though the ground station records all telemetry data, the sample rates tend to be substantially lower and vary depending on the available transmission bandwidth [213]. The onboard data logger, on the other hand, delivers higher and more consistent sample rates.

Therefore, the data log on the SD card was used for post flight analysis. All data logged on the SD card of the Pixhawk were downloaded to a computer after a session of flight tests and categorised. The tools available within Mission Planner, were used to create MATLAB MAT-files from the data logger's binary files. The MAT files comprised all of the variables and system parameters recorded by the data logger. A MATLAB script was created specifically to analyse these files. This script enabled parameter visualisation and comparison, error detection, sample frequency analysis, and filter design for specific variables.

3.5 Chapter Summary

This chapter summarised the materials and different methods used in this research. Specific details are presented in respective chapters.

Chapter 4

Multibody Dynamics for Bioinspired Vehicles

The main objective of this chapter is to introduce the various mathematical models that will be used throughout this thesis. The chapter starts out introducing the dragonfly-inspired straight-wing aircraft. Next, the nonlinear multibody equations of motion are developed using simplified idealised mathematical representations (templates) with enough complexity to simulate the effects of articulated appendages during insect flight and by extension, insect-inspired air vehicles with moving appendages. The method presented employs a compact tensor-based invariant approach of the Newton-Euler method, making it more suitable for computational implementation and modern control design. At the conclusion of this chapter, only the models for the forces and moments acting on the vehicle remain to be determined.

4.1 Introduction

Modelling is important to control system design and engineering. It allows the desired system to be represented mathematically and simulated by an appropriate computer simulation program. In order to generate realistic results from the simulation, it is critical to model the biomimetic insect-inspired aircraft with sufficient accuracy, taking into account all major factors that

influence its dynamics. Meanwhile, although evidence exists of abdominal movements in flying insects, previous works often ignored the effects of the observed abdominal movements [23], [24], [150], or mostly focused on hover and near hover flight conditions [137], in cases where these effects were considered. Hence, the potential influence abdominal motion has on the forward flight dynamics of insects remains underexplored. In addition, despite the intuitive and recursive nature of Newton-Euler formulation, the typical Newton-Euler multibody modelling approach for insect-inspired aircraft uses vector formulation which has to first be converted to matrix form before direct implementation in numerical simulation tools such as MATLAB/Simulink, reducing the simulation efficiency. Therefore, this chapter describes the derivation of the nonlinear, six DoF aircraft equations of motion that incorporate biomimetic appendages, following a tensor-based invariant approach. The method includes the effects of time-varying mass and inertial properties associated with appendage motions. More so, with tensor-based equations, computational implementation takes a more direct form, improving simulation efficiency. Since the centre of mass of the aircraft changes with time during appendage articulation, the equations are written in a reference frame that is geometrically fixed on the aircraft.

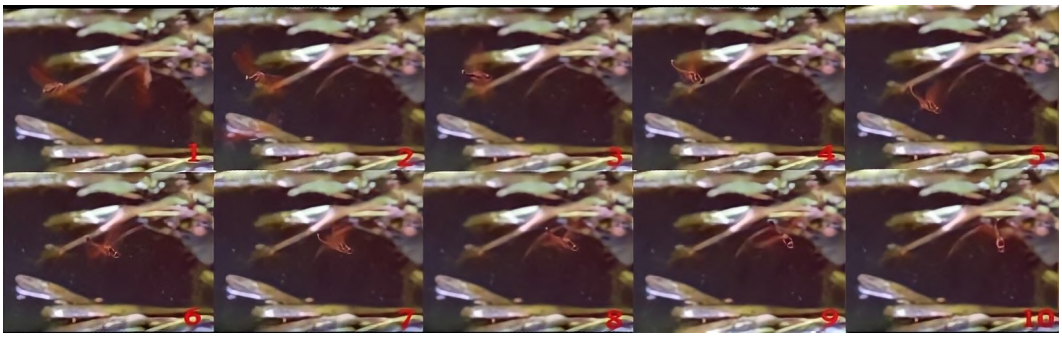
This chapter aims to address the following research question:

1. Can an efficient matrix-based framework for mathematical modelling of appendage movements be developed for simulation and control system design?

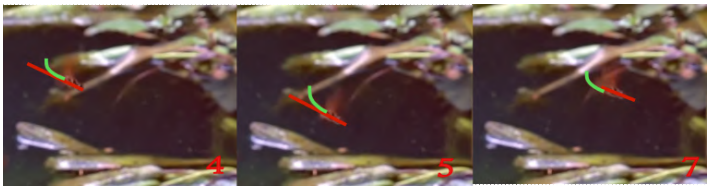
4.2 Development of the Multibody Equations of Motion

To develop equations of motion that reflect the effect of abdominal movement, a series of forward flight dragonfly manoeuvres were observed and are shown in Figures 4.1–4.3. Note the nature of abdominal motion in flight by curving to reshape the abdomen relative to the body in Figure 4.1, and the apparent deflection of the abdomen relative to the body about the pitch axis in Figure 4.2, and yaw axis in Figure 4.3.

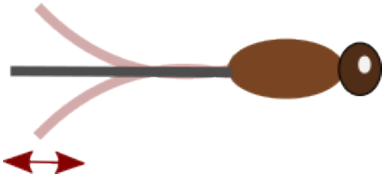
It is important to note that throughout this thesis when referring to biological data for dragonflies, we have gleaned observations from multiple studies in the literature when exploring flight and performance. Different species are likely to have different abdominal articulation, dynamic characteristics and kinematic options. Variations in the thorax and abdomen between species are quite significant, as shown in Figure 3.2 .



(a) Dragonflies in longitudinal flight. The frame rate in these is 30 fps and every 5th frame is shown.



(b) Specific images showing abdominal reshaping by curving in flight. The green line represents the centreline of the abdomen and the red line represents the centreline of the body.



(c) Simplified representation of the abdominal motion (side view).

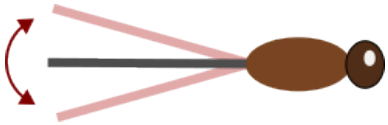
Figure 4.1: Free flying dragonfly (Video taken from [214]).



(a) A dragonfly performing a longitudinal manoeuvre. The frame rate in these is 24 fps and every 10^{th} frame is shown.



(b) Specific frames that show the motion of the abdomen. The green line represents the centreline of the abdomen and the red line represents the centreline of the body.

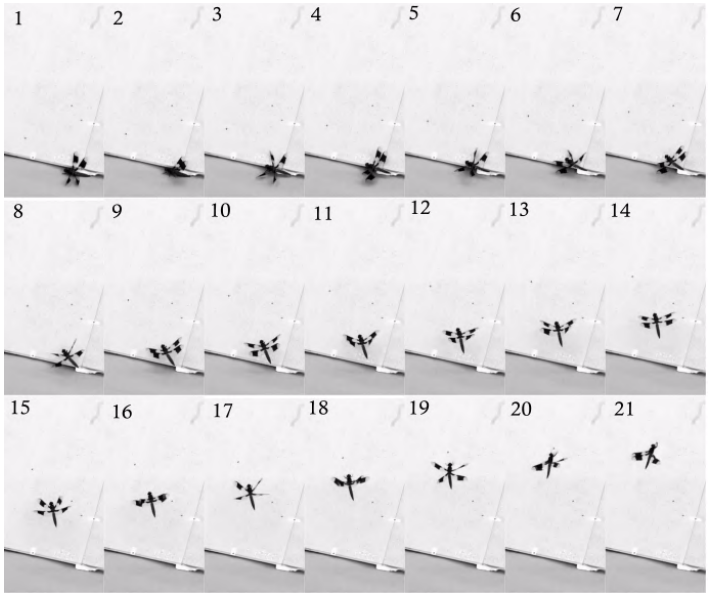


(c) Simplified representation of the abdominal motion (side view).

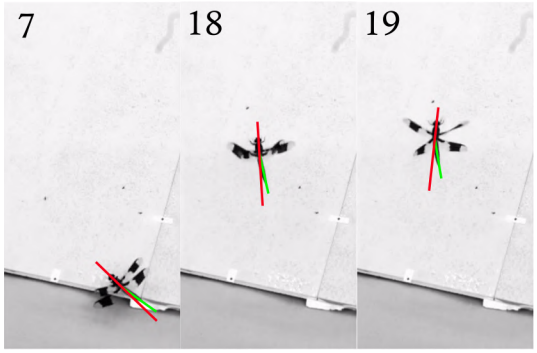
Figure 4.2: Dragonfly in diving manoeuvre (Video taken from [215]).

It is important to reiterate that the simplified model representation of the biomimetic articulated abdomen system was deduced only after careful consideration, based on its complexity, representativeness, feasibility, and ease of use for modern control system design and development. Therefore, a dragonfly-inspired straight-wing aircraft is considered, which includes an articulated abdomen. The fore and hind wings are combined to form single wings with elevons, thus, the equations of motion are simplified to a two-body problem. The dragonfly head/thorax/wings combination is abstracted as a rigid body and will be referred to as the *central body*. The central body typically has six degrees of freedom, three translational and three rotational. The abdomen as the second rigid body will be modelled as a point mass. Additionally, the abdomen will be interchangeably referred to as the *tail* in this thesis.

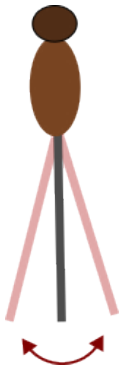
With the curving of the abdomen, the dragonfly is capable of bending/shortening and straightening/elongation of the abdomen, which is modelled to reflect translational movement of the abdominal mass along an axis. However, the deflection of the abdomen is simply modelled as the rotational movement of the abdominal mass about an axis. Therefore, two sets of dynamic equations for the DISWA are derived for the two modes of tail actuation



(a) A dragonfly performing a lateral manoeuvre. The frame rate in these is 28 fps and every 10^{th} frame is shown.



(b) Specific frames with abdominal movements . Green line represents the centreline of the abdomen and the red line represents the centreline of the body.



(c) Simplified representation of the abdominal motion (top view).

Figure 4.3: Dragonfly (*Plathemis lydia*) in turning flight for prey capture (Video taken from [216]).

considered. The first set of equations representing Model 1, will be used for modelling the translational motion of the abdomen, while the second set of equations represented, as Model 2, models the rotational movements of the abdomen.

The derivation presented in this chapter is facilitated by the mathematical tools for invariant tensor formulation of EoMs presented in the modelling and simulation of aerospace vehicle dynamics textbook by Zipfel [196]. Similar standard notations are used, however, specified to the models and problems formulated in this thesis. The tensor formulation enabled the effect of these changes to be reflected in all three respective translational and rotational axis for Model 1 and Model 2 aircraft. Since this is an isolated study of the effects of abdominal motions, the two-body model provides useful insight, however, the models can easily be extended for a system with more than two rigid bodies. In addition, to properly reflect the effects associated with dynamic changes in combined cg position and inertia, the dynamic equations presented in this study are referenced to point b, the centre of mass of the central body, which is geometrically fixed on the aircraft.

4.2.1 Preliminaries

This section briefly introduces the concept of the rotational time derivative operator, which is used throughout the text. A brief description is presented below; more details about the rotational time derivative and its application in modelling can be found in [196]. Consider two arbitrary frames A and O, with relative angular velocity of ω^{OA} , and a vector a, associated with frame A. For clarity, a vector associated with a frame implies it is constant, as it is fixed relative to the associated frame. In addition, vector a transforms similarly to a first-order tensor given the coordinate systems of frames A and O as in

$$[a]^O = [R]^{OA}[a]^A \tag{4.1}$$

where $[R]^{OA}$ is the transformation matrix from the coordinate system of frame A to frame O. Transformation matrices are applicable to second-order tensors (equivalent to matrices) as well.

Given that the time rate of change of vector a with respect to frame A is given by $[\frac{da}{dt}]^A$, the time rate of change of vector a, expressed in frame O, can be obtained by applying the

classical *Euler transformation* using *ordinary time derivatives* as

$$\left[\frac{da}{dt}\right]^A = \left[\frac{da}{dt}\right]^O + \Omega^{OA}\, a \tag{4.2}$$

where Ω^{OA} is the skew symmetric matrix of the angular velocity vector ω^{OA}. The resulting expression on the right hand side (RHS) of Equation (4.2) does not preserve the tensorial formulation due to the time-dependent nature of the derivative of vector a.

To preserve the tensor formulation during Euler transformation, a time operator called the *rotational time derivative* is used instead of the *ordinary time derivative* and was first introduced in Wrede's textbook [217] on vector and tensor analysis. The operator depends only on a frame of reference such that the *rotational time derivative* of a vector a regarding frame A is expressed as $D^A\, a$. A change in reference frame of vector a from frame A to O is obtained through *Euler transformation* [196] with the *rotational time derivative*, using the following relationship

$$D^A a = D^O a + \Omega^{OA} a \tag{4.3}$$

Thus, the vector a can be expressed in the coordinate system of any frame due to the tensor properties the *rotational time derivative* possesses as in

$$[D^A\, a]^O = [R]^{OA} [D^A\, a]^A \tag{4.4}$$

The time rate of change of vector a with respect to its associated frame A can be written as $[D^A\, a]^A$. It is important to note that rotational time derivatives expressed in their own associated frame become ordinary time derivatives ready for numerical integration as in

$$[D^A a]^A = \frac{da}{dt}. \tag{4.5}$$

In the case of a multibody aircraft, the use of fixed body reference frames and displacement vectors between points in the associated reference frames enables the equations to be derived

in tensor form, and to be both compact and coordinate-independent (invariant).

4.2.2 Reference Frames and Coordinate Systems

The reference frames and associated coordinate systems used for the development of equations of motion are as follows and shown in Figure 4.4b.

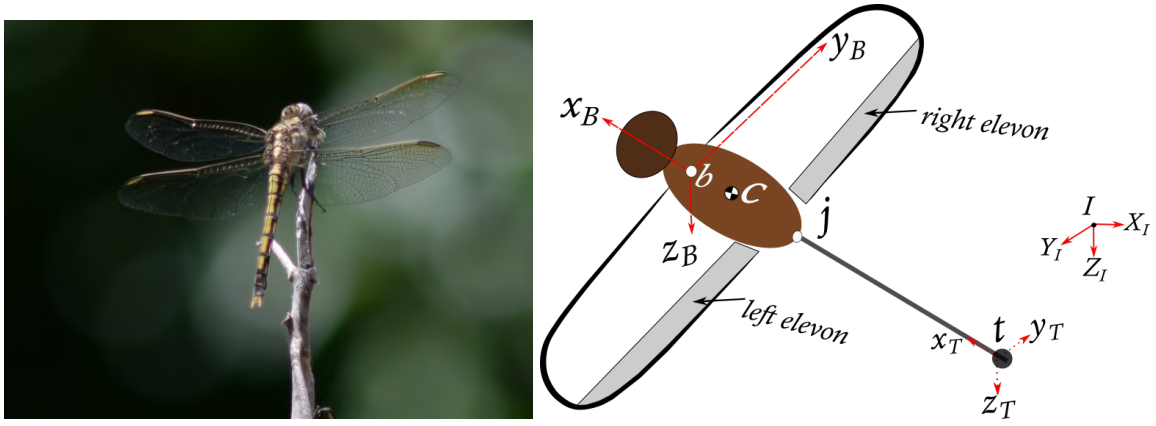
(a) The inertial reference frame $I\{X_I, Y_I, Z_I\}$: The Earth frame is assumed to be the inertial frame with its origin, I fixed at an arbitrary point relative to the Earth's surface. The orientation of the inertial frame is such that the X_I axis is positive facing North, Y_I axis is positive facing East and Z_I axis is positive downwards towards Earth's centre of gravity.

(b) The body-fixed reference frame $B\{x_B, y_B, z_B\}$: The origin is located at the centre of mass of the *central body*, point b. The body frame is oriented such that x_B axis lies on the plane of symmetry of the aircraft and points in the forward direction towards the head of the aircraft. The y_B axis is perpendicular to the x_B axis, pointing towards the right side of the aircraft and the z_B axis is positive downwards and lies on the plane of symmetry.

(c) The abdominal/tail reference frame $T\{x_T, y_T, z_T\}$: This reference frame originates from the centre of mass of the tail with its orientation the same as that of the body frame coordinate system when the tail is not deflected.

4.2.3 Reference Points

Reference points are introduced for each individual part of the aircraft model and are shown in Figure 4.4b. The reference point for the central body is its centre of mass, point b, associated with frame B. The reference point for the tail is its centre of mass, point t, associated with frame T. The tail joint, j, serves as an intermediate reference point. It will be mostly associated with frame B except in cases where it is stated to be associated with frame T. The



(a) (b)

Figure 4.4: Description of the DISWA: (**a**) Photograph of an Australian emerald dragonfly, *Hemicordulia australiae*. (**b**) Reference points and coordinate systems of the dragonfly-inspired straight-wing aircraft (DISWA).

centre of mass of the whole aircraft (rigid body C) is located at point c and is associated with frame B.

4.2.4 Orientation and Transformation Matrices

The numerical simulation framework will rely on the appropriate transformation matrices to ultimately yield the EoMs in the body-fixed coordinate system. The standard transformation matrices of a rotation angle μ, about x, y and z axes of the coordinate systems are expressed as [196]

$$R_{\mu|_x} = \begin{bmatrix} 1 & 0 & 0 \\ 0 & c\,\mu & s\,\mu \\ 0 & -s\,\mu & c\mu \end{bmatrix} R_{\mu|_y} = \begin{bmatrix} c\,\mu & 0 & -s\,\mu \\ 0 & 1 & 0 \\ s\,\mu & 0 & c\mu \end{bmatrix} R_{\mu|_z} = \begin{bmatrix} c\,\mu & s\,\mu & 0 \\ -s\,\mu & c\,\mu & 0 \\ 0 & 0 & 1 \end{bmatrix} \tag{4.6}$$

where $s\,\mu$ and $c\,\mu$ represent the sin and cosine functions of μ, respectively. Given any two arbitrary coordinate systems, the transformation matrices can be obtained using relationships between the rotation angles and axes of rotation in Equation (4.6).

The attitude of the central body with respect to the inertial frame is described by the Euler angles ψ (yaw), θ (pitch) and ϕ (roll). The transformation matrix from inertial to body coordinate system, $[R]^{BI}$, is obtained using the z-y-x rotational sequence of the Euler angles

as in

$$[R]^{BI} = R_{\psi|_z} R_{\theta|_y} R_{\phi|_x} \tag{4.7}$$

The transformation matrix from body to inertial coordinate system is obtained as the transpose of the $[R]^{BI}$ matrix, $[R]^{IB} = [R']^{BI}$.

Euler angles ψ_T (tail yaw), θ_T (tail pitch) and ϕ_T (tail roll) are used to specify the orientation of the abdomen relative to the central body. The transformation matrix from the body to tail coordinate system also follows the z-y-x rotational sequence as in

$$[R]^{TB} = R_{\psi_T|_z} R_{\theta_T|_y} R_{\phi_T|_x} \tag{4.8}$$

4.2.5 Kinematics

The velocities of each of the bodies will be defined in this section using the rotational time derivative operator where applicable and displacement vector between points. The velocities are ultimately expressed in the preferred B frame. Given that the displacement vector of the central body relative to the inertial frame is s_{bI}, the translational velocity of the central body regarding the inertial frame is expressed as $D^I s_{bI}$. The translational velocity of the central body in the body frame can then be obtained using the inertial to body transformation matrix [196]

$$[D^B s_{bI}]^B = [R]^{BI} \, [D^I s_{bI}]^I \tag{4.9}$$

where the term $[D^B s_{bI}]^B = [u, v, w]$, and u, v, w are the body velocity components.

The angular velocity of the central body relative to the inertial frame, expressed in the B frame, is introduced as $[\omega^{BI}]^B = [p, q, r]$. The relationships between the rate of change of kinematic parameters and the angular velocities for the central body follow the sequence of

rotations and are calculated according to

$$[\omega^{BI}]^B = \begin{bmatrix} \dot{\phi} \\ 0 \\ 0 \end{bmatrix} + R_{\phi|_x} \begin{bmatrix} 0 \\ \dot{\theta} \\ 0 \end{bmatrix} + R_{\phi|_x} R_{\theta|_y} \begin{bmatrix} 0 \\ 0 \\ \dot{\psi} \end{bmatrix} \tag{4.10}$$

4.2.5.1 Model 1 Abdominal Kinematic Equations

Using the centre of mass of the abdomen t as reference point, the displacement of the joint with respect to the inertial frame can be expressed as a summation of displacement vectors as in

$$s_{tI} = s_{tb} + s_{bI} \tag{4.11}$$

Therefore, the relative translational velocity of the abdomen with respect to the inertial frame is expressed as

$$D^I s_{tI} = D^I s_{tb} + D^I s_{bI} \tag{4.12}$$

By applying a Euler transformation, Equation 4.12 can be written in the body frame as

$$D^I s_{tI} = D^B s_{tb} + \Omega^{BI} s_{tb} + D^B s_{bI} + \Omega^{BI} s_{bI} \tag{4.13}$$

4.2.5.2 Model 2 Abdominal Kinematic Equations

Using the abdominal joint j as the reference point, the displacement of the joint with respect to the inertial frame can be expressed as a summation of displacement vectors as in [196]

$$s_{jI} = s_{jb} + s_{bI} \tag{4.14}$$

Hence, the relative translational velocity of the joint with respect to the inertial frame is expressed as

$$D^I s_{jI} = D^I s_{jb} + D^I s_{bI} \tag{4.15}$$

Since $D^I s_{jb}$ is not readily available for measurement, a simpler expression is established by applying an Euler transformation of $D^I s_{jb}$. Equation (4.15) becomes

$$D^I s_{jI} = D^B s_{jb} + \Omega^{BI} s_{jb} + D^I s_{bI} \tag{4.16}$$

Noting that $D^B s_{jb} = 0$, since s_{jb} is associated with frame B, simplifies Equation (4.16) to

$$[D^I s_{jI}]^I = \Omega^{BI} s_{jb} + D^I s_{bI} \tag{4.17}$$

Similar to Equation (4.9), the abdominal joint relative velocity can be obtained using the inertial to body transformation matrix.

For the rotational kinematic equations for Model 2, let the Euler angle derivatives for the abdomen be $(\dot{\phi}_T, \dot{\theta}_T, \dot{\psi}_T)$, respectively. The angular velocity of the abdomen relative to the body frame and expressed in the T frame is introduced as $[\omega^{TB}]^T = [p_T, q_T, r_T]$. The relationships between the rate of change of kinematic parameters and the angular velocities follow the sequence of rotations and are calculated according to

$$[\omega^{TB}]^T = \begin{bmatrix} \dot{\phi}_T \\ 0 \\ 0 \end{bmatrix} + R_{\phi_T|_x} \begin{bmatrix} 0 \\ \dot{\theta}_T \\ 0 \end{bmatrix} + R_{\phi_T|_x} R_{\theta_T|_y} \begin{bmatrix} 0 \\ 0 \\ \dot{\psi}_T \end{bmatrix} \tag{4.18}$$

4.3 Multibody Equations of Motion

Next, the equations of motion are derived using Newtonian and Eulerian mechanics. The equations will be derived using points defined in their associated reference frames and related using invariant displacement vectors. The approach presented in this section allows the tensor nature of the equations to be preserved. EoMs are required for translational, rotational and abdominal motions for Model 1 and Model 2.

4.3.1 Model 1: Multibody Equations of Motion

4.3.1.1 Translational Dynamics

The translational dynamic equations are developed as follows [150], [196]:

$$D^I\left(\sum_k m^{B_k} D^I s_{B_k I}\right) = \sum_k F_k \tag{4.19}$$

where $\sum_k F_k$ is the contributing sum of all the forces acting on the aircraft from each rigid body as in $\sum_k F_k = F_B + F_T$.

Using the reference points b and t. Separating the individual contributions of the central body and the tail with $s_{B_k I} = s_{bI} + s_{tI}$ and $s_{tI} = s_{tb} + s_{bI}$ gives

$$D^I\left(m^B D^I s_{bI} + m^T D^I s_{tb} + m^T D^I s_{bI}\right) = F_B + F_T \tag{4.20}$$

Merging the first and third terms of the LHS of Equation (4.20) and introducing $D^I s_{bI} = V_b^I$ results in

$$\underbrace{m\ D^I V_b^I}_{\text{Term I}} + \underbrace{m^T D^I s_{tb}}_{\text{Term II}} = \underbrace{F_B + F_T}_{\text{Term III}} \tag{4.21}$$

Since $Term\ I$ of Equation (4.21) relates to the body frame, the Euler transformation is used to represent this term in the body-fixed frame as

$$m\ D^I V_b^I = m\ (D^B V_b^I + \Omega^{BI} V_b^I) \tag{4.22}$$

For term $Term\ II$ of Equation (4.21), the rotational time derivative $D^I s_{tb}$ is transformed to the body frame, using Equation (4.3) as in

$$m^T D^I D^I s_{tb} = m^T D^I (D^B s_{tb} + \Omega^{BI} s_{tb}) \tag{4.23}$$

The vector s_{tb} is not constant in the body frame. Additionally, the RHS of Equation (4.23) can be rewritten using the Euler transformation, resulting in

$$\begin{aligned} m^T D^I (D^B s_{tb} + \Omega^{BI} s_{tb}) &= m^T [D^B (D^B s_{tb} + \Omega^{BI} s_{tb}) + \Omega^{BI} (D^B s_{tb} + \Omega^{BI} s_{tb})] \\ &= m^T \begin{bmatrix} D^B D^B s_{tb} + D^B \Omega^{BI} s_{tb} + \Omega^{BI} D^B s_{tb} \\ +\Omega^{BI} D^B s_{tb} + \Omega^{BI} \Omega^{BI} s_{tb} \end{bmatrix} \end{aligned} \tag{4.24}$$

The translational dynamic equations of motion in an invariant tensor form can then be expressed as

$$m\ (D^B V_b^I + \Omega^{BI} V_b^I) + m^T \begin{bmatrix} D^B D^B s_{tb} + D^B \Omega^{BI} s_{tb} + 2\Omega^{BI} D^B s_{tb} + \Omega^{BI} \Omega^{BI} s_{tb} \end{bmatrix} = F_B + F_T \tag{4.25}$$

Representing the translational dynamic equations in the body coordinate frame for simulation, and rewriting $D^B s_{tb} = \dot{s}_{tb}$ and $D^B D^B s_{tb} = D^B \dot{s}_{tb} = \ddot{s}_{tb}$ gives.

$$m \left([\dot{V}_B^I]^B + [\Omega^{BI}]^B [V_b^I]^B \right) + m^T \begin{bmatrix} [\ddot{s}_{tb}]^B + [\dot{\Omega}^{BI}]^B [s_{tb}]^B \\ + 2[\Omega^{BI}]^B [\dot{s}_{tb}]^B + [\Omega^{BI}]^B [\Omega^{BI}]^B [s_{tb}]^B \end{bmatrix} = F_{B+T} \tag{4.26}$$

4.3.1.2 Rotational Dynamics

For a system of k clustered rigid bodies, the rotational dynamic equations are developed as the sum of their individual contributions based on Euler's law, as follows [150], [196]:

$$\underbrace{\sum_{k} D^{I}\left(I_{B_k}^{B_k}\omega^{B_k I}\right)}_{\text{Term I}} + \underbrace{\sum_{k} D^{I}\left(m^{B_k} S_{B_k I} D^{I} s_{B_k I}\right)}_{\text{Term II}} = \sum_{k} M_k + \sum_{k} S_{B_k I} F_k \tag{4.27}$$

where the expression $\sum_k M_k + \sum_k S_{B_k I} F_k$ on the RHS of Equation (4.27) is the contributing sum of all the moments acting on the aircraft from each rigid body as in $\sum_k M_k + \sum_k S_{B_k I} F_k = M_B + M_T + S_{bI} F_B + S_{tI} F_T$.

Again, $Term\ I$ in Equation (4.27) is given as

$$\sum_{k} D^{I}\left(I_{B_k}^{B_k}\omega^{B_k I}\right) = D^{I}\left(I_{b}^{B}\omega^{BI}\right) \tag{4.28}$$

Applying the chain rule and Euler transformation to each term on the RHS of Equation (4.28) leads to

$$\sum_{k} D^{I}\left(I_{B_k}^{B_k}\omega^{B_k I}\right) = \omega^{BI} D^{B} I_{b}^{B} + I_{b}^{B} D^{B}\omega^{BI} + \Omega^{BI} I_{b}^{B}\omega^{BI} \tag{4.29}$$

With the moment of inertia of the body being constant in its corresponding frame, the first term on the RHS of Equation (4.29) vanishes, hence,

$$\sum_{k} D^{I}\left(I_{B_k}^{B_k}\omega^{B_k I}\right) = I_{b}^{B} D^{B}\omega^{BI} + \Omega^{BI} I_{b}^{B}\omega^{BI} \tag{4.30}$$

Applying the chain rule to $Term\ II$ in Equation (4.27) yields

$$\sum_{k} D^{I}\left(m^{B_k} S_{B_k I} D^{I} s_{B_k I}\right) = \sum_{k} m^{B_k}\left(D^{I} S_{B_k I} D^{I} s_{B_k I} + S_{B_k I} D^{I} D^{I} s_{B_k I}\right) \tag{4.31}$$

The cross-product of the vector derivatives is zero; therefore, the first term on the RHS of

Equation (4.31) is zero. Additionally, the body and abdominal contributions are separated for the second term, leading to

$$\sum_k D^I\left(m^{B_k} S_{B_k I} D^I s_{B_k I}\right) = m^B S_{BI} D^I D^I s_{bI} + m^T S_{tI} D^I D^I s_{tI} \tag{4.32}$$

Using Euler transformation, the first term on the RHS of Equation (4.32) becomes

$$m^B S_{bI} D^I D^I s_{bI} = m^B S_{bI} (D^B V_b^I + \Omega^{BI} V_b^I) \tag{4.33}$$

The second term on the RHS of Equation (4.32) could be developed using the vector expansion $s_{tI} = s_{tb} + s_{bI}$, and performing Euler transformation results in

$$m^T S_{tI} D^I D^I s_{tI} = m^T S_{tI} D^I D^I (s_{tb} + s_{bI}) = m^T S_{tI} D^I D^I s_{tb} + m^T S_{tI} D^I D^I s_{bI} \tag{4.34}$$

where using the Euler transformation,

$$m^T S_{tI} D^I D^I s_{bI} = m^T S_{tI} D^I V_b^I = m^T S_{tI} (D^B V_b^I + \Omega^{BI} V_b^I) \tag{4.35}$$

and

$$m^T S_{tI} D^I D^I s_{tb} = m^T S_{tI} D^I (D^B s_{tb} + \Omega^{BI} s_{tb}) \tag{4.36}$$

The expression $D^I(D^B s_{tb} + \Omega^{BI} s_{tb})$ on the RHS of Equation 4.36 has already been derived in the translational dynamics. Hence, Equation 4.36 becomes

$$m^T S_{tI} D^I D^I s_{tb} = m^T S_{tI} \left(D^B D^B s_{tb} + D^B \Omega^{BI} s_{tb} + \Omega^{BI} D^B s_{tb} + \Omega^{BI} D^B s_{tb} + \Omega^{BI} \Omega^{BI} s_{tb} \right) \tag{4.37}$$

Finally, substituting Equations (4.33) and (4.37) into Equation (4.32) and further substituting Equations (4.30) and (4.32) into Equation (4.27), Equation 4.38 is obtained as

$$\begin{aligned} & m^T S_{tI} \left[\begin{array}{c} D^B D^B s_{tb} + D^B \Omega^{BI} s_{tb} + \Omega^{BI} D^B s_{tb} + \Omega^{BI} D^B s_{tb} + \Omega^{BI} \Omega^{BI} s_{tb} \\ + D^B V_b^I + \Omega^{BI} V_b^I \end{array} \right] \\ & + I_b^B D^B \omega^{BI} + \Omega^{BI} I_b^B \omega^{BI} + m^B S_{bI} (D^B V_b^I + \Omega^{BI} V_b^I) = M_B + M_T + S_{bI} F_B + S_{tI} F_T \end{aligned} \tag{4.38}$$

The last two terms on the RHS of Equation 4.38 can be written as the sum of contributions from individual parts

$$S_{bI} F_B + S_{tI} F_T = S_{bI} F_B + \left(S_{tb} + S_{bI} \right) F_T \quad = S_{bI} F_{B+T} + S_{tb} F_T \tag{4.39}$$

Multiplying both sides of Equation (4.25) by S_{bI} and inserting into Equation (4.32) results in corresponding terms being cancelled from both sides. Therefore, the rotational dynamic equations of motion in an invariant tensor form are

$$\begin{aligned} m^T S_{tb} \left[\begin{array}{c} D^B D^B s_{tb} + D^B \Omega^{BI} s_{tb} + \Omega^{BI} D^B s_{tb} + \Omega^{BI} D^B s_{tb} \\ + \Omega^{BI} \Omega^{BI} s_{tb} + D^B V_b^I + \Omega^{BI} V_b^I \end{array} \right] & \\ + I_b^B D^B \omega^{BI} + \Omega^{BI} I_b^B \omega^{BI} = M_{B+T} + S_{tb} F_T & \end{aligned} \tag{4.40}$$

For numerical simulations, these equations are expressed in the body frame coordinate system as follows

$$\begin{aligned} & m^T [S_{tb}]^B \left[\begin{array}{c} [\ddot{s}_{tb}]^B + [\dot{\Omega}^{BI}]^B [s_{tb}]^B + 2[\Omega^{BI}]^B [\dot{s}_{tb}]^B \\ + [\Omega^{BI}]^B [\Omega^{BI}]^B [s_{tb}]^B + [\dot{V}_B^I]^B + [\Omega^{BI}]^B [V_b^I]^B \end{array} \right] \\ & + [I_b^B]^B [\dot{\omega}^{BI}]^B + [\Omega^{BI}]^B [I_b^B]^B [\omega^{BI}]^B = [M_{B+T}]^B + \left[[S_{tb}]^B [F_T]^B \right] \end{aligned} \tag{4.41}$$

4.3.2 Model 2: Multibody Equations of Motion

The equations developed for Model 2 for a two-body (central body and the abdomen) multibody are similar to those presented by Sakhei in [150] for a three-body (left wing, right wing and the body) multibody, which also follows the invariant tensor formulation of Zipfel [196]. However, the equations in [150] are for a three-body flapping wing multibody, which considered the mass effects of the wing, whereas, the equations for Model 2 are for a two-body fixed wing multibody model with articulated non-lifting appendage (abdomen) wings, and uses the point mass assumption for the abdomen to further simplify the equations.

4.3.2.1 Translational Dynamics

For a system of k clustered rigid bodies, the translational dynamic equations are developed as the sum of their individual contributions, considering their respective centres of mass at B_k, with respect to the inertial frame I as follows [150], [196]:

$$D^I\left(\sum_k m^{B_k} D^I s_{B_k I}\right) = \sum_k F_k \tag{4.42}$$

where $\sum_k F_k$ is the contributing sum of all the forces acting on the aircraft from each rigid body as in $\sum_k F_k = F_B + F_T$.

Recall three previously introduced reference points b, j and t. Separating the individual contributions of the central body and the tail with $s_{B_k I} = s_{bI} + s_{tI}$ and $s_{tI} = s_{tj} + s_{jb} + s_{bI}$ gives

$$D^I\left(m^B D^I s_{bI} + m^T D^I s_{tj} + m^T D^I s_{jb} + m^T D^I s_{bI}\right) = F_B + F_T \tag{4.43}$$

The first term on the left hand side (LHS) of Equation (4.43) represents the contribution of the central body, while the second, third and fourth terms represent the contributions of the tail. Merging the first and fourth terms of the LHS of Equation (4.43) and introducing $D^I s_{bI} = V_b^I$

results in

$$\underbrace{m\ D^I V_b^I}_{\text{Term I}} + \underbrace{m^T D^I s_{tj}}_{\text{Term II}} + \underbrace{m^T D^I D^I s_{jb}}_{\text{Term III}} = \underbrace{F_B + F_T}_{\text{Term IV}} \tag{4.44}$$

Since $Term\ I$ of Equation (4.44) relates to the body frame, the Euler transformation is used to represent this term in the body-fixed frame as

$$m\ D^I V_b^I = m\ (D^B V_b^I + \Omega^{BI} V_b^I) \tag{4.45}$$

$Term\ II$ of Equation (4.44) relates to the tail frame, therefore, the rotational time derivative $D^I s_{tj}$ is transformed to the tail frame, using Equation (4.3) as in

$$m^T D^I D^I s_{tj} = m^T D^I (D^T s_{tj} + \Omega^{TI} s_{tj}) \tag{4.46}$$

The vector s_{tj} is constant in the tail frame, hence, $D^T s_{tj} = 0$ in Equation (4.46). Additionally, rewriting $\Omega^{TI} = \Omega^{TB} + \Omega^{BI}$ results in

$$m^T D^I D^I s_{tj} = m^T D^I (\Omega^{TB} s_{tj} + \Omega^{BI} s_{tj}) \tag{4.47}$$

In addition, the rotational time derivatives of Ω^{TB} and Ω^{BI} should be transformed into their associated frames, which are the tail and body frames, respectively. Therefore, Equation (4.47) becomes

$$\begin{aligned} m^T D^I D^I s_{tj} &= m^T [D^T (\Omega^{TB} s_{tj}) + \Omega^{TI} \Omega^{TB} s_{tj} + D^B (\Omega^{BI} s_{tj}) + \Omega^{BI} \Omega^{BI} s_{tj}] \\ &= m^T \begin{bmatrix} D^T \Omega^{TB} s_{tj} + \Omega^{TB} D^T s_{tj} + \Omega^{TI} \Omega^{TB} s_{tj} \\ + D^B (\Omega^{BI} s_{tj}) + \Omega^{BI} D^B s_{tj} + \Omega^{BI} \Omega^{BI} s_{tj} \end{bmatrix} \end{aligned} \tag{4.48}$$

Again, since $D^T s_{tj} = 0$, the second term on the RHS of Equation (4.48) vanishes. Additionally, rewriting $\Omega^{TI} = \Omega^{TB} + \Omega^{BI}$ and using the Euler transformation $D^B s_{tj} = D^W s_{tj} + \Omega^{TB} s_{tj}$

results in

$$m^T D^I D^I s_{tj} = m^T \left[\begin{array}{c} D^T \Omega^{TB} s_{tj} + \Omega^{TB} \Omega^{TB} s_{tj} + \Omega^{BI} D^T s_{tj} + D^B \Omega^{BI} s_{tj} \\ +2\Omega^{BI} \Omega^{TB} s_{tj} + \Omega^{BI} \Omega^{BI} s_{tj} \end{array} \right] \tag{4.49}$$

However, $D^T s_{tj} = 0$; therefore, the final expression for $Term\ II$ in Equation (4.44) is

$$m^T D^I D^I s_{tj} = m^T \left[\begin{array}{c} D^T \Omega^{TB} s_{tj} + \Omega^{TB} \Omega^{TB} s_{tj} \\ +D^B \Omega^{BI} s_{tj} + 2\Omega^{BI} \Omega^{TB} s_{tj} + \Omega^{BI} \Omega^{BI} s_{tj} \end{array} \right] \tag{4.50}$$

$Term\ III$ of Equation (4.44) should be transformed to the body frame as

$$m^T D^I D^I s_{jb} = m^T D^I (D^B s_{jb} + \Omega^{BI} s_{jb}) \tag{4.51}$$

Considering $D^B s_{jb} = 0$ since s_{jb} is fixed in the body frame and transforming the rotational derivative to the body frame gives

$$m^T D^I D^I s_{jb} = m^T [D^B \Omega^{BI} s_{jb} + \Omega^{BI} \Omega^{BI} s_{jb}] \tag{4.52}$$

Finally, $Term\ IV$ of Equation (4.44) represents the sum of all external forces acting on the aircraft. Substituting Equation (4.45), (4.50) and (4.52) into Equation (4.44) gives the translational dynamic equations of motion in an invariant tensor form as

$$m\ (D^B V_b^I + \Omega^{BI} V_b^I) + m^T \left[\begin{array}{c} D^T \Omega^{TB} s_{tj} + \Omega^{TB} \Omega^{TB} s_{tj} + D^B \Omega^{BI} (s_{tj} + s_{jb}) \\ +\Omega^{BI} \Omega^{BI} (s_{tj} + s_{jb}) + 2\Omega^{BI} \Omega^{TB} s_{tj} \end{array} \right] = F_B + F_T \tag{4.53}$$

To use this equation in a simulation framework, all terms in Equation (4.53) must be written as body coordinate frames using transformation matrices.

$$
\begin{aligned}
& m\left([\dot{V}_B^I]^B + [\Omega^{BI}]^B[V_b^I]^B\right) + m^T\Bigg([R]^{BT}\left([\dot{\Omega}^{TB}]^T[s_{tj}]^T + [\Omega^{TB}]^T[\Omega^{TB}]^T[s_{tj}]^T\right)\Big) \\
& + [\dot{\Omega}^{BI}]^B([R]^{BT}[s_{tj}]^T + [s_{jb}]^B) + \left([\Omega^{BI}]^B\,[\Omega^{BI}]^B([R]^{BT}[s_{tj}]^T + [s_{jb}]^B)\right) \\
& + \left(2\,\Omega^{BI}[R]^{BT}([\Omega^{TB}]^T[s_{tj}]^T)\right)\Bigg) = F_{B+T}
\end{aligned} \tag{4.54}
$$

4.3.2.2 Rotational Dynamics

For a system of k clustered rigid bodies, the rotational dynamic equations are developed as the sum of their individual contributions based on Euler's law, as follows [150], [196]:

$$
\underbrace{\sum_k D^I\left(I_{B_k}^{B_k}\omega^{B_kI}\right)}_{\text{Term I}} + \underbrace{\sum_k D^I\left(m^{B_k}S_{B_kI}D^I s_{B_kI}\right)}_{\text{Term II}} = \sum_k M_k + \sum_k S_{B_kI}F_k \tag{4.55}
$$

where the expression $\sum_k M_k + \sum_k S_{B_kI}F_k$ on the RHS of Equation (4.55) is the contributing sum of all the moments acting on the aircraft from each rigid body as in $\sum_k M_k + \sum_k S_{B_kI}F_k = M_B + M_T + S_{bI}F_B + S_{tI}F_T$. For the system being considered in this thesis, $Term\ I$ in Equation (4.55) is given as

$$
\sum_k D^I\left(I_{B_k}^{B_k}\omega^{B_kI}\right) = D^I\left(I_b^B\omega^{BI}\right) \tag{4.56}
$$

Applying the chain rule and Euler transformation, the RHS of Equation (4.56) leads to

$$
\sum_k D^I\left(I_{B_k}^{B_k}\omega^{B_kI}\right) = \omega^{BI}D^BI_b^B + I_b^BD^B\omega^{BI} + \Omega^{BI}I_b^B\omega^{BI} \tag{4.57}
$$

Since the moment of inertia of the body is constant in its corresponding frame, the first term on the RHS of Equation (4.57) vanishes.

Applying the chain rule to $Term\ II$ in Equation (4.55) yields

$$\sum_k D^I\left(m^{B_k} S_{B_k I} D^I s_{B_k I}\right) = \sum_k m^{B_k}\left(D^I S_{B_k I} D^I s_{B_k I} + S_{B_k I} D^I D^I s_{B_k I}\right) \tag{4.58}$$

The cross-product of the vector derivatives is zero; therefore, the first term on the RHS of Equation (4.58) is zero. Additionally, the body and abdominal contributions are separated, leading to

$$\sum_k D^I\left(m^{B_k} S_{B_k I} D^I s_{B_k I}\right) = m^B S_{BI} D^I D^I s_{bI} + m^T S_{tI} D^I D^I s_{tI} \tag{4.59}$$

Using Euler transformation, the first term on the RHS of Equation (4.59) becomes

$$m^B S_{bI} D^I D^I s_{bI} = m^B S_{bI}(D^B V_b^I + \Omega^{BI} V_b^I) \tag{4.60}$$

The second term on the RHS of Equation (4.59) could be developed using the vector expansion $s_{tI} = s_{tj} + s_{jb} + s_{bI}$ and performing Euler transformation, results in

$$m^T S_{tI} D^I D^I s_{tI} = m^T S_{tI} D^I\left(D^T s_{tj} + \Omega^{TI} s_{tj} + D^B s_{jb} + \Omega^{BI} s_{jb} + V_b^I\right) \tag{4.61}$$

As s_{tj} and s_{jb} are constant in their corresponding frames, the first and third terms of the equation above vanish. Additionally, the rotational time derivatives of the last two terms can be transformed to the body frame as follows

$$D^I(\Omega^{BI} s_{jb}) = D^B \Omega^{BI} s_{jb} + \Omega^{BI}\Omega^{BI} s_{jb} \quad \text{and} \quad D^I V_b^I = D^B V_b^I + \Omega^{BI} V_b^I \tag{4.62}$$

Only the rotational derivative of the second term on the RHS of Equation (4.61) needs to be calculated. Using the expansion of the angular velocity tensor $\Omega^{TI} = \Omega^{TB} + \Omega^{BI}$ and

performing the Euler transformation results in

$$D^I\left(\Omega^{TI}s_{tj}\right) = D^T\Omega^{TB}s_{tj} + \Omega^{TI}\Omega^{TB}s_{tj} + D^B(\Omega^{BI}s_{tj}) + \Omega^{BI}\Omega^{BI}s_{tj} \tag{4.63}$$

Ω^{TI} in the second term of RHS the above equation should be substituted using $\Omega^{TI} = \Omega^{TB} + \Omega^{BI}$. For the third term on the RHS of Equation 4.63, taking the rotational time derivative of the term, applying the Euler transformation, $D^B s_{tj} = D^T s_{tj} + \Omega^{TB} D^B s_{tj}$ and considering that $D^T s_{tj} = 0$. The third term is simplified to

$$D^B(\Omega^{BI}s_{tj}) = D^B(\Omega^{BI}s_{tj}) + \Omega^{TI}\Omega^{TB}s_{tj} \tag{4.64}$$

Substituting Equation (4.64) into Equation (4.63) and then substituting Equations (4.62) and (4.63) into Equation (4.61) gives

$$m^T S_{tI} D^I D^I s_{tI} = m^T S_{tI} \begin{bmatrix} D^T\Omega^{TB}s_{tj} + \Omega^{TB}\Omega^{TB}s_{tj} \\ +D^B\Omega^{BI}s_{tj} + 2\Omega^{BI}\Omega^{TB}s_{tj} + \Omega^{BI}\Omega^{BI}s_{tj} \\ +D^B\Omega^{BI}s_{jb} + \Omega^{BI}\Omega^{BI}s_{jb} + D^B V_b^I + \Omega^{BI}V_b^I \end{bmatrix} \tag{4.65}$$

Finally, substituting Equations (4.60) and (4.65) into Equation (4.59) and further substituting Equations (4.57) and (4.59) into Equation (4.55), Equation 4.66 is obtained as

$$\begin{aligned} &m^T S_{tI} \begin{bmatrix} D^T\Omega^{TB}s_{tj} + \Omega^{TB}\Omega^{TB}s_{tj} \\ +D^B\Omega^{BI}s_{tj} + 2\Omega^{BI}\Omega^{TB}s_{tj} + \Omega^{BI}\Omega^{BI}s_{tj} \\ +D^B\Omega^{BI}s_{jb} + \Omega^{BI}\Omega^{BI}s_{jb} + D^B V_b^I + \Omega^{BI}V_b^I \end{bmatrix} \\ &+ I_b^B D^B\omega^{BI} + \Omega^{BI} I_b^B \omega^{BI} + m^B S_{bI}(D^B V_b^I + \Omega^{BI}V_b^I) = M_B + M_T + S_{bI}F_B + S_{tI}F_T \end{aligned} \tag{4.66}$$

The last two terms on the RHS of Equation 4.66 can be written as the sum of contributions from individual parts

$$S_{bI}F_B + S_{tI}F_T = S_{bI}F_B + \left(S_{tb} + S_{bI}\right)F_T \quad = S_{bI}F_{B+T} + S_{tb}F_T \tag{4.67}$$

Multiplying both sides of Equation (4.53) by S_{bI} and inserting into Equation (4.59) results in corresponding terms being cancelled from both sides. Therefore, the rotational dynamic equations of motion in an invariant tensor form are

$$m^T S_{tb}\begin{bmatrix} D^T\Omega^{TB}s_{tj} + \Omega^{TB}\Omega^{TB}s_{tj} \\ +D^B\Omega^{BI}(s_{tj}+s_{jb}) + \Omega^{BI}\Omega^{BI}(s_{tj}+s_{jb}) \\ 2\Omega^{BI}\Omega^{TB}s_{tj} + D^B V_b^I + \Omega^{BI}V_b^I \end{bmatrix} + I_b^B D^B\omega^{BI} + \Omega^{BI}I_b^B\omega^{BI} = M_{B+T} + S_{tb}F_T \tag{4.68}$$

For numerical simulations, these equations must be expressed in the body frame coordinate system as follows

$$\begin{aligned} &m^T([R]^{BT}[S_{tj}]^T + [S_{jb}]^B)\Big([R]^{BT}\left([\dot{\Omega}^{TB}]^T[s_{tj}]^T + [\Omega^{TB}]^T[\Omega^{TB}]^T[s_{tj}]^T\right) \\ &+ [\dot{\Omega}^{BI}]^B([R]^{BT}[s_{tj}]^T + [s_{jb}]^B) + \left([\Omega^{BI}]^B\,[\Omega^{BI}]^B([R]^{BT}[s_{tj}]^T + [s_{jb}]^B)\right) \\ &+ \left(2\,\Omega^{BI}[R]^{BT}([\Omega^{TB}]^T[s_{tj}]^T)\right) + \left([\dot{V}_B^I]^B + [\Omega^{BI}]^B[V_b^I]^B\right)\Big) \\ &+ [I_b^B]^B[\dot{\omega}^{BI}]^B + [\Omega^{BI}]^B[I_b^B]^B[\omega^{BI}]^B = [M_{B+T}]^B + \left[[S_{tb}]^B[F_T]^B\right] \end{aligned} \tag{4.69}$$

4.4 Chapter Summary

In this chapter, the nonlinear multibody equations of motion for a dragonfly-inspired straight-wing aircraft with an articulated abdomen were derived using a tensor-based formulation of the Newton-Euler method. Two sets of EoMs were derived based on abdominal movements, to represent translational and rotational abdominal motion. Only the forces and moments acting on the vehicle were not modelled and will be presented in subsequent chapters.

Chapter 5

Performance Analysis of Bioinspired Vehicle Motion

In the previous chapter, the equations of motion were derived for a multibody dragonfly-inspired straight-wing aircraft with an articulated abdomen. In this chapter, those equations are programmed into MATLAB/Simulink for the purposes of simulating the effects of appendage movements on forward flight performance and manoeuvrability. Therefore, the analysis in this chapter addresses the effects observed abdominal movements have on various areas of forward flight performance through simulation. Specifically, the effects of abdominal movements on steady cruise and turning flight performance are examined. The utility of an articulated appendage for maintaining balance and initiating a quasi-steady fixed-thrust pull up manoeuvre is also investigated.

5.1 Introduction

In recent years, the desire for SUAVs and MAVs to perform increasingly complex missions such as flying inside a building with obstacles of unknown size and location continue to increase. As the levels of complexity of the mission increase, higher levels of manoeuvrability are required, beyond the conventional flight envelope which is achievable using conventional aerodynamic control surfaces such as elevator, rudder, and so on [218]. Achieving a level of manoeuvrability

beyond the limits provided by conventional aerodynamic control surfaces is described as supermanoeuvrability [10], and dragonflies are known to demonstrate supermanoeuvrability as apex predators among insects. Therefore, evolution creates constant pressure for optimisation of biological systems, with analogous commercial and operational pressures driving the optimisation of technical systems, including UAVs.

The abdomen of the dragonfly, for instance, has evolved to serve many purposes. It houses the digestive tract, and has anatomical features related to reproduction, while also being required to bend for mating and oviposition [219]. In addition, the movement of the abdomen in flight has been suggested to play a less obvious role in maintaining balance, enhancing stability and achieving extra manoeuvrability in some situations. Most of the previous works have focused on the effects of abdominal movements on hover flight, while the effect it has on forward flight has received less attention. Therefore, the analysis in this chapter addresses the effects observed abdominal movements have on various areas of forward flight performance through simulation. The performance parameters that define the vehicle's steady performance and manoeuvrability characteristics for the DISWA were carefully selected given that it is not a question of whether the abdomen exists or is in use or not, but a question of what effects it has on performance and manoeuvrability, given that it is already present and is capable of different motions.

This chapter aims to address the following research question:

1. What are the effects of appendage movements on forward flight, considering dynamic/inertial effects only?

5.2 Longitudinal Flight

As mentioned earlier, the movement of the abdomen has been observed in the longitudinal flight of dragonflies, as shown in Figure 4.1 and 4.2. Based on these observations, two abdominal articulation modes that affect longitudinal flight are considered, and their utilisation

for trimming for and re-balancing in steady level flight, as well as for a pull up manoeuvre are investigated:

1. Tail contraction and extension, illustrated in Figure 5.1a. As this motion uses Model 1 EoMs, this will be referred to as "Model 1" and,
2. Tail up down wag movement, illustrated in Figure 5.1b. As this motion uses Model 1 EoMs and will be referred to as "Model 2".



(a) (b)

Figure 5.1: Dragonfly side view showing longitudinal tail actuation modes. (**a**) Tail contraction and extension. (**b**) Tail up down wag movement.

5.2.1 Dynamic Equations of Motion

Two sets of dynamic equations are presented for the two modes of tail actuation considered. The first set of equations represents Model 1, used for modelling the linear motion, that is the contraction and extension of the DISWA tail during flight (see Figure 5.1a). The second set of equations representing Model 2, was used to model the up and down wag movement of the DISWA tail during flight, shown in Figure 5.1b. In the equations presented in this section, when the reference frame of a vector or tensor is not specified, the default is to use the body-fixed reference frame B.

5.2.1.1 Model 1: Aircraft Dynamics

With the aircraft configuration in Figure 5.1a, representative of a linear moving mass, the change in the overall cg position of the aircraft with respect to point b, written in the body frame is expressed as

$$\triangle s_{cb} = \frac{m^T s_{tb}}{m} \tag{5.1}$$

Also, the inertia matrix of the whole aircraft C about point b is given by

$$I_b^C = I_b^B + m^T \left[(s'_{tb}\, s_{tb}) \mathbb{I}_{3\times 3} - s_{tb}\, s'_{tb} \right] \tag{5.2}$$

and $\mathbb{I}_{3\times3}$ is a 3×3 identity matrix.

The translational and rotational dynamic equations, already derived in Chapter 4, are then given by Equations 5.3 and 5.4 respectively

$$m\dot{V}_B^I + m\left(\Omega^{BI}V_B^I\right) + \left(m^T\left[\ddot{s}_{tb} + \Omega^{BI}\left(\Omega^{BI}s_{tb} + 2\dot{s}_{tb}\right) + S_{tb}\dot{\omega}^{BI}\right]\right) = F_{B+T} \tag{5.3}$$

$$\begin{aligned} &I_b^C\dot{\omega}^{BI} + \left(\Omega^{BI}[I_b^B]^B\omega^{BI}\right) + \left(S_{tb}m^T\left[\omega'^{BI}s_{tb}\ \omega^{BI} + \ddot{s}_{tb}\right] + \right. \\ &\left. S_{tb}\ m^T\left[\Omega^{BI}V_B^I + \dot{V}_B^I\right] + 2m^T\left[(s'_{tb}\dot{s}_{tb})\mathbb{I} - \dot{s}_{tb}s'_{tb}\right]\omega^{BI}\right) = M_{B+T} + S_{t_b}F_T \end{aligned} \tag{5.4}$$

where s_{tb}, $\dot{s}_{tb}$ and $\ddot{s}_{tb}$ are the linear position, velocity and acceleration of the tail mass with respect to point b in the body frame.

5.2.1.2 Model 2: Aircraft Dynamics

For Model 2, the change in cg position and the total inertia matrix of the whole system is also estimated using Equations (5.1)–(5.2), however,

$$s_{tb} = [R]^{BT}[s_{tj}]^T + s_{jb} \tag{5.5}$$

Also, Model 2 translational and rotational dynamic equations, already derived in Chapter 4 are presented as

$$\begin{aligned} &m\dot{V}_B^I + m\left(\Omega^{BI}\ V_B^I\right) + m^T\left(\left[R\right]^{BT}\left(\left[\dot{\Omega}^{TB}\right]^T[s_{tj}]^T + \left[\Omega^{TB}\right]^T\left(\left[\Omega^{TB}\right]^T[s_{tj}]^T\right)\right)\right. \\ &+ \left(\dot{\Omega}^{BI}\left([R]^{BT}[s_{tj}]^T + s_{jb}\right)\right) + \left(\Omega^{BI}\ \Omega^{BI}\left([R]^{BT}[s_{tj}]^T + s_{jb}\right)\right) \\ &\left. + \left(2\ \Omega^{BI}[R]^{BT}\left(\left[\Omega^{TB}\right]^T[s_{tj}]^T\right)\right)\right) = F_{B+T} \end{aligned} \tag{5.6}$$

$$I_b^C \dot{\omega}^{BI} + \Omega^{BI} I_b^B \omega^{BI} + m^T \left([R]^{BT} [S_{tj}]^T + S_{jb} \right) \Bigg[[R]^{BT} \left([\dot{\Omega}^{TB}]^T [s_{tj}]^T + [\Omega^{TB}]^T ([\Omega^{TB}]^T [s_{tj}]^T) \right)$$
$$+ \left(\Omega^{BI} \; \Omega^{BI} ([R]^{BT} [s_{tj}]^T + s_{jb}) \right) + \left(2 \, \Omega^{BI} [R]^{BT} ([\Omega^{TB}]^T [s_{tj}]^T) \right) + \dot{V}_B^I + \Omega^{BI} \; V_B^I \Bigg] = M_{B+T} + S_{tb} F_T \tag{5.7}$$

5.2.2 Forces and Moments

The resultant forces and moments acting on the aircraft expressed as contributions from the central body and the abdomen, are represented by the RHS of Equations (4.54) and (4.69) respectively. The forces and moments acting on the aircraft are due to aerodynamics (F_A, M_A), gravity (F_G, M_G), and propulsion (F_P, M_P), which ultimately must be represented in the body frame coordinate system as follows

$$[F_{B+T}]^B = [F_A]^B + [F_G]^B + [F_P]^B \tag{5.8}$$

$$[M_{B+T}]^B + \left[[s_{tb}]^B \times [F_T]^B \right] = [M_A]^B + [M_G]^B \tag{5.9}$$

The propulsive force is assumed to act parallel to the aircraft x_B axis and produces no moments, which yields

$$[F_P]^B = \begin{bmatrix} T_n \\ 0 \\ 0 \end{bmatrix} \tag{5.10}$$

The gravitational force model for both dynamic models is also the same and is detailed in [220], however, the gravitational moments for both tail actuation modes differ. For Model 1, the gravitational moment is

$$[M_G]^B = s_{tb} \times [R]^{BI} \begin{bmatrix} 0 \\ 0 \\ m^T g \end{bmatrix}. \tag{5.11}$$

where g is the acceleration due to gravity. However, for Model 2, the gravitational moment produced by the tail is given by

$$[M_G]^B = ([R]^{BT}[s_{tj}]^T + s_{jb}) \times [R]^{BI} \begin{bmatrix} 0 \\ 0 \\ m^T g \end{bmatrix} \tag{5.12}$$

The mathematical models developed in this thesis make the assumption that the aerodynamic contributions from the body and tail of dragonfly are independent and additive. However, the analyses presented in Chapters 5-7 focus only on the dynamic effects. In addition, the aerodynamic properties of the tail were ignored as these effects were assumed to have little influence on the aerodynamics of the DISWA, compared to the head/thorax/wings combination. The effects of including the aerodynamic contributions of the tail are later examined in Chapter 8.

The resultant aerodynamic forces and moments produced for fixed wing aircraft are well established [59], [220] and are represented as

$$[F_A]^B = \frac{1}{2}\rho V^2 S_{ref} \begin{bmatrix} C_x \\ C_y \\ C_z \end{bmatrix} \quad \text{and} \quad [M_A]^B = \frac{1}{2}\rho V^2 S_{ref} \begin{bmatrix} C_l\, b_{ref} \\ C_m\, c_{ref} \\ C_n\, b_{ref} \end{bmatrix} \tag{5.13}$$

where ρ is the density of air, c_{ref}, b_{ref} and S_{ref} are the respective reference chord, span and area of the wing. $C_{(x,y,z,l,m,n)}$ are the dimensionless aerodynamic coefficients.

5.2.3 Control Effectors

The control effectors used in the longitudinal flight analysis vary with the flight regime. For propulsion, the control input used in this study is the thrust (T_n). The aerodynamic control surfaces are the left and right elevons, denoted by η_l and η_r respectively and located on the trailing edges of the wings as shown in Figure 4.4b in Chapter 4. The elevons, depending on the desired flight regime, function as elevators or ailerons. The combined deflections of the elevons as elevators δ_e or ailerons δ_a are according to [220]

$$\begin{pmatrix} \delta_e \\ \delta_a \end{pmatrix} = \begin{pmatrix} 1 & 1 \\ -1 & 1 \end{pmatrix} \begin{pmatrix} \eta_r \\ \eta_l \end{pmatrix} \tag{5.14}$$

With regards to the longitudinal motion of the aircraft model in this study, the two main functions of the

elevators are for longitudinal trim and/or longitudinal control. When deflected, the camber of the airfoil of the wing is changed and the lift coefficient (C_L) changes consequently. Therefore, elevator deflection increases or decreases wing lift and pitching moment [221]. The tail mass linear displacement or angular deflection on the other hand, functions as an alternative moment generator, changing pitching moment [42]. For Model 1, the control inputs are the tail mass positions ($s_{tb_x}, s_{tb_y}, s_{tb_z}$). While for Model 2, the control inputs are the tail mass angular deflections (ϕ_T, θ_T, ψ_T) relative to the body frame. Where applicable, a downward deflection of a control surface or tail deflection is positive and an upward deflection is negative.

5.2.4 Aircraft Model Specifications

This section presents the specifications of the conceptual DISWA used for simulation. Although dragonfly inspired, the DISWA is a fixed wing platform. The primary inspiration from dragonflies was the abdominal movement, compromised against the need to preserve static margin for fixed wing flight. In addition, the DISWA had a requirement to potentially be created from current UAV technology, with reasonable actuator sizes, and likely substantial multibody effects from abdominal movements. This need for the possibility of a practical implementation, and characteristics of current small UAVs constrained the DISWA design. Hence, the values of the DISWA were selected to ensure the system was similar in scale to small fixed wing drones (about 14 times the wing span of the dragonflies presented in [222]). Estimating the effective aspect ratio (AR) of the fore and hind wing in [222], resulted in an inappropriate low value, considering the DISWA is a fixed wing platform, hence, an ($AR = 7.3$) was selected as dragonflies are characterised by high AR wings [189], [223]. The value of the wing span was then determined (b_{ref}) using [29]

$$b_{ref} = AR \times c_{ref}. \tag{5.15}$$

The Phoenix airfoil (Figure 5.2) [224]–[226] was selected for this study. It is a relatively thin (thickness below 10%), low Reynolds number, reflexed airfoil, often used in small tailless aircraft to ensure longitudinal static stability, such as the solar powered flying wing UAV developed in [224].

Tailless aircraft do not possess conventional vertical stabilisers and often exhibit poor lateral dynamic

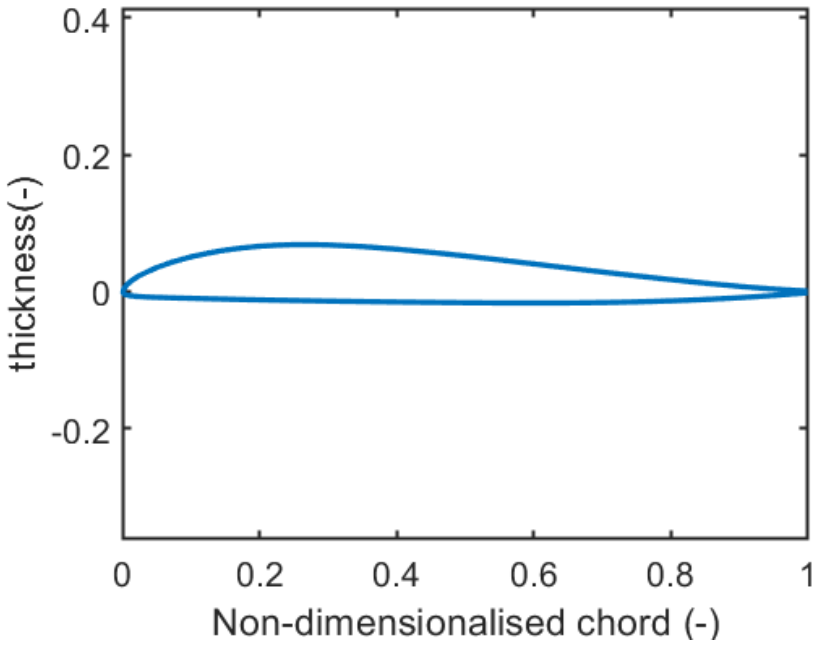
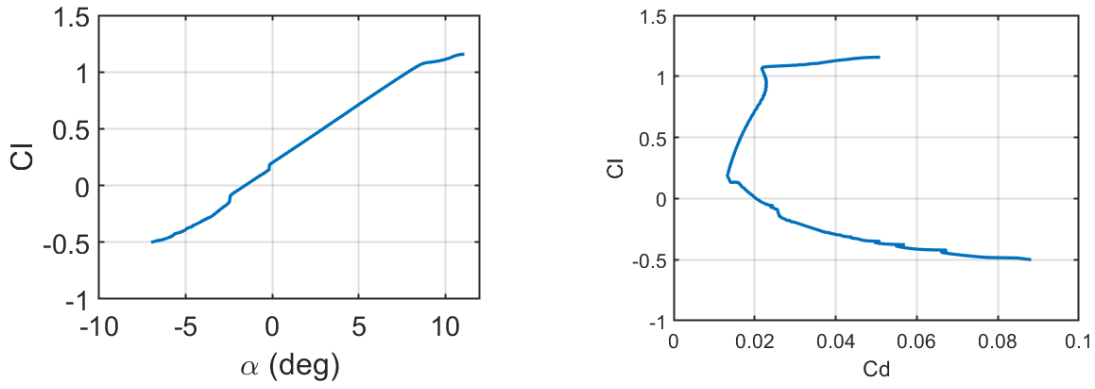


Figure 5.2: Phoenix airfoil.

stability [227]. To improve lateral stability, a positive dihedral of 3° was applied along the wing span and the wing was twisted at the root by 3° to reduce stall tendencies at the tip [227], [228]. The aerodynamic characteristics of the airfoil which was evaluated in XFLR5 at $Re = 10^5$ are presented in Figure 5.3.



(a) (b)

Figure 5.3: Phoenix airfoil characteristics. (**a**) Lift curve. (**b**) Drag polar.

In addition, XFLR5 was used for the initial distribution of the point masses and initial estimation of moments of inertia of the aircraft. The tail mass was chosen as 0.06 kg, making it approximately 15% of the total mass of the aircraft. The maximum tail/abdominal length was chosen to be 0.4 m, which was about 1.33× the body length. Again, these values were chosen with consideration to the fixed

wing assumption and using [192], [219], [222] as guides. Furthermore, the aircraft was assumed to be symmetrical about the $x-z$ plane, therefore, $I_{xy} = I_{yz} = 0$. I_{xz} was also neglected in comparison with the moments of inertia.

The physical properties of the DISWA model used for simulation, are summarised in Table 5.1. The datum with respect to which the position values were obtained was chosen as the leading edge of the wing.

Table 5.1: Aircraft model (DISWA) physical properties.

Parameter	Value	Parameter	Value
m^B (kg)	0.325	m^T (kg)	0.06
Body length, l_B (m)	0.3	Tail length, $l_{T_{max}}$ (m)	0.4
Max. body diameter, $d_{B_{max}}$ (m)	0.14	Tail diameter, d_T (m)	0.05
$I_{xx_b}^B$ (kg·m^2)	0.00187	b_{ref} (m)	1.4
$I_{yy_b}^B$ (kg·m^2)	0.01117	c_{ref} (m)	0.19434
$I_{zz_b}^B$ (kg·m^2)	0.00934	S_{ref} (m^2)	0.26865
cg_b^B (m)	[−0.064; 0; 0.003]	ARP (m)	[0.025; 0; 0]

5.2.5 Simulation Environment

The implementation of the mathematical models was carried out in the MATLAB/Simulink simulation environment [208]. Figure 5.4 shows the Simulink model of the aircraft. The "Actuator model" produces the control inputs to the "Aircraft model" which contains the nonlinear equations of motion to then produce the aircraft state vector $(u, v, w, p, q, r, \phi, \theta, \psi, x, y, H)$.

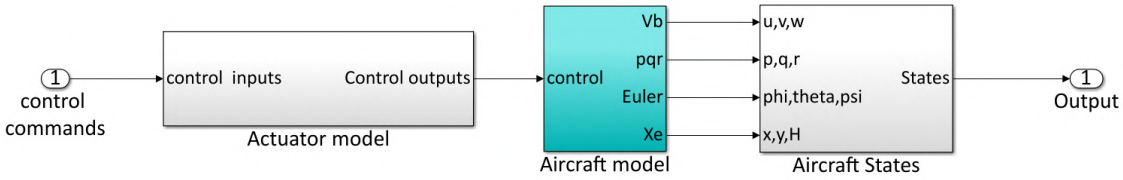


Figure 5.4: Aircraft model in Simulink.

It is important to note that since the analyses presented in this chapter focus on static stability and instantaneous performance, this implies the positions of the mass actuators are fixed in the body frame and $\ddot{s}_{tb} = \dot{s}_{tb} = \dot{\Omega}^{TB} = \Omega^{TB} = 0$. Therefore, the actuator dynamics for the simulation model were ignored. The modelling constraints presented in Table 5.2 were considered in simulation of the aircraft model.

Table 5.2: Parameter constraints.

Description	Limitation	Unit
Angle of attack	$\|\alpha\| \leq 20$	°
Sideslip	$\|\beta\| \leq 30$	°
Roll	$\|\phi\| \leq 30$	°
Pitch	$\|\theta\| \leq 30$	°
Yaw	$\|\psi\| \leq 30$	°
Airspeed	$V \leq 15$	m/s

The control effectors for longitudinal flight, as well as the physical constraints of the control inputs are shown in Table 5.3. The neutral position of the tail for Model 2 was considered to be when it was fully extended with no deflection and the tail angular deflection limits were relative to the neutral position.

Table 5.3: Physical constraints of longitudinal control inputs.

Limitations	Unit
$-20 \leq \delta_e \leq 20$	°
$-60 \leq \theta_T \leq 60$	°
$0.464 \leq s_{tb_x} \leq 0.664$	m

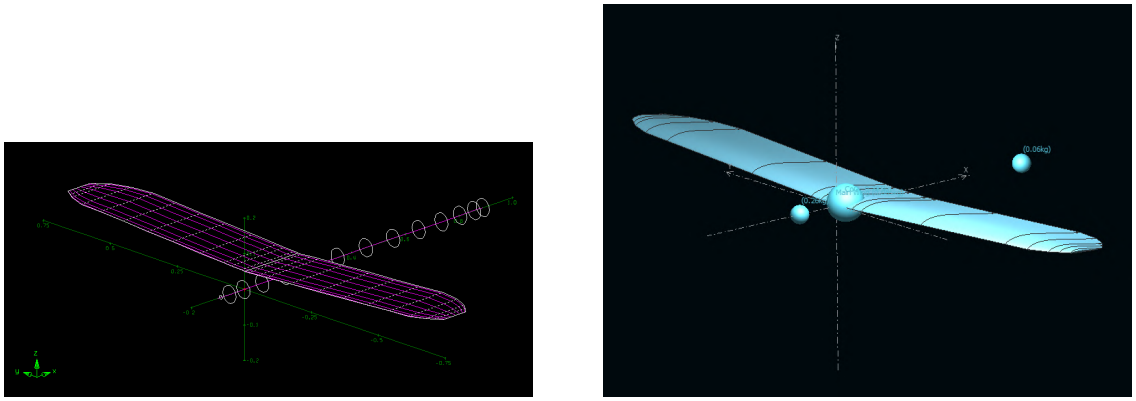
The constraint values presented in Tables 5.2 and 5.3 were conservatively chosen based on reasonable specifications that obey the general physical laws that apply to fixed wing air vehicles, and based on values used for aircraft of similar size in the literature [42], [229], [230].

5.2.6 Aerodynamic Model for Simulation

XFLR5 and AVL were used to establish the aerodynamic model of the aircraft for simulation. The aircraft AVL model shown in Figure 5.5a includes a fuselage, however, as recommended in the AVL documentation [202], it was excluded from the AVL model used to generate aerodynamic data. This aerodynamic data consists of look up tables that cover a range of angles of attack and sideslip angles (-25° $\leq \alpha \leq$ +25° and -30° $\leq \beta \leq$ +30°), and used in the simulation of the nonlinear model in Simulink. See Appendix A for the AVL geometry file used for the DISWA in this study. All manoeuvres considered in the longitudinal study assume zero sideslip, $\beta = 0$. The aerodynamic data used in the

simulation were obtained with respect to an arbitrarily chosen aerodynamic reference point (ARP). Doing so enabled the aerodynamic moments at any point in the body frame to be calculated as the sum of the aerodynamic moments at the ARP and the cross product of the aerodynamic forces and corresponding lever arms $\Delta_{x_b - x_{ARP}}$, $\Delta_{y_b - y_{ARP}}$ and $\Delta_{z_b - z_{ARP}}$. For example, the aerodynamic moments at point b are [29]

$$[M_A]^B = M_{A_{ARP}} + [F_A]^B \times \begin{bmatrix} \Delta_{x_b - x_{ARP}} \\ \Delta_{y_b - y_{ARP}} \\ \Delta_{z_b - z_{ARP}} \end{bmatrix} \tag{5.16}$$



(a) (b)

Figure 5.5: Aircraft model with no abdominal deflection. (**a**) AVL model. (**b**) Mass distribution in XFLR5.

5.2.7 Analyses and Results

In this section, the analyses involving the use of the abdomen for steady cruise performance, correction of imbalance and performance in a pull up manoeuvre are presented.

5.2.7.1 Trim for Steady Cruise Flight

First, to verify the correctness of the models developed in section 5.2.1, Model 1 and Model 2 were trimmed for steady cruise flight, given the same longitudinal positioning of the tail mass. In steady state flight, translational and rotational velocity components in body frame are constant so, $\dot{u} = \dot{v} = \dot{w} = \dot{p} = \dot{q} = \dot{r} = 0$. Additionally, for the steady wings level flight condition, the body frame angular rates, $p = q = r = 0$, since the Euler rates are constant. The roll angle, ($\phi = 0$) and the yaw

angle, ($\psi = 0$) were also assumed. Since cruise altitude is constant, $\dot{z} = 0$ and a $\dot{y} = 0$ condition was imposed. The position of the tail mass in the body frame was fixed, $\ddot{s}_{tb} = \dot{s}_{tb} = 0$ for Model 1 and $\dot{\omega}_{TB} = \omega_{TB} = 0$ for Model 2.

For both models, the objective was to calculate the nominal values of the pitch angle (θ_0) and control inputs (δ_{e_0}) and (T_{n_0}) for cruise speed $V_0 = 10$ m/s and height $H_0 = 100$ m. Also, there was no tail deflection ($\theta_{T_0} = 0$) and the tail position was fixed at ($s_{tb_{x0}} = 0.564$ m) for both models. No tail deflection infers that for Model 2, ($s_{tj_0} = 0.264$ m) and ($s_{jb_0} = 0.3$ m). The models were trimmed using the MATLAB/Simulink linear analysis tool [208]. The trim results are presented in Table 5.4.

Table 5.4: Steady level trim flight condition for Model 1 and Model 2

Model Type	V_0 (m/s)	H_0 (m)	$s_{tb_{x0}}$ (m)	$\theta_{T_0}(^\circ)$	$\theta_0(^\circ)$	$\delta_{e_0}(^\circ)$	T_{n_0} (N)
Model 1	10	100	0.564	-	-0.252	-1.79	0.825
Model 2				0	-0.252	-1.79	0.825

From the results presented in Table 5.4, the trim results estimated using Models 1 and 2 produced the same trim results.

5.2.7.2 Steady Cruise Trim Analyses

Next, the effects of the abdominal movements on the vehicle's performance in steady cruise flight were analysed by evaluating the power required, and the ability to trim the aircraft using only the elevator (A-C) or a combination of both the elevator and articulated abdominal (C-C). In addition, none of the effectors should reach its saturation limit as per Table 5.3, while keeping the aircraft within the modelling constraints as per Table 5.2.

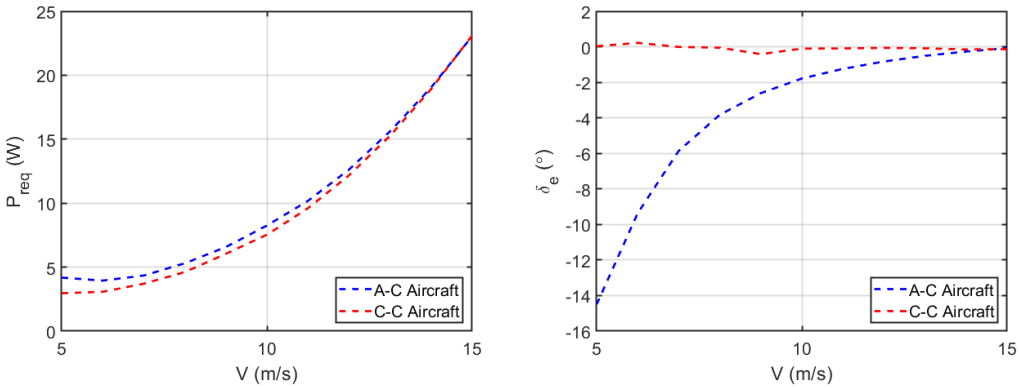
For steady cruise, lift balances the gravitational force ($L = W$) and the net thrust balances the drag ($T_n = D$). The energy required E_{req} in cruise as a function of time can be estimated by:

$$E_{req} = \int_t^{tf} P_{req} dt, \tag{5.17}$$

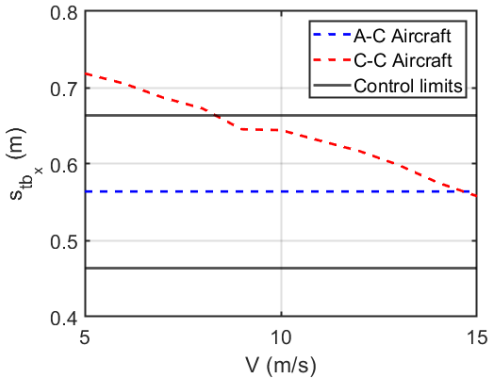
The power required P_{req} is equivalent to the energy required for one second in cruise. Therefore, ($P_{req} = DV$) quantifies the performance in terms of energy as well. Lastly, the analysis in this section assumes that there is always sufficient thrust to overcome the drag.

5.2.7.2.1 Model 1

With this model, the aim was to trim the aircraft for a steady cruise flight condition at various cruise speeds ranging from $V_0 = 5 - 10$ m/s and height $H_0 = 100$ m. The aircraft was first trimmed using only the elevator deflection, while the tail position was fixed at ($s_{tb_{x0}} = 0.664$ m), a fully extended tail was assumed. Then, the aircraft was trimmed using the elevator deflection and the translational actuation of the tail. Figures 5.6a–c show the variation of the power required, elevator deflection and tail position, respectively over the cruise speed range considered.



(a) Power required variation with cruise speed (b) Elevator deflection variation with cruise speed



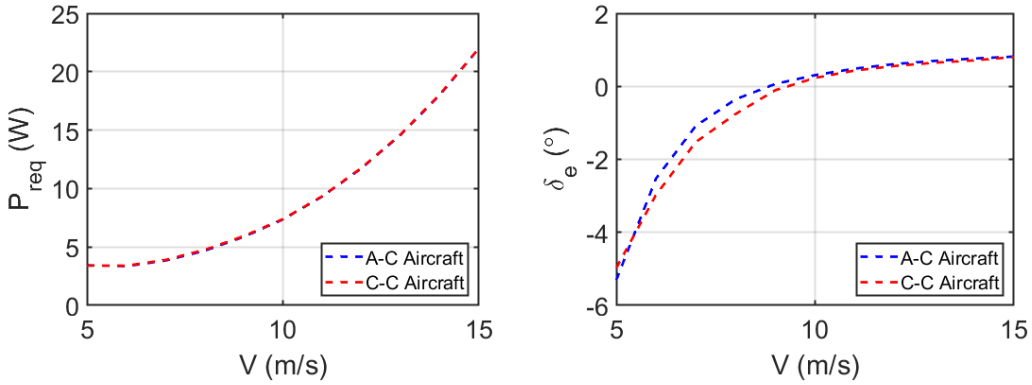
(c) Tail position variation with cruise speed

Figure 5.6: Trimmed steady cruise flight performance using Model 1.

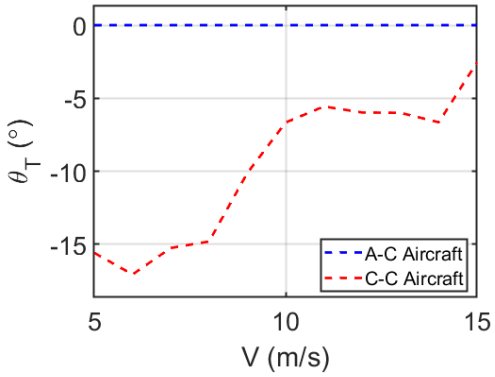
5.2.7.2.2 Model 2

For this model, the capability to use either the elevator deflection (A-C aircraft) or a combination of the elevator deflection and tail angular deflection (C–C aircraft) to trim the aircraft in steady cruising flight was examined. The cruise speed range considered was from $V_0 = 5 - 10$ m/s at a height $H_0 = 100$ m. The aircraft was first trimmed using only the elevator deflection, while the tail position was undeflected.

Then, the aircraft was trimmed using the elevator deflection and the rotational actuation of the tail. The results are shown in Figures 5.6a–c, as plots of the variation of the power required, elevator deflection and tail angular position, respectively over the cruise speed range considered.



(a) Power required variation with cruise speed (b) Elevator deflection variation with cruise speed



(c) Tail position variation with cruise speed

Figure 5.7: Trimmed steady cruise flight performance using Model 2.

5.2.7.2.3 Discussion

Several points may be noted from the results presented in Figure 5.6. Of particular importance are the power required, Figure 5.6a and the tail position, Figure 5.6c. From Figure 5.6c, one can observe that the limits of the trimmability range for Model 1 were solely determined by the linear mass actuator limits ($0.464 \leq s_{tb_x} \leq 0.664$), hence, the valid cruise speed range for the C-C aircraft was from about 8.3 to 15 m/s. However, the A-C aircraft was able to trim for all the cruise speeds considered (5–15m/s), without exceeding the elevator and abdominal position limits. In the case of the C-C aircraft, the tail mass starts fully extended and moves forward towards the nose as speed increases. When compared to the A-C aircraft, an average of 5.40% less power was required by the C-C aircraft. This indicates the benefit of using mass actuation rather than elevator at some cruise speeds.

For Model 2, both the A-C and C-C aircraft were able to achieve trim steady cruise flight condition for all the cruise speeds considered, without reaching the limits of the control effectors as is shown in Figures 5.6b and c. However, in comparison with the A-C aircraft, 0.39% more power was required on average by the C-C aircraft (see Figure 5.6a). This is because the deflected abdomen moves the combined cg position of the aircraft forward, generating greater induced drag.

5.2.7.3 Correction of Imbalance in Cruise Flight

An essential aircraft handling parameter is static stability, however, imbalance during flight is caused by many factors such as load distribution and fuel burn. The ability of an air vehicle to correct for imbalance during steady flight is desirable. Therefore, modelling of balance and control surface effects allows analysis of efficiency in steady flight. Where the main focus is longitudinal motion, static stability theory can be applied to cruise conditions, as well as to quasi-steady manoeuvres. A way to determine the static longitudinal stability of an aircraft is through the change in pitching moment with lift, $\frac{dC_m}{dC_L}$. This derivative must be negative for a stable aircraft. In addition, the pitching moment at zero angle of attack must be positive. The same condition applies using the change in pitching moment with angle of attack as an indicator in some cases, i.e., $\frac{dC_m}{d\alpha} < 0$ is indicative of a stable aircraft [59], [231]. Another measure of static stability is the static margin (SM), which will be used to analyse the static stability of the aircraft in consideration in this study due to its simplistic and intuitive nature. The SM of an aircraft is given by [29]

$$SM = \frac{X_{NP} - X_{cg_m}}{c_{ref}}, \tag{5.18}$$

where X_{NP} is the neutral point (NP), X_{cg_m} is the cg position of the whole aircraft along X_B axis.

Generally, if cg is ahead of the NP, then SM is positive and the aircraft is stable. The larger the SM, the more stable and less manoeuvrable an aircraft is. However, if the cg is behind the NP, resulting in a negative SM, the aircraft is unstable in pitch, making it difficult or impossible for humans to pilot [29]. The SM value is usually chosen based on the desired performance of the aircraft in terms of handling qualities and usually ranges from ($10\% \leq SM \leq 5\%$), for piloted aircraft. Considering the dragonfly's high level of manoeuvrability, control effects of four wings and fast nervous system for control, a $SM = 0$ or even negative can have advantages [232], [233]. There are consequences for all settings of SM, which go beyond the scope of this study.

For both tail actuation modes, the analysis was treated as an instantaneous performance problem. Therefore, the tail position s_{tb}, or angular deflection θ_T was known prior to the analysis, which was then used to calculate the cg_m and inertia values in MATLAB/Simulink, [208]. The energy was evaluated at constant velocity in steady cruise flight. The use of tail linear displacement to correct longitudinal imbalance (depicted in Figure 5.1a), was demonstrated. To do this, an artificial physical disturbance that caused an imbalance in level flight was introduced as an added mass D, located at an arbitrarily chosen point d in the body frame. One could relate the introduction of a disturbance mass in flight to a scenario where the dragonfly caught prey during flight using mandibles or forelimbs, causing cg_m to shift forward, creating an immediate pitching moment that requires trim, and reducing longitudinal manoeuvrability of the aircraft, both of which are undesirable. However, by changing tail mass position or angular deflection, the aircraft was able to return to trim and preferable stability conditions prior to the addition of the disturbance mass. It should be noted that for consistency, the a priori values of s_{tb} or θ_T after correction of imbalance were deliberately set in this study; the static margin after correction of imbalance was the same as that of the initially undisturbed and balanced aircraft, which was indicated by the values of the combined cg position.

The neutral point of the aircraft planform analysed in this study was estimated in AVL, as ($X_{NP} = 0.046$ m). In order to isolate the tail mass movement, rigid body B and the disturbance mass D were combined to form a rigid body A with a constant mass and mass distribution. The mass and inertia properties of the newly defined rigid body A, which is the combined disturbance mass and the central body, excluding the tail, were estimated in XFLR5 and are listed in Table 5.5. The disturbance mass of D=0.04 kg was specifically chosen due to the constraints of the fixed wing planform, to ensure a statically stable aircraft and for consistency in analysis between the two actuation modes. The conventional method to instantaneously correct imbalance or disturbance of aircraft is to use aerodynamic control surfaces to create opposing forces. The control effort δ_e and power required for Models 1 and 2, were calculated for a stable trimmable steady cruise flight condition at airspeeds ranging from (V= 5–15 m/s) with an increment of 0.5 m/s. The evaluations carried out for both tail actuation modes are described in the sections that follow.

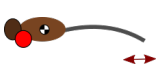
Table 5.5: Disturbed DISWA mass properties without the tail.

Parameter	Value
m^D (kg)	0.04
x_d (m)	−0.05
cg_A (m)	[−0.062;0;0.003]
${I_{xx}}_a^A$ (kg·m^2)	0.00934
${I_{yy}}_a^A$ (kg·m^2)	0.00188
${I_{zz}}_a^A$ (kg·m^2)	0.01118

5.2.7.3.1 Model 1

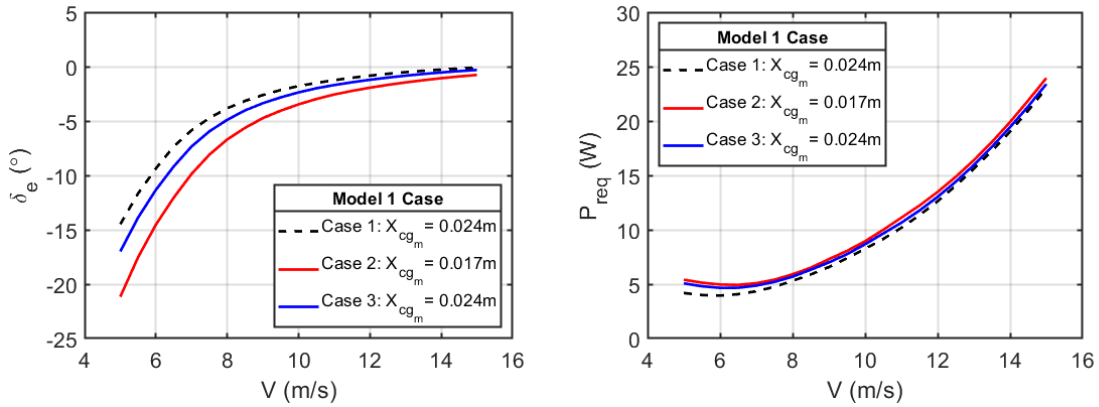
With this model, the use of tail linear positioning to regain a balanced, energy efficient cruising flight condition after the sudden addition of an unbalanced mass was examined. Table 5.6 presents a summary of the three cases considered with side view illustrations. The first case considered was the nominal undisturbed case with an initial static margin of $SM_{Model\ 1} = 11.8\%$, where the tail was initially somewhat contracted prior to the disturbance. In the second case, the disturbance mass was introduced, however, the tail was left in its initial position and played no role in correcting flight. Considering the position where the disturbance mass was added, the corrective reaction required was for mass to be moved backward by extending the tail. Therefore, the third case considered was a case where the tail was extended such that the tail mass was now halfway between the initial position and the maximum possible position in an effort to correct for imbalance.

Table 5.6: Model 1 cases for correction of imbalance.

Model 1 Case	Description	Illustration
Case 1	Initially balanced with contracted tail, $m = 0.385$ kg, $s_{tb_x} = 0.564$ m.	
Case 2	Disturbed and unbalanced with contracted tail, $m = 0.425$ kg, $s_{tb_x} = 0.564$ m.	
Case 3	Disturbed and balanced with extended tail, $m = 0.425$ kg, $s_{tb_x} = 0.614$ m.	

Note: ● represents the added mass.

Plots of elevator deflection to trim the aircraft and power required for the range of airspeed considered were estimated using the MATLAB/Simulink linear analysis tool [208]. The results are shown in Figure 5.8a,b respectively and summarised in Table 5.7.



(a) (b)

Figure 5.8: Model 1 trim in steady level powered flight for a range of airspeed. (**a**) Elevator deflection. (**b**) Power required.

Table 5.7: Trimmed steady cruise elevator deflection and power required for Model 1 cases.

Model 1 Case	**Range of δ_e**	**Range of P_{req}**
Case 1	$-14.5°$ to $-0.0798°$	4.18 W to 23 W
Case 2	$-21.2°$ to $-0.763°$	5.4 W to 24 W
Case 3	$-17°$ to $-0.309°$	5.07 W to 23.4 W

5.2.7.3.2 Model 2

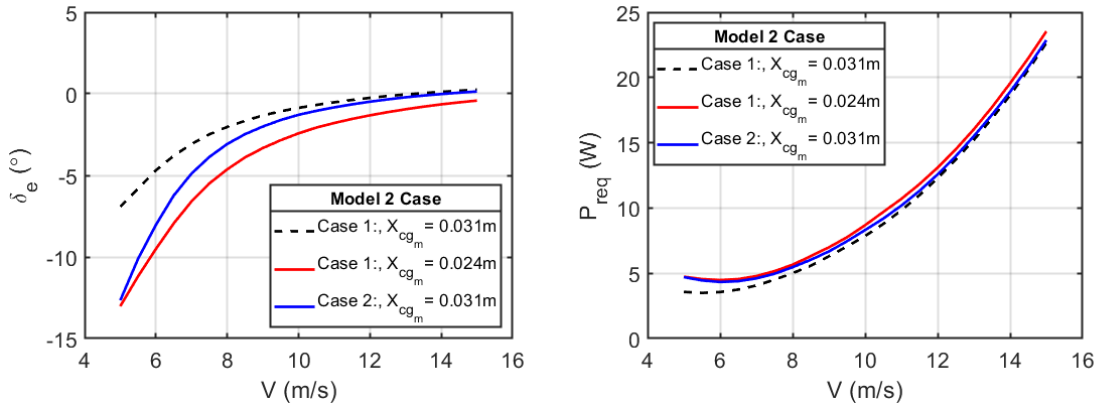
For this model, the use of tail angular deflection to regain balance in the cruising flight condition after the sudden addition of an unbalanced mass was examined. Again, three cases were considered, which are summarised in Table 5.8 with side view illustrations. The first case, being the nominal undisturbed case with an initial static margin of $SM_{Model\ 2} = 7.7\%$, where the tail was deflected upwards to its maximum possible deflection angle. In the second case, the disturbance mass was added, however, the tail was left in its initially deflected position and played no role in correcting flight. Again, considering the position where the disturbance mass was added, the corrective reaction required was for the tail mass to be deflected towards its neutral position, thus increasing distance of the mass from the centre of gravity. Therefore, in the third case considered, in an effort to correct for imbalance, the tail moved to its neutral position, meaning no deflection.

Plots of elevator deflection required to trim Model 2 aircraft and power required for a range of airspeed are shown in Figure 5.9a,b respectively. Table 5.9 presents a summary of results for trimmed steady cruise for Model 2.

Table 5.8: Model 2 cases for correction of imbalance.

Model 2 Case	Description	Illustration
Case 1	Initially balanced with deflected tail, $m = 0.385$ kg, $\theta_T = -30°$.	
Case 2	Disturbed and unbalanced with deflected tail, $m = 0.425$ kg, $\theta_T = -30°$.	
Case 3	Disturbed and balanced with undeflected tail, $m = 0.425$ kg, $\theta_T = 0°$	

Note: ● represents the added mass.



(a) (b)

Figure 5.9: Model 2 trim in steady level powered flight for a range of airspeeds. (**a**) Elevator deflection vs. airspeed. (**b**) Power required vs. airspeed.

Table 5.9: Trimmed steady cruise elevator deflection and power required for Model 2 cases.

Model 2 Case	Range of δ_e	Range of P_{req}
Case 1	$-6.9°$ to $0.251°$	3.57 W to 22.6 W
Case 2	$-13°$ to $-0.415°$	4.74 W to 23.5 W
Case 3	$-12.7°$ to $0.142°$	4.71 W to 22.9 W

5.2.7.3.3 Discussion

It is safe to assume that passive stability for a four winged flapping craft, capable of nearly holonomic locomotion [234], is not a necessary precondition in the same way that it is for a fixed wing aircraft. Yet, the stability of the surrogate fixed wing aircraft would be adversely affected by cg_m variations, as a zero or negative stability margin would lead to a departure from controlled flight.

For Models 1 and 2 aircraft and for all cases relating to correction of imbalance in steady level flight, the plots for elevator deflection required to trim with respect to airspeed are consistent; the amount of

elevator deflection required to trim decreased with increased speed because higher air speeds require less lift coefficient C_L and consequently less angle of attack [221]. The power required plots as a function of airspeed also present consistent results as increased weight results in more lift required and consequently, an increase in induced drag (see Figures 5.8 and 5.9) [221].

Although the power required after both models were disturbed was obviously higher than the initial condition, performance improved in the form of lower power required compared to before the tail was moved to compensate for imbalance, however, the magnitude of power saved was different for each model due to differences in initial configurations.

Specifically, for Model 1 with a linearly displaceable tail mass as in Figure 5.1a, an average increase in elevator deflection of 161% was observed after the disturbance mass was introduced, compared to 55% after correction of imbalance was performed by linearly extending the tail. In addition, results showed an average of 12% increase in energy required after the disturbance mass was introduced, compared to 7% after correction of imbalance was performed by linearly extending the tail.

For Model 2 with a deflectable tail as in Figure 5.1b, an average increase in elevator deflection of 116% was observed after the disturbance mass was introduced, compared to 46% after correction of imbalance was performed by moving the tail to its neutral position, which had zero deflection. The results showed an average of 13% increase in power required before, compared to 9% after correction of imbalance. Overall, for steady cruise, a 4–5% average in propulsive power savings is quite substantial for an electrically powered aircraft.

It is worth mentioning that the abdomen is not the only movable appendage in insects. Appendix C presents a supplementary analysis born as a result of observing hoverflies holding station near flowers. Leg movements were noted after wind gusts disrupted the hover position. Hence, the possibility of using leg movements, a moving mass control strategy, for hover control was evaluated using a minimal dynamic model. The resulting conclusions make it appear feasible as a horizontal acceleration of around 5.2% of the acceleration due to gravity was created by the leg movements. Appendix C is only intended to be supplementary to the study presented in this section.

5.2.7.4 Steady Pull up Manoeuvre

In this section, a quasi-steady pull up manoeuvre is considered to investigate the effects of abdominal movements on manoeuvre performance. The most appropriate framework for such evaluation is associated with the performance analysis of fighter aircraft and aerobatics [235] using energy manoeuvrability. Energy manoeuvrability involves the analysis of manoeuvrability, expressed in terms of energy and energy rate. An aircraft with a higher energy level and energy rate has the manoeuvring advantage against its adversary in combat [236]. Although energy manoeuvrability is not directly concerned with electrical energy consumption, the use of appropriate energy manoeuvrability strategies can result in reduced electrical energy consumption. The energy manoeuvrability equations used in this study are outlined below.

Summing the forces acting on an aircraft, parallel to the flight path as shown in Figure 5.10, the velocity change equation yields [237], [238],

$$m\,\dot{V} = T_n - D - mgsin(\gamma), \tag{5.19}$$

where γ is the flight path angle

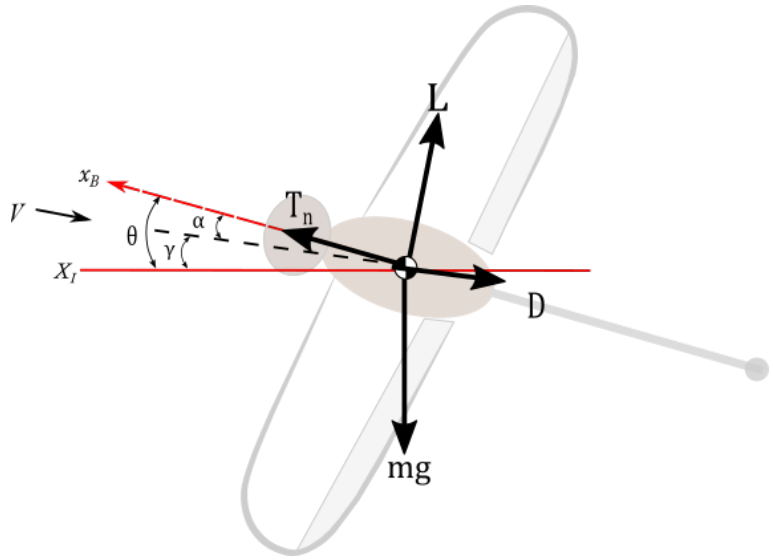


Figure 5.10: Forces acting on the aircraft model in flight.

The total energy or energy state of an aircraft, consists of kinetic energy in the form of airspeed, and potential energy in the form of altitude.

$$E = \frac{1}{2}mV^2 + mgH, \tag{5.20}$$

where H is the height.

To enable comparison of manoeuvre performance of various aircraft, it is more convenient to use the specific energy E_s, which is the energy per unit mass. The specific energy is sometimes called the energy height,

$$E_s = H + \frac{V^2}{2g}. \tag{5.21}$$

The energy state of an aircraft can be changed by applying power. The rate of change of specific energy $\dot{E}_s$, also known as specific excess power P_s is

$$\dot{E}_s = P_s = \dot{H} + \frac{V}{g}\dot{V}. \tag{5.22}$$

Using the kinematic relation that $\dot{H} = Vsin(\gamma)$ and the expression of $\dot{V}$ from Equation 5.19, Equation 5.22 becomes

$$P_s = \frac{T_n - D}{W}V. \tag{5.23}$$

The specific excess power and specific energy were the performance parameters used to evaluate the performance of a pull up manoeuvre from trim in this section. A quasi-steady analysis for a pull up manoeuvre was executed using Models 1 and 2. An aircraft flying initially in steady level flight at a speed V_0 was subjected to a small change in the longitudinal control effector of choice (mass shift or control surface), causing it to pull up with a corresponding quasi-steady angle of attack α, and body pitch rate q. This was computed by enforcing ($\dot{\alpha} = \dot{q} = 0$). As the pull up progressed, the airspeed and flight path angle changed at a slow rate in comparison to the AoA and pitch rate [29], [239]. Traditionally, this manoeuvre is initiated using elevator deflection, δ_e. However, as mentioned earlier, Models 1 and 2 provide alternative ways to generate pitching moment for a pull up manoeuvre.

In both cases, the aircraft was initially trimmed for steady level flight using the elevator before the manoeuvre was initiated. The wings-level fixed-thrust pull up manoeuvre was defined by trajectory and estimated the additional control effort required for the same manoeuvre, using the elevator compared to tail linear displacement or using the elevator compared to tail angular deflection. The purpose was to compare the pull up effort using the traditional elevator to the two alternative tail actuation methods and

estimate which has more energy advantage. As this is a manoeuvre, energy manoeuvrability is of more interest, hence, this investigation was limited to cruising power manoeuvres, so $\Delta T_n = 0$. To enable comparison, the energy state and energy rate were compared by estimating the specific energy E_s, and specific excess power P_s for the first three seconds after the manoeuvre was initiated. Since this was an open loop control analysis, the additional control effort required to achieve the same pull up trajectory in each scenario was pre-estimated in Simulink.

5.2.7.4.1 Model 1

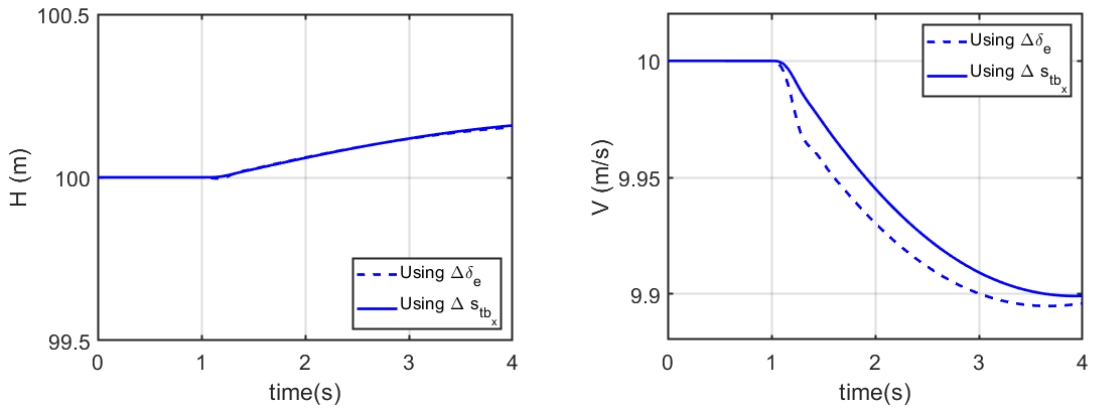
With this model, alternative pitching moment was generated when the tail mass moved along the body x_B axis (see Figure 5.1a). The aircraft was initially trimmed for a cruise speed of V = 10 m/s, H = 100 m and a tail mass position of (s_{tb_0} = 0.564 m). The solutions to this trim condition for Model 1 are presented in Section 5.2.7.1 and Table 5.4. The load factor $n = \frac{L}{W}$, associated with a pull up manoeuvre was selected such that the aircraft dynamic response provided a good response to capture the flight dynamics and remained within the operating regime of interest. The additional control effort required for approximately the same pull up manoeuvre trajectory was estimated as $\Delta\delta_e \approx -1.5°$ using the elevator and $\Delta s_{tb_x} \approx 0.069$ m using tail linear displacement.

The simulation was run for four seconds and excitation to the control inputs was applied using a pulse for 0.25 s, at t=+1 s into the simulation. The time history for airspeed V and trajectory H as excited by change in elevator deflection or tail linear displacement are shown in Figure 5.11. The specific excess power and specific energy as effected using elevator deflection or tail linear displacement are shown in Figure 5.12 with respect to time.

The results in terms of average specific energy and specific excess power using either elevator deflection or tail mass linear displacement for the same pull up manoeuvre are summarised in Table 5.10.

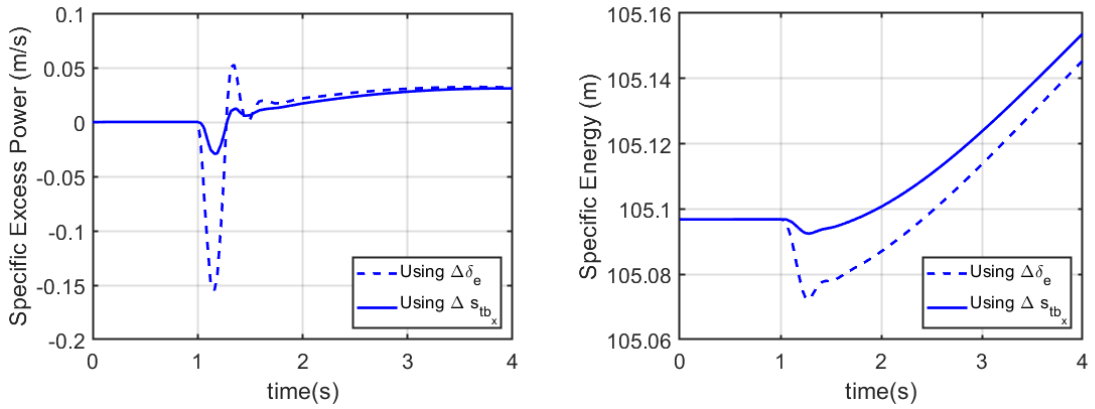
Table 5.10: Aircraft Model 1 pull up manoeuvre control effector comparison using $\Delta\delta_e$ or Δs_{tb_x}.

Control Effector Used	**Average Specific Energy (m)**	**Average Specific Excess Power (m/s)**
$\Delta\delta_e(°)$	105.096	−0.007
Δs_{tb_x} (m)	105.105	0.0069



(a) (b)

Figure 5.11: Model 1 aircraft pull up manoeuvre time response. (**a**) Airspeed. (**b**) Height.



(a) (b)

Figure 5.12: Model 1 aircraft pull up manoeuvre time response. (**a**) Specific excess power. (**b**) Specific energy.

5.2.7.4.2 Model 2

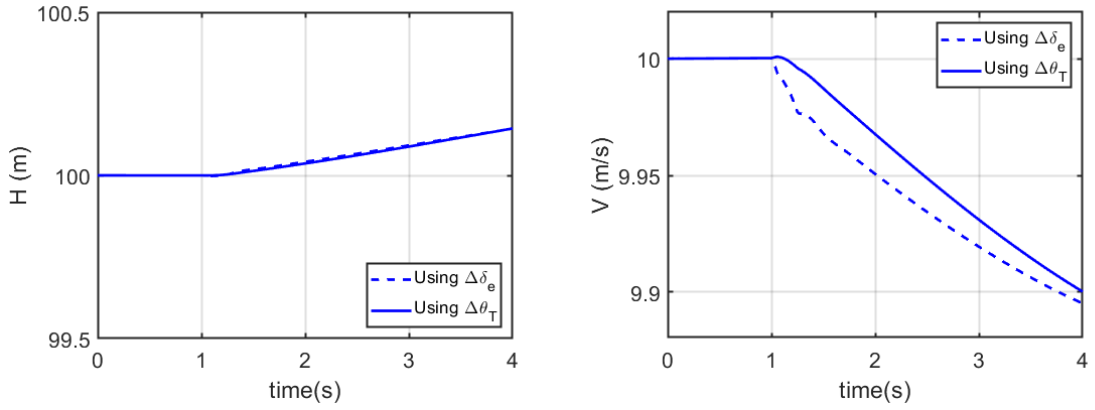
With this model, the tail mass generated pitching moment by wagging the tail up and down is shown (see Figure 5.1b). Table 5.11 shows the initial steady level flight condition values before the pull up manoeuvre was initiated. The additional control effort required for a similar pull up manoeuvre was estimated as $\Delta\delta_e = -0.58°$ using the elevator and $\Delta\theta_T = 53.5\ °$ using tail angular deflection.

Table 5.11: Aircraft Model 2 trim condition before pull up.

V_0 (m/s)	H_0 (m)	$s_{jb_{x0}}$ (m)	$s_{tj_{x0}}$ (m)	θ_{T_0} (°)	θ_0 (°)	δ_{e_0} (°)	T_{n_0} (N)
10	100	0.264	0.4	−30	−0.66	−0.863	0.786

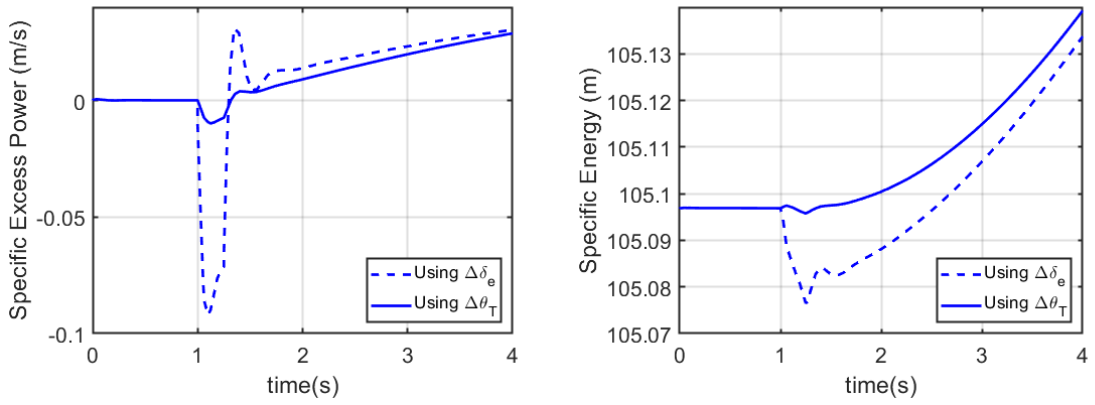
For a duration of four seconds, the pull up manoeuvre was initiated using a pulsed input signal (applied

at t=+1 in the simulation for 0.25 s). The time history comparisons for airspeed and trajectory are shown in Figure 5.13, and specific excess power and specific energy are shown in Figure 5.14. Table 5.12 shows a summary of the average specific energy and power used in the pull up manoeuvre using Model 2.



(a) (b)

Figure 5.13: Model 2 aircraft pull up manoeuvre time response. (**a**) Airspeed. (**b**) Height.



(a) (b)

Figure 5.14: Model 2 aircraft pull up manoeuvre time response. (**a**) Specific excess power. (**b**) Specific energy.

Table 5.12: Aircraft Model 2 pull up manoeuvre control effector comparison using $\Delta\delta_e$ or $\Delta\theta_T$.

Control Effector Used	**Average Specific Energy (m)**	**Average Specific Excess Power (m/s)**
$\Delta\delta_e(^\circ)$	105.093	−0.014
$\Delta\theta_T(^\circ)$	105.103	0.0043

5.2.7.4.3 Discussion

The two alternative moment generation mechanisms were able to achieve the same pull up manoeuvre as the elevator as shown in Figures 5.11a and 5.13a. In the case of Model 1, more specific energy and specific excess power were being retained on average when using tail displacement for manoeuvre in comparison with using the elevator (see Table 5.10). Looking across a short time period near the manoeuvre, the reduction in specific excess power available after using tail movement was around -0.03 m/s, whereas it was -0.15 m/s using control surface deflection. For the Model 2 aircraft, more specific energy and excess power were retained when using tail angular deflection in comparison with using the elevator (see Table 5.12). Again, the transient specific excess power drop was negligible when using tail movement, but around 0.1m/s when using control surface deflection.

Generally, an aircraft that is able to maintain a higher specific energy and excess power has a manoeuvre advantage [235]. The negative average P_s observed when using the elevator to initiate the manoeuvre results from the drag being greater than available thrust, which results in decreased energy. This is due to the additional drag induced as a result of elevator deflection [220], [235].

Although the percentage savings in specific energy states and rates caused by using either of the tail actuation modes as opposed to using the conventional elevator may seem small in magnitude, they make a difference in combat. A dragonfly in pursuit of prey for instance, but particularly in territorial conflict, is engaged in pure aerial combat. In such bouts, dragonflies may be required to make the same or a combination of energy consuming manoeuvres in sequence in a life or death conflict to deplete the opponent's energy. The transient advantage of using a more energy efficient control effector to initiate a manoeuvre is substantial by the standards of optimisation of flying systems.

5.3 Lateral-directional Flight

Trimmability of any aircraft configuration is central to viability. Achievable operating conditions for aerial vehicles are limited by various factors such as design, physical parameters, and limitations on control effectors [240]. Loss of control can occur at any point during aircraft operation, once any of the constraints imposed by any of these factors is violated. Therefore, in a situation where an aircraft is impaired due to the failure of conventional control effectors, the existence of alternative

control effectors is bound to improve trimmability, agility and manoeuvrability of such aircraft. The introduction of additional control effectors to any air vehicle alters the aircraft dynamics, causing the flight envelope to change. In addition, one of the more interesting aspects of performance is turning flight. The question that drives the analysis in this section is whether there are benefits of the articulated abdomen in terms of trimmability range for steady turning flight, given the modelling and control input constraints of the simulated aircraft and its dynamics. As the abdominal articulation represented by Model 2 is more representative of what is observed in insects, only Model 2 was used for analysis of turning flight (see Figure 5.15).

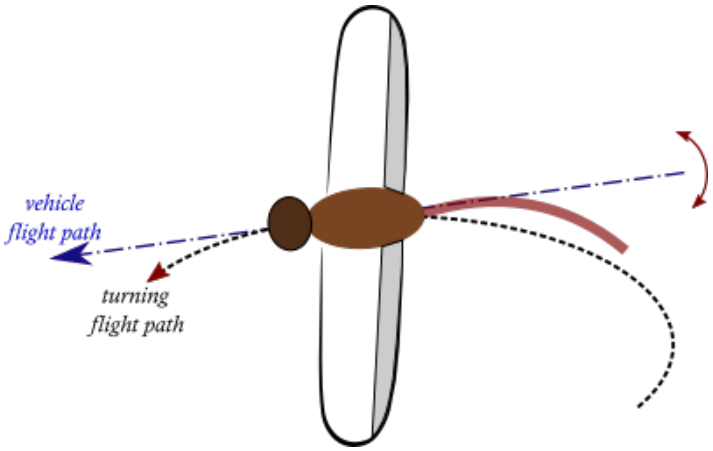


Figure 5.15: Plan view of showing abdominal articulation in turning flight.

5.3.1 Steady Turn Trim Analyses

In this section, two modes of turning flight are compared according to control effector used to explore the differences in the trim with different turn rates. The left and right elevons, η_l and η_r, are considered as aerodynamic control surfaces. Therefore, the first turning mode that uses only the elevons will be referred to as aerosurface controlled (A-C) aircraft. The second turning mode which uses the elevons as well as yaw-like abdominal articulation ψ_T, will be referred to as combined controlled aircraft (C-C). Using only the abdominal yaw angle the controller was unable to provide the necessary moment to trim the aircraft in the steady turn manoeuvre was attempted, however, no trim solution was found, hence, that capability was not considered.

Again, the trim analysis was carried out in the MATLAB/Simulink environment [208], using MATLAB's trim algorithm that employs sequential quadratic programming [241]. The same aircraft model used for analysis in Section 5.2 was used here. The steady turn flight condition was determined by specifying

the airspeed V, the flight path angle γ and the rate of turn $\dot{\psi}$. The trim analysis was carried out for two rates of turn, $\dot{\psi} = 1$ and 5 °/s. The flight path angle for all analyses was set to $\gamma = 0$ and the airspeeds varied for the feasible airspeed ranges for both the A-C and C-C aircraft, depending on the first variable to reach its preset constraints on modelling parameters and control inputs in Table 5.2 and 5.13. The aim was to achieve a steady coordinated turn, that is, without sideslip.

Table 5.13: Physical constraints of lateral-directional control inputs.

Limitations	Unit
$-20 \leq \eta_l \leq 20$	°
$-20 \leq \eta_r \leq 20$	°
$-60 \leq \psi_T \leq 60$	°

The equations of motion were then solved to estimate the aerodynamic angles α and β, the Euler angles that describe the roll ϕ, pitch θ and yaw ψ of the body respectively, and the control inputs (left elevon η_l, right elevon η_r, thrust required T_n, and abdominal yaw angle ψ_T), for the above specified flight condition. However, only the trim results for variation in sideslip and abdominal yaw angle with airspeeds of the viable trim points are presented. These parameters were specifically chosen because for a coordinated turn, the sideslip, β, is zero and non-zero if the turn is uncoordinated. Also, the use of the abdominal yaw angle ψ_T for control is the major difference between the A-C and C-C aircraft configurations. The results for sideslip and abdominal yaw angle variation with airspeed are shown in Figures 5.16 and 5.17, while that of power required is shown in Figure 5.18.

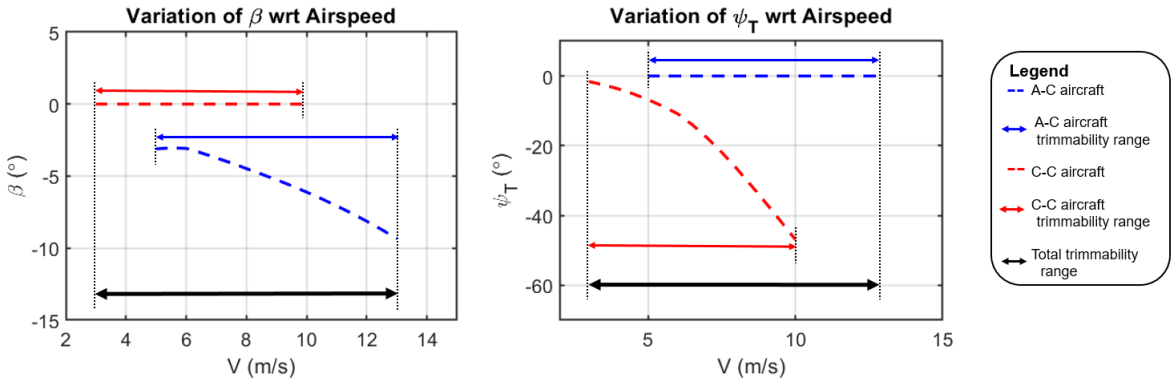


Figure 5.16: Sideslip β and abdominal yaw ψ_T variation with airspeed for $\dot{\psi} = 1$°/s in steady turn.

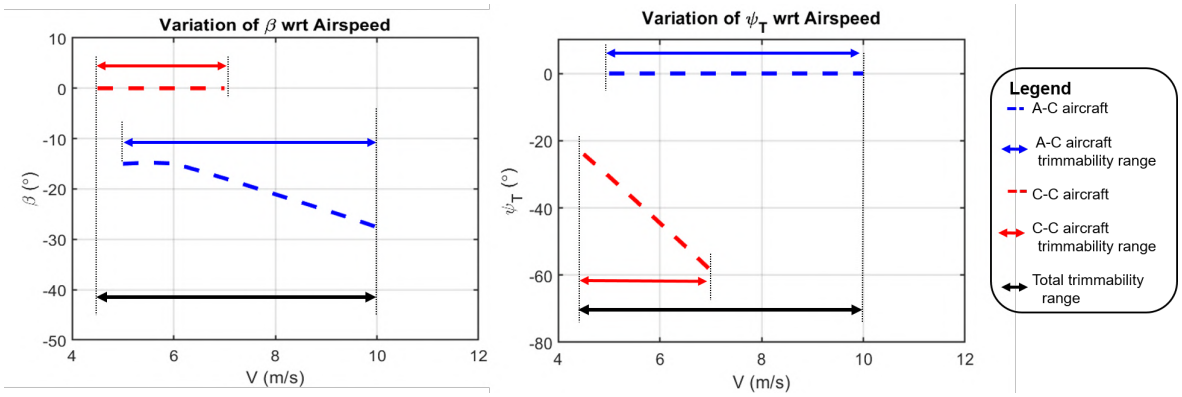
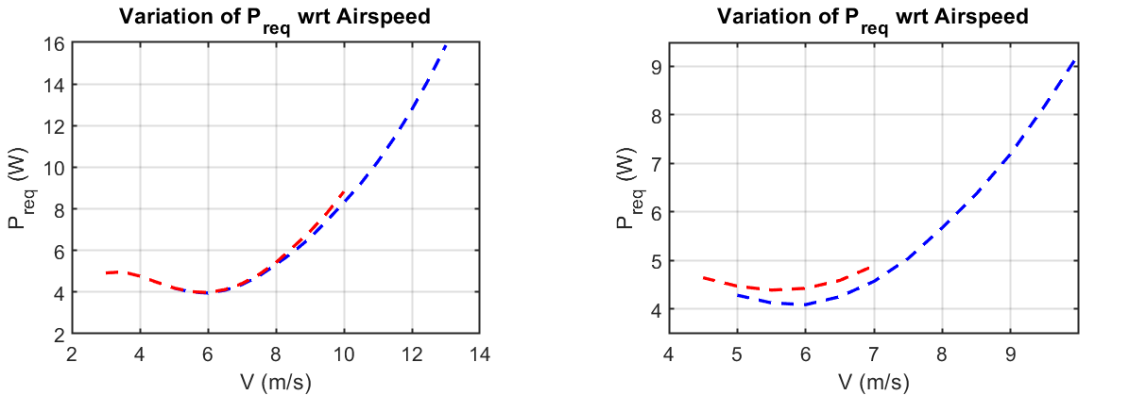


Figure 5.17: Sideslip β and abdominal yaw ψ_T variation with airspeed for $\dot{\psi} = 5°/s$ in steady turn.



(a) Variation of power required with airspeed for $\dot{\psi} = 1°/s$.

(b) Variation of energy required with airspeed for $\dot{\psi} = 5°/s$.

Figure 5.18: Power required variation with airspeed. (**a**) $\dot{\psi} = 1°/s$. (**b**) $\dot{\psi} = 5°/s$.

5.3.2 Discussion

The first observation in Figures 5.16 and 5.17 is that for both yaw rates, the A-C aircraft was unable to attain the specified flight condition with zero sideslip angle, while the C-C aircraft was able to achieve zero sideslip angle. Also, the higher yaw rate of $\dot{\psi} = 5$ °/s, required a higher abdominal yaw angle to trim.

The lower and upper limits of the feasible speed range are different for each aircraft configuration. This is because the first variable to reach its upper or lower limit (see Table 5.2 and 5.13) varies depending on the aircraft configuration. For both yaw rates, A-C aircraft has the largest feasible speed ranges (5–13 m/s for $\dot{\psi} = 1$ °/s, and 5–10 m/s for $\dot{\psi} = 5$ °/s), especially near the upper limit, which is higher speeds. In addition, the lower and upper airspeed limits for the A-C aircraft were set by the angle of attack and sideslip angle reaching their maximum limits of |20| ° and |30| °, respectively for both yaw

rates.

In the case of the C-C aircraft, for both yaw rates, its feasible speed ranges near lower speeds (3–10 m/s for $\dot{\psi} = 1$ °/s, and 4.5–7 m/s for $\dot{\psi} = 5$ °/s). In addition, the lower and upper airspeed limits for the C-C aircraft were set by the angle of attack and abdominal yaw angle reaching their maximum absolute limits of 20 ° and 60 °, respectively for both yaw rates.

It should be noted that the coordinated turn which could only be achieved by the C-C aircraft in both turn cases came at a higher cost of power for the same airspeed range. For the 1 m/s turn rate, the C-C aircraft required 2.98% more power for the airspeed range from 5-10 m/s than the A-C aircraft as shown in Figure 5.18a. In the higher turn rate, the C-C aircraft required 6.76% more average power for the airspeed range from 5-7 m/s than the A-C aircraft as shown in Figure 5.18b

The analyses indicate that aero-actuation, would be more useful at higher airspeeds, while combined control would be more effective at low flight speeds. Furthermore, the total trimmability airspeed range increased by having two control effectors.

5.4 Summary

In this chapter, the research mathematically expressed the basic means by which the abdomen of an efficient natural flyer like the dragonfly might be used to save energy and reduce peak power requirements in flight. The abdomen might save energy with reactive responses to achieve longitudinal balance and pull up manoeuvres by manipulating moments. Active creation of torques is possible through the movement of the abdomen. From the analysis of a simulation model of a fixed wing aircraft with an articulated tail structure, it has been shown that the amount of energy that might be saved by these techniques can be substantial. It has been demonstrated that flight power increase would be required to substitute for the transient effects that can be generated using the movement of the abdomen, while the possibility of trimming balance through tail posture might save energy for as long as the imbalance exists.

Results from the flight performance analysis of steady turning flight demonstrate the benefits of using aerosurfaces in combination with yaw abdominal articulation, due to increased combined trimmability range, as in the case of the combined controlled aircraft (C–C), compared to using only aerosurfaces, as

in the case of the aero-controlled aircraft (A-C). With respect to the analysis in this study, in a situation where it is required for the air vehicle to be able to perform coordinated and uncoordinated turns, the aircraft with combined control is preferable, not only due to the increased combined trimmability range but also because the additional control effectors can potentially improve manoeuvrability. Perhaps, to develop bio-inspired air vehicles that can rival the dragonfly, the same solutions should be adapted, including their anatomical features.

Chapter 6

Multibody Control System Design

The previous chapter focused on the analysis of the static or steady and quasi-steady behaviour of the DISWA. In this chapter, the dynamic behaviour of the aircraft is investigated and analysed. First, the linearisation of equations of motion is presented. Then, controllability analyses based on linearised state-space matrices are presented. Finally, control design procedures for longitudinal and lateral-directional stabilisation and attitude control of the aircraft using three possible control effector solutions: (1) Aerosurface controlled (A-C) (2) Articulated mass controlled, and (3) Combined controlled (C–C) – Combination of aerosurface and articulated appendage mass, are presented.

6.1 Introduction

Small UAVs of the near future are imagined to have manoeuvrability as a high priority. Our conceptual DISWA, suffers from instability and difficulty of control in its purest form [242], [243], due to the lack of conventional stabilising surfaces and associated control surfaces. Thus, given the instability associated with the dynamics of the air vehicle, a flight controller capable of providing, maintaining and improving handling characteristics is required. In addition, the availability of multiple effectors makes the flight control design of input redundant or overactuated systems more complex with additional theoretical challenges.

This chapter aims to answer the question of whether the dynamics model is suitable for modern control law development for stabilisation and control. In addition, it explores the flight control potential of an articulated abdomen using the DISWA. Linear control strategies were implemented to focus on two

particular autonomous design problems. The first is a stabilisation autopilot, in which the goal is to maintain a desired trimmed flight condition, this is generally known as the standard regulator problem. Specifically, the Linear Quadratic Regulator (LQR) method was used for stabilisation. The second is an attitude reference tracking problem, in which the aircraft controller attempts to achieve a desired attitude. To achieve this a linear quadratic integral controller (LQI) was designed and implemented to maintain attitude (pitch and yaw) of the DISWA. The controllers were designed to meet predefined performance requirements. LQR and LQI control offer the advantage of simplicity in design, and application for Multiple-Input-Multiple-Output (MIMO) systems in terms of control effort allocation.

This chapter aims to address the following research question:

1. Is the multibody dynamics model suitable for modern optimal control law development for stabilisation and control?

6.2 Explicit Equations of Motion

The final set of EoMs for simulation in Equations 4.54 and 4.69 are in implicit form and can be rewritten as Equations 6.1 and 6.2 below, respectively

$$
\begin{aligned}
&m\left([\dot{V}_B^I]^B + [\omega^{BI}]^B \times [V_b^I]^B\right) + m^T\Bigg([R]^{BT}\left([\dot{\omega}^{TB}]^T \times [s_{tj}]^T + [\omega^{TB}]^T \times [\omega^{TB}]^T \times [s_{tj}]^T\right)\Bigg) \\
&+ [\dot{\omega}^{BI}]^B \times ([R]^{BT}[s_{tj}]^T + [s_{jb}]^B) + \Big([\omega^{BI}]^B \times [\omega^{BI}]^B \times ([R]^{BT}[s_{tj}]^T + [s_{jb}]^B)\Big) \\
&+ \Big(2\,\omega^{BI} \times [R]^{BT}([\omega^{TB}]^T \times [s_{tj}]^T)\Big)\Bigg) = \sum_k [F_{B+T}]^B
\end{aligned}
\tag{6.1}
$$

$$
\begin{aligned}
& m^T\left([R]^{BT}[s_{tj}]^T + [s_{jb}]^B\right)\Bigg([R]^{BT}\left([\dot{\omega}^{TB}]^T \times [s_{tj}]^T + [\omega^{TB}]^T \times [\omega^{TB}]^T \times [s_{tj}]^T\right) \\
& + [\dot{\omega}^{BI}]^B \times \left([R]^{BT}[s_{tj}]^T + [s_{jb}]^B\right) + \left([\omega^{BI}]^B \times [\omega^{BI}]^B \times \left([R]^{BT}[s_{tj}]^T + [s_{jb}]^B\right)\right) \\
& + \left(2\,\omega^{BI} \times [R]^{BT}\left([\omega^{TB}]^T \times [s_{tj}]^T\right)\right) + \left([\dot{V}_B^I]^B + [\omega^{BI}]^B \times [V_b^I]^B\right)\Bigg) \\
& + [R]^{BT}[I_t^T]^T\left([\dot{\omega}^{TB}]^T + [R']^{BT}\dot{\omega}^{BI} - [\omega^{TB}]^T \times [R']^{BT}[\omega^{BI}]^B\right) \\
& + \left(\left([R]^{BT}[\omega^{TB}]^T + [\omega^{BI}]^B\right) \times [R]^{BT}[I_t^T]^T\left([\omega^{TB}]^T + [R']^{BT}[\omega^{BI}]^B\right)\right) \\
& + [I_b^B]^B[\dot{\omega}^{BI}]^B + [\omega^{BI}]^B \times [I_b^B]^B[\omega^{BI}]^B = [M_{B+T}]^B + \left[[S_{tb}]^B[F_T]^B\right]
\end{aligned}
\tag{6.2}
$$

For dynamic simulation purposes in the MATLAB/Simulink Environment, the implicit ordinary differential equations solver, $solver(ode15i)$, results in unreliable propagation of the state of the system at trim conditions [150]. This is because for the $ode15i$ solver, the inability to provide consistent initial conditions for states and their derivatives can lead to unexpected propagation of system states [150]. This issue can be addressed by rearranging the translation and rotation equations of motion to form an explicit set of ordinary differential equations. With the assumption that the abdomen is a point mass and introducing the following notation:

$$
\begin{bmatrix} s_1 \\ s_2 \\ s_3 \end{bmatrix} = [R]^{BT}[s_{tj}]^T + [s_{jb}]^B \quad \text{and} \quad \begin{bmatrix} I_{xx} & I_{xy} & I_{xy} \\ I_{yx} & I_{yy} & I_{yz} \\ I_{zx} & I_{zy} & I_{zz} \end{bmatrix} = [I_b^B]^B \tag{6.3}
$$

In addition, by keeping the terms related to the time derivative states $[\dot{V}_b^I]^B = (\dot{u}, \dot{v}, \dot{w})$ and $[\dot{\Omega}^{BI}]^B = (\dot{p}, \dot{q}, \dot{r})$ on the left hand side of Equations 6.1 and 6.2, and transferring the remaining terms to the right hand side, leads to Equations 6.5 and 6.5 below, respectively

$$
m^T \begin{bmatrix} \dot{p} \\ \dot{q} \\ \dot{r} \end{bmatrix} \times \begin{bmatrix} s_1 \\ s_2 \\ s_3 \end{bmatrix} + m \begin{bmatrix} \dot{u} \\ \dot{v} \\ \dot{w} \end{bmatrix} = RHS_F \tag{6.4}
$$

$$
m^T \begin{bmatrix} s_1 \\ s_2 \\ s_3 \end{bmatrix} \times \begin{bmatrix} \dot{p} \\ \dot{q} \\ \dot{r} \end{bmatrix} \times \begin{bmatrix} s_1 \\ s_2 \\ s_3 \end{bmatrix} + m^T \begin{bmatrix} s_1 \\ s_2 \\ s_3 \end{bmatrix} \times \begin{bmatrix} \dot{u} \\ \dot{v} \\ \dot{w} \end{bmatrix} + \begin{bmatrix} I_{xx} & I_{xy} & I_{xy} \\ I_{yx} & I_{yy} & I_{yz} \\ I_{zx} & I_{zy} & I_{zz} \end{bmatrix} \begin{bmatrix} \dot{p} \\ \dot{q} \\ \dot{r} \end{bmatrix} = RHS_M \tag{6.5}
$$

where RHS_F and RHS_M are the remaining terms of the left hand side of the equations of motion transferred to the right hand side, as well as external forces and moments. The resulting expression for the translational and rotational equations in matrix form is

$$\left[\begin{array}{cccccc} m & 0 & 0 & 0 & m^T s_3 & -m^T s_2 \\ 0 & m & 0 & -m^T s_3 & 0 & m^T s_1 \\ 0 & 0 & m & m^T s_2 & -m^T s_1 & 0 \\ \hline 0 & -m^T s_3 & m^T s_2 & m^T(s_2^2+s_3^2)+I_{xx} & m^T(-s_1 s_2)+I_{xy} & m^T(-s_1 s_3)+I_{xz} \\ m^T s_3 & 0 & -m^T s_1 & m^T(-s_1 s_2)+I_{xy} & m^T(s_1^2+s_3^2)+I_{yy} & m^T(-s_2 s_3)+I_{yz} \\ -m^T s_2 & m^T s_1 & 0 & m^T(-s_1 s_3)+I_{xz} & m^T(-s_2 s_3)+I_{yz} & m^T(s_1^2+s_2^2)+I_{zz} \end{array}\right] \left[\begin{array}{c} \dot{u} \\ \dot{v} \\ \dot{w} \\ \hline \dot{p} \\ \dot{q} \\ \dot{r} \end{array}\right] = \left[\begin{array}{c} RHS_F \\ \hline RHS_M \end{array}\right] \tag{6.6}$$

With the explicit expression in Equation 6.6, the set of differential equations could be solved using an explicit solver (e.g. $ode45$), and the numeric inverse of the 6×6 matrix on the left hand side of Equation 6.6 can be obtained at each iteration.

6.2.1 Abdominal Motion

The primary principle for abdominal motion is to reposition the gravitational force to modify the corresponding moment, where the secondary effect may be a result of the inertial force caused by abdominal motion. Therefore, to describe the dynamic effects of abdominal motions, additional equations are required as the differential terms $[\dot{\omega}^{TB}]^T$ are generated through actuated joints of the abdomen. For the purpose of control in the study, the abdomen has been constrained to 2 DoF, relative to the central body, i.e. the abdominal pitch and yaw motions. The 2 DoF actuation of the abdomen can be considered as revolute joints for each DoF.

In designing the articulated mass servo controllers for each DoF, independent joint control (IJC) is considered as IJC controls the deflection of each joint independently. Consider the pitch angular motion θ_T of the abdomen about point j, relative to the body. The objective of the servo actuator is to choose an input θ_T^c, such that the actual deflection output of the articulated mass θ_T, is achieved. To do this, a PID controller is designed to control the servo torque as shown in Figure 6.1. The servo dynamics is given by

$$I_{act}\ddot{\theta}_T + \kappa\dot{\theta}_T = \tau_{ly} + \tau_{ay} \tag{6.7}$$

where I_{act} is the inertia the actuator system, κ is the damping constant, τ_{ly} is the load torque due to gravity and τ_{ay} is the torque applied at the joint to actuate the abdomen.

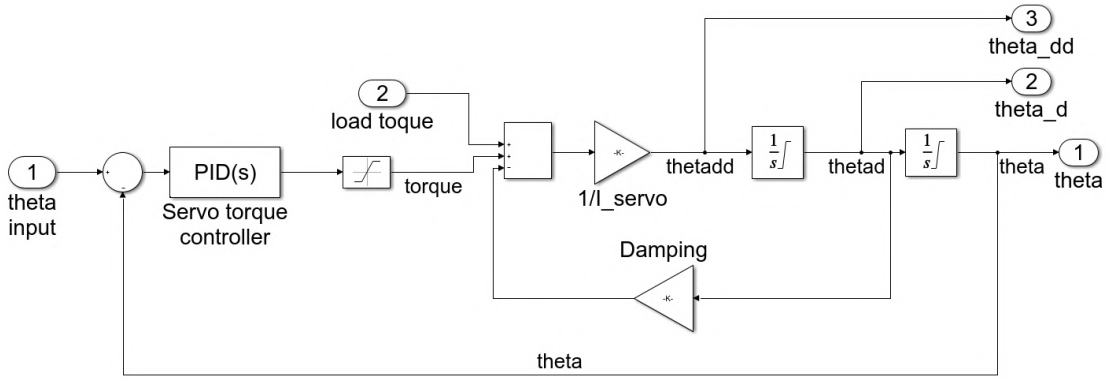


Figure 6.1: Simulink diagram for actuator dynamics.

6.3 Linearisation of Equations of Motion

The nonlinear equations of motion have been derived in Sections 4.3 and 5.2.2, which can be represented as functions of the form,

$$\begin{aligned} \dot{\mathbf{x}} &= f(\mathbf{x}, \mathbf{u}) \\ \mathbf{y} &= g(\mathbf{x}, \mathbf{u}) \end{aligned} \tag{6.8}$$

where $\mathbf{x} \in \mathbb{R}^n$, $\mathbf{u} \in \mathbb{R}^m$ and $\mathbf{y} \in \mathbb{R}^p$ represent the states, inputs and outputs of the system, respectively.

Linearisation of the model is based on small perturbation theory [59]. The aim is to represent the system in a linear state space form,

$$\begin{aligned} \Delta\dot{\mathbf{x}} &= \mathbf{A}\Delta\mathbf{x} + \mathbf{B}\Delta\mathbf{u} \\ \Delta\mathbf{y} &= \mathbf{C}\Delta\mathbf{x} + \mathbf{D}\Delta\mathbf{x} \end{aligned} \tag{6.9}$$

where matrix $\mathbf{A} \in \mathbb{R}^{n\times n}$ is the system matrix, $\mathbf{B} \in \mathbb{R}^{n\times m}$ is the input matrix, $\mathbf{C} \in \mathbb{R}^{l\times n}$ is the output matrix, $\mathbf{D} \in \mathbb{R}^{l\times m}$ is the feedthrough matrix, and (**A,B**) can be stabilised. It is assumed that all of the states X are measurable.

To obtain the state space representation, each variable of Equations 4.54 and 4.69 is assumed to have a nominal value at trimmed flight condition, plus a small disturbance value such that $\Delta\mathbf{x} = \mathbf{x} - \mathbf{x}_0$ and $\Delta\mathbf{u} = \mathbf{u} - \mathbf{u}_0$. The variables are expressed in terms of the perturbation variables using a Taylor series

expansion about the trimmed flight condition as

$$\dot{\mathbf{x}} \approx f(\mathbf{x}, \mathbf{u}) + \left.\frac{\partial f}{\partial \mathbf{x}}\right|_{\mathbf{x}=\mathbf{x}_0,\mathbf{u}=\mathbf{u}_0} (\mathbf{x} - \mathbf{x}_0) + \left.\frac{\partial f}{\partial \mathbf{u}}\right|_{\mathbf{x}=\mathbf{x}_0,\mathbf{u}=\mathbf{u}_0} (\mathbf{u} - \mathbf{u}_0) \tag{6.10}$$

The constant matrices are determined by calculating the derivatives of each state with respect to all variables:

$$\begin{aligned} \mathbf{A} &\equiv \left.\frac{\partial f}{\partial \mathbf{x}}\right|_{\mathbf{x}=\mathbf{x}_0,\mathbf{u}=\mathbf{u}_0} & \mathbf{B} &\equiv \left.\frac{\partial f}{\partial \mathbf{u}}\right|_{\mathbf{x}=\mathbf{x}_0,\mathbf{u}=\mathbf{u}_0} \\ \mathbf{C} &\equiv \left.\frac{\partial g}{\partial \mathbf{x}}\right|_{\mathbf{x}=\mathbf{x}_0,\mathbf{u}=\mathbf{u}_0} & \mathbf{D} &\equiv \left.\frac{\partial g}{\partial \mathbf{u}}\right|_{\mathbf{x}=\mathbf{x}_0,\mathbf{u}=\mathbf{u}_0} \end{aligned} \tag{6.11}$$

The Δ signs in Equation 6.9 are dropped from here forward in this chapter for a cleaner presentation of the state space equations.

6.4 Stability

In response to the control inputs, the stability of the dynamic model can be determined by evaluating the eigenvalues of the linearised system. The roots of Equation 6.12 are known as the characteristic roots or the eigenvalues, λ, of the state matrix $\mathbf{A}$.

$$|\lambda_{n\times n}\mathbb{I}_{n\times n} - \mathbf{A}_{n\times n}| = 0 \tag{6.12}$$

Each eigenvalue can be either a real number or one of a pair of complex conjugate numbers. The aircraft is unstable at the reference condition if any of the eigenvalues has a real part greater than zero.

6.5 Controllability and Observability

In designing linear control systems, controllability and observability of the system should be investigated. Controllability determines the possibility of achieving the desired response of the system states $\mathbf{x}$ using the input $\mathbf{u}$. To check the controllability (C) of a system, the matrix given in Equation 6.13 is used. The dimension of the vector space formed by the columns of a matrix is its rank. If the rank of a matrix is equal to the number of columns or rows, it is said to have full rank (or to both). If the controllability

matrix has full rank, then the system is controllable [59].

$$C = [\mathbf{B}, \mathbf{AB}, \mathbf{A}^2\mathbf{B}, \cdots, \mathbf{A}^{n-1}\mathbf{B}] \tag{6.13}$$

Observability (O) on the other hand, is to know the possibility of determining all the states from the output and input signals. The system is observable if the matrix in Equation 6.14 is full rank [59].

$$O = \begin{bmatrix} \mathbf{C} \\ \mathbf{CA} \\ \vdots \\ \mathbf{CA}^{n-1} \end{bmatrix} \tag{6.14}$$

6.6 Control System Design

In this section, two control schemes are proposed, which are the Linear Quadratic Regulator (LQR) for stabilisation and the linear quadratic integral (LQI) controller for command tracking.

6.6.1 Linear Quadratic Regulator Control Theory

The control law for an optimal linear quadratic regulator (LQR) is presented in this section. For the system described in Equation (6.9), consider a cost function $\mathbf{J}$ defined as

$$\mathbf{J} = \int_0^\infty (\mathbf{x}'\mathbf{Q}\mathbf{x} + \mathbf{u}'\mathbf{R}\,\mathbf{u})dt$$

where $\mathbf{Q} = \mathbf{Q}', \mathbf{Q} \in \mathbb{R}^{n\times n}$ is a positive semidefinite weighting matrix for the states and $\mathbf{R} = \mathbf{R}', \mathbf{R} \in \mathbf{R}^{m\times m}$ is a positive definite weighting matrix for the control inputs. The optimal control input is given by

$$\begin{gathered} \mathbf{u}(t) = -\mathbf{K}\mathbf{x}(t) \\ \text{where the gain } \mathbf{K} = \mathbf{R}^{-1}\mathbf{B}'\mathbf{P} \end{gathered} \tag{6.15}$$

$\mathbf{P}$ represents the unique positive semidefinite and symmetric solution to the Algebraic Riccati Equation (ARE)

$$\mathbf{A}'\mathbf{P} + \mathbf{P}\mathbf{A} + \mathbf{Q} - \mathbf{P}\mathbf{B}\mathbf{R}^{-1}\mathbf{B}'\mathbf{P} = 0 \tag{6.16}$$

If the pair $(\mathbf{A}, \mathbf{B})$ is stabilisable and the pair $(\mathbf{A}, \mathbf{Q})$ is detectable, then Equation (6.16) has a unique positive definite solution $\mathbf{P}$ such that the optimal control

$$\mathbf{u} = -\mathbf{R}^{-1}\mathbf{B}'\mathbf{P}\mathbf{x} \tag{6.17}$$

is asymptotically stabilising [244], [245].

The control objective is to regulate the states $\mathbf{x}$ of the aircraft given a disturbance. The high level block diagram of the stabilising control system is shown in Figure 6.2.

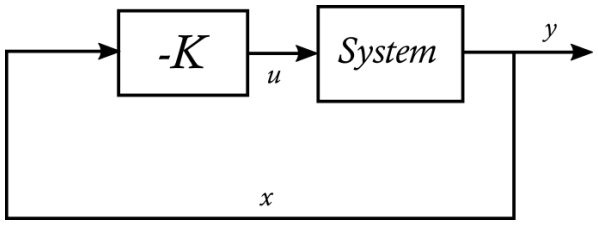


Figure 6.2: Linear quadratic regulator (LQR) control system block diagram.

6.6.2 Linear Quadratic Integral (LQI) Control

Since the aim of the command tracking controller is to track a non-zero reference input, integral control is also added to improve the tracking performance of the LQR controller, hence the term linear quadratic integral (LQI) control. LQI is therefore, an augmented version of the LQR controller that designs an optimal controller, using full state feedback to optimise the quadratic cost function. Additional states are introduced into the system as the integrals of the error e, between the reference command and the actual output of the system. For the output equation in Equation 6.9, the LQI state feedback control law is given by

$$\mathbf{u} = -\mathbf{K}[\mathbf{x}; \mathbf{x}_i] = -\mathbf{K}\mathbf{z} \tag{6.18}$$

where $\mathbf{z}$ are the states of the augmented system and $\mathbf{x}_i$ are the additional integral states. Upon introducing the integral states, the state–space representation of the augmented system becomes

$$\begin{bmatrix} \dot{\mathbf{x}} \\ \dot{\mathbf{x}}_i \end{bmatrix} = \begin{bmatrix} \mathbf{A} & 0 \\ -\mathbf{C} & 0 \end{bmatrix} \begin{bmatrix} \dot{\mathbf{x}} \\ \dot{\mathbf{x}}_i \end{bmatrix} + \begin{bmatrix} \mathbf{B} \\ -\mathbf{D} \end{bmatrix} \mathbf{u} \tag{6.19}$$

Equation (6.19) above implies that

$$\begin{cases} \dot{\mathbf{z}} & = \hat{\mathbf{A}}_{aug}\mathbf{z} + \hat{\mathbf{B}}_{aug}\mathbf{u} \\ \mathbf{y} & \mathbf{Cx} + \mathbf{Du} \end{cases} \tag{6.20}$$

Hence, the general cost function for the augmented system is the given by

$$\mathbf{J} = \int_0^\infty (\mathbf{z}'\mathbf{Q}\mathbf{z} + \mathbf{u}'\mathbf{R}\mathbf{u})dt$$

where $\mathbf{z}, \mathbf{u}, \mathbf{Q}$, and $\mathbf{R}$ represent the augmented state vector, control vector, state weight matrix and input weight matrix, respectively. For the augmented system, $\mathbf{Q}$ and $\mathbf{R}$ are design parameters that can be adjusted to meet the design requirements of the controller.

Let the control objective be for the output $\mathbf{y}$ to track a constant reference signal $\mathbf{r}$, such that $\mathbf{y} = \mathbf{r}$ is reached asymptotically. The high level block diagram of the control system is shown in Figure 6.3.

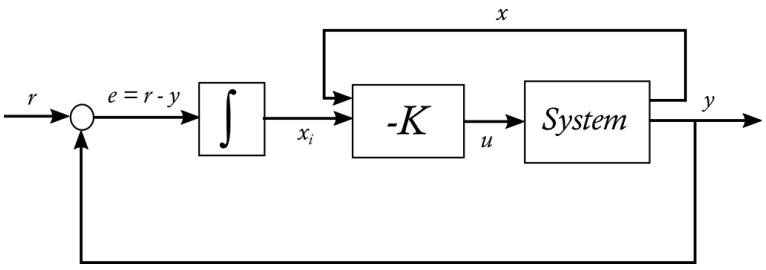


Figure 6.3: Linear quadratic integral (LQI) control system block diagram.

6.7 Simulation and Results

The flight dynamics model of the conceptual DISWA was simulated in the MATLAB/Simulink environment [208].

6.7.1 Model Validation

The verification/validation of the proposed multibody model presented in Sections 4.3 and 5.2.2 are presented in this section. The states and control inputs for the aircraft considered are given in

Equations 6.21 and 6.22, respectively.

$$\mathbf{x} = (u, v, w, p, q, r, \phi, \theta, \psi, X, Y, Z)^T, \tag{6.21}$$

$$\mathbf{u} = (\delta_e, \delta_a, T_n, \phi_T, \theta_T, \psi_T)^T, \tag{6.22}$$

The single-body and multibody model of the same aircraft should present the same longitudinal trim results. The translational and rotational flight dynamics equations of motion for a single rigid body not referenced to the centre of mass have been derived by Bacon and Gregory in [246] as

$$\begin{aligned} & m\left([\dot{V}_b^I]^B + [\Omega^{BI}]^B[V_b^I]^B\right) + \left([\dot{\Omega}^{BI}]^B m[s_{cb}]^B\right) \\ & + \left([\Omega^{BI}]^B\,([\Omega^{BI}]^B m[s_{cb}]^B)\right) = [F]^B \end{aligned} \tag{6.23}$$

$$\begin{aligned} & \left(m[S_{cb}]^B[\dot{V}_b^I]^B\right) + \left(m[\Omega^{BI}]^B([S_{cb}]^B[V_b^I]^B)\right) \\ & \left(m[V_b^I]^B([\Omega^{BI}]^B[S_{cb}]^B)\right) + [I_b^C]^B[\dot{\omega}^{BI}]^B \\ & + \left([\Omega^{BI}]^B[I_b^C]^B[\omega^{BI}]^B\right) = [M]^B + \left[[S_{cb}]^B[F]^B\right] \end{aligned} \tag{6.24}$$

The longitudinal trim results of the single-body model in [246] and the multibody model presented in this paper are calculated and compared. For the single-body model, the rotation of the abdomen was not considered during the estimation for longitudinal trim. The longitudinal trim using the single-body model can be described as follows: for a given airspeed V and a fixed abdominal pitch angle θ_T, the objective is to estimate the appropriate longitudinal pitch angle θ and control elevator δ_e and thrust T_n, to make the longitudinal rates, $\dot{u}, \dot{w}, \dot{q}$ and $\dot{h}$, approach zero.

In the case of the multibody model, the longitudinal trim can be described as follows: for a given airspeed V and a fixed abdominal pitch angle θ_T, the objective is to estimate the appropriate longitudinal pitch angle θ and controls, elevator δ_e and thrust T_n, required to keep the abdomen pitch angle θ_T at a given value to make the longitudinal rates $\dot{u}, \dot{w}, \dot{q}, \dot{h}$ and $[\dot{\omega}^{TB}]^T$ approach zero. Because the abdominal motion dynamics are included in the multibody model, the torque τ_{ay} required to keep the abdominal pitch inclination angle at the specified value can also be estimated. A PID independent joint

controller was implemented for the abdominal joint. The PID controller was tuned using automatic PID tuner, which is available as part of the control system toolbox in Simulink. The parameters for the IJC are specified in Table 6.1.

Table 6.1: Abdomen servo mechanism parameters.

Parameter	**Value**	**Unit**
$\mathbf{K}_p$	0.036	
$\mathbf{K}_I$	0.336	
$\mathbf{K}_D$	6.8×10^{-4}	
I_{act}	1.086×10^{-5}	kg$\cdot$ m^2
κ	4.34×10^{-4}	N$\cdot$m $\cdot$s

The longitudinal trim problem was solved in MATLAB for an airspeed V_0 = 10 m/s, a height H_0 = 100 m and abdominal pitch inclination angles $\theta_{T_0} = 0, -10$ and $-30°$. The results are presented in Table 6.2.

Table 6.2: Single-body vs multibody trim results at steady cruise trim condition.

V_0 (m/s)	H_0 (m)	θ_{T_0} (°)	**Model Type**	θ_0 (°)	δ_{e0} (°)	T_{n_0} (N)	τ_{ay0} (Nm)
10	100	0	Single-body	−11.35	0.228	0.679	-
			Multibody	−11.35	0.228	0.679	−0.235
		−10	Single-body	−10.66	0.0707	0.683	-
			Multibody	−10.66	0.0707	0.683	−0.232
		−30	Single-body	−6.02	−0.96	0.708	-
			Multibody	−6.02	−0.96	0.708	−0.204

Remark: *As shown in Table 6.2, the trim results for the DISWA using the single-body model and multibody model are similar at various flight speeds. The only difference is the motor torque τ_{ay}, acting on the abdomen which represents the amount of torque needed to keep the abdominal pitch inclination angle at the specified values and can be treated as a disturbance torque for control purposes.*

6.7.2 Aircraft Linearisation

Trimming and linearisation of the model was done numerically in the MATLAB/Simulink environment.

6.7.2.1 Aircraft in Trimmed Steady Cruise Flight

The aircraft trim data corresponding to steady cruise flight condition was estimated for an airspeed of V_0 = 10 m/s and height H_0 = 100 m for an undeflected abdomen. For steady cruise, the aircraft flies with constant translational and angular velocity components in body frame, $(\dot{u}, \dot{v}, \dot{w}, \dot{p}, \dot{q}, \dot{r} = 0)$. Furthermore, $(v, p, r, \phi, \psi = 0)$. Only the elevator δ_e and thrust T_n were used as control inputs to trim the aircraft. MATLAB's trim algorithm that uses sequential quadratic programming was used to obtain the trim solution. The resulting trimmed steady cruise flight condition parameters are presented in Table 6.3. Additional simulation constraints on rates are given in Equation 6.25.

Table 6.3: Aircraft initial state and control inputs at steady cruise trim condition.

State ($\mathbf{x}_0$)		**Control Input** ($\mathbf{u}_0$)	
u_0=10 (m/s)	p_0=0 (°/s)	δ_{e_0}= 0.228 (°)	ϕ_{T_0}=0 (°)
v_0=0 (m/s)	q_0=0 (°/s)	δ_{a_0}=0 (°)	θ_{T_0}=0 (°)
w_0=-0.198 (m/s)	r_0=0 (°/s)	T_{n_0}=0.68 (N)	ψ_{T_0}=0 (°)
X_0=0 (m)	ϕ_0=0 (°)		
Y_0=0 (m)	θ_0=-1.13 (°)		
Z_0= -100 (m)	ψ_0=0 (°)		

$$\begin{cases} |p| \leq 30\ ^\circ/s,\ |q| \leq 30\ ^\circ/s,\ |r| \leq 30\ ^\circ/s \end{cases} \tag{6.25}$$

The time history plot at trimmed steady cruise is shown in Figure 6.4. It shows the trajectory (Figure 6.4a), attitudes Figure 6.4b, velocity components Figure 6.4c, angular velocities Figure 6.4d, and control inputs Figure 6.4e, remain constant for the whole simulation time, which implies that the aircraft is flying in steady cruise flight.

6.7.2.2 Linear State Space Model

The linearisation algorithm in MATLAB was also used to linearise the trimmed aircraft. The longitudinal part of the linearised model consists of the following states: $\mathbf{x}_{long} = [u\ w\ q\ \theta\ H]'$, and control inputs: $\mathbf{u}_{long} = [\delta_e\ \theta_T]'$. The lateral-directional part consists of the following states: $\mathbf{x}_{lat} = [v\ p\ r\ \phi\ \psi]'$, and control inputs: $\mathbf{u}_{long} = [\delta_a\ \phi_T]'$. The actuator dynamics for the abdominal joint was included in the linear system. The longitudinal state and control matrices, as well as the

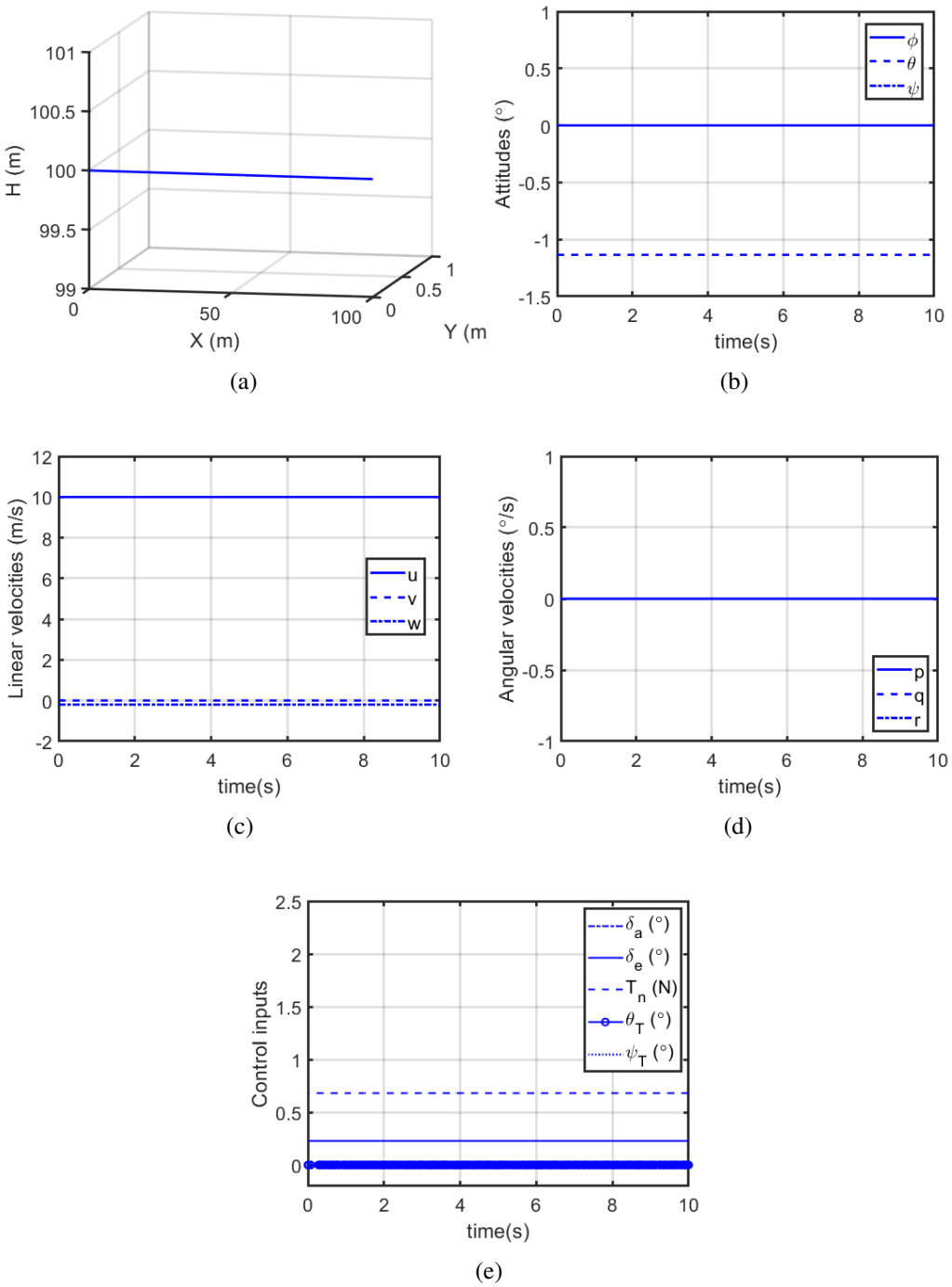


Figure 6.4: Time response at trimmed steady cruise flight: (a) Flight trajectory. (b) Attitudes (ϕ, θ, ψ). (c) Linear velocities (u, v, w). (d) Angular velocities (p, q, r). (e) Control inputs $(\delta_e, \delta_a, T_n, \theta_T, \psi_T)$.

lateral state and control matrices, are given in Equations 6.26 and 6.27, respectively.

$$A_{long} = \begin{bmatrix} \text{-0.39} & 0.18 & 0.13 & \text{-9.81} \\ \text{-3.16} & \text{-26.62} & 6.82 & 0.26 \\ \text{-7.80} & \text{-67.08} & \text{-8.74} & 0.64 \\ 0 & 0 & 1 & 0 \end{bmatrix}, \quad B_{long} = \begin{bmatrix} 0 & 0 \\ \text{-2.2} & 1.65 \\ \text{-6.43} & \text{-190.03} \\ 0 & 0 \end{bmatrix} \tag{6.26}$$

$$A_{lat} = \begin{bmatrix} -0.25 & -0.32 & -9.91 & 12.22 & 0 \\ -14.09 & -85.94 & 12.47 & 0 & 0 \\ 0.45 & -0.014 & -0.49 & -23.33 & 0 \\ 0 & 1 & -0.02 & 0 & 0 \\ 0 & 0 & 1 & 0 & 0 \end{bmatrix}, \quad B_{lat} = \begin{bmatrix} -0.033 & -7.11 \\ -18.71 & 0 \\ 0.32 & -137.27 \\ 0 & 0 \\ 0 & 0 \end{bmatrix} \tag{6.27}$$

6.7.3 Validation of Linearised Aircraft Model

The purpose of this section is to validate the linear model by comparing the linear model to the nonlinear model, to check they match each other accurately enough. To do this, the response of both models to small perturbations in the input commands is compared. The longitudinal and lateral-directional motions are considered separately, with the appropriate controller architecture.

6.7.3.1 Stability

The eigenvalues of the longitudinal state matrix, $\mathbf{A}_{long}$ in Equation 6.26, indicate that the system is stable

$$eig(\mathbf{A}_{long}) = \begin{bmatrix} -17.73 \pm 19.58i \\ -0.15 \pm 0.24i \end{bmatrix} \tag{6.28}$$

The eigenvalues of the lateral-directional state matrix, $\mathbf{A}_{lat}$ in Equation 6.27, reveals that the system is unstable

$$eig(\mathbf{A}_{lat}) = \begin{bmatrix} 0.25 \pm 1.99i \\ -85.98 \\ -0.97\text{-}2 \end{bmatrix} \tag{6.29}$$

6.7.3.2 Longitudinal Perturbation Response

The longitudinal dynamics outputs (u, w, q, θ, H) in response to the linear and nonlinear models to a doublet elevator control input is shown in Figures 6.5 a–f, while the response to an abdominal pitch doublet control input is shown in Figures 6.6 a–f.

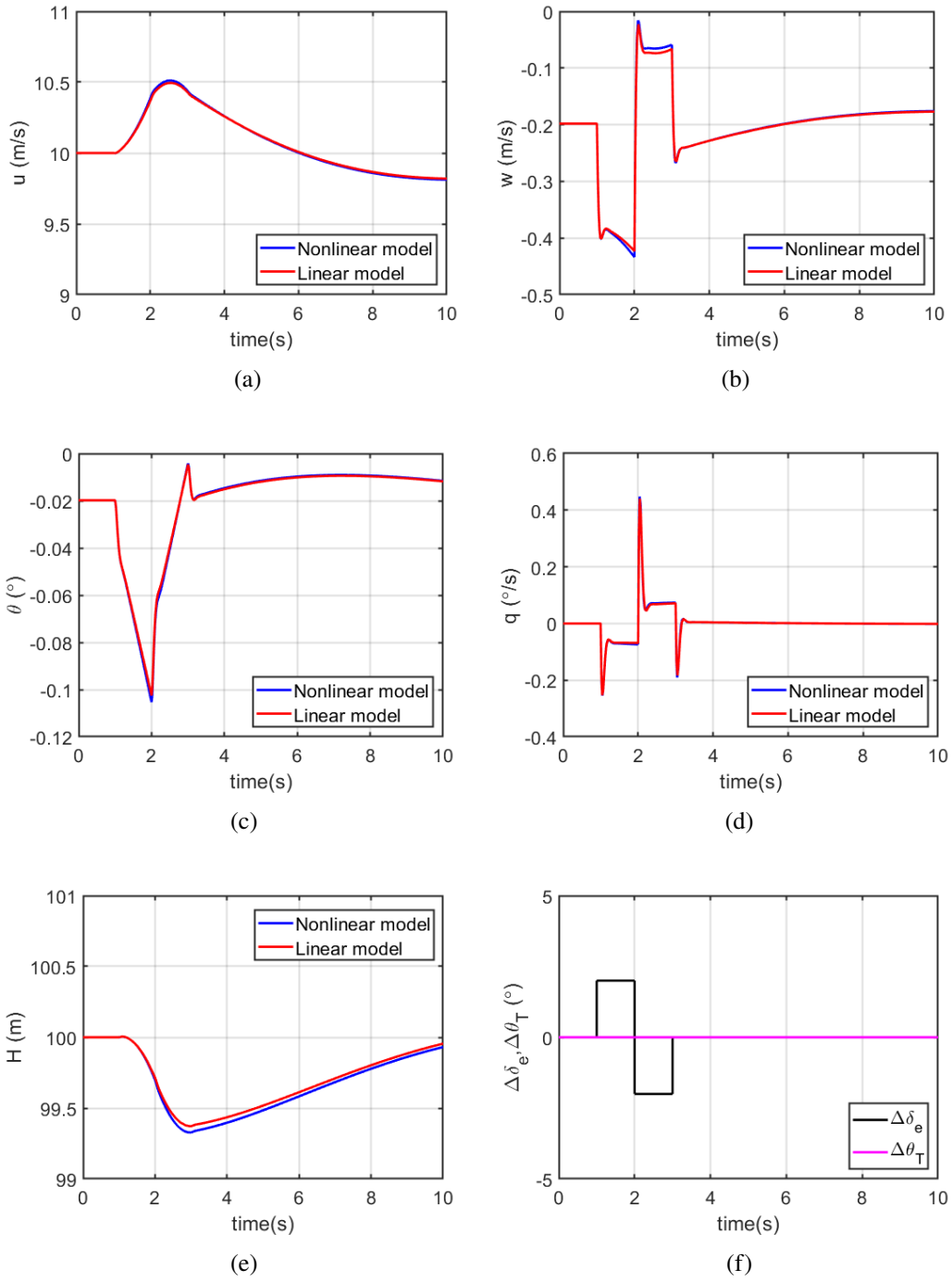


Figure 6.5: Response of longitudinal states due to elevator doublet input: (a) Forward velocity (u). (b) Vertical velocity (w). (c) Pitch rate (q). (d) Pitch angle (θ). (e) Height (H). (f) Control input perturbations ($\Delta\delta_e, \Delta\theta_T$).

Remark: *It can be seen that in both perturbation cases of elevator and abdominal pitch angle, the linear model closely matches the nonlinear model. The linear model can therefore be considered a good approximation around the equilibrium condition.*

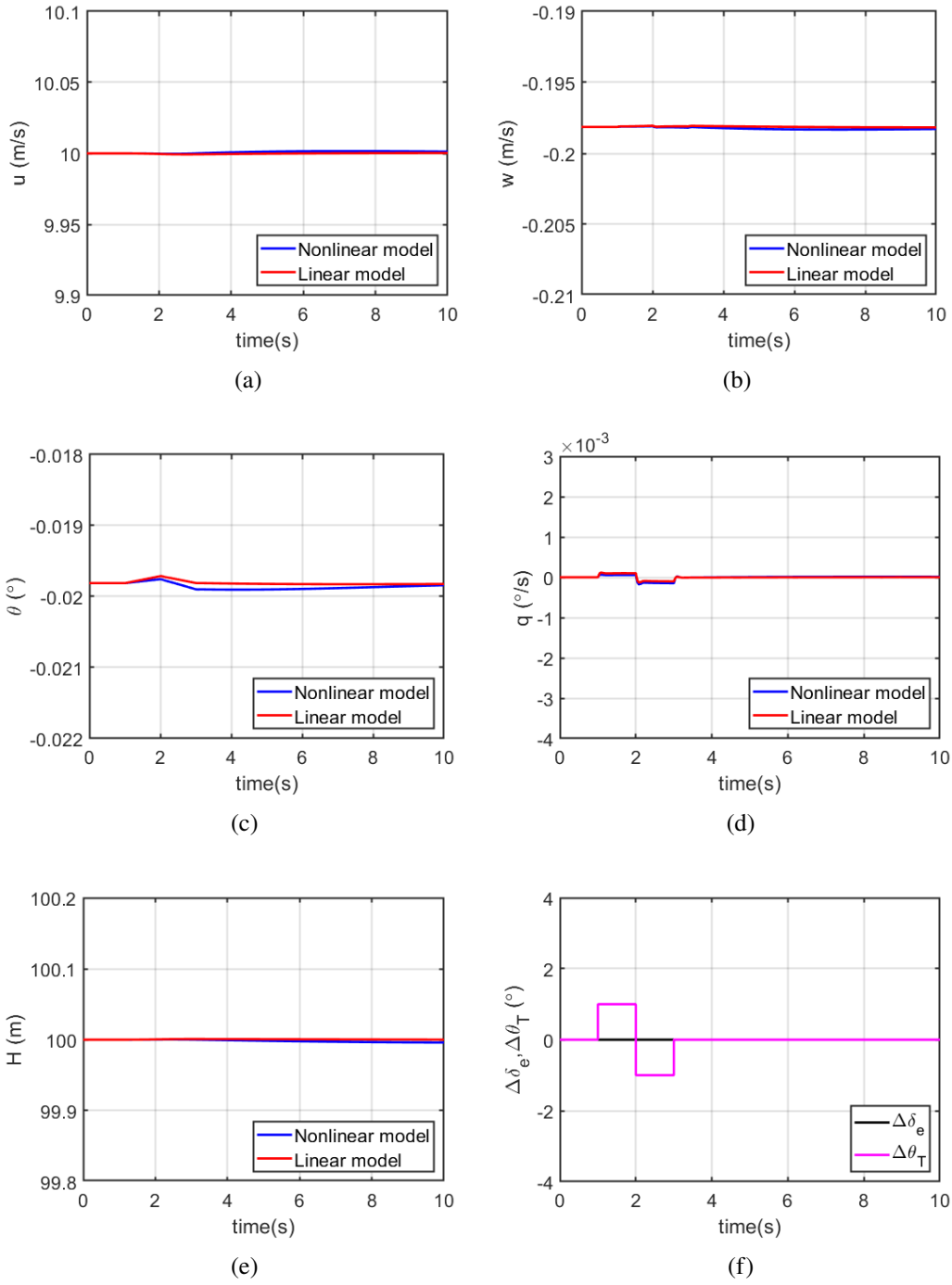


Figure 6.6: Response of longitudinal states due to abdominal pitch doublet input: (a) Forward velocity (u). (b) Vertical velocity (w). (c) Pitch rate (q). (d) Pitch angle (θ). (e) Height (H). (f) Control input perturbations ($\Delta\delta_e, \Delta\theta_T$).

6.7.3.3 Lateral-Directional Perturbation Response

The Doublet response of the lateral-directional dynamics ($v\ p\ r\ \phi\ \psi$) to each control input for the linear and nonlinear model is shown in Figures 6.7a-f and 6.8a-f.

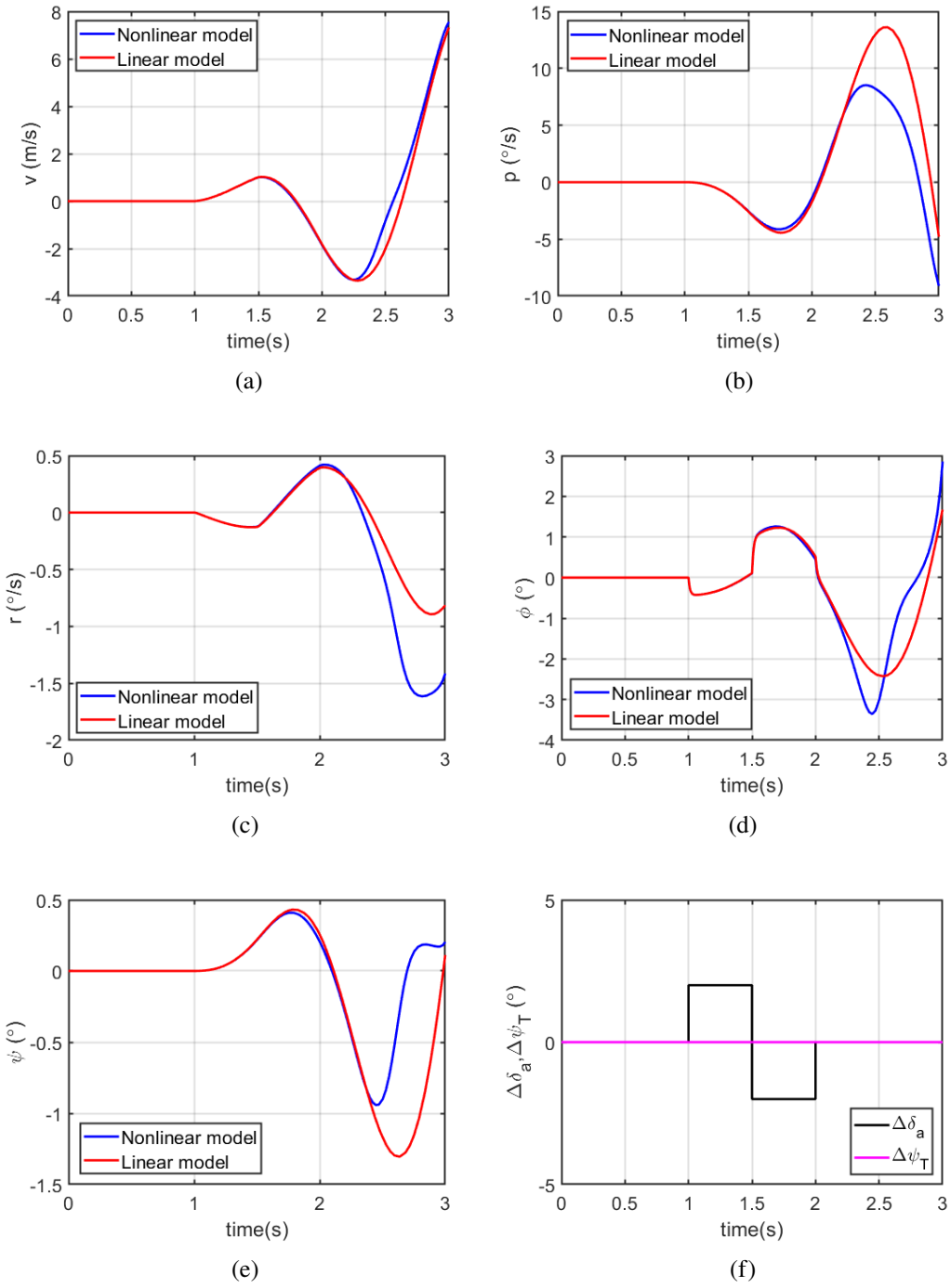


Figure 6.7: Response of lateral-directional states due to aileron doublet input: (a) Sideway velocity (v). (b) Roll rate (p). (c) Yaw rate (r). (d) Roll angle (ϕ). (e) Yaw angle (ψ). (f) Control inputs ($\Delta\delta_a, \Delta\psi_T$).

Remark: *The lateral-directional dynamics were severely affected by the absence of vertical tail as the aircraft shows a dynamically unstable behaviour for both the linear and nonlinear model. However, dynamic instabilities can be handled by an automatic controller. In addition, the response of the linear model closely matches that of the nonlinear model.*

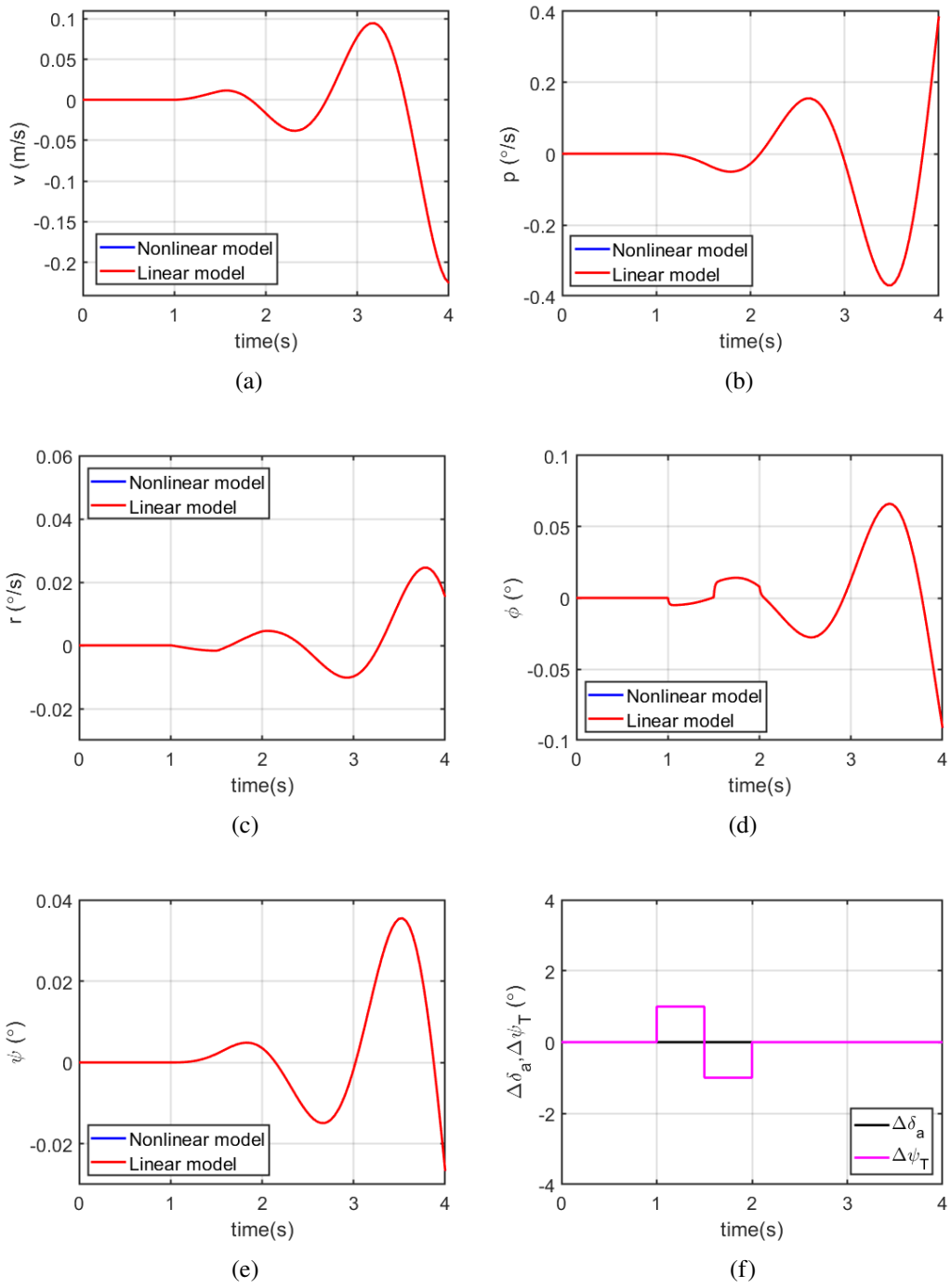


Figure 6.8: Response of lateral-directional states due to abdominal yaw doublet input: (a) Sideway velocity (v). (b) Roll rate (p). (c) Yaw rate (r). (d) Roll angle (ϕ). (e) Yaw angle (ψ). (f) Control inputs ($\Delta\delta_a, \Delta\psi_T$).

6.7.4 Effect of Abdomen Mass on Longitudinal Stability

The effect of abdominal mass on the longitudinal dynamic stability of the aircraft of interest was investigated using the eigenvalues of the state matrix of the linearised model. Five abdominal mass

values were considered as a percentage of the central body mass of the aircraft namely: 6%, 11%, 16%, 21% and 26%. These values were chosen such that they resulted in negative and positive static margin values as a statically stable aircraft can be dynamically unstable; however, a dynamically unstable aircraft cannot be statically stable. Each time, the aircraft was trimmed and linearised about steady cruise flight condition for an airspeed of V_0 = 10m/s and height H_0 = 100m for an undeflected abdomen. The obtained eigenvalues of the various **A** matrices are summarised in Table 6.4.

Table 6.4: Effect of abdominal mass as a percentage of central body mass on longitudinal stability.

Percentage of Central Body Mass (%)	**Static Margin** (%)	**Eigenvalues**	**Dynamic Stability**
6	37.3	-20.80 ± 28.21i -0.22 ± 0.95i	Stable
11	24.6	-18.81 ± 23.02i -0.20 ± 0.69	Stable
16	9.5	-18.00 ± 20.39 -0.16 ± 0.41	Stable
21	-2.7	-17.52 ± 18.91i -0.34 0.06	Unstable
26	-13.9	-17.24 ± 17.77i -0.55 0.385	Unstable

6.7.5 Aircraft Stabilisation and Control

In this section, a stabilisation autopilot and attitude tracking controller are implemented in simulation for both lateral-directional and longitudinal motion. For the stabilisation autopilot, it is desired to design a LQR, such that the closed-loop response to an initial condition settles down in about five seconds, with a steady state error of less than 1%. In the case of the attitude tracking controller, it is desired that the reference value of the pitch angle θ_{ref} or yaw angle ψ_{ref} be tracked with an overshoot of less than 4%, a steady state error of less than 1%, and a settling time of less than four seconds. From a practical standpoint, it is desirable that all states and control effectors remain within physical limits. Also, the aircraft was assumed to be cruising at a constant altitude and airspeed, and changes in θ do not affect the speed of the aircraft. Therefore, the corresponding axial velocity u components were ignored. In addition, thrust was assumed to be constant, therefore, the effects of changes in thrust were

ignored. The z_B axis velocity w was replaced with the angle of attack α using the relationship ($\alpha = \frac{w}{u_0}$), and the y_B axis velocity v was replaced with the sideslip angle, β, using the relationship $\beta = \frac{v}{u_0}$.

6.7.5.1 Longitudinal Motion Regulator

The linearised model used for longitudinal motion control consists of the following states: $\mathbf{x}_{long} = [\alpha\ q\ \theta]'$, and control inputs: $\mathbf{u}_{long} = [\delta_e\ \theta_T]'$.

$$\begin{aligned} \mathbf{A}_{long} &= \begin{bmatrix} -2.66 & 0.68 & 0.025 \\ -67.54 & -8.74 & 0.64 \\ 0 & 1 & 0 \end{bmatrix}, \quad \mathbf{B}_{long} = \begin{bmatrix} -2.20 & 1.65 \\ -6.43 & -190.03 \\ 0 & 0 \end{bmatrix} \\ \mathbf{C}_{long} &= \begin{bmatrix} 1 & 1 & 1 \end{bmatrix}, \qquad \mathbf{D}_{long} = \begin{bmatrix} 0 & 0 \\ 0 & 0 \\ 0 & 0 \end{bmatrix} \end{aligned} \tag{6.30}$$

Checking the observability and controllability of the linearised model in Equation 6.30 with MATLAB functions ctrb($\mathbf{A}_{long}$, $\mathbf{B}_{long}$) and obsv($\mathbf{A}_{long}$, $\mathbf{C}_{long}$), respectively, showed fully ranked matrices ($rank(\mathcal{O}_{long}) = rank(\mathcal{C}_{long}) = 3$). Therefore, the longitudinal model is controllable and observable.

Based on the control effector used, three aircraft longitudinal motion regulation strategies were implemented and compared for performance: aerosurface regulated (ASR), articulated mass regulated (AMR), and Hybrid regulated (HR), which uses a combination of aerosurface and articulated mass.

1. ASR$_{long}$: Prioritised use of elevator for stabilisation, interpreted as *cheap* elevator cost and *expensive* abdominal pitch cost.

2. AMR$_{long}$: Prioritised use of abdominal pitch for stabilisation, interpreted as *expensive* elevator cost and *cheap* abdominal pitch cost.

3. HR$_{long}$: Relatively evenly prioritised use of elevator and abdominal pitch for stabilisation, interpreted as *cheap* elevator cost, *cheap* abdominal pitch cost.

The same state-weighting matrices ($\mathbf{Q}_{long} = diag[1\ 1\ 1]$) and closed-loop initial conditions ($\mathbf{x}_0 = [2°;\ 2°/s;\ 0°]$), were selected and used for all cases considered. Then, the optimal gains were calculated using MATLAB's lqr(A,B,Q,R) function. A summary of the cases considered for longitudinal motion

regulation is presented in Table 6.5. The selected gains resulted in the closed-loop step response shown in Figure 6.9 for the states, while the control efforts are shown in Figure 6.10. The performance characteristics of the stabilisation strategies in terms of settling time and steady state error, are summarised in Tables 6.6 and 6.7, respectively.

Table 6.5: Simulation parameters for longitudinal motion stabilisation cases.

Longitudinal motion stabilisation case	$\mathbf{R}_{long}$	$\mathbf{K}_{long}$
ASR_{long}	$\text{diag}\,[2\times10^{-2}\ 2\times10^{5}]$	$\begin{bmatrix}-30.60 & 2.03 & 7.36\\ 0 & 0 & 0\end{bmatrix}$
AMR_{long}	$\text{diag}\,[2\times10^{5}\ 2\times10^{-2}]$	$\begin{bmatrix}0 & 0 & 0\\ -0.13 & -7.04 & -7.07\end{bmatrix}$
HR_{long}	$\text{diag}\,[2\times10^{-2}\ 2\times10^{-2}]$	$\begin{bmatrix}-5.78 & -0.28 & -0.09\\ 0.38 & -7.03 & -7.07\end{bmatrix}$

Table 6.6: Comparison of settling times for the different longitudinal motion stabilisation cases.

Longitudinal state variable	**ASR$_{long}$**		**AMR$_{long}$**		**HR$_{long}$**	
	Settling time (s)	**Percentage difference (%)**	**Settling time (s)**	**Percentage difference (%)**	**Settling time (s)**	**Percentage difference (%)**
α (°)	5.9122×10^{-1}	-8.8176×10^{1}	1.2333	-7.5335×10^{1}	2.4357×10^{-1}	-9.5129×10^{1}
q (°/s)	1.6489	-6.7022×10^{1}	2.6420×10^{-1}	-9.4716×10^{1}	1.3079×10^{-2}	-9.9738×10^{1}
θ (°)	4.1987	-1.6027×10^{1}	4.8426	-3.1476	4.0692	-1.8617×10^{1}

Table 6.7: Comparison of steady state error for the different longitudinal motion stabilisation cases.

Longitudinal state variable	**ASR$_{long}$**		**AMR$_{long}$**		**HR$_{long}$**	
	Steady state error (%)	**Percentage difference (%)**	**Steady state error (%)**	**Percentage difference (\%)**	**Steady state error (%)**	**Percentage difference (%)**
α (°)	1.2604×10^{-2}	-9.8740×10^{1}	5.7921×10^{-4}	-9.9942×10^{1}	4.8359×10^{-7}	-1.0000×10^{2}
q (°/s)	1.0593×10^{-1}	-8.9407×10^{1}	2.2522×10^{-3}	-9.9775×10^{1}	5.3455×10^{-5}	-9.9995×10^{1}
θ (°)	1.9257×10^{-2}	-9.8074×10^{1}	2.2952×10^{-3}	-9.9770×10^{1}	5.3493×10^{-5}	-9.9995×10^{1}

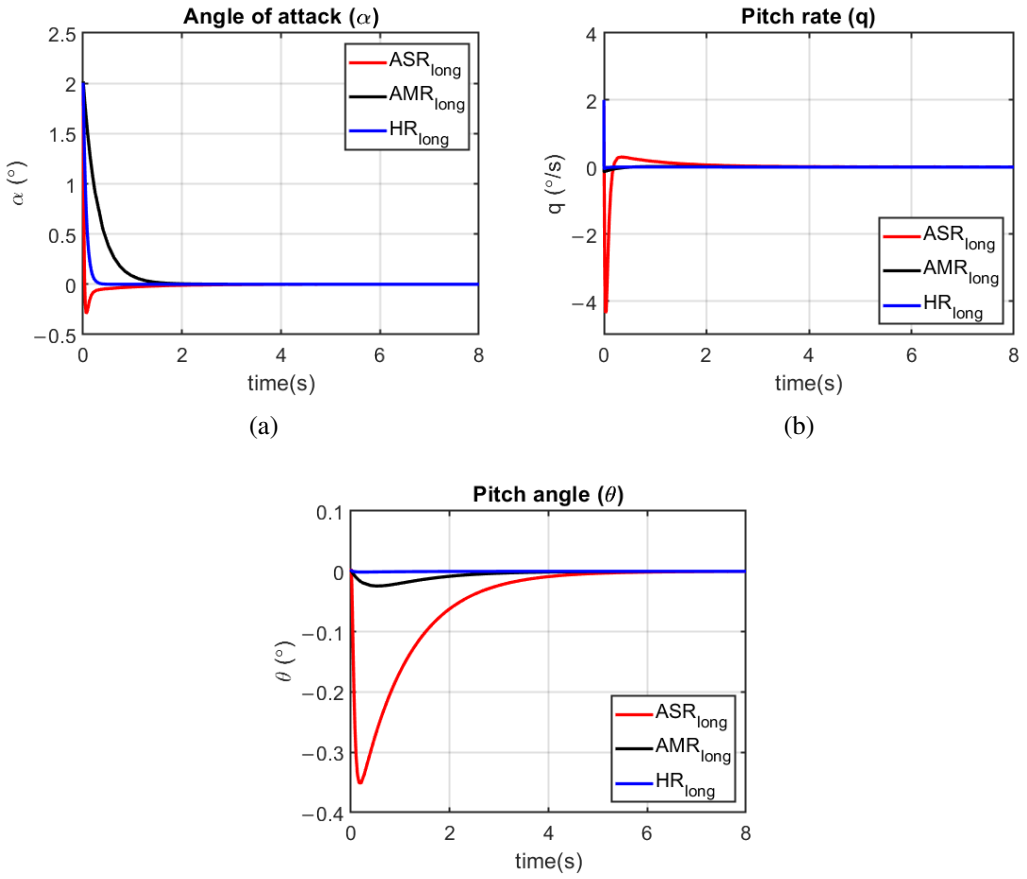
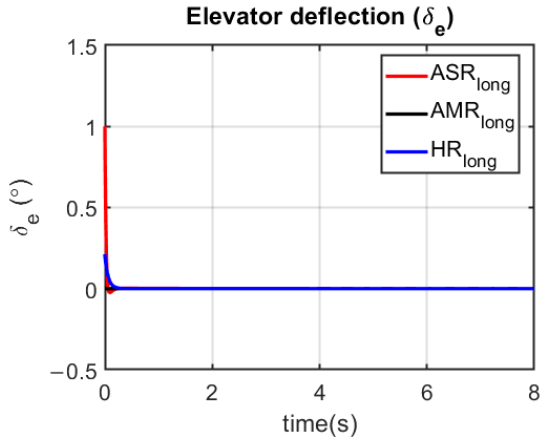


Figure 6.9: Time histories of the longitudinal states: (**a**) angle of attack (α). (**b**) pitch rate (q). (**c**) pitch angle (θ).

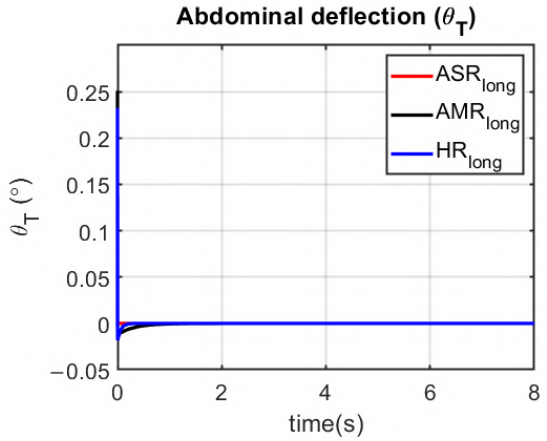
6.7.5.2 Lateral-Directional Motion Regulator

The lateral-directional part consists of the following states: $\mathbf{x}_{lat} = [\beta\ p\ r\ \phi\ \psi]'$, and control inputs: $\mathbf{u}_{long} = [\delta_a\ \phi_T]'$.

$$\mathbf{A}_{lat} = \begin{bmatrix} -0.025 & -0.032 & -0.99 & 1.22 & 0 & 0 \\ -14.09 & -85.94 & 12.47 & 0 & 0 & 0 \\ 0.45 & -0.014 & -0.49 & -23.33 & 0 & 0 \\ 0 & 1 & -0.02 & 0 & 0 & 0 \\ 0 & 0 & 1 & 0 & 0 & 0 \end{bmatrix}, \quad \mathbf{B}_{lat} = \begin{bmatrix} -0.032 & -7.11 \\ -18.71 & 0 \\ 0.32 & -137.27 \\ 0 & 0 \\ 0 & 0 \end{bmatrix}$$
$$\mathbf{C}_{lat} = \begin{bmatrix} 1 & 1 & 1 & 1 & 1 \end{bmatrix}, \qquad \mathbf{D}_{lat} = \begin{bmatrix} 0 & 0 \\ 0 & 0 \\ 0 & 0 \\ 0 & 0 \\ 0 & 0 \end{bmatrix} \tag{6.31}$$



(a)



(b)

Figure 6.10: Time histories of the longitudinal control inputs: (**a**) elevator deflection (δ_e). (**b**) abdominal pitch angle (θ_T).

Checking the observability and controllability of the linearised model in Equation 6.31 with MATLAB functions ctrb($\mathbf{A}_{lat}, \mathbf{B}_{lat}$) and obsv($\mathbf{A}_{lat}$, $\mathbf{C}_{lat}$), respectively, showed fully ranked matrices ($rank(O_{lat}) = rank(C_{lat}) = 5$). Therefore, the longitudinal model is controllable and observable.

Based on the control effector used, three aircraft longitudinal motion regulation strategies were implemented and compared for performance: aerosurface regulated (ASR), articulated mass regulated (AMR), and Hybrid regulated (HR), which uses a combination of aerosurface and articulated mass.

1. ASR$_{lat}$: Prioritised use of aileron for stabilisation, interpreted as *cheap* aileron cost and *expensive* abdominal yaw cost.

2. AMR$_{lat}$: Prioritised use of abdominal yaw for stabilisation, interpreted as *expensive* aileron cost and *cheap* abdominal yaw cost.

3. HR$_{lat}$: Relatively evenly prioritised use of aileron and abdominal yaw for stabilisation, interpreted as *cheap* aileron cost, *cheap* abdominal yaw cost.

The same state-weighting matrices ($\mathbf{Q}_{lat} = diag[1\ 1\ 1\ 1\ 1]$) and closed-loop initial conditions ($\mathbf{x}_0 = [2°;\ 0°/s;\ 2°/s;\ 0°;\ 0°]$), were selected and used for all cases considered. Then, the optimal gains were calculated using MATLAB's lqr(A,B,Q,R) function. A summary of the cases considered for lateral-directional motion regulation are presented in Table 6.8. The selected gains resulted in the closed-loop response shown in Figure 6.11 for the states, while the control efforts are shown in Figure 6.12. The performance characteristics of the stabilisation strategies in terms of settling time and steady state error, are summarised in Tables 6.9 and 6.10, respectively.

Table 6.8: Simulation parameters for lateral-directional motion stabilisation cases.

Lateral-directional motion stabilisation case	$\mathbf{R}_{lat}$	$\mathbf{K}_{lat}$
ASR$_{lat}$	diag $[2\times10^{-3}\ 2\times10^{6}]$	$\begin{bmatrix}-64.60 & -65.10 & 85.26 & -432.07 & 30.86\\ 0 & 0 & 0 & 0 & 0\end{bmatrix}$
AMR$_{lat}$	diag $[2\times10^{6}\ 2\times10^{-3}]$	$\begin{bmatrix}0 & 0 & 0 & 0 & 0\\ 20.69 & -7.66 & -71.89 & -249.16 & -70.71\end{bmatrix}$
HR$_{lat}$	diag $[2\times10^{-3}\ 2\times10^{-3}]$	$\begin{bmatrix}-61.01 & -66.22 & 3.24 & -147.35 & -33.29\\ 33.20 & -0.73 & -72.53 & 21.54 & -62.39\end{bmatrix}$

6.7.5.3 Pitch Attitude Control

For the longitudinal controller, the variable being controlled is pitch angle, hence, ($y_{long} = e_\theta$). The longitudinal augmented states considered are $\mathbf{z}_{long} = [\alpha\ q\ \theta\ e_\theta]'$, and the longitudinal control inputs: $\mathbf{u}_{long} = [\delta_e\ \theta_T]'$. The resulting augmented matrices are

$$\hat{\mathbf{A}}_{long} = \begin{bmatrix}-2.66 & 0.68 & 0.025 & 0\\ -67.54 & -8.74 & 0.64 & 0\\ 0 & 1 & 0 & 0\\ 0 & 0 & -1 & 0\end{bmatrix},\quad \hat{\mathbf{B}}_{long} = \begin{bmatrix}-2.20 & 1.65\\ -6.43 & -190.03\\ 0 & 0\\ 0 & 0\end{bmatrix} \tag{6.32}$$

$$\hat{\mathbf{C}}_{long} = \begin{bmatrix}0 & 0 & 0 & 1\end{bmatrix},\qquad \hat{\mathbf{D}}_{long} = \begin{bmatrix}0 & 0\end{bmatrix}$$

Table 6.9: Comparison of settling times for the different lateral-directional motion stabilisation cases.

Lateral-directional state variable	**ASR$_{lat}$**		**AMR$_{lat}$**		**HR$_{lat}$**	
	Settling time (s)	**Percentage difference (%)**	**Settling time (s)**	**Percentage difference (%)**	**Settling time (s)**	**Percentage difference (%)**
β (°)	7.8912	5.7823×10^{1}	9.4101	8.8203×10^{1}	2.2567	-5.4866×10^{1}
p (°/s)	1.5360	-6.9280×10^{1}	9.3294	8.6588×10^{1}	3.4820	-3.0360×10^{1}
r (°)	2.5646	-4.8708×10^{1}	8.9490	7.8979×10^{1}	3.3380	-3.3240×10^{1}
ϕ (°)	4.6939	-6.1214	9.6347	9.2694×10^{1}	3.6993	-2.6013×10^{1}
ψ (°)	9.1571	8.3143×10^{1}	9.5520	9.1039×10^{1}	4.5235	-9.5301

Table 6.10: Comparison of steady state error for the different lateral-directional motion stabilisation cases.

Lateral-directional state variable	**ASR$_{lat}$**		**AMR$_{lat}$**		**HR$_{lat}$**	
	Steady state error (%)	**Percentage difference (%)**	**Steady state error (%)**	**Percentage difference (%)**	**Steady state error (%)**	**Percentage difference (%)**
β (°)	5.6631×10^{1}	5.5631×10^{3}	1.4419×10^{1}	1.3419×10^{3}	2.9103×10^{-5}	-9.9997×10^{1}
p (°/s)	1.8515×10^{-2}	-9.8149×10^{1}	1.6210	6.2100×10^{1}	1.7183×10^{-3}	-9.9828×10^{1}
r (°)	2.5406	1.5406×10^{2}	5.0952	4.0952×10^{2}	2.7378×10^{-3}	-9.9726×10^{1}
ϕ (°)	1.3532	3.5316×10^{1}	3.9679	2.9679×10^{2}	1.5108×10^{-3}	-9.9849×10^{1}
ψ (°)	1.0801×10^{2}	1.0701×10^{4}	1.4777×10^{1}	1.3777×10^{3}	2.6602×10^{-3}	-9.9734×10^{1}

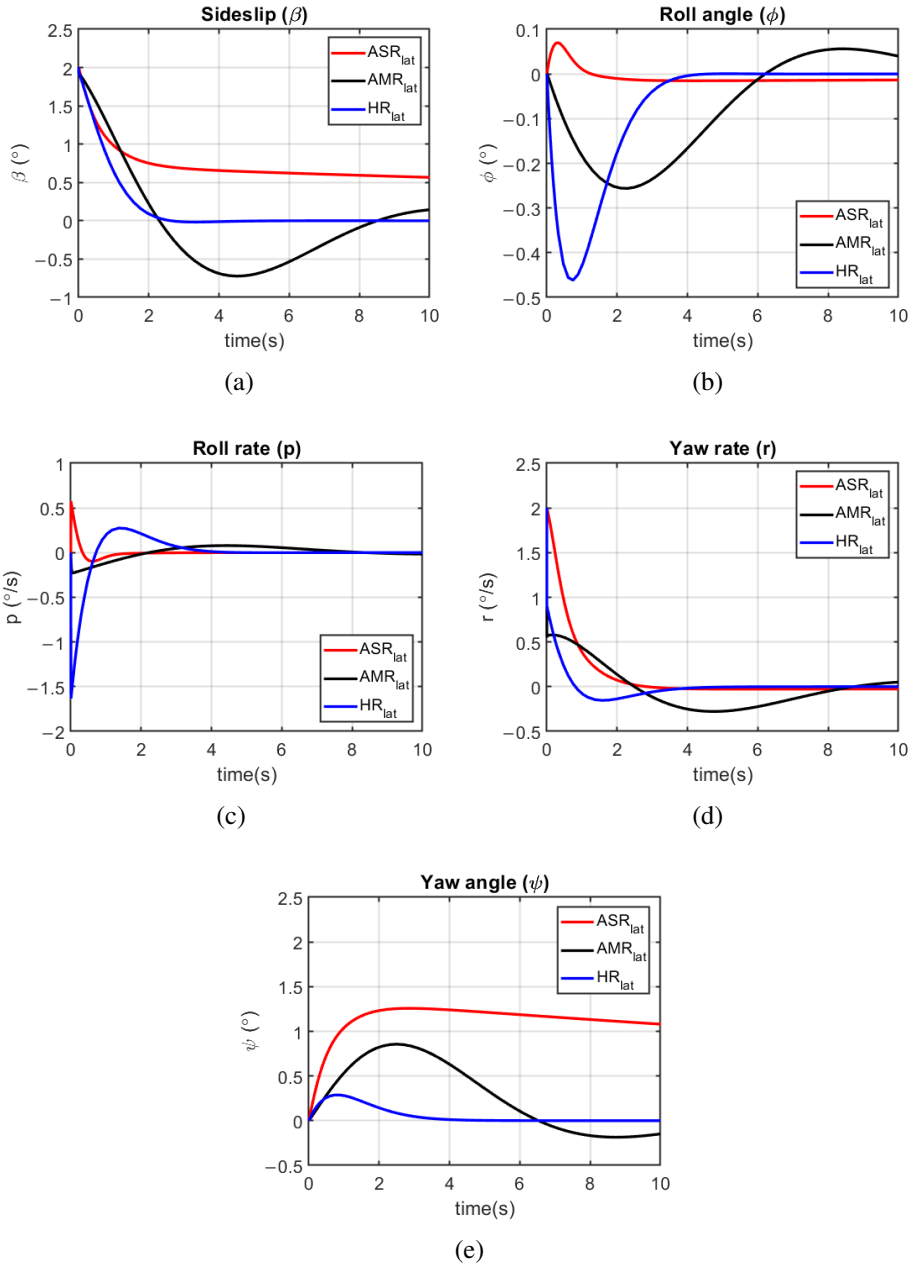
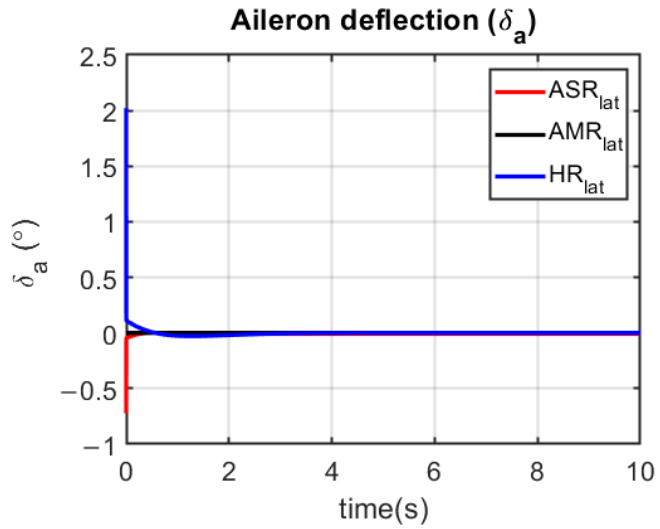


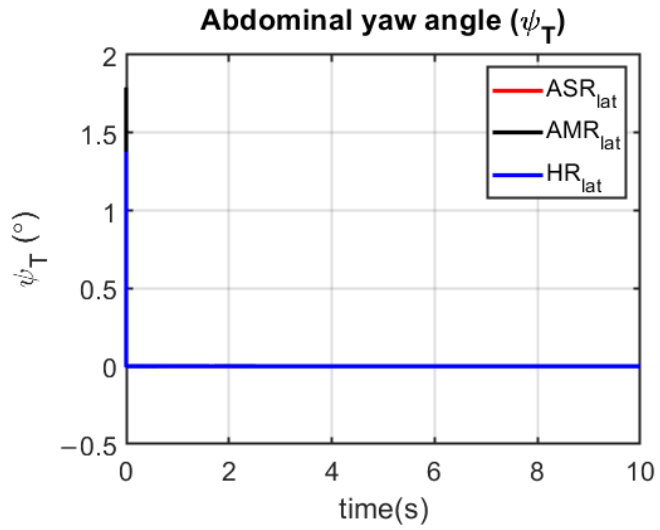
Figure 6.11: Time response of the lateral states: (**a**) sideslip (β). (**b**) roll angle (ϕ). (**c**) roll rate (p). (**d**) yaw rate (r). (**e**) yaw angle (ψ).

The obtained longitudinal linearised model in Equation 6.32 was checked to be controllable and observable using the MATLAB functions ctrb($\hat{\mathbf{A}}_{long}, \hat{\mathbf{B}}_{long}$) and obsv($\hat{\mathbf{A}}_{long}$, $\hat{\mathbf{C}}_{long}$), respectively. The observability and controllability matrices were fully ranked ($rank(\mathcal{O}_{long}) = rank(\mathcal{C}_{long}) = 4$). Therefore, the longitudinal model is controllable and observable.

Three pitch control (PC) strategies were investigated based on the selection of weighting matrices $\mathbf{R}_{long}$ to reflect the following:



(a)



(b)

Figure 6.12: Time histories of the lateral control inputs: (**a**) aileron deflection (δ_a). (**b**) abdominal yaw angle (ψ_T).

1. PC 1: Prioritised use of elevator for pitch angle control, interpreted as *cheap* elevator cost and *expensive* abdominal pitch cost.

2. PC 2: Prioritised use of abdominal pitch for pitch angle control, interpreted as *expensive* elevator cost and *cheap* abdominal pitch cost.

3. PC 3: Relatively evenly prioritised use of elevator and abdominal pitch for pitch angle control, interpreted as *cheap* elevator cost, *cheap* abdominal pitch cost.

The same state-weighting matrices $\mathbf{Q}_{long} = diag[4\ 6\ 4\ 500]$, which were selected using Bryson's rule

as a guide [247], were used for all cases considered. Then, the optimal gains were calculated using MATLAB's lqr(A,B,Q,R) function. A summary of the cases considered for pitch angle control is presented in Table 6.11. As the control objective was to track a reference pitch angle while keeping all states and control efforts within bounds, the performance characteristics for all cases are compared in terms of settling time, overshoot and steady-state error. The selected gains resulted in the closed-loop step response shown in Figure 6.13 for the states, while the control efforts are shown in Figure 6.14. The performance characteristics of the control strategies are summarised in Table 6.12.

Table 6.11: Simulation parameters for pitch control (PC) cases.

Pitch Control (PC) Case	$\mathbf{R}_{long}$	$\mathbf{K}_{long}$
PC 1	diag $[2\times10^{-2}\ 8\times10^{7}]$	$\begin{bmatrix}-87.68 & 10.29 & 93.47 & -158.11\\ 0 & 0 & 0 & 0\end{bmatrix}$
PC 2	diag $[8\times10^{7}\ 2\times10^{-2}]$	$\begin{bmatrix}0 & 0 & 0 & 0\\ 0.03 & -17.30 & -75.53 & 158.06\end{bmatrix}$
PC 3	diag $[2\times10^{-2}\ 2\times10^{-2}]$	$\begin{bmatrix}-12.78 & -0.69 & -1.98 & 4.22\\ 0.69 & -17.29 & -75.38 & 158.06\end{bmatrix}$

6.7.5.4 Yaw Attitude Control

For the yaw angle controller, the variable being controlled is the yaw angle, hence, ($y_{lat} = e_{\psi}$). This is because the aircraft considered is proposed to adopt a skid to turn (STT) strategy to prove yaw control capability. The lateral augmented states considered were $\mathbf{z}_{lat} = [\beta\ p\ r\ \phi\ \psi\ e_{\psi}]'$, and the control inputs: $\mathbf{u}_{lat} = [\delta_a\ \psi_T]'$. The resulting augmented matrices are

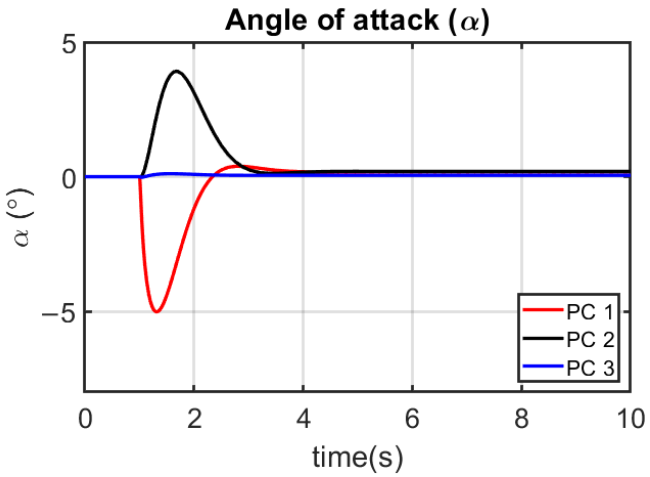
$$\hat{\mathbf{A}}_{lat} = \begin{bmatrix}-0.025 & -0.032 & -0.99 & 1.22 & 0 & 0\\ -14.09 & -85.94 & 12.47 & 0 & 0 & 0\\ 0.45 & -0.014 & -0.49 & -23.33 & 0 & 0\\ 0 & 1 & -0.02 & 0 & 0 & 0\\ 0 & 0 & 1 & 0 & 0 & 0\\ 0 & 0 & 0 & 0 & -1 & 0\end{bmatrix}, \quad \hat{\mathbf{B}}_{lat} = \begin{bmatrix}-0.032 & -7.11\\ -18.71 & 0\\ 0.32 & -137.27\\ 0 & 0\\ 0 & 0\\ 0 & 0\end{bmatrix} \tag{6.33}$$

$$\hat{\mathbf{C}}_{lat} = \begin{bmatrix}0 & 0 & 0 & 0 & 0 & 1\end{bmatrix}, \qquad \hat{\mathbf{D}}_{lat} = \begin{bmatrix}0 & 0\end{bmatrix}$$

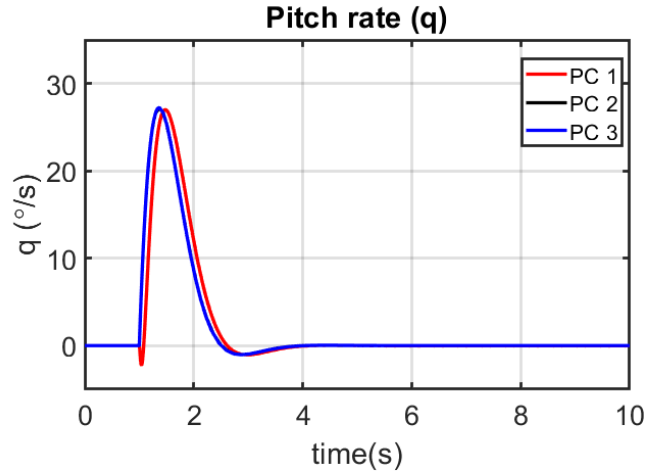
Checking the controllablity and observability of the lateral-directional linearised model in Equation 6.26, using MATLAB functions ctrb($\hat{\mathbf{A}}_{lat}, \hat{\mathbf{B}}_{lat}$) and obsv($\hat{\mathbf{A}}_{lat}, \hat{\mathbf{C}}_{lat}$), respectively resulted in fully ranked matrices ($rank(\mathcal{O}_{lat}) = rank(\mathcal{C}_{lat}) = 6$). Therefore, the lateral-directional model is controllable and observable.

Table 6.12: Comparison of performance characteristics for the different pitch control (PC) cases.

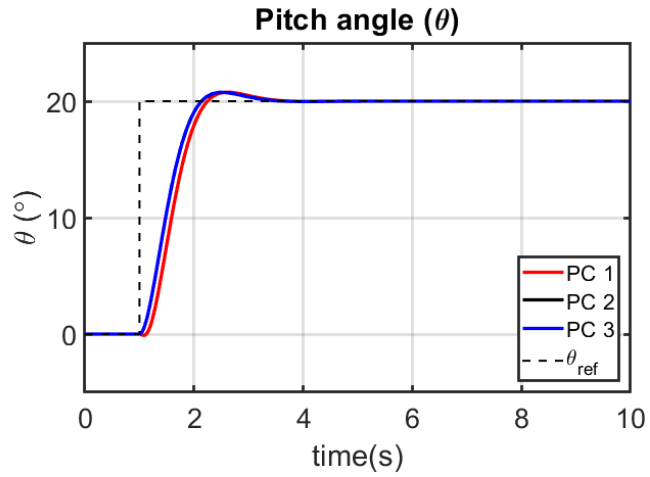
Characteristic	**Settling time**		**Overshoot**		**Steady-state error**	
	Value (s)	**Percentage difference (%)**	**Value (s)**	**Percentage difference (%)**	**Value (s)**	**Percentage difference (%)**
PC 1	3.0759	-2.3103×10^{1}	3.8402	−3.9943	1.6330×10^{-4}	-9.9984×10^{1}
PC 2	2.9702	-2.5745×10^{1}	3.8167	−4.5815	4.7561×10^{-7}	-1.0000×10^{2}
PC 3	2.9648	-2.5879×10^{1}	3.8090	−4.7739	5.2835×10^{-7}	-1.0000×10^{2}



(a)

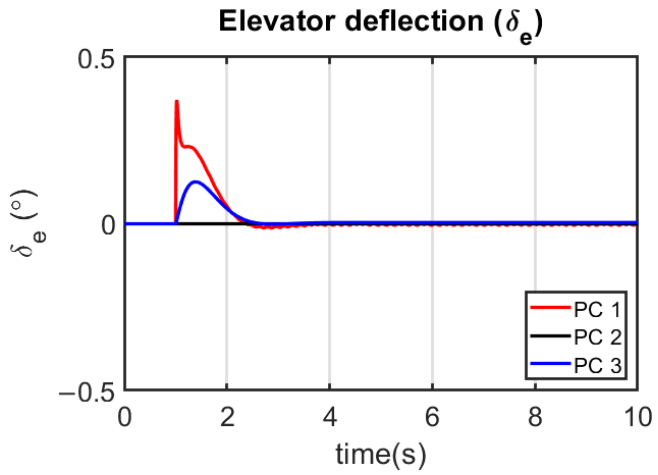


(b)

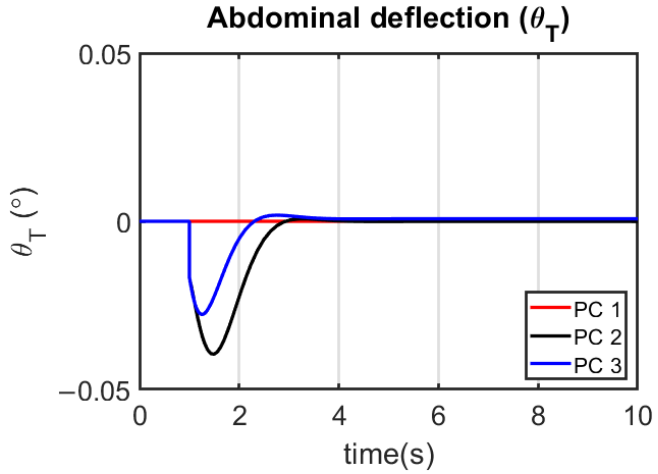


(c)

Figure 6.13: Time histories of the longitudinal states: (**a**) angle of attack (α). (**b**) pitch rate (q). (**c**) pitch angle (θ).



(a)



(b)

Figure 6.14: Time histories of the longitudinal control inputs: (**a**) elevator deflection (δ_e). (**b**) abdominal pitch angle (θ_T).

Again, three yaw control (YC) strategies were investigated based on the selection of weighting matrices $\mathbf{R}_{lat}$ to reflect the following:

1. YC 1: Prioritised use of aileron for yaw angle control, interpreted as *cheap* aileron cost, *expensive* abdominal yaw cost.

2. YC 2: Prioritised use of abdominal yaw for yaw angle control, interpreted as *expensive* aileron cost, *cheap* abdominal yaw cost.

3. YC 3: Relatively evenly prioritised use of elevator and abdominal pitch for yaw angle control, interpreted as *cheap* aileron cost, *cheap* abdominal yaw cost.

The same state weighing matrix $Q_{lat} = diag[6\ 6\ 6\ 3\ 3\ 500]$ was used for all cases considered. The choice of the state weighing matrix was also influenced by the need to minimise sideslip when the aircraft is turning. The estimated optimal gains as well as other parameters for the yaw controllers are presented in Table 6.13. The state trajectory and control effort responses are shown in Figures 6.15 and 6.16, respectively. Also, a comparison of performance characteristics is presented in Table 6.14

Table 6.13: Simulation parameters for yaw control (YC) cases.

Roll Control (YC) Case	$\mathbf{R}_{lat}$	$\mathbf{K}_{lat}$
YC 1	diag $[1\ 8\times10^{7}]$	$\begin{bmatrix} -0.68 & -0.92 & 6.30 & -33.16 & 18.01 & -22.35 \\ 0 & 0 & 0 & 0 & 0 & 0 \end{bmatrix}$
YC 2	diag $[8\times10^{7}\ 2]$	$\begin{bmatrix} 0 & 0 & 0 & 0 & 0 & 0 \\ -0.86 & -0.08 & -1.72 & 0.27 & -8.68 & 15.81 \end{bmatrix}$
YC 3	diag [10 10]	$\begin{bmatrix} -0.31 & -0.09 & 0.01 & -2.59 & -0.03 & -0.38 \\ -0.06 & -0.03 & -0.8 & -0.05 & -3.55 & 7.06 \end{bmatrix}$

6.7.6 Discussion

6.7.6.1 Effect of Abdominal Mass on Longitudinal Stability

From the results presented in Table 6.4, the longitudinal stability of the aircraft decreases with increasing mass of the abdomen. This is associated with the static margin of the aircraft. A statically stable aircraft can be dynamically unstable; however, the reverse is not the case. The aircraft was stable up until 16%; however, as it became statically unstable from 21%, it also became dynamically unstable. Additionally, one can observe two complex conjugate pairs of eigenvalues for the dynamically stable system (6–16%). The highly damped pairs are the short-period modes, and the lightly damped modes represent the phugoid modes. For dynamically unstable systems in general, control systems must be designed that can stabilise the aircraft during flight.

6.7.6.2 Longitudinal Motion Regulator

The stabilised system's initial longitudinal state responses are shown in Figure 6.9a–c. The results confirm that the use of elevator or/and the abdominal pitch angle was able to regulate all the longitudinal states. In addition, the control inputs required to stabilise the system fall within the limits (Figure 6.10a–b). From results presented in Tables 6.6 and 6.7, all the stabilisation methods were able to achieve a settling time of less than five seconds, and a steady state error of less than 1%, as per the requirements.

Table 6.14: Comparison of performance characteristics for the different yaw control (YC) cases.

Characteristic	**Settling time**		**Overshoot**		**Steady-state error**	
	Value (s)	**Percentage difference (%)**	**Value (s)**	**Percentage difference (%)**	**Value (s)**	**Percentage difference (%)**
YC 1	3.3340	-1.6650×10^{1}	5.7970	4.4925×10^{1}	2.3719×10^{-3}	-9.9763×10^{1}
YC 2	6.2492	5.6230×10^{1}	8.8679×10^{-1}	-7.7830×10^{1}	1.9997	9.9974×10^{1}
YC 3	2.8863	-2.7842×10^{1}	2.9492	-2.6270×10^{1}	3.5689×10^{-2}	-9.6431×10^{1}

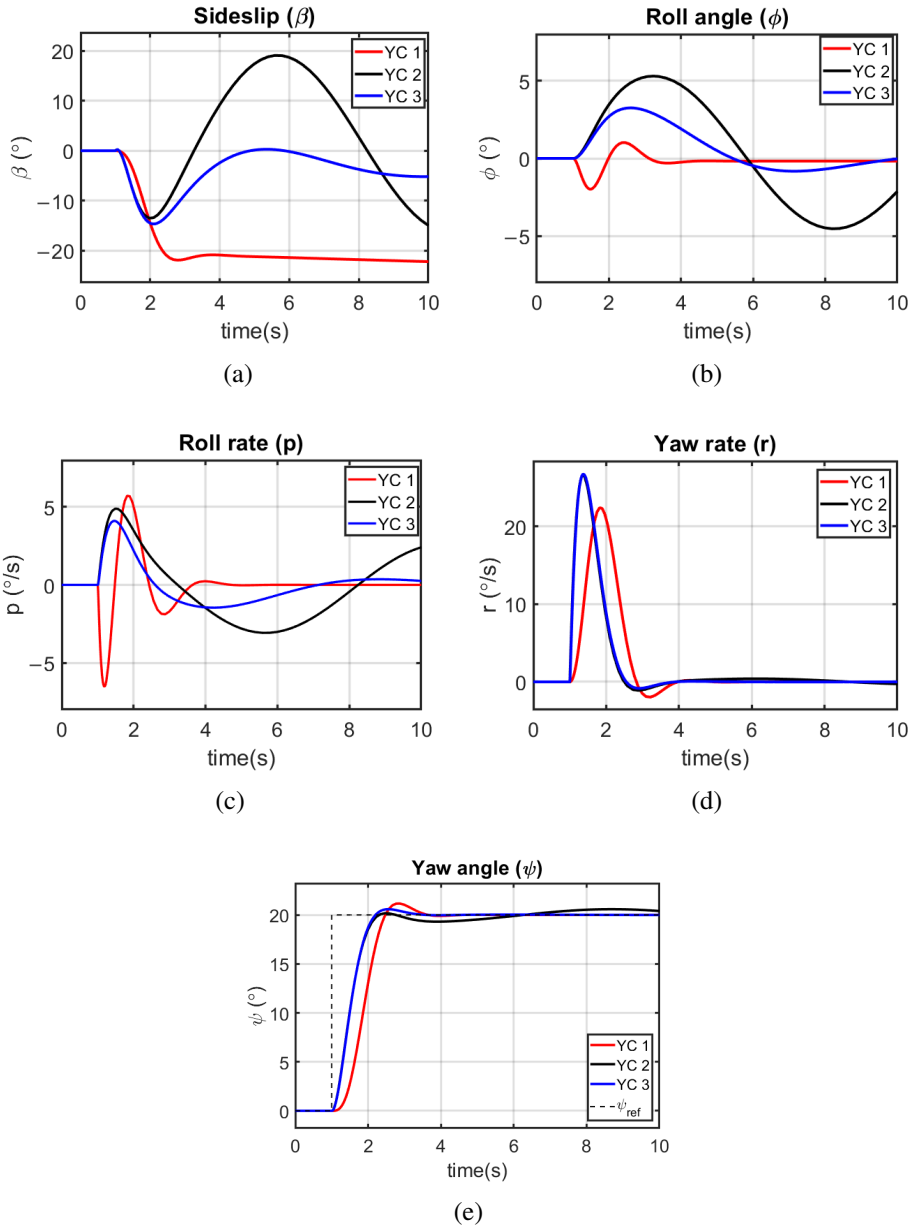
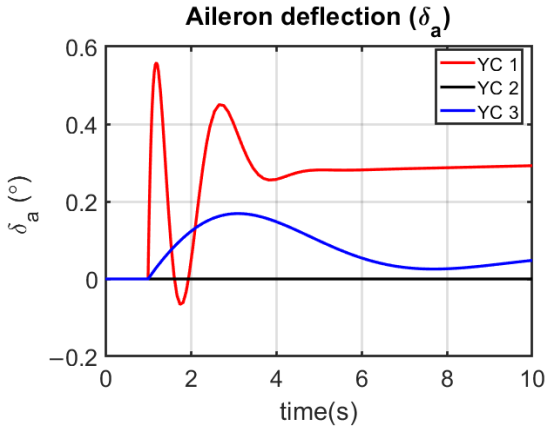


Figure 6.15: Time response of the lateral states: (**a**) sideslip (β). (**b**) roll angle (ϕ). (**c**) roll rate (p). (**d**) yaw rate (r). (**e**) yaw angle (ψ).

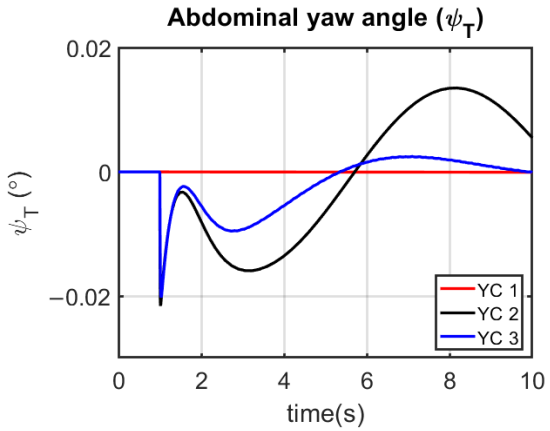
Of the three methods however, the hybrid regulator had the best performance, as it achieved the least settling time for all longitudinal states.

6.7.6.3 Lateral-Directional Motion Regulator

The initial state and control input response plots for lateral-directional motion stabilisation are shown in Figures 6.11a–e and 6.12a–b, respectively. Although the control inputs did not exceed the set limits, only the hybrid regulator was able to stabilise all the lateral-directional states. In addition, the results



(a)



(b)

Figure 6.16: Time histories of the lateral control inputs: (**a**) aileron deflection (δ_a). (**b**) abdominal yaw angle (ψ_T).

presented in Tables 6.9 and 6.10, show that only the hybrid regulator met the desired requirements of a settling time of less than five seconds, and a steady state error of less than 1% for all the lateral directional states.

6.7.6.4 Pitch Attitude Control

The longitudinal control input plots in Figure 6.14 show which longitudinal control effectors were prioritised for use in pitch-up control. For PC 1, the elevator was used exclusively, indicated by a downward elevator deflection in Figure 6.14a, and no abdominal deflection in Figure 6.14b. PC 2 used abdominal pitch deflection exclusively as seen in Figure 6.14a, and no elevator deflection in Figure 6.14b. A downward elevator and upward abdominal pitch deflection shown in Figures 6.14a,b, respectively, show that the elevator and abdomen were simultaneously used for control in PC 3.

The effects of the control effector choice on longitudinal states over time according to the controller used are shown in Figure 6.13. The angle of attack α time history in Figure 6.13a reveals that exclusive use of a positive elevator deflection (PC 1) caused an initial decrease in angle of attack as expected. Similar results have been obtained in [248], [249] for tailless aircraft. The deflection of the elevator causes a change in the camber of the airfoil of the wing and consequently changes the lift coefficient. A positive elevator deflection for a reflex airfoil, as in the case of the aircraft wing in this study, decreases the wing lift and pitching moment, resulting in a decrease in angle of attack. However, the exclusive deflection of the abdomen (PC 2) shifts the combined cg forward, and consequently causes a change in lift and drag reference offset, as well as gravitational moments, therefore generating control moments. The resulting effect is the initial increase in angle of attack. In the case of PC 3, these effects are combined and reduced. Regarding the time histories of the pitch rate q (Figure 6.13b) for the three pitch controllers, an increase in pitch angle resulted in an increase in pitch rate, as expected.

The simulation results presented in Figures 6.13 and 6.14 and Table 6.12 showed that the PC 3 controller had better tracking performance for pitch angle than the PC 1 and PC 2 controllers, with a settling time of 2.96 s and the least overshoot of 3.81%. The PC 1 controller was the poorest performer of the three controllers with the highest overshoot of 3.84% and the longest settling time of 3.08 s. All three controllers had zero steady-state error and fell within the set performance requirements. The corresponding control efforts for elevator deflection δ_e and abdominal pitch angle are well within the physical bounds with maximum absolute deflections being 0.37° and, 0.04° respectively. The states also fall within the simulation constraints set for α and q, with the maximum absolute values of 5.00° and 27.14°/s, respectively. For parallel comparison, the results indicate that a dragonfly using its abdomen in conjunction with its wings would obtain improved controllability and control performance compared to using the wings alone.

6.7.6.5 Yaw Attitude Control

Figure 6.16 shows the lateral–directional control input plots for yaw angle control. YC 1 uses ailerons exclusively and zero abdominal yaw deflection, abdominal yaw deflection exclusively and zero aileron deflection for YC 2, and both aileron and abdominal yaw deflection for YC 3. The transient response for the lateral–directional dynamic response in terms of sideslip angle β, roll angle ϕ and roll rate p are presented in Figures 6.15a–c. Note that prior to implementation of a controller, the aircraft

was laterally unstable (Equation (6.29), which is not unusual for tailless aircraft [248], [250]. Similar behaviour can be observed based on the effect of yaw control effector choice on the transient of these states. The exclusive use of the aileron (YC 1) produces the most stable response in β, ϕ and p, while using the abdominal yaw alone for control (YC 2) caused the aircraft to be more unstable as a result of dynamic effects of the oscillatory movement of the abdomen as seen in Figure 6.16b. Simultaneously using both ailerons and abdominal yaw (YC 3), on the other hand, reduced the instability experienced with the exclusive use of abdominal yaw in YC 2. The main remark regarding the state evolution of roll angle (Figure 6.15b) and roll rate (Figure 6.15c) is the presence of a strong coupling between lateral and directional dynamics, caused by aileron and abdominal yaw deflection.

A yaw controller generates a sideslip to induce a turn and a significant problem associated with turning of a rudderless aircraft is adverse yaw resulting from the differential lift and drag on the left and right wing. The sideslip angle β is a key performance indicator for aircraft turn coordination, i.e., with zero sideslip angle $\beta = 0$. The time history for sideslip angle β in Figure 6.15a shows that the exclusive use of ailerons (YC 1) and exclusive use of abdominal yaw (YC 2) resulted in negative sideslip. However, simultaneously using ailerons and abdominal yaw achieved better turn coordination over time. Regarding the time histories of the yaw rate r (Figure 6.15d), for the three yaw controllers, an increase in yaw angle resulted in an increase in yaw rate as expected.

From the simulation results presented in Figures 6.15 and 6.16 and Table 6.14, it can be observed that YC 3 has a better response in terms of settling time of 2.29 s compared to that of YC 1 and YC 2 with settling times of 3.33 s and 6.25 s, respectively. In terms of overshoot, YC 2 has the least overshoot 0.89%, compared to YC 1 and YC 3 with overshoots of 5.80% and 2.95%, respectively. YC 2 gives the highest steady-state error of 2%, with the steady-state errors of YC 1 and YC 3 being 0% and 0.04%, respectively. In addition, the corresponding control efforts for aileron deflection δ_a and abdominal yaw angle fall within the set limits with maximum absolute deflections being 0.056° and, 0.013° respectively. The states also fall within the simulation constraints set for β, p and r, with maximum absolute values of 22.24°, 6.53°/s and 26.56°/s, respectively. Of all the controllers, only YC 3 meets the controller performance requirements. For insects, the lack of a dedicated yaw-controlling surface similar to the aerodynamic rudder of many aircraft causes inherent instability on the lateral axis; however, “ruddering” movements of the abdomen have been observed in tethered turning locusts [251],

and the dragonfly turning sequence shown in Figure 4.3a also appears to show a yaw deflection of the abdomen when turning. The results attest to the potential use of a yaw-like abdominal airframe-based control mechanism that can be beneficial for the reduction of sideslip during turns (see Figure 6.15a) as sideslip is a critical control state of the entire aircraft.

The results obtained for yaw control are consistent with the observation in the analysis by Eturk in [42] that used internal moving mass for turn, trim and trajectory control. With the internal moving mass, the aircraft was able to achieve trimmed turning flight with no sideslip, which was not possible using conventional aerodynamic control surfaces. Unlike that study, however, reaction torques are apparent, due to the size and mass of the appendage.

6.8 Summary

A tensor based multibody flight dynamics simulation model of a dragonfly inspired straight flying wing aircraft that considers abdominal articulation was presented in this chapter. The longitudinal and lateral-directional flight altering effects of the mechanism have been demonstrated dynamically in simulation. Stabilisation and attitude control design based on optimal control theory was implemented for longitudinal and lateral-directional flight using aerosurfaces and/or abdominal motions. The results indicate the benefit of abdominal articulation of insects, especially for minimising sideslip angle for lateral stabilisation and control. Although the implementation might be difficult and of questionable utility considering the relatively staid missions of current drones, dragonflies with vastly higher performance have been observed to employ some of these mechanisms.

These results raise a number of questions about the utility of using multibody masses to control aircraft. From the control structure, it is clear that a degree of control is achievable using something like an abdomen, and also that the aircraft is completely controllable using this method. The results with the representative control system illustrate this, at least for the domain in which the small angle approximation applies, which is generally quite large in practice.

Chapter 7

Articulated Appendage Test Bed

This chapter covers the steps taken to design and demonstrate a practical and controllable appendage system. To the best of our knowledge, there is no standard unmanned aircraft with this function. Therefore, a physical model in the form of a radio controlled flying wing Phantom FX-61 aircraft was fitted with an articulated mass and flown to establish that a suitable test bed for mass-shift based control laws could be created with readily available components.

7.1 Introduction

In the sections that follow, an overview of the experimental aircraft used to conduct flight tests is first presented. The avionics equipment for actuation, data processing, navigation and communication are detailed. Next, the simulation model of the aircraft is developed, including the aerodynamic model, actuators and the motor. Experimental flight test data and simulation in open loop are then compared in both longitudinal and lateral-directional flight.

This chapter aims to address the following research question:

1. Is this biologically inspired appendage movement feasible for controlling the flight of a SUAV?

7.2 Overview of Experimental Aircraft

The modified Phantom FX-61 flying wing aircraft, depicted in Figure 7.1, was used as the test bed. It is a flying wing RC aircraft with right and left elevons as aerodynamic control surfaces. The modification was in the form of an articulated mass mechanism attached to the dorsal surface of the central fuselage area of the aircraft, ahead of the centre of gravity. The positioning of the mass was to ensure a statically balanced aircraft. In addition, the mechanism was switchable to deflect along either the longitudinal axis or lateral axis. A summary of important physical parameters is provided in Table 7.1.



Figure 7.1: Modified Phantom FX-61 flying wing aircraft.

Table 7.1: Summary of important aircraft geometry

Parameter	Value	Unit
S_{ref}	0.44	m^2
b_{ref}	1.55	m
c_{ref}	0.33	m
m_{max}	2.2	kg

7.2.1 Hardware Description

Onboard electronics are necessary for actuation, power, and navigation of the aircraft during flight. Most of the electronics used were already available and were chosen for that reason. Others were selected based on technical features and cost. The main hardware/electronics (see Figure 7.2) for the aircraft are briefly discussed in the sections that follow.

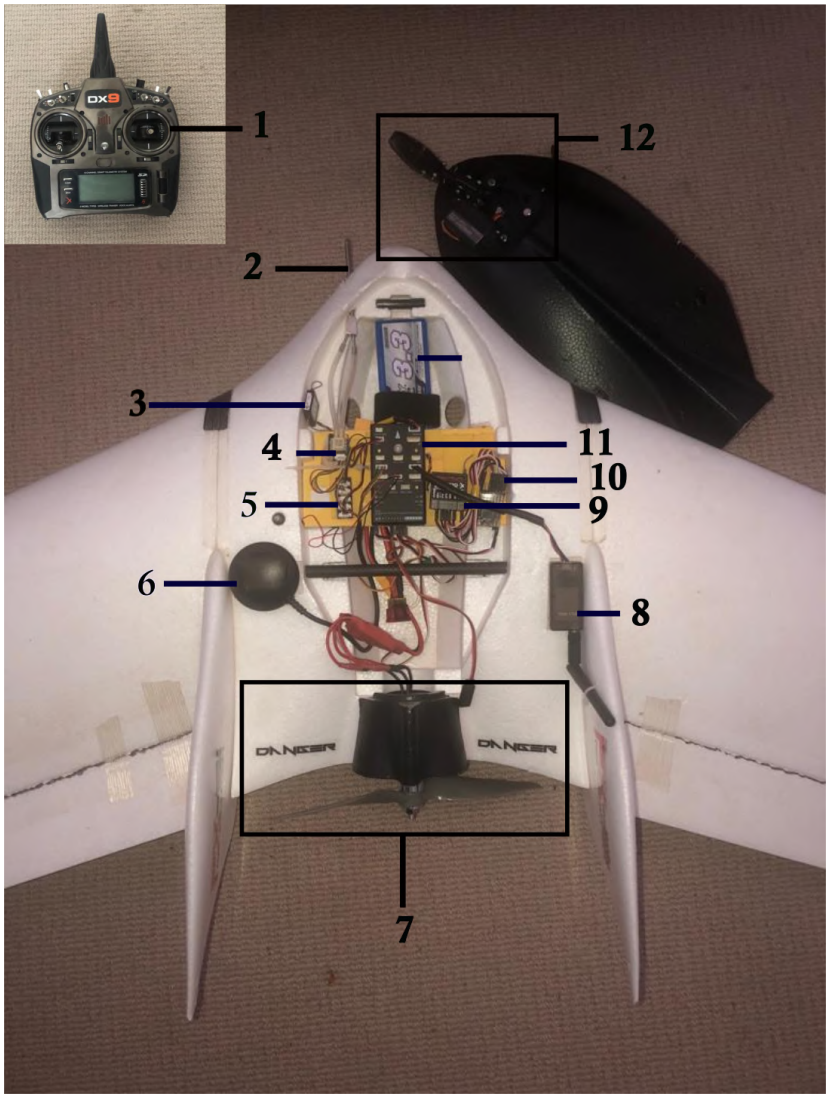


Figure 7.2: Aircraft hardware components:
[1] Radio controller [2] Pitot tube [3] Voltage regulator
[4] Differential pressure sensor [5] I2C Hub [6] GPS
[7] Motor and propeller [8] Telemetry Radio [9] Receiver
[10] RC signal multiplexer [11] Pixhawk autopilot [12] Battery
[13] Articulated mass and mounting unit

7.2.1.1 Flight Controller

The Pixhawk flight controller was used, which is supported by both the PX4 and ArduPilot software stacks. In this study it turned out that it is very versatile and capable of managing and logging additional systems on top of its flight control function.

7.2.1.2 Global Positioning System

An essential part of the autopilot system, the global position system (GPS) receiver, allows the autopilot to know where it is in space and is essential for mission scripting. The APM comes equipped with a connector that allows the user to plug the GPS directly into the board. The Quanum LEA-6H GPS with compass module was chosen for the aircraft.

7.2.1.3 Airspeed Sensor

The airspeed sensor is a combination of a differential pressure sensor, pitot static probe, I2C connection, and two rubber tubes. With this airspeed sensor, the autopilot is able to fly by airspeed and not by ground speed. This provides higher mission flight fidelity, especially in windy conditions. The pitot tube was connected to the rubber tubing, and the airspeed sensor was connected to the autopilot through an I2C connection. An MPXV7002 differential pressure transducer was used.

7.2.1.4 Wireless Telemetry

The telemetry system provides a connection to the aircraft via a 915 MHz radio modem. Telemetry allows real-time reading of parameters and attitude, as well as writing them for setup and tuning.

7.2.1.4.1 Radio Control

The radio system used was a Spektrum DX9 Black 9-Channel DSMX Transmitter with an AR7610 7-Channel DSMX High Speed Receiver.

7.2.1.5 Power Module

A 10 S power module was used to reliably power servos without using multiple batteries. It also read the voltage and current of the battery and reported them to the ground station.

7.2.1.6 Propulsion System

The propulsion system consisted of a propeller, an electronic speed control unit, and a brushless DC motor. A Turnigy Aerodrive SK3 3542 800 kV brushless outrunner motor was used, controlled by a Turnigy Plush 40 Amp electronic speed controller, and an APC 9×6 folding propeller.

7.2.1.7 Battery

One Turnigy 3300mAh 3S 30C Lipo battery was used to power all avionics. The battery specifications are shown in Table 7.2

Table 7.2: Turnigy 3300mAh 3S 30C lipo battery technical specifications. Source: Hobbyking.com

Specification	Value and Unit
Minimum Capacity	3300 mAh
Configuration	3S1P / 11.1v / 3Cell
Constant Discharge	30 C
Peak Discharge (10 s)	40 C
Pack Weight	0.297 kg
Pack Size	137 x 43 x 22mm
Charge Plug	JST-XH
Discharge Plug	XT-60

7.2.1.8 Control Surface Servos

Each aerosurface was controlled by a Hextronik HXT900 Servo, linked to the elevon horns with stiff wire. The technical specifications of the servo are given in Table 7.3.

Table 7.3: Hextronik HXT900 servo technical specifications. Source: Hobbyking.com

Specification	Value and Unit
Size	23×12×23 mm
Voltage	3 V - 6 V
Weight	9.8 g
Speed	0.12 s/60°
Torque	1.6 kg.cm

7.2.1.9 Mechanical Design of Articulated Mass

A custom articulated mass was designed in openSCAD [252], a free software package for creating solid 3D CAD models, and 3D-printed with a Prusa i3 MK3S+ 3D printer. The design was such that the hollow part of the bob mass could be filled with lead to increase the mass. The dimensions for the components of the articulated mass mechanism are shown in Figure B.1, while the assembled articulated bob is shown in Figure 7.3. The bob mass which was connected to the servo using a carbon rod (see Figure 7.2), weighed 0.101kg ($\approx$ 7% of the total body mass), and was chosen to ensure longitudinal static stability of the flying wing aircraft.



Figure 7.3: Articulated mass bob.

In addition, the articulated mass was restricted to pitch and yaw movements (two DoF) such that it could be mounted in line with either the pitch or yaw axis of the aircraft. The Turnigy TGY-4409MD was used for the articulated mass deflection, with rotation range of about 90 °. The technical specifications of the servo are given in Table 7.4.

Table 7.4: Turnigy TGY-4409MD servo technical specifications. Source: Hobbyking.com

Specification	**Value and Unit**
Size	41×20.3×29.5 mm
Voltage	4.8 V - 6 V
Weight	44 g
Speed	0.13 s/60° at 4.8V
Stall torque	8.65 kg.cm at 4.8V

7.2.2 Software Description

The operation of this aircraft necessitated the use of two types of software. The flight controller, which runs on the onboard computer, was in charge of flight control, while the ground station software was in charge of telemetry and higher level commands. The software used are described in this section.

7.2.2.1 Flight Controller Software

The flight controller software, which runs on the onboard computer, was in charge of managing the aircraft's attitude, altitude, and position. Most flight controller boards have internal (gyroscope, accelerometer, barometer, magnetometer) and external sensors (airspeed, GPS, magnetometer), to accomplish this.

7.2.2.2 Ground Station Software

The Mission Planner free ground station software (Version 1.3.75) was used. Despite the fact that only a few of the program's features were necessary for the flight data recorder, it was considered the most appropriate software for the application. Data flash logs stored on the APM can be interpreted by Mission Planner, and data flash logs delivered by the APM can be recorded. In addition, the Mission Planner software can be used on both computers and mobile devices [253].

7.3 Theoretical Model

The flight dynamics model of an aircraft with an articulated appendage was derived in Chapter 4. This section describes the development of the blocks required for the simulation of the physical/experimental aircraft in the Matlab/Simulink environment.

7.3.1 Aerodynamic Model

AVL was used to compute the aerodynamic data for the Phantom. The AVL geometry file for the Phantom and a sample output file are found in Appendix A. Using the aircraft geometry, the aerodynamic properties were computed for a sweep of AoA and sideslip angles, and stored in look up tables in the Simulink model. The airfoil used was the S5010 (see Figure 7.4), suitable for low Reynolds number flying wing flyers. The thickness of the airfoil was about 9.8%. With the airfoil chosen, its characteristics were calculated with the XFOIL airfoil analysis tool built into XFLR5 to particularly estimate the viscous drag to be provided to AVL. The inertia properties of the aircraft were estimated using the XFLR5 software. The aircraft model in AVL and XFLR5 is shown in Figure 7.5.

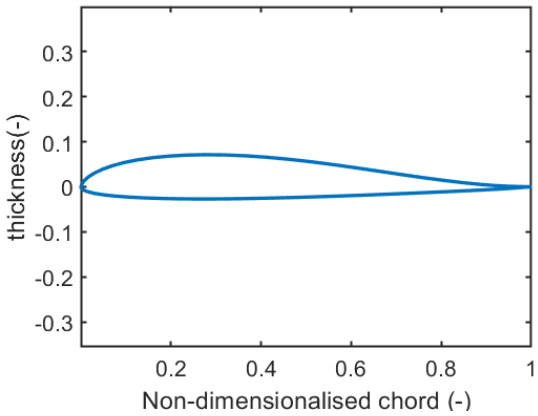
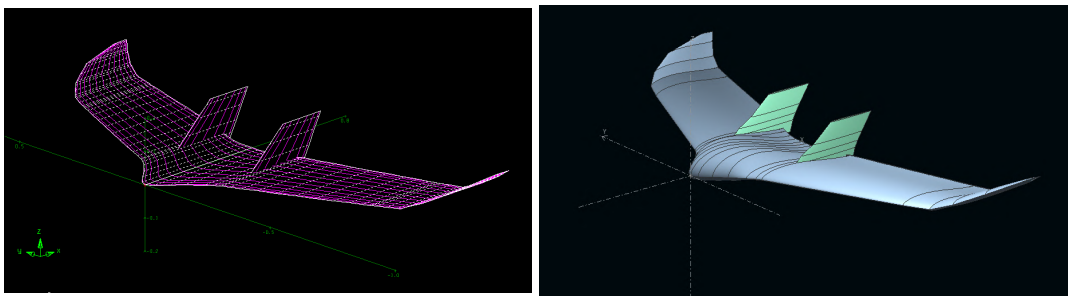


Figure 7.4: S5010 airfoil.



(a) (b)

Figure 7.5: Aircraft model: (**a**) In AVL. (**b**) In XFLR5.

The aerodynamic force (C_x, C_y, C_z) and moment (C_l, C_m, C_n) coefficients were calculated in aircraft body axes.

$$\begin{aligned} C_x &= f(\alpha, \hat{q}, \delta_e); \quad C_y = f(\beta, \hat{p}, \hat{r}, \delta_a); \quad C_z = f(\alpha, \hat{q}, \delta_e) \\ C_l &= f(\beta, \hat{p}, \hat{r}, \delta_a); \quad C_m = f(\alpha, \hat{q}, \delta_e); \quad C_n = f(\beta, \hat{p}, \hat{r}, \delta_a) \end{aligned} \tag{7.1}$$

where $\hat{p} = \frac{b_{ref}\, p}{2V}$, $\hat{q} = \frac{c_{ref}\, q}{2V}$ and $\hat{r} = \frac{b_{ref}\, r}{2V}$ are the normalised body rates. The right and left elevons were mixed to act as an elevator or aileron based on the equations defined in Equation 5.14 in Chapter 5.

7.3.2 Actuator Model

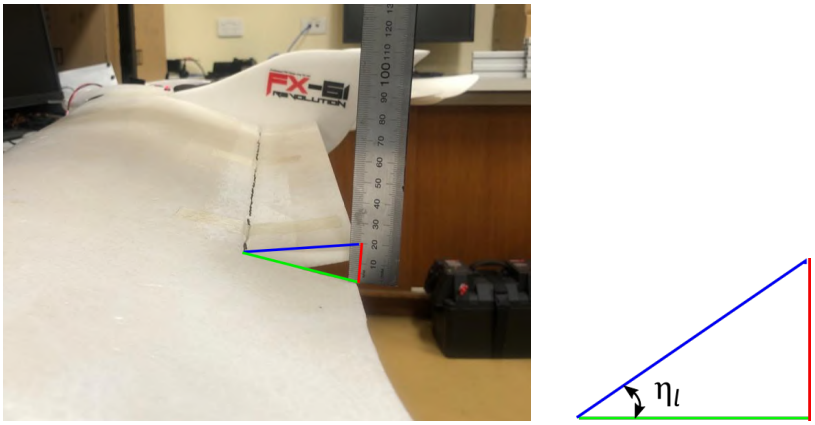
In simulation, only the actuator model for the articulated mass was considered. The servo was modelled as a first-order system which accounts for time lag. For the articulated mass servo, the Turnigy TGY-4409MD, a time lag of $\approx 20\, ms$ was introduced. The angular deflection rate and angular deflection

are the outputs of the actuator model. While the servo is only capable of moving at rates less than 460 °/s, the maximum/minimum rotation angles of the servos were limited by the maximum/minimum deflection angles of the articulated mass (see Table 7.5). The actuator model assumes the control effector is firmly connected to the servo arm with no deformation, ($\theta_{arm} = \theta_T = \psi_T$). The transfer functions of the angular deflection rate and angle deflection output from the actuators are:

$$\dot{\theta}_T, \dot{\psi}_T = \frac{50\ s}{s+50}, \quad \theta, \psi_T = \frac{50\ s}{s+50} \tag{7.2}$$

7.3.3 Control Effector Deflection Angles Calibration

The control effectors used here were the same as in Section 5.2.3 of Chapter 5. With regard to the deflection angle of the aerosurfaces and articulated mass, the sensors on the Pixhawk were unable to directly detect the deflection angles. In fact, the pulse width modulation (PWM) command values were the only ones that can be obtained. A specific calibration was thus used to find a relationship between servo signals and deflection angles. For the elevons, the approach was to measure the initial height between the wing surface and the elevon, the final height between them after deflection, and estimate the angle using the difference in height. Figure 7.6 shows the set-up for left elevon upward deflection calibration for instance. Since the lengths of all the sides of the triangle are known, the deflection angle can be estimated using Pythagoras theorem.



(a) (b)

Figure 7.6: Set-up for left elevon calibration: (**a**) Upward deflection (**b**) Deflection angle estimation.

The elevator and aileron deflections were then calculated using the relationship presented in Section 5.2.3 of Chapter 5, and the corresponding PWM signal value was read in mission planner software.

For the articulated mass, three longitudinal deflection positions were considered in flight as neutral, intermediate and maximum deflections as shown in Figures 7.7a, 7.7b and 7.7c, respectively. The intermediate deflection is the mid-point between the neutral and maximum deflection. Three lateral deflection positions in flight were considered as well, neutral, left and right deflections shown in Figures 7.8a, 7.8b and 7.8c, respectively.

The deflection angle was measured, and the corresponding PWM signal value was read in mission planner software.



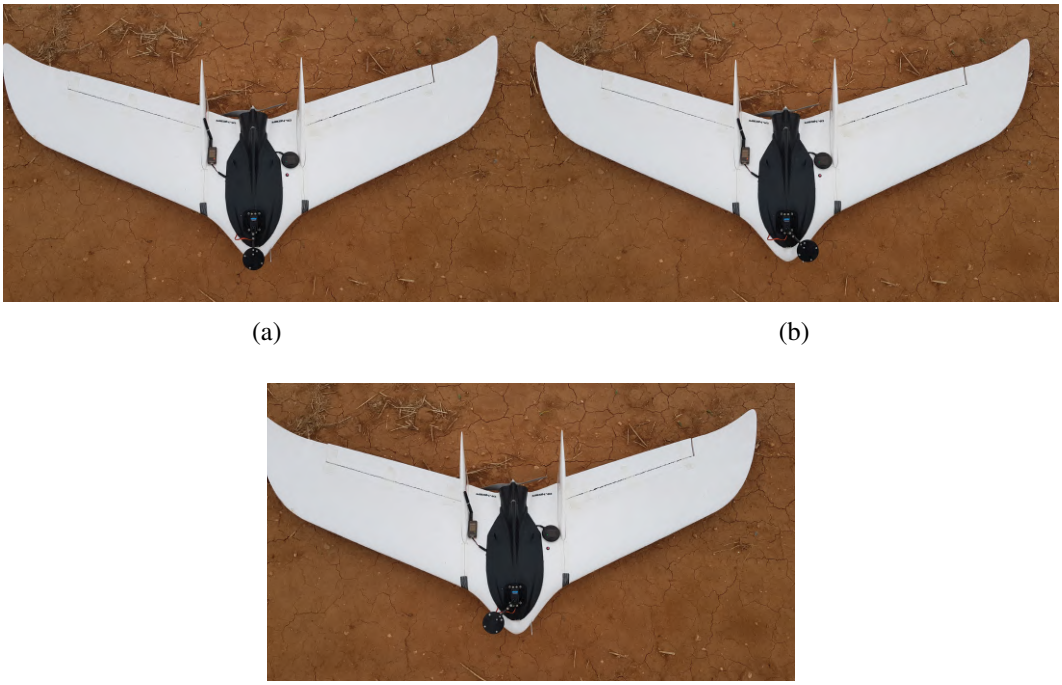
(a) (b)



(c)

Figure 7.7: Articulated mass positions in longitudinal flight: (**a**) Neutral. (**b**) Intermediate. (**c**) Maximum.

The estimated limits of deflection for the elevator, aileron and articulated mass are presented in Table 7.5.



(a) (b)

(c)

Figure 7.8: Articulated mass positions in lateral-directional flight: (**a**) Neutral (**b**) Left. (**c**) Right.

Table 7.5: Physical constraints of control effectors.

Limitations
$-11^\circ \leq \delta_e \leq 11^\circ$
$-11^\circ \leq \delta_a \leq 11^\circ$
$0^\circ \leq \theta_T \leq 80^\circ$
$-40^\circ \leq \psi_T \leq 40^\circ$

7.4 Flight Testing Procedure

This section discusses the details of the flight testing process. Flight testing of the Phantom FX-61 UAV transpired in January 2022. The flight test location was Mallala, located about 58 km north of Adelaide, South Australia.

Manual flight testing of the aircraft was carried out using a radio transmitter to control the aircraft from the ground. Before commencing the flight, trim conditions and control calibration was accomplished in manual flight. Trim conditions were influenced by ambient conditions as well as the effective load and centre of gravity (weight and balance). During manual flight, adjustments were made to the aerodynamic control surfaces (elevons) and engine thrust for trimming the UAV for steady-state level

flight. To isolate the effects of articulating the mass in flight, the aerosurface deflections were either zero or constant throughout the deflection procedure of the articulated mass.

7.5 Model Comparison with Flight Data

In the comparison of simulation to flight test, manoeuvres were extracted from flight test data. To reduce the noise in the raw flight data, the Gaussian filter in MATLAB was applied with a filter time constant of 50 s samples, to smooth the raw data. Figures 7.9 shows an example of raw flight data for pitch rate q.

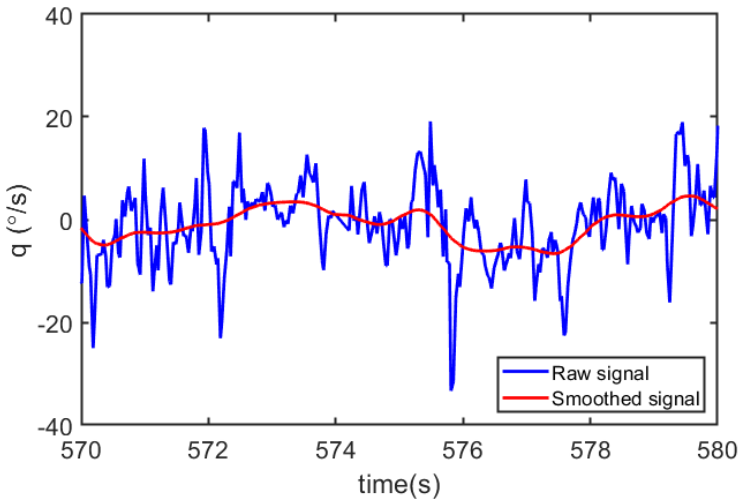


Figure 7.9: Flight data signal processing showing the raw flight data and smoothed data.

For both lateral and longitudinal flights, the simulation model was first trimmed. Then, only the corresponding inputs of mass articulation from the flight tests were fed into the simulation model. The simulated and flight test results were then compared. Two flight tests were carried out as follows:

Flight 1–Articulated mass in longitudinal flight.

Flight 2–Articulated mass in lateral flight.

The physical properties of the theoretical aircraft model from XFLR5 used in simulation for the different flights are provided in Table 7.6. The displacement values are relative to the nose of the aircraft.

Table 7.6: Physical properties of physical model for simulation.

Parameter	Flight 1	Flight 2
$m^B\ (kg)$	1.31	
$m^T\ (kg)$	0.101	
l_T (m)	0.065	
$ARP\ (m)$	[0.25; 0; 0]	
$cg_b^B\ (m)$	[0.297; 0; -0.004]	[0.298; 0; -0.004]
$j_b^B\ (m)$	[0.085; 0; -0.05]	[0.085; 0; -0.03]
${I_{xx}}_b^B\ (kg.m^2)$	0.126	0.126
${I_{yy}}_b^B\ (kg.m^2)$	0.0183	0.017
${I_{zz}}_b^B\ (kg.m^2)$	0.145	0.143
${I_{xz}}_b^B\ (kg.m^2)$	-0.00026	-0.00025

7.5.1 Flight 1 – Articulated Mass in Longitudinal Flight

The comparisons between simulation and flight test data of the effect of longitudinal appendage motion are shown in Figure 7.10.

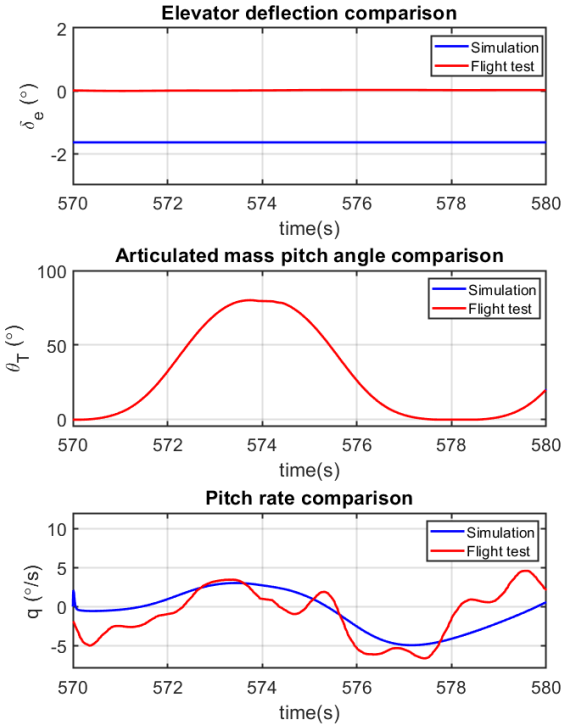


Figure 7.10: Comparison of simulation and flight log data of the elevator δ_e, articulated mass pitch angle θ_T, pitch rate q

7.5.2 Flight 2 – Articulated Mass in Lateral-directional Flight

The effects of articulating the mass in the lateral axis are shown in Figure 7.11.

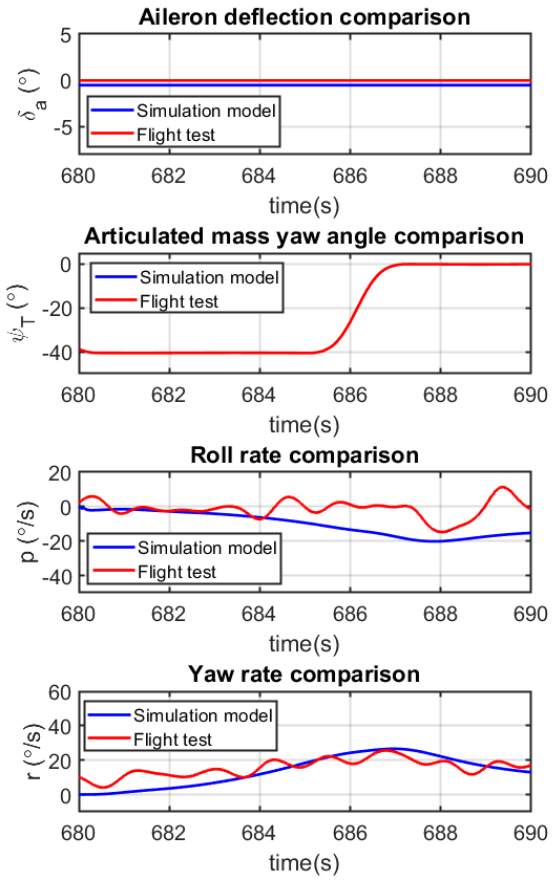


Figure 7.11: Comparison of simulation and flight log data of the aileron δ_a, articulated mass yaw angle ψ_T, roll rate p, and yaw rate r

7.6 Discussion

Since this project's goal was to examine the effects of articulating a mass in flight, it is more important that the model behaves qualitatively correctly, rather than it predicting the magnitudes accurately. However, satisfying both conditions is desirable. The model was considered to be satisfactory if the direction of rates matched the measured data and the magnitudes of the peak values were not significantly off.

The first thing that can be observed is that there is general agreement in the magnitude of effects between the simulation model and the flight test data in terms of the trend and given the limits of models, environment and instrumentation. For the pitch rate, compared to the flight test data, the simulation generally underpredicted the effects of the appendage movement, reflected as a peak and trough region (see Figure 7.10). In the peak region, the mean and peak values in the simulation were respectively 11.54% and 12.14% less than in the flight test. However, for the roll and yaw rates, the simulation tended to over-predict the effects of the appendage movement, reflected as a trough and peak region, respectively (see Figure 7.11). For roll rate and in the trough region, the mean and peak values in the simulation were respectively 51.87% and 36.48% more than in the flight test. For yaw rate and in the peak region, the mean and peak values in the simulation were respectively 18.22% and 23.89% more than in the flight test.

Although the articulated mass was only $\approx 7\%$ of the total body mass, one can see from Figures 7.10 and 7.11, that articulation of the mass in flight resulted in changes in body rates and by extension, the orientation of the aircraft.

For longitudinal appendage motion shown in Figure 7.10, the upward deflection of the mass resulted in an increase in pitch rate q and by extension, the pitch angle, θ. This is due to backward shift in the overall cg of the aircraft, which causes the aircraft to pitch up. Also, during the actuation process, the elevator control remained untouched.

The results presented in Figure 7.11 for the lateral appendage motion show that the lateral articulation of the mass (change in articulated mass yaw angle from it's lower limit to neutral position) in flight resulted in changes in the roll and yaw rates, p and r, respectively. Specifically, it resulted in a decrease in roll rate p, and increase in yaw rate r. During the mass articulation, the aileron input value was constant, showing that there was no additional aileron input provided. These changes in rates can also be extended to mean a change in roll and yaw angles, ϕ and ψ, as only then can changes be observed in the rates.

The true servomotor dynamics was somewhat unknown, since there was no feedback channel. A full implementation could make software changes to the Pixhawk flight controller to log the position of the appendage using a rotary actuator (for example a potentiometer). Observations of the weight in motion on the ground showed clear motion artefacts including shuddering related to the controller

inside the servomotor. The servomotor was not a high quality unit, and was certainly not designed to swing weights on long arms against no resistance. We do not know, for example, if the servo motor was oscillating the weight in flight, effecting the entire aircraft, since there are indications of this. However, the experiment was a success, because the resources of the Pixhawk and all of the software tools worked with the solution and allowed analysis. The next logical step is to create control algorithms on the Pixhawk to undertake control using modern methods. The ecosystem of tools surrounding Pixhawk makes this a reasonable near term research goal.

Noise or vibration was present in all of the measurements, particularly on the yaw and roll axes. This appears to be caused by movement of the autopilot itself, but there are many other possibilities caused by this unique configuration. For example, the mass of the appendage might be interacting with the hatch cover to press on the Pixhawk, the servo might be stressing the power supply of the Phantom, causing sensors to be unreliable and to follow oscillations in the servomotor power use, the servomotor controller could be unstable and oscillating the entire aircraft, or combinations of these. Otherwise, the appendage motion functionality was achieved without difficulty and with no software changes needed.

Overall, the results demonstrate the effectiveness of mass articulation in longitudinal and lateral flight. In addition, the model dynamics as well as its global behaviour were coherent with the experimental data. However, they do not match exactly for various reasons. (1) The assumption was that the aircraft was initialised from trim during simulations, but in reality, especially with manual flight, the aircraft will be in a transient state, resulting in a mismatch in initial state between the model and flight test data. (2) Gust disturbances acting on the UAV during flight were not measured or simulated. So the response of the UAV due to gusts cannot be predicted.

This feasibility study aims to inform the choices of future studies that will be able to compare the energetics of biomimetic mass shift control vs. aerodynamic control.

7.7 Summary

Both a simulation model and experimental platform were designed and compared to allow the development of a testbed on which multibody dynamics and modern control methods can be tested. The

results obtained from flight test and simulation were similar and comparable in effects. The capability for practical experimental multibody flight control was successfully developed.

Chapter 8

Aerodynamic Loading Effects on the Appendage

The aerodynamic effects of the abdomen appendage was previously ignored for the DISWA based on the assumption that the abdomen's dynamic effects dominated in comparison with its aerodynamic effects, and compared to the aerodynamic effects of the head/thorax/wings combination. However, appendages in insects, exist in various shapes and sizes, which affect the level of both the inertial and aerodynamic contribution to the overall system. This chapter investigates the effects of the individual dynamic/inertial and aerodynamic contributions of appendages in insect forward flight performance and manoeuvrability, hence the simplified mathematical model of the DISWA with a deflectable abdomen (Model 2) was revisited and modified to include the aerodynamic effects of the abdomen. The comparative analysis evaluated how significantly these effects affect the steady flight and manoeuvre performance of the DISWA in the longitudinal and lateral axis, and also investigated the effects of other variables such as increased abdominal area and angular rate of deflection.

8.1 Introduction

The range of body sizes and shapes of flying insects are so diverse, with body lengths spanning six orders of magnitude. For instance, the body length of fairy wasps (*Dicopomorpha echmepterygis*) is approximately 0.13 mm [254], while that of extinct massive protodonates is estimated to be around 350 mm. There is also a considerable amount of variation in the body shape of flying insects, just as there is in body size. For example, dragonfly and damselfly abdomens are elongated, while flying

beetle bodies are stout. The mechanisms of appendage movement in flying systems can be classified based on the operation by way of inertia and operation based on aerodynamic torque [255]. Depending on the mass, size and shape of the appendage, the contributions of either of these mechanisms to the overall system vary, hence, the significance of these contributions comes into question. This can be addressed by including the aerodynamic loading of the appendage in the mathematical model, which also enables the design and optimisation of the shape and weights of appendages in the design of biomimetic aircraft.

Using the DISWA model with a deflectable abdomen (Model 2), the aerodynamic contribution from the abdomen was included to investigate its effect on steady cruise flight and pull up manoeuvre performance. The effectiveness associated with abdominal deflection for manoeuvring is also evaluated, specifically how some physical and kinematic properties of the abdomen affect the manoeuvre effectiveness. Three distinct models used throughout this chapter are defined as follows: (1) The simplified or "inertia" model, which includes only the dynamic/inertial effects of the deflectable abdomen, (2) A modified or "inertia + aero" model, which includes the inertial and aerodynamic effects of the deflectable abdomen, and (3) The modified model with twice the nominal abdominal area, which is equivalent to increasing the effective area (aerodynamic contribution) of the abdomen without a weight penalty.

This chapter aims to address the following research question:

1. What are the effects of appendage movements in forward flight, considering the combined aerodynamic and dynamic/inertial effects?

8.2 Aerodynamic Loading of Abdomen

Recall that our model assumes that the aerodynamic contributions of the dragonfly's body and tail are independent and additive. The elongated abdomen of the dragonfly and the DISWA is comparable to thin long cylinders. It is also assumed that compared to the drag, the lift force produced by the abdomen is negligible [256]. The drag force of a cylinder inclined at an angle μ to the airflow V, can be decomposed into the normal F_{N_D} and tangential F_{T_D} directions as shown in Figure 8.1.

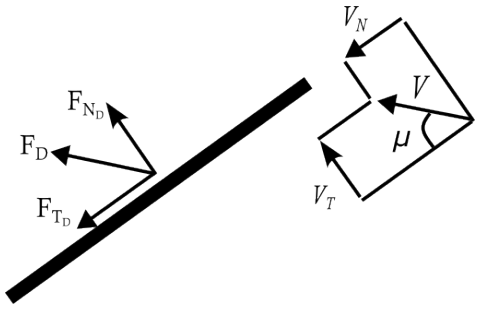


Figure 8.1: Inclined cylindrical bar in a flow.

These forces can be derived from Equation 8.1 [256]

$$F_{N_D} = \frac{C_N}{2}\rho V_N^2 S_{ref}, \quad F_{T_D} = \frac{C_T}{2}\rho V_T^2 S_{ref} \tag{8.1}$$

where V_N and V_T are the normal and tangential component of the velocity V, respectively. The S_{ref} used is the projected plan area of the body, equal to the product of body diameter, (d_t) and length (l_t).

Therefore, the aerodynamic drag is estimated in terms of normal and tangential forces. The resolved coefficients C_N and C_T both vary with Reynolds number and the global approximation model of these coefficients is given by Ellington [256]. The estimation of Re is based on the length of the abdomen. The normal drag coefficient C'_N of very (infinitely) long cylinders is given by [256]

$$C'_N = 1.1 + 22/Re \tag{8.2}$$

where the Re, is based on the length of the cylinder, l_t. For cylinders with finite length, the normal drag coefficient is given by [256]

$$C_N/C'_N = 0.57 + 0.34e^{-7.6d_t/l_t} \tag{8.3}$$

The results using the conceptual DISWA with $(l_t/d_t = 8)$ for local airspeeds ranging from 5 to 15m/s results in $Re = 10^5$. Figure 8.2 shows the variation in drag coefficient as a function of Re for a circular cylinder [257]. C_D decreases monotonically from high values for low Re to near one at Re $\approx$ 300,000. At this point, the C_D suddenly drops from around 1 to around 0.3, a phenomenon known as the drag

crisis. After that, C_D returns to around 0.6 for Re = 10^7.

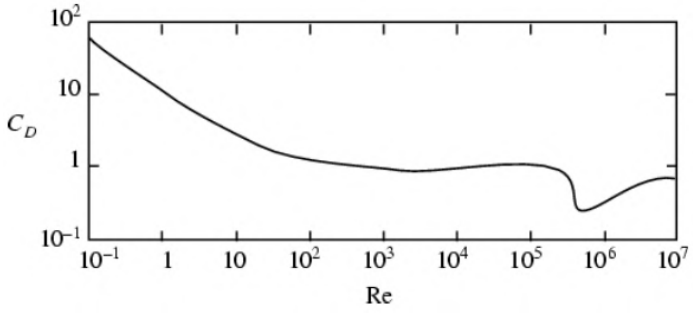


Figure 8.2: Variation of cylinder drag coefficient with Reynolds number [257].

In this study, it is assumed that the drag coefficient across the range of Reynolds numbers tested is fairly constant and is solely dependent on the inclination angle relative to the airflow (see Figure 8.1). For an inclined cylinder, the effect of the inclination angle can be represented by revising Equation 8.1 as [258]

$$F_{N_D} = \frac{C_N}{2}\rho S_{ref} V^2 sin^2(\mu), \quad F_{T_D} = \frac{C_T}{2}\rho S_{ref} V^2 cos^2(\mu) \tag{8.4}$$

However, research has shown that the classic decomposition in Equation 8.4 does not match experimental data very well, particularly for small angles of attack [258]. Hence, the load function method is a more practical approach, in which [258]

$$F_{N_D} = 0.5\rho S_{ref} V_N^2 f_N(\mu), \quad F_{T_D} = 0.5\rho S_{ref} V_T^2 f_T(\mu) \tag{8.5}$$

Lift and drag coefficients are related to the normal and tangential coefficients by [59]

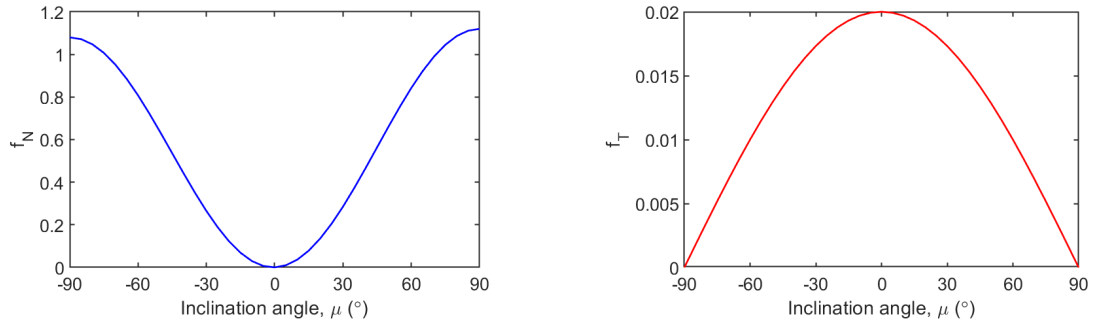
$$\begin{bmatrix} C_L \\ C_D \end{bmatrix} = \begin{bmatrix} c\,\mu & -s\,\mu \\ s\,\mu & c\mu \end{bmatrix} \begin{bmatrix} C_N \\ C_T \end{bmatrix} \tag{8.6}$$

Therefore, considering the lift and drag coefficients of a cylinder originally given by Hoerner [206], the approximation of load functions $f_N(\mu)$ and $f_T(\mu)$ in [258] are used

$$f_N(\mu) = 0.02\sin(\mu) + 1.1\sin^4(\mu) + 1.1\sin^2(\mu)\cos^2(\mu) \tag{8.7}$$

$$f_T(\mu) = 0.02\cos(\mu) \tag{8.8}$$

The resulting plots showing the variation of load functions with inclination angle are shown in Figure 8.3. Note that the angle is in degrees.



(a) Variation of normal drag load function with inclination angle.

(b) Variation of tangential drag load function with inclination angle.

Figure 8.3: Variation of drag load functions with inclination angle.

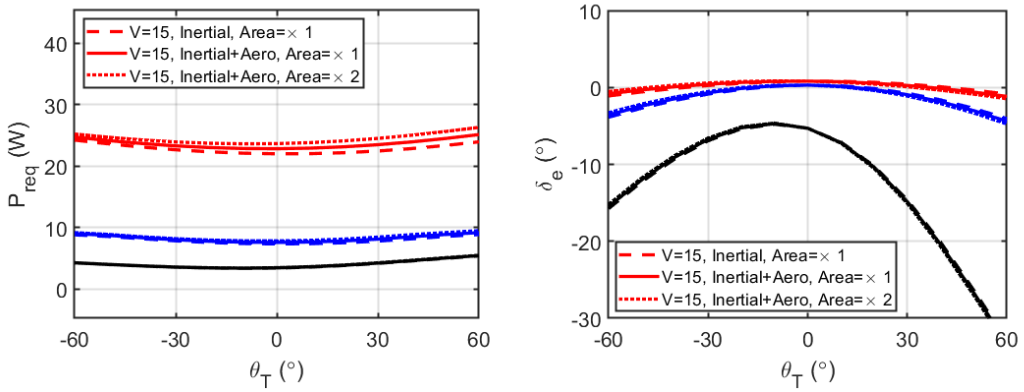
The aerodynamic torque due to the resulting drag of the abdomen is estimated by $[s_{tb}]^B \times [F_D]^B$. The inclination angle between the airflow and the local longitudinal axis is given by the abdomen effective angle of attack α_T and is obtained as $\alpha_T = \theta + \theta_T - \text{atan}\frac{[V_{T_z}^I]^T}{[V_{T_x}^I]^T}$. Because of the symmetry of the cylinder, the same estimation will be used for the inclination angle between the airflow and the local lateral axis, the effective sideslip angle β_T, which is obtained similarly to the abdomen effective angle of attack.

8.3 Performance Analysis

8.3.1 Steady Cruise Flight

As mentioned earlier, the abdomens of insects come in different shapes and sizes, factors that contribute to the aerodynamic and inertial effects of the abdomen. The performance analysis carried out in this section focused on steady cruise, where the effect of including the abdominal aerodynamic loading and

increasing the abdominal area at various cruise speeds was investigated. The abdominal pitch angle was varied (from -60 ° to 60 °) while trimming the aircraft using the elevator for three cruise speeds, 5, 10 and 15 m/s, at a height of ($H_0 = 100m$). The analysis compared results from the simplified model, the modified model, and the modified model with twice the nominal abdominal area. The performance metrics used were the power required and the control effort from the elevator. The specifications of the conceptual DISWA listed in Tables 5.1, 5.3 and 5.2 still apply. The results for the power required, and elevator deflection are shown in Figures 8.4a and b, respectively.



(a) Power required vs. Abdominal pitch angle. (b) Elevator deflection vs. Abdominal pitch angle.

Figure 8.4: Steady cruise flight performance parameters variation with abdominal pitch angle. The black, blue and red lines represent results for V=5, 10 and 15 m/s, respectively.

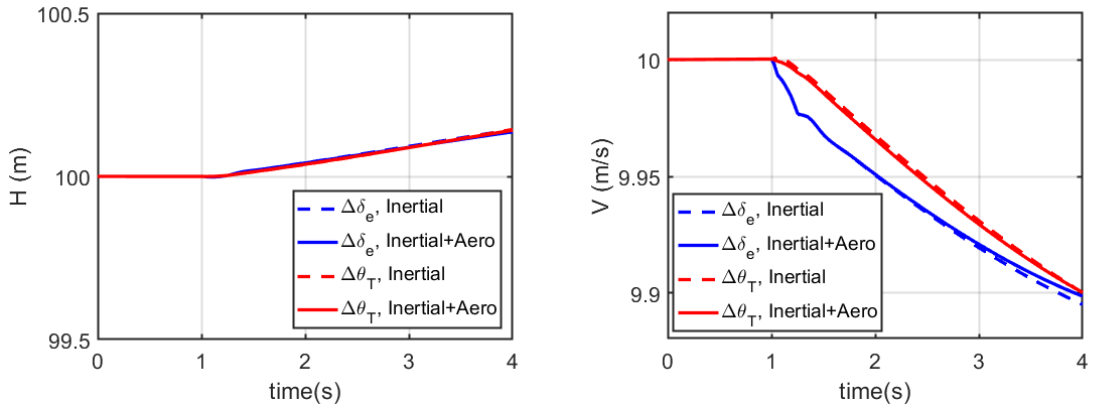
Table 8.1: Percentage average variation of steady cruise flight performance parameters compared to the simplified/inertial model

V (m/s)	Percentage average variation (%)			
	Power required		Elevator deflection	
	1×	2×	1×	2×
5	0.7667	1.5317	0.1656	0.3290
10	3.0853	6.1339	0.5732	1.2012
15	3.6385	7.2757	-3.2011	-6.9674

8.3.2 Quasi-steady Pull Up Manoeuvre

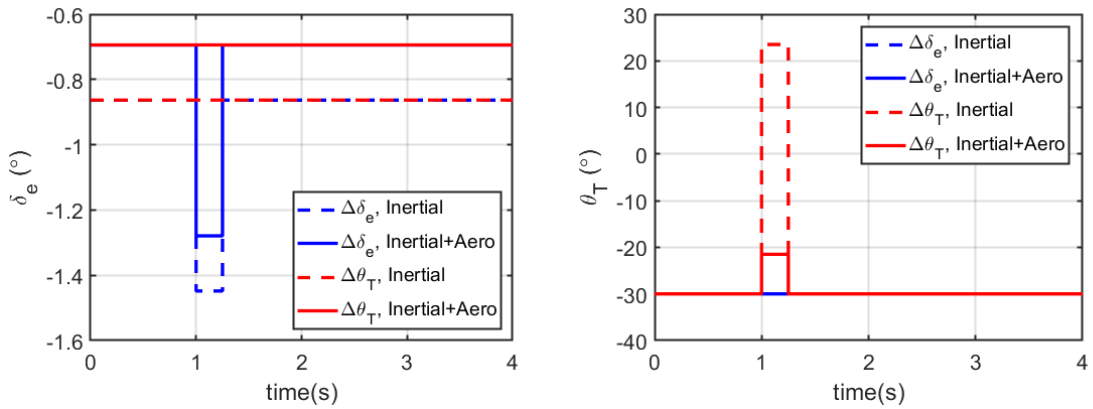
Similar to the analysis carried out in Section 5.2.7.4, an open loop fixed-thrust pull manoeuvre performance is analysed in this section. The manoeuvrability advantage in utilising either the elevator or abdominal deflection to initiate a manoeuvre from trimmed cruise flight was examined, using the simplified and modified models. The same energy-based performance metrics (specific energy and specific excess power) were used for comparison.

For a duration of four seconds, the pull up manoeuvre was initiated using a pulsed input signal (applied at t=+1 in the simulation for 0.25 s). The time history for airspeed and trajectory are shown in Figure 8.5, while the corresponding elevator deflection and abdominal pitch control inputs are shown in Figure 8.6, and specific excess power and specific energy as a function of time are shown in Figure 8.7. Table 8.2 summarises the average specific energy and power over 4 s, using the various models and control effector combinations.



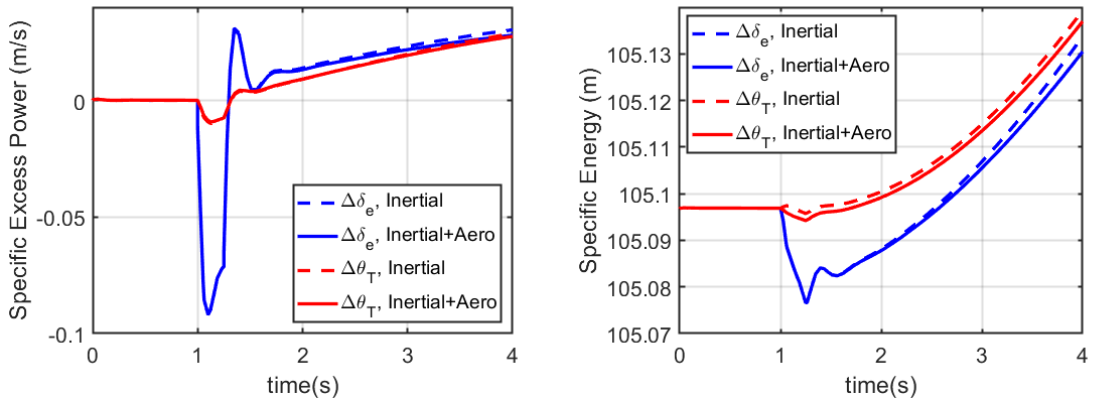
(a) (b)

Figure 8.5: Pull up manoeuvre states time response. (**a**) Airspeed. (**b**) Height.



(a) (b)

Figure 8.6: Pull up manoeuvre longitudinal control inputs time response. (**a**) Elevator deflection. (**b**) Abdominal pitch angle.



(a) (b)

Figure 8.7: Pull up manoeuvre energy state and rate time response. (**a**) Specific excess power. (**b**) Specific energy.

Table 8.2: Energy manoeuvrability comparison using $\Delta\delta_e$ or $\Delta\theta_T$.

Control effector and model used	**Average Specific Energy (m)**	**Average Specific Excess Power (m/s)**
$\Delta\delta_e$, Inertial	105.093	-0.014
$\Delta\theta_T$, Inertial	105.103	0.0043
$\Delta\delta_e$, Inertial + Aero	105.0927	-0.0138
$\Delta\theta_T$, Inertial + Aero	105.1015	0.0042

8.3.3 Discussion

In analysing the effect the inclusion of the abdominal aerodynamic load has on longitudinal performance, Figures 8.4a showed that the power required increased with increasing airspeed, while Figures 8.4b showed that the absolute values of elevator deflection angle required decreased with increasing airspeed.

From the summary presented in Table 8.1, including the aerodynamic loading on the abdomen, increased the average power required. In addition, the power required increased with increasing cruise speed, with the least increase of 0.77% recorded for V=5 m/s, and the highest increase of 3.64%, recorded for V=15m/s. The overall increase in power required was due to the introduced additional drag from the abdomen, increasing the total drag, hence the power and energy required consequentially. The elevator deflection angle initially increased in average value by 0.17% at V=5m/s but decreased by an average of 3.20% at V=15m/s.

Furthermore, increasing the abdominal area further increases the power required. Compared to the nominal abdominal area, an increase in area by a factor of 2 caused the average power required to increase by a minimum of 1.53% at V=5 m/s, and a maximum of 7.28% at V=15m/s. Therefore, aerodynamic effects become more significant as the area of the abdomen increases, especially at higher speed. This is because the drag force is directly proportional to the area, hence increasing the area of the abdomen increases the total drag force which causes an increase in power required in steady cruise flight. With twice the abdominal area, the elevator deflection angle initially increased in average value by 0.33% at V=5m/s but decreased by an average of 6.97% at V=15m/s. In addition, from Figures 8.4c, the least cruise speed of 5 m/s, required the highest absolute elevator deflection angles to trim, and the results for that particular cruise speed were only valid for abdominal pitch angles between -60° and 40°, where the lower limit of the elevator deflection angle of -20° was exceeded.

The specified pull up manoeuvre trajectory (Figure 8.5a) was achievable using the various models and control effector combinations considered. However, with the inclusion of the abdomen, the modified models required less control effort from the abdomen to initiate the manoeuvre from trim, compared to the simplified models (see Figure 8.6). It is worth noting that the abdomen already started off deflected and so reducing the deflection angle reduces the overall drag and the control effort required in return. With the modified model, the average specific excess power and energy reduced whether using the elevator or abdomen deflection, albeit by a minute amount (less than 0.001% on average). From the summary presented in Table 8.2, even with the inclusion of the aerodynamic loading of the abdomen, using the abdomen deflection still maintained a higher manoeuvre advantage as the average specific energy and excess power were higher than the aerosurface alternative.

8.4 Manoeuvring Using Abdominal Deflection

Manoeuvrability is very essential for survival in the insect world. Throughout missions, aircraft manoeuvre is one of the critical factors that determine its outcome. As opposed to steady flight conditions, manoeuvrability has to do with transient responses, hence, acceleration is an important component of manoeuvrability. Therefore, in flight, manoeuvrability can simply be described by the ability to change the magnitude of the velocity vector (acceleration or deceleration) and/or change in its attitude. For our investigation in this section, manoeuvrability is strictly related to enabling dynamic behaviours or initiating manoeuvres with the deflection of the abdomen from trimmed cruise flight with fixed thrust. It measures the open loop capabilities of the aircraft, hence, the objective is quickness and the quicker, the better. To ensure consistency in the abdominal deflection motion, we defined a linear segment with parabolic blends (LSPD) for the trajectory, a simple trapezoidal profile for velocity and polynomial segments for acceleration and deceleration. The *lspb* function in the Robotics toolbox in MATLAB was used to generate the LSPD trajectories such that it chooses the velocity of the linear segment. Figure 8.8 below shows an example of a 0° to 1° deflection, with the velocity and acceleration profile generated using the *lspd* function in MATLAB. In the sections that follow, the effects of the aerodynamic load of the abdomen, increased abdominal area and different abdominal angular velocities on effectiveness are analysed in both longitudinal and lateral axes.

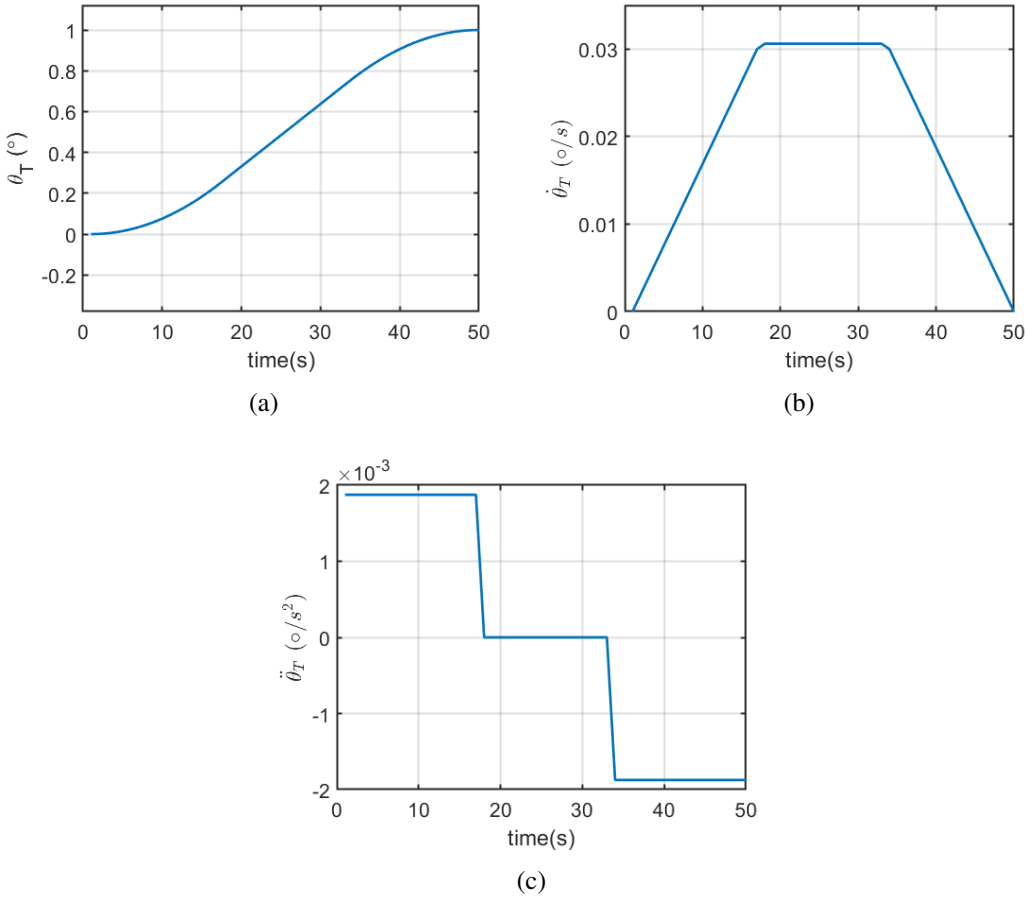


Figure 8.8: Linear segment with parabolic blend (LSPB): (**a**) Angular deflection. (**b**) Angular velocity. (**b**) Angular acceleration.

8.4.1 Manoeuvring Using Longitudinal Abdominal Deflection

This section uses comparative analysis to investigate the various factors that affect the manoeuvrability due deflection of the abdomen along the longitudinal axis (as in Figure 4.2). The metric used to quantify effectiveness is the maximum achievable rate of change in velocity and/or attitude over a specific time period. The longitudinal aerosurface (elevator) was not at any point used for initiating a manoeuvre from trim.

8.4.1.1 Effect of Increased Abdominal Area on Longitudinal Manoeuvring

The effects of including the aerodynamic loading of the abdomen and increasing the abdominal area on the effectiveness for longitudinal manoeuvring are the subject of investigation in this section. The aircraft was trimmed to a steady cruise flight of V=10m/s and a height H=100m/s. Then, the abdomen was deflected upwards from 0 to -10 ° using a pre-defined velocity profile. The analysis compared three

models; the simplified model, the modified model and the modified model with twice (2×) the nominal abdominal area. Only the first 3 s after initiation of the manoeuvre with the abdomen are presented below in Figures 8.9 and 8.10, while Table 8.3 shows the percentage average variations compared to the simplified model with nominal abdominal area.

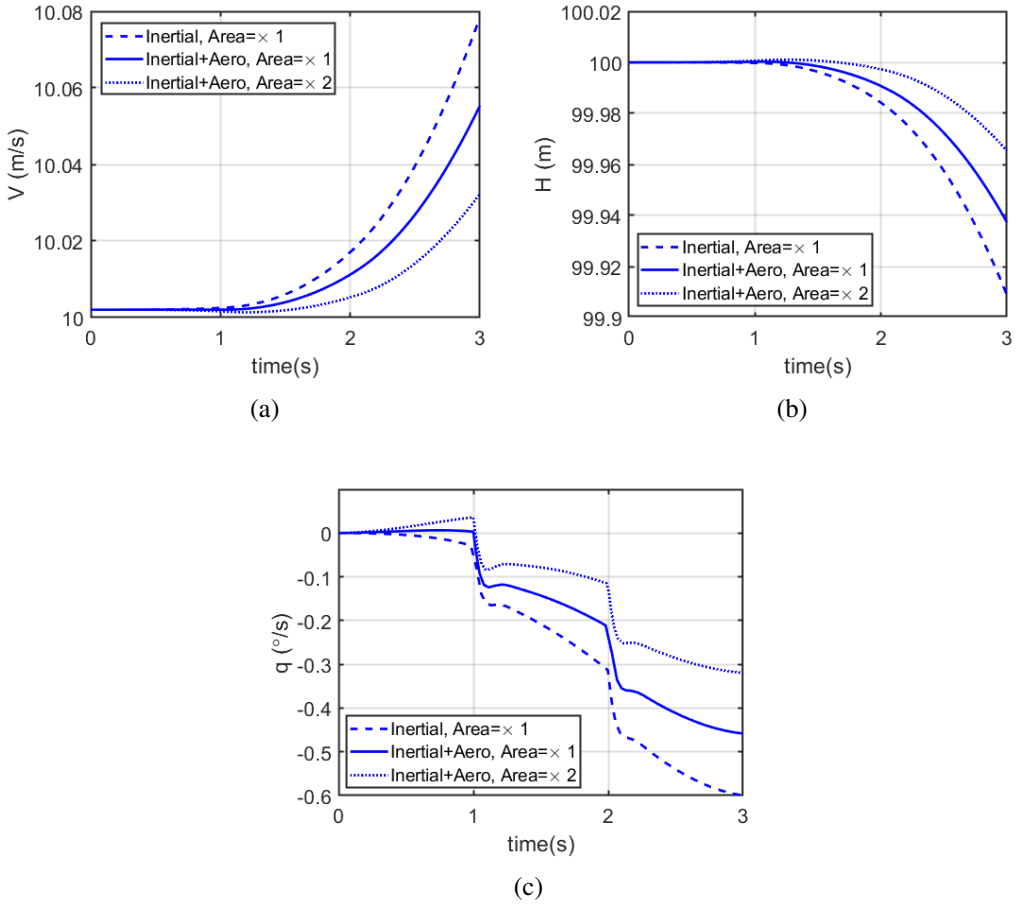


Figure 8.9: Time history comparing the longitudinal states: (**a**) Velocity. (**b**) Height. (**c**) Pitch rate.

Table 8.3: Percentage average variation compared to the simplified model with nominal abdominal area

	Percentage average variation (%)		
Modified model	**Velocity**	**Height**	**Pitch rate**
Area × 1	-5.5190×10^{-2}	6.4369×10^{-3}	-3.0245×10^{1}
Area × 2	-1.0675×10^{-1}	1.2404×10^{-2}	-5.6702×10^{1}

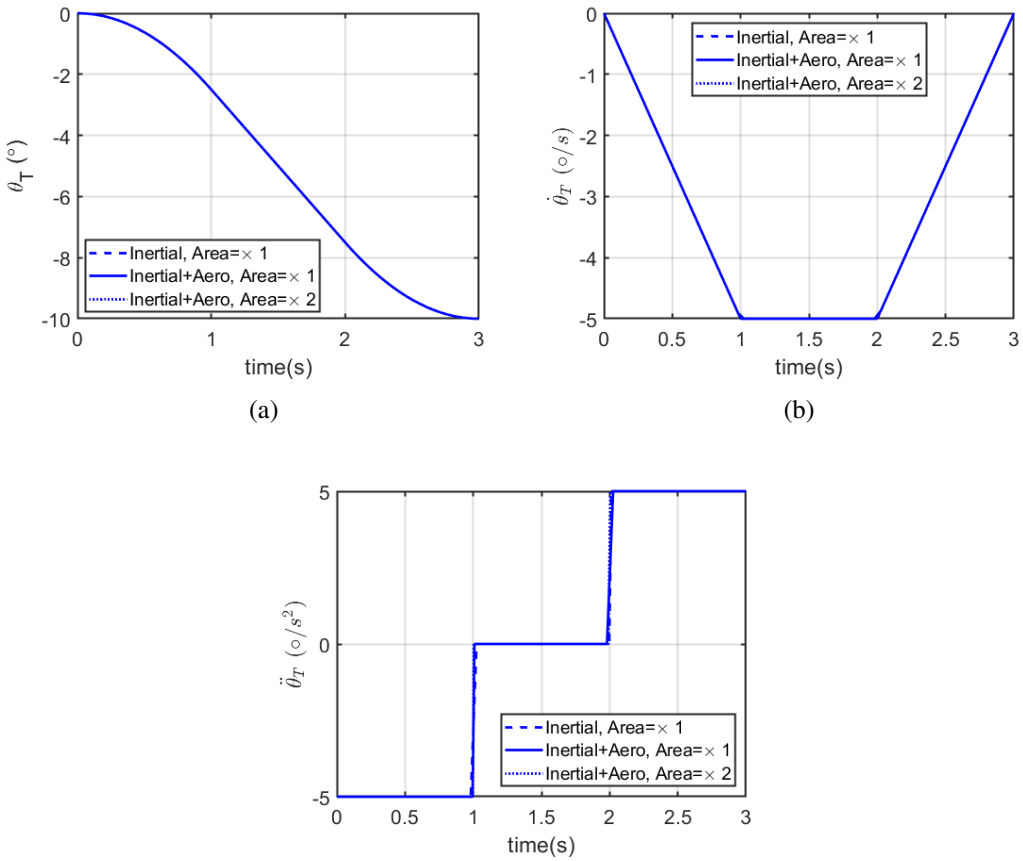


Figure 8.10: Time history of control inputs for longitudinal manoeuvre: Abdominal pitch angle, abdominal pitch rate and abdominal pitch acceleration.

8.4.1.2 Effect of Abdominal Angular Speed on Longitudinal Manoeuvring

Another factor that influences effectiveness is the angular velocity of the abdomen. In this section, using the modified model, we investigate the effect of abdominal pitch rate on effectiveness for longitudinal manoeuvring. The aircraft was trimmed to steady cruise flight of V=10m/s and a height H=100m/s. Then, for three abdominal pitch rates, defined by velocity profiles, an upward deflection of the abdomen from 0 to -10 ° was initiated and was classed as either fast, average or slow. The fast was set to be deflected from 0 to -10 ° in 3 s, while the average and slow were set to be deflected in 5 s and 10 s, respectively. The first 3 s after initiation of the manoeuvre with the abdomen are presented in Figures 8.11 and 8.13 below.

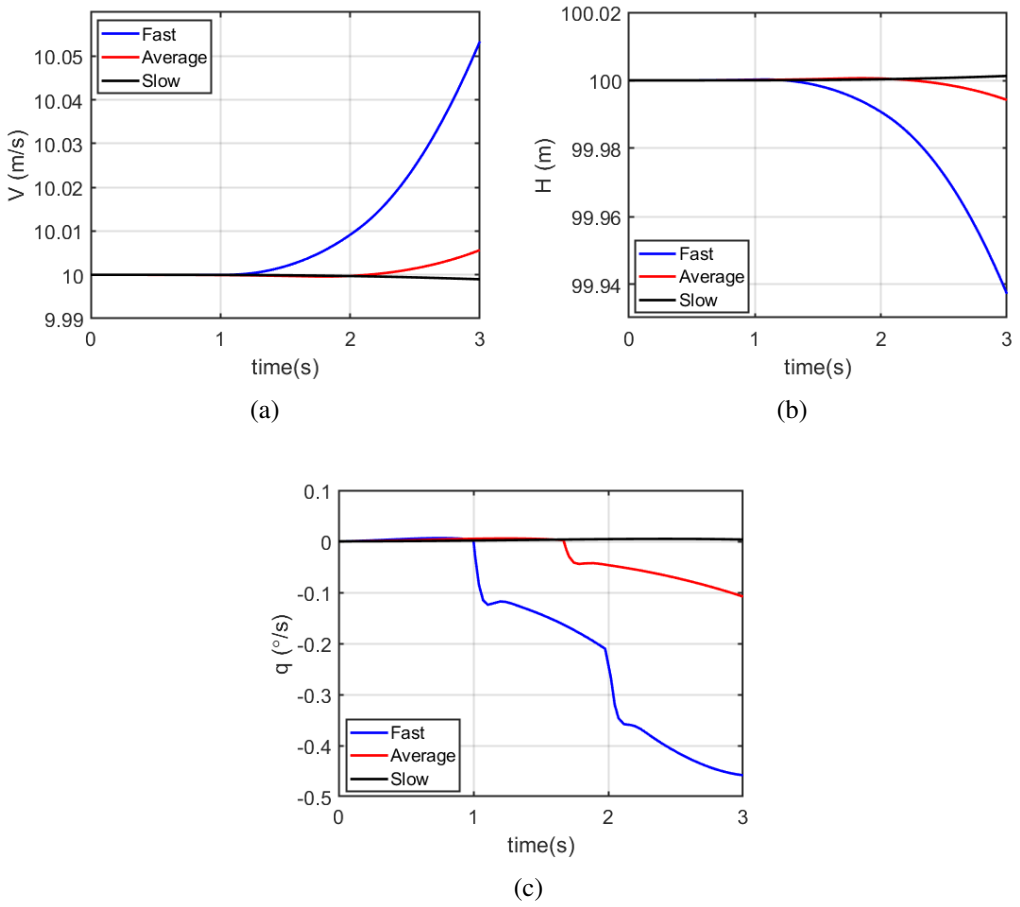


Figure 8.11: Time history comparison of the longitudinal states due to abdominal pitch rate: (**a**) Velocity. (**b**) Height. (**c**) Pitch rate.

Figure 8.12: The forces on an aircraft in flight.

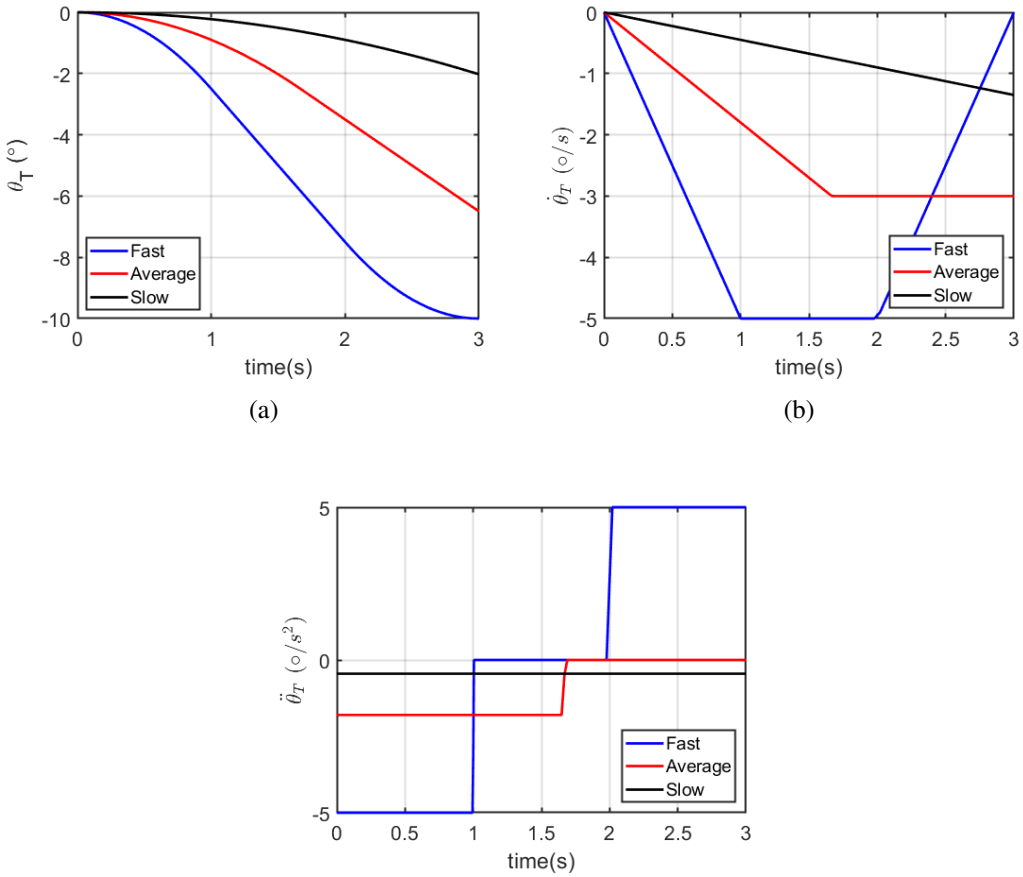


Figure 8.13: Time history of control inputs for longitudinal manoeuvre: Abdominal pitch angle, abdominal pitch rate and abdominal pitch acceleration.

8.4.1.3 Discussion

The time history of the longitudinal states in Figures 8.9 and 8.11, show that the upward deflection of the abdomen from steady cruise initiates a dive manoeuvre. Of the three models in Figure 8.9 and using the same deflection rate, the simplified model was the most effective with the maximum average acceleration and absolute pitch rate after 3 s. Considering the percentage average variations summarised in Table 8.3, the inclusion of aerodynamic effects of the abdomen reduced manoeuvre effectiveness for acceleration and rate of pitch by about 0.06% and 30.26%, respectively, however, the effectiveness was further reduced by about 0.11% and 56.70%, respectively using twice the abdominal area. The reduction in effectiveness experienced is due to the additional drag from the abdomen, which increases with the area.

From Figures 8.11, increasing the deflection rate of the abdomen increases dive manoeuvre performance, and thus effectiveness. At the 3 s time mark, the abdomen with the fastest deflection rate achieved the maximum average acceleration and absolute pitch rate, followed by the average and then the slow abdominal deflection rate.

8.4.2 Manoeuvring Using Lateral Abdominal Deflection

This section uses comparative analysis to investigate the various factors that affect the manoeuvrability due to the deflection of the abdomen along the lateral axis (as in Figure 4.3). The metric used to quantify effectiveness is the maximum achievable rate of change in velocity and/or attitude over a specific time period. The aerosurfaces (left and right elevons) were not at any point used to initiate the manoeuvre from trim.

8.4.2.1 Effect of Increased Abdominal Area on Lateral Manoeuvring

This investigation examined the effect of abdominal area on lateral manoeuvring effectiveness. The aircraft was first trimmed to a steady cruise flight of V=10m/s and height H=100m/s. Then, the abdomen was deflected rightward from 0 to -5 ° at the same rate. The results from the simplified model, modified model and modified model with twice the abdominal area were compared. The trajectories, time histories for lateral-directional states and control inputs are shown in figures 8.14, 8.15 and 8.16, respectively.

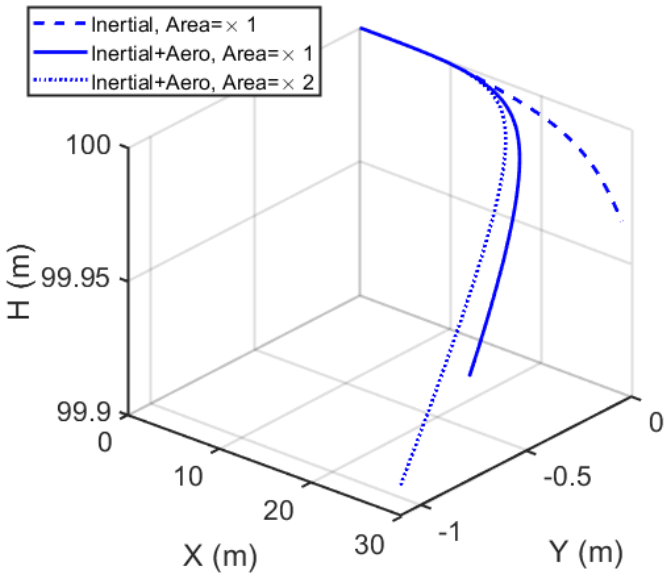


Figure 8.14: Flight trajectories.

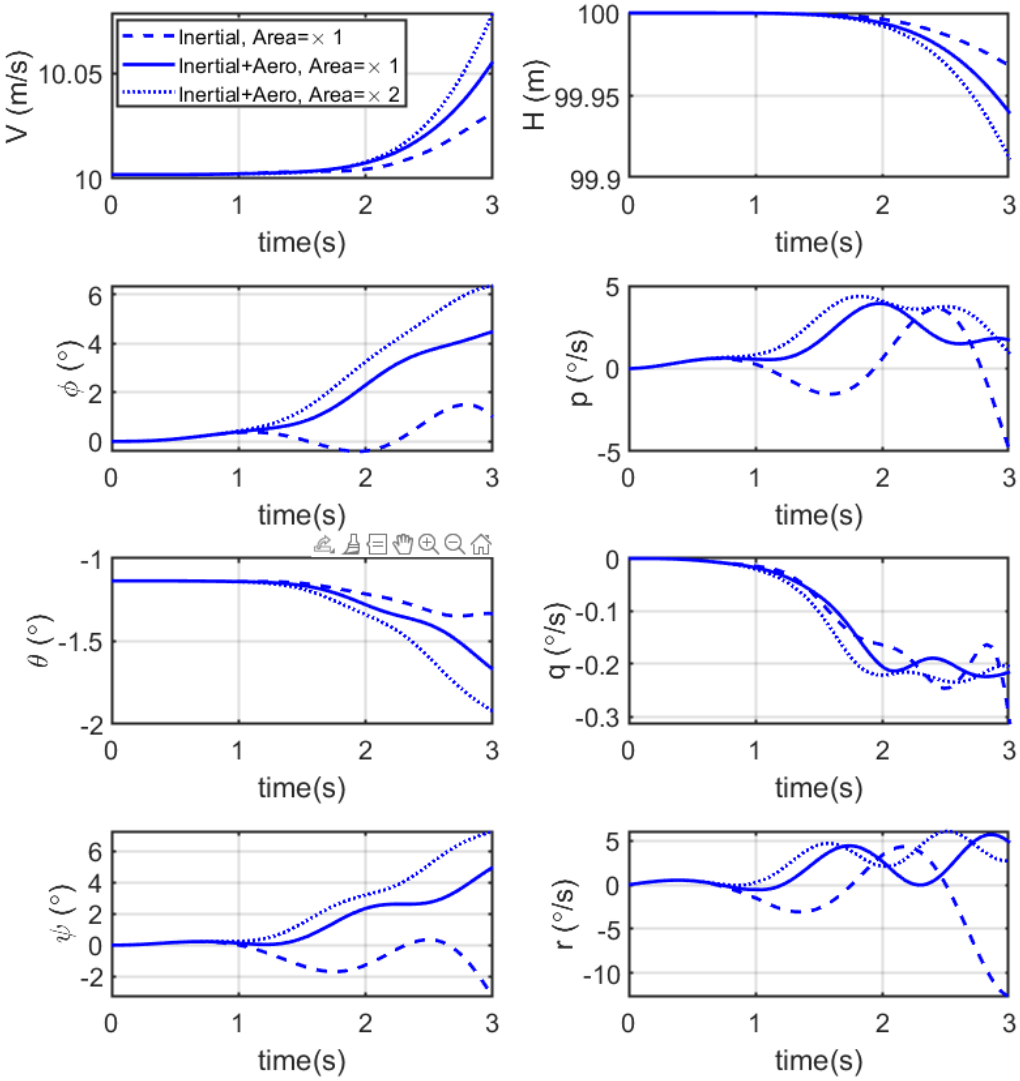


Figure 8.15: Time response comparison of the lateral-directional states: Velocity and height, roll angle and roll rate, pitch angle and pitch rate, yaw angle and yaw rate.

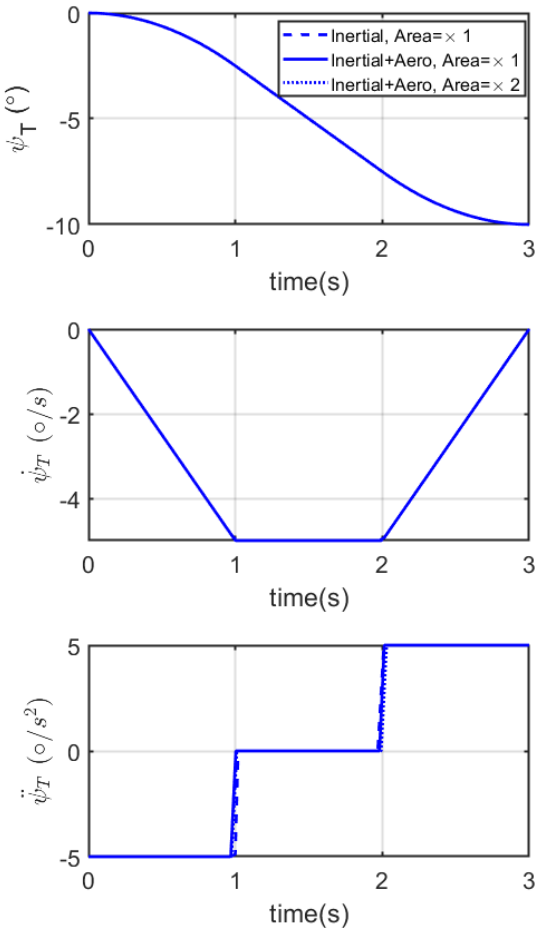


Figure 8.16: Time history of control inputs for lateral-directional manoeuvre: Abdominal yaw angle, abdominal yaw rate, abdominal yaw acceleration.

8.4.2.2 Effect of Abdominal Angular Speed on Lateral Manoeuvring

To investigate the effect of the abdominal yaw rate on the effectiveness for lateral manoeuvring, the aircraft was trimmed to steady cruise flight of V=10m/s and a height H=100m/s. Then, for three abdominal yaw rates, the abdomen was deflected along the lateral axis and compared for effectiveness. The velocity profiles were defined to represent a rightward deflection of the abdomen, that is, from 0 to -5 ° and were classed under fast, average and slow. The fast was set to be deflected in 3 s, while the average and slow were set to be achieved in 5 and 10s, respectively. The trajectories, time histories for lateral-directional states, and control inputs for the first 3 s after initiation of the manoeuvre with the abdomen are presented in Figures 8.17, 8.18 and 8.19, respectively.

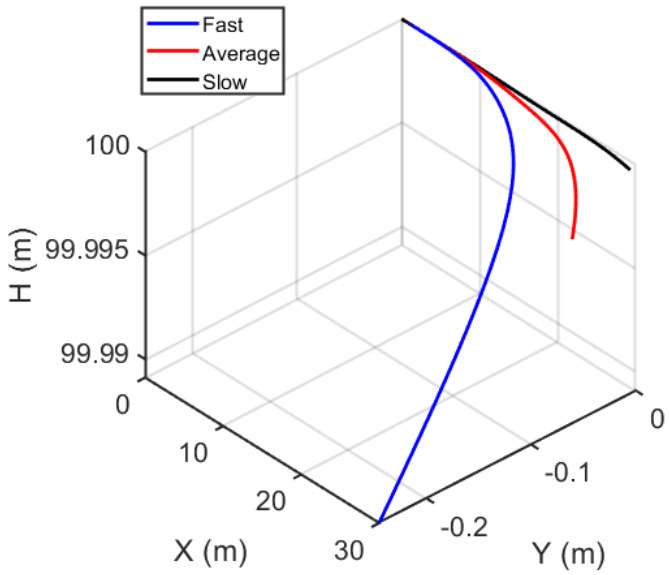


Figure 8.17: Flight trajectory due to rightward abdominal deflection.

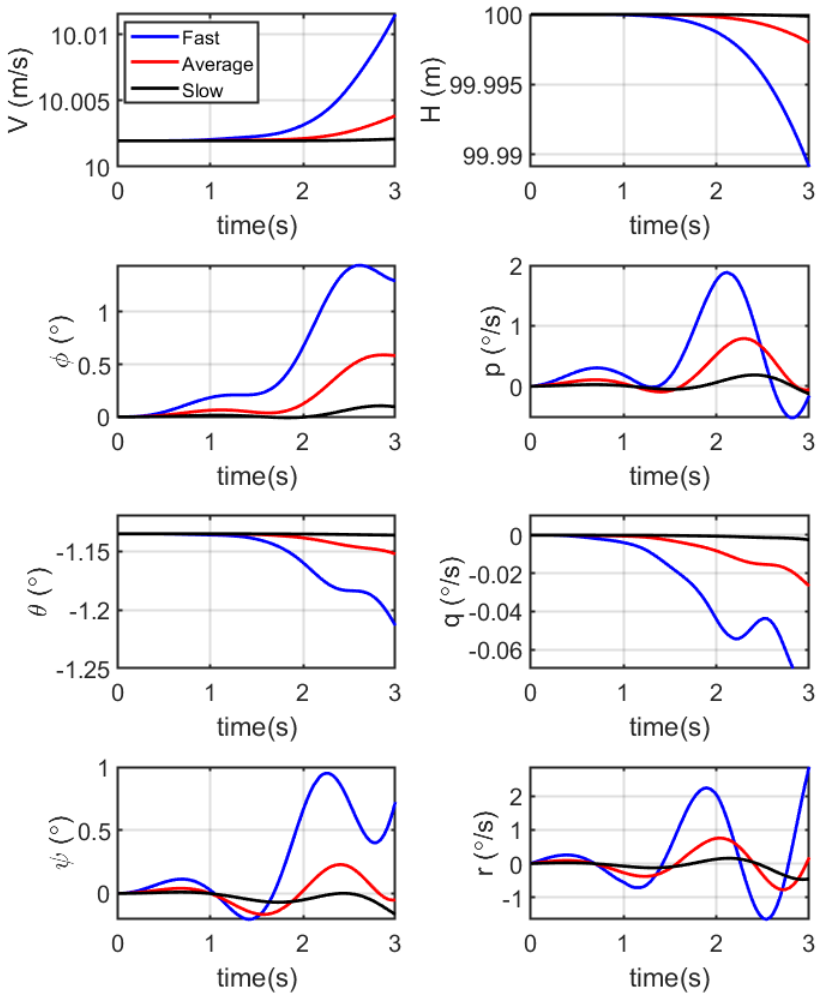


Figure 8.18: Time response comparison of the lateral-directional states: Velocity and height, roll angle and roll rate, pitch angle and pitch rate, yaw angle and yaw rate.

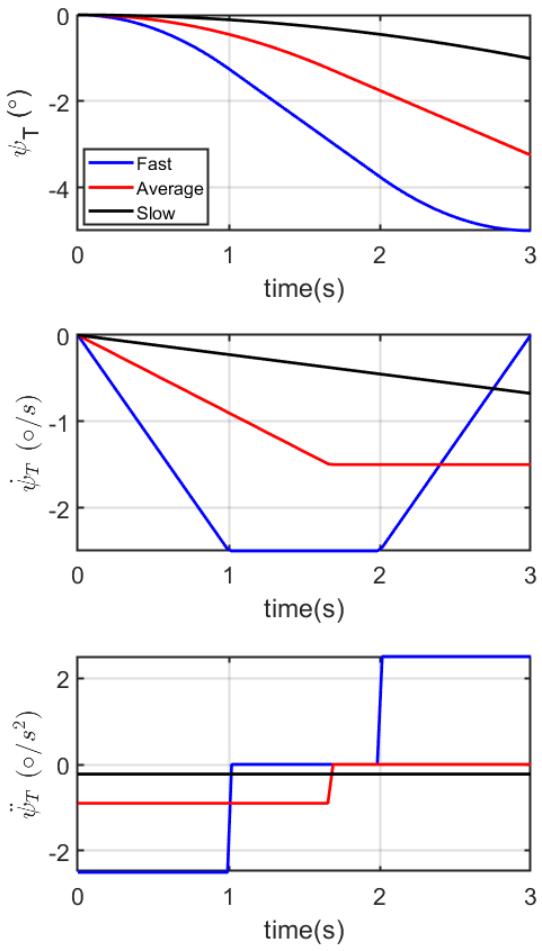


Figure 8.19: Time history of control inputs for lateral-directional manoeuvre: Abdominal yaw angle, abdominal yaw rate, abdominal yaw acceleration.

8.4.2.3 Discussion

From Figures 8.14 and 8.17, the rightward deflection of the abdomen initiates a right turn from steady cruise flight. Although the propagation of the roll, pitch and yaw rates over time in Figures 8.15 and 8.18 are quite oscillatory, useful conclusions can still be drawn. From the time response of the roll, pitch and yaw angles in Figure 8.15, it is evident that the aerodynamic effects of the abdomen increases the magnitude of drag dependent steering manoeuvres and introduces a non-transient torque input, unlike the inertial effect that ceases once the abdomen stops accelerating or decelerating. Increasing abdominal area shows the combination of inertial effect, that does not change with drag area, and drag based steering that becomes increasingly effective at producing torques, accelerating and losing height as the abdominal area increases. Increasing the abdominal yaw rate also has similar effects. The slower the abdominal yaw rate, the less effective the abdomen was at effecting changes in attitude and velocity.

8.5 Summary

This chapter investigated the effects of mass, shape and size on the dynamic/inertial and aerodynamic contributions of a deflectable appendage, and how these contributions affect the forward flight performance and manoeuvrability of insects. Considering a cylindrical abdomen as the deflectable appendage, results showed that the aerodynamic contribution of the abdomen (mainly drag) increased with increasing area, thereby reducing performance due to increased power and energy required in steady cruise flight. However, initiation of a steady pull up manoeuvre from trim using the abdomen instead of elevator, provides a higher manoeuvre advantage. The results also showed that it is indeed possible for the abdomen to initiate dives and turns, however, the manoeuvre effectiveness depends on shape and deflection rate. For the dive manoeuvre, the effectiveness worsened with increased size but improved with a faster deflecting rate, whereas, for turning, the effectiveness improved with increased size and faster deflecting rate. In insects, the additional manoeuvre capability provided by the abdomen should contribute to adequate manoeuvring for hunting and during evasive manoeuvres. For aircraft, this would improve the operating capabilities in terms of manoeuvrability required for complex missions. Finally, depending on the size of the appendage, ignoring the aerodynamic contribution could still provide useful insights, however, the aerodynamic effects should be factored in for a better understanding of the effects.

Chapter 9

Conclusion and Future Work

This chapter summarises the significant findings in this thesis and how they relate to the research questions asked, and the implications of the results. In addition, the outcomes have raised new research questions and possibilities for new prototype aircraft.

9.1 Summary of Findings and Contributions

The aim of this study was to investigate the effects of insect appendage motions in forward flight modes, taking inspiration from the dragonfly. At the beginning of this study, there was an absence in the literature of quantitative study of flight dynamics associated with insect abdominal movement. There was also a paucity of appropriate frameworks to formulate flight dynamics with articulated lifting and non-lifting appendages, such as fuselage/abdomen and undercarriage/legs, even considering large aircraft. Moreover, expressing and modelling the effects of appendage movements on forward flight of insects had not been considered, as much of the work in the literature focused on hover. Furthermore, direct experimental validation of these mathematical models has been absent from the literature, as has consideration of dynamic control effects with articulated appendages in fixed wing aircraft.

The key conclusions drawn from this research are presented below with respect to the research questions underlying the aims and objectives of the study that were established by discovering knowledge gaps in aircraft flight dynamics and performance.

1. Can an efficient matrix-based framework for mathematical modelling of appendage movements be developed for simulation and control system design?

In Chapter 4, two sets of multibody equations of motion were derived to account for the respective translational and rotational movement of an appendage mass, using the Newton-Euler method. It was not certain that an efficient framework could be developed, nor would be numerically reliable when used for simulation, without actual implementation. The conventional vector formulation was replaced with a tensor-based invariant approach, a desirable form for simulation purposes and a necessary form for modern control design. The formulation included the effects of time-varying mass and inertia properties associated with appendage movement, as well as external forces and moments. The equations were written in a reference frame that was geometrically fixed to the aircraft due to the time-varying combined centre of mass due to appendage articulation. Even though the derived equations were specified for a dragonfly-inspired straight-wing aircraft with an articulated abdomen, the generic formulation of the equations allows the modelling of any aircraft with time-varying mass and inertia properties. The application of the derived equations in simulation has not only demonstrated the convenience of implementation but also the versatility of the equations in terms of analysing various types of flight conditions and scenarios. Although similar formulations exist for flapping wing aircraft, no formulation had considered non-lifting components that could be classified as appendages. For the first time, tensor-based invariant formulation of the Newton-Euler method has been developed for translational movement of non-wing appendages.

2. What are the effects of appendage movement on forward flight, considering dynamic/inertial effects only, and considering the combined aerodynamic and dynamic/inertial effects?

   Based on performance criteria, Chapters 5 and 8 pursued an understanding of the dynamic/inertial and aerodynamic effects of an articulated appendage on forward flight through analysis of various forward flight conditions and scenarios, using a DISWA with an articulated abdomen. In the developed multibody flight dynamics models, the aerodynamic contribution of the appendage was modelled as an additive component, ensuring the relative effect of dynamic and aerodynamic effects. Also, the use of either of the following control effector solutions was considered for trimming, re-trimming to recover balance, manoeuvring, stabilisation, and control.

   The dynamic effect an articulated appendage has on steady cruise performance was evaluated based on the power and control effort required to trim the aircraft at various cruise speeds. The cost on performance for trimming the DISWA for steady cruise flight using either aerosurface or combined aerosurface and articulated appendage mass actuation was investigated. Results

obtained showed that combined actuation had lower power required using the translational movement of the appendage, compared to using the aerosurface. Rotational actuation of the appendage on the other hand, compared to the elevator, reduced performance by increasing the power required, albeit by an average of 1%. In addition, the performance of the rotational mass movement was further reduced by the inclusion of the aerodynamics of the abdomen and further degraded as the area of the appendage increased. The cost on performance for re-trimming the DISWA to maintain balance using either appendage actuation mode was also investigated. Results indicate that both the translational and rotational actuation modes improved re-trimming performance by reducing the power and consequently energy required.

To compare the obtainable manoeuvre advantage using the aerosurface or either of the mass actuation modes, the initiation of a fixed thrust steady pull up manoeuvre from a trimmed cruise was considered. Both mass actuation modes demonstrated higher manoeuvre advantage than the elevator deflection for the same pull up manoeuvre trajectory. Manoeuvrability using the deflecting abdomen was also investigated for effectiveness. Various factors that were investigated included the pure dynamic effects and the combination of dynamic and aerodynamic effects as well as the effects of area and deflection rate. The upward deflection was able to initiate a dive and the rightward deflection, a right turn. However, effectiveness was adversely affected by the aerodynamic contribution of the appendage which increased with area. The effectiveness for turning on the other hand, increased due to the aerodynamic contribution and with area. The effectiveness increased with higher deflection rates for both diving and turning manoeuvres.

The observations made so far encourage further investigation into the kinematics of the appendages with respect to their role in performance and control. Simulations provide a useful understanding of theories regarding the inertial and aerodynamic contributions of insect appendages to their manoeuvrability.

Appendages in insects exist in various shapes and sizes. These physical characteristics affect the level of both the inertia and aerodynamic contribution to their overall flight system. Therefore, depending on the model and objective, either of these contributions has been assumed to be negligible and ignored. The findings of this study suggest that computing (or measuring) the aerodynamic forces and moments on the wing pair and the body separately could be a good approximation for investigating the aerodynamics and flight dynamics of a flapping insect in forward flights or manoeuvre. Therefore, the decision to include the aerodynamics of an

appendage is largely dependent on the shape of the appendage. These effects should be included in the model to fully capture all the contributing dynamics and will enable the optimisation between inertial and aerodynamics when designing an appendage.

3. Is the multibody dynamics model suitable for modern optimal control law development for stabilisation and control?

   Flight control system design was carried out on the DISWA model in Chapter 6. Optimal control methods were applied to address the critical challenges associated with flight control system design for these novel over-actuated systems. In this study, the simulation of various control strategies was developed and assessed for performance in both longitudinal and lateral directional flight. For attitude regulation of the aircraft, Aerosurface regulated (ASR), articulated mass regulated (AMR), and Hybrid regulated (HR) cases were considered. Although all three regulators were able to regulate all the longitudinal states, the hybrid regulator had the best performance, as it achieved the least settling time and steady state error. However, only the hybrid regulator was able to regulate all lateral-directional states. Similarly, for attitude control, aerosurface controlled (A-C), articulated mass controlled (A-M), and combined/hybrid controlled (C-C) cases were considered. The hybrid controller had better tracking performance for pitch angle in terms of settling time, percentage overshoot and steady state error, than the aerosurface and articulated mass controller. Whereas for yaw angle control, the hybrid controller performed better in terms of settling time and steady state error compared to the articulated mass and aerosurface control options. Finally, for parallel comparison, the results indicate that a dragonfly using its abdomen in conjunction with its wings could obtain improved controllability and control performance compared to using wings alone.

4. Is this biologically inspired appendage movement feasible for controlling the flight of a SUAV?

   Algebraic and simulation results in Chapters 5 and 8, demonstrated that appendage movement on the scale of SUAVs (the DISWA) could achieve manoeuvre and show energy advantages over conventional control surfaces, depending on assumptions about system characteristics and system integration. A SUAS was developed and test flown to demonstrate the feasibility of applying appendage articulation to control a SUAV. The necessary components were integrated into the system, and control effects on multiple axes showed that they were comparable to the mathematical model behaviour.

The outcomes of the research demonstrated that biological appendage movement is feasible for controlling the flight of an SUAV. The discovered energy advantage may indicate that under some circumstances, appendage motion might be more effective and efficient than aerodynamic controls. Early consideration of the role of the dragonfly abdomen revealed that it is multifunctional, and thus the way the appendage is integrated into the system is the primary factor in realising its advantage.

In Chapter 7, the research practically demonstrated that applying biological observations (appendage articulation) could be tested on available unmanned aerial vehicle hardware, and that actuator effects are observable. This allowed comparison between the model and real performance. Having achieved basic integration of the articulated mass in flight with an open source autopilot, it is now possible to consider using the same integration technique with modified autopilot software to develop controllers that exploit moving mass control input.

So, this biomimetic project has reached a suitable conclusion and a full cycle of insight into aeronautical engineering and biology: An insect behaviour was conjectured based on observations by other researchers who had not fully appreciated the aeronautical implications; The significance of the behaviour was analysed using aeronautical performance and control techniques; Then, a more efficient mathematical technique for multibody dynamics of an aircraft was developed, allowing modern control of such craft, with validation on real aircraft flights; Finally an unreported insect behaviour was observed through the lens of understanding articulated appendages for performance and control.

9.2 Future Work

The findings presented pose some interesting questions and topics for further research. These are logically grouped into a domain of numerical simulation and a domain of flight control of insect inspired systems.

Whilst the results obtained in this study illustrate the potential energy effectiveness achieved by insects in flight, the performance model fidelity was deliberately limited to maximise algebraic rather than numerical techniques. The aircraft dynamics model could be made more comprehensive by including actuator dynamics to quantify the energy required by the actuator to move the tail mass when correcting for imbalance, as well as for dynamic manoeuvres.

Although testing was done in the range in which aircraft have conventional aerodynamics and aerodynamic control, in future it is worth considering aircraft moving between attached and separated flow regimes, possibly at very low Reynolds numbers and during decelerating manoeuvres when aerodynamic forces might be usefully supplemented by an inertial input.

Furthermore, only one value of actuated mass was considered for control design. Simulation results show the actuated mass ratio to the mass of the aircraft has effects on the effectiveness of the mechanism. Therefore, control sensitivity may be increased using a heavier mass. Finding an optimal mass for such a mechanism should be considered for future analysis, and should also be considered in terms of aircraft design, since some heavy subsystems such as batteries might be useful in this regard.

Additionally, the LQI control design procedure followed in this study can be extended for robustness to include uncertainties and actuator dynamics. Control allocation strategies can also be added to address issues such as actuator input saturation and rate limits, actuator redundancy, and fault tolerance of actuators and effectors.

Abdominal postures should be explored in high speed footage of dragonflies when capturing prey and across the cycle of feeding and flying, possibly in existing high speed video footage such as Rüppell's publicly available contributions [16]. Likewise, the hoverfly leg lowering supplementary feasibility study awaits more robust data, and high quality video, with perhaps a comprehensive ethological study to elicit and isolate the leg lowering behaviour.

Several years of scientific work and possible engineering development have emerged as follow-on activities. New areas in biomimetics and new, more agile and efficient aerial vehicles could be developed that exploit the phenomenon.

Appendix A

Athena Vortex Lattice Aerodynamic Models

The geometry files and sample output files for AVL are presented in this section for both the DISWA and Phantom FX-61. More information on how to use the AVL tool can be found in [202].

A.1 Input Geometry File

The AVL input geometry files used to generate the aerodynamic data of the DISWA and Phantom FX-61 used in this study are presented in Sections A.1.1 and A.1.2, respectively. The aerodynamic coefficients and stability derivatives are functions of the aerodynamic angles. To generate the data as a function of the angle of attack for instance, AVL is capable of sweeping through a range of AoA.

A.1.1 DISWA

```
DISWA
0.0                             !   Mach
0     0     0.0                 !   iYsym  iZsym  Zsym
0.26865     0.19434     1.40 !   Sref   Cref   Bref   reference area, chord, span
0.025     0.0   0.0 !   Xref   Yref   Zref   moment reference location (arp.)
0.020                !   CDp
SURFACE
Main Wing
8  1.  12  1.  !  Nchord   Cspace   Nspan  Sspace
```

```
YDUPLICATE
0.
ANGLE
3.0
TRANSLATE
0.     0.     0.05
SECTION
     0.000       0.000       0.0      0.200       0.      0      0.
AFIL
phoenix.dat
SECTION
     0.000       0.05       0.0026       0.200       0.      0      0.
AFIL
phoenix.dat
CDCL
-0.377   0.054   0.171    0.02   1.15    0.05
     0.000       0.080       0.0042      0.200       0.      0      0.
AFIL
phoenix.dat
CDCL
-0.377   0.054   0.171    0.02   1.15    0.05
CONTROL
elevator 1.     0.8     0. 1. 0.     1.
CONTROL
aileron 1.      0.8     0. 1. 0.     -1.
SECTION
     0.000       0.27       0.0141      0.200       0.      0      0.
AFIL
phoenix.dat
CDCL
-0.377   0.054   0.171    0.02   1.15    0.05
CONTROL
elevator 1.     0.8     0. 1. 0.     1.
CONTROL
aileron 1.      0.8     0. 1. 0.     -1.
SECTION
```

```
     0.000       0.54       0.0283      0.200       0.      0      0.
AFIL
phoenix.dat
CDCL
-0.377   0.054   0.171    0.02   1.15    0.05
CONTROL
elevator 1.     0.8     0. 1. 0.     1.
CONTROL
aileron 1.      0.8     0. 1. 0.     -1.
SECTION
     0.000       0.6099       0.0317     0.185       0.      0      0.
AFIL
phoenix.dat
CDCL
-0.377   0.054   0.171    0.02   1.15    0.05
CONTROL
elevator 1.     0.8     0. 1. 0.     1.
CONTROL
aileron 1.      0.8     0. 1. 0.     -1.
SECTION
     0.015      0.6599       0.0338     0.145       0.      0      0.
AFIL
phoenix.dat
CDCL
-0.377   0.054   0.171    0.02   1.15    0.05
CONTROL
elevator 1.     0.8     0. 1. 0.     1.
CONTROL
aileron 1.      0.8     0. 1. 0.     -1.
SECTION
     0.0275      0.6799       0.0345     0.115       0.      0      0.
AFIL
phoenix.dat
CDCL
-0.377   0.054   0.171    0.02   1.15    0.05
CONTROL
```

```
elevator 1.      0.8      0. 1. 0.      1.
CONTROL
aileron 1.       0.8      0. 1. 0.      -1.
SECTION
     0.04         0.7          0.0351         0.085        0.       0       0.
AFIL
phoenix.dat
CDCL
-0.377   0.054   0.171    0.02   1.15    0.05
CONTROL
elevator 1.      0.8      0. 1. 0.      1.
CONTROL
aileron 1.       0.8      0. 1. 0.      -1.
```

A.1.2 Phantom FX-61

```
Phantom
0.0                                !   Mach
0     0     0.0                    !   iYsym  iZsym  Zsym
0.45236     0.30370     1.56000  !   Sref   Cref   Bref   reference area, chord, span
0.25    0.0     0.0 !   Xref   Yref   Zref   moment reference location (arp.)
0.020                  !   CDp
SURFACE
Main Wing
13       1.0
YDUPLICATE
0.0
SECTION
   0.0000    0.0000    0.0000    0.4300   0.000   1    1
AFIL
S5010.dat
SECTION
   0.0100    0.0220    0.0000    0.4200   0.000    1    1
AFIL
S5010.dat
CDCL
```

```
-0.497   0.042    0.    0.008    1.254   0.029
SECTION
   0.0400    0.0500    0.0000    0.3900   0.000    1    1
AFIL
S5010.dat
CDCL
-0.497   0.042    0.    0.008    1.254   0.029
SECTION
   0.0750    0.0800    0.0000    0.3600   0.000   1    1
AFIL
S5010.dat
CDCL
-0.497   0.042    0.    0.008    1.254   0.029
SECTION
   0.1120    0.1180    0.0000    0.3350   0.000    1    1
AFIL
S5010.dat
CDCL
-0.497   0.042    0.    0.008    1.254   0.029
SECTION
   0.1300    0.1400    0.0000    0.3250   0.000   1    1
AFIL
S5010.dat
CDCL
-0.497   0.042    0.    0.008    1.254   0.029
SECTION
   0.1400    0.1550    0.0000    0.3300   0.000   12    1
AFIL
S5010.dat
CDCL
-0.497   0.042    0.    0.008    1.254   0.029
CONTROL
elevator 1.     0.8     0. 1. 0.     1.
CONTROL
aileron 1.      0.8     0. 1. 0.     -1.
SECTION
```

```
   0.3300    0.5750    0.0000    0.2650   0.000   4    1
AFIL
S5010.dat
CDCL
-0.497   0.042    0.    0.008    1.254   0.029
CONTROL
elevator 1.     0.8     0. 1. 0.     1.
CONTROL
aileron 1.      0.8     0. 1. 0.     -1.
SECTION
   0.3700    0.6500    0.0000    0.2500   0.000   4    1
AFIL
S5010.dat
CDCL
-0.497   0.042    0.    0.008    1.254   0.029
SECTION
   0.4200    0.6970    0.0171    0.2200   0.000    4    1
AFIL
S5010.dat
CDCL
-0.497   0.042    0.    0.008    1.254   0.029
SECTION
   0.5050    0.7403    0.0421    0.1650   0.000    4    1
AFIL
S5010.dat
CDCL
-0.497   0.042    0.    0.008    1.254   0.029
SECTION
   0.6400    0.7633    0.0614    0.0500   0.000    4    1
AFIL
S5010.dat
CDCL
-0.497   0.042    0.    0.008    1.254   0.029
SURFACE                     | (keyword)
Fin
7        1.0
```

```
YDUPLICATE
0.0000
TRANSLATE
0.255  0.145  -0.02
SECTION
   0.   0.0    0.0    0.23   0.000    5    1
AFIL
NACA0005.dat
SECTION
0.15   0.0    0.135    0.15   0.000    5    1
AFIL
NACA0005.dat
```

A.2 Output of Aerodynamic Data

The results for the aerodynamic coefficients for the aircraft taken from AVL are presented in this section. These coefficients are a run case of an AoA of 2° and no sideslip or bank angle.

A.2.1 DISWA

```
 ---------------------------------------------------------------
 Vortex Lattice Output -- Total Forces

 Configuration: DISWA_2deg_AoA
     # Surfaces =   2
     # Strips   =  24
     # Vortices = 192

  Sref = 0.26865       Cref = 0.19434       Bref =  1.4000
  Xref = 0.25000E-01   Yref =  0.0000       Zref =  0.0000

 Standard axis orientation,  X fwd, Z down

 Run case:  -unnamed-
```

```
 Alpha =   2.00000     pb/2V =  -0.00000     p'b/2V =  -0.00000
 Beta  =   0.00000     qc/2V =   0.00000
 Mach  =     0.000     rb/2V =  -0.00000     r'b/2V =  -0.00000

 CXtot =  -0.04979     Cltot =   0.00000     Cl'tot =   0.00000
 CYtot =   0.00000     Cmtot =  -0.04424
 CZtot =  -0.47364     Cntot =  -0.00000     Cn'tot =  -0.00000

 CLtot =   0.47162
 CDtot =   0.06629
 CDvis =   0.05651     CDind = 0.0097766
 CLff  =   0.47135     CDff  = 0.0098603    | Trefftz
 CYff  =  -0.00000         e =    0.9831    | Plane

  elevator        =   0.00000
  aileron         =   0.00000

------------------------------------------------------------

Geometry-axis derivatives...

                  axial   vel. u     sideslip vel. v      normal  vel. w
                ----------------    ----------------    ----------------
x force CX  |    CXu =  -0.135334    CXv =   0.000000    CXw =   0.322378
y force CY  |    CYu =   0.000000    CYv =  -0.064436    CYw =   0.000000
z force CZ  |    CZu =  -0.786216    CZv =   0.000000    CZw =  -4.617061
x mom.  Cl  |    Clu =   0.000000    Clv =  -0.078923    Clw =   0.000000
y mom.  Cm  |    Cmu =  -0.057699    Cmv =   0.000000    Cmw =  -0.662162
z mom.  Cn  |    Cnu =  -0.000000    Cnv =  -0.002741    Cnw =  -0.000000

                     roll rate  p       pitch rate  q         yaw rate  r
                ----------------    ----------------    ----------------
x force CX  |    CXp =   0.000000    CXq =  -0.023851    CXr =  -0.000000
y force CY  |    CYp =  -0.007513    CYq =   0.000000    CYr =   0.018955
z force CZ  |    CZp =   0.000000    CZq =  -5.316251    CZr =  -0.000000
x mom.  Cl  |    Clp =  -0.495548    Clq =   0.000000    Clr =   0.107775
```

```
y mom.  Cm  |    Cmp =   0.000000    Cmq =  -1.411515    Cmr =  -0.000000
z mom.  Cn  |    Cnp =  -0.041393    Cnq =  -0.000000    Cnr =  -0.009895

                 elevator     d1     aileron      d2
                 ----------------    ----------------
x force CX  |   CXd1 =  -0.001607   CXd2 =   0.000000
y force CY  |   CYd1 =   0.000000   CYd2 =  -0.001375
z force CZ  |   CZd1 =  -0.035348   CZd2 =   0.000000
x mom.  Cl  |   Cld1 =   0.000000   Cld2 =  -0.007387
y mom.  Cm  |   Cmd1 =  -0.012815   Cmd2 =   0.000000
z mom.  Cn  |   Cnd1 =  -0.000000   Cnd2 =   0.000483
```

A.2.2 Phantom FX-61

```
---------------------------------------------------------------
Vortex Lattice Output -- Total Forces

Configuration: Phantom_2deg_AoA
    # Surfaces =   4
    # Strips   =  78
    # Vortices = 954

 Sref = 0.45236       Cref = 0.30370       Bref =  1.5600
 Xref = 0.25000       Yref =  0.0000       Zref =  0.0000

Standard axis orientation,  X fwd, Z down

Run case:  -unnamed-

 Alpha =   2.00000     pb/2V =  -0.00000     p'b/2V =  -0.00000
 Beta  =   0.00000     qc/2V =   0.00000
 Mach  =     0.000     rb/2V =  -0.00000     r'b/2V =  -0.00000

 CXtot =  -0.02402     Cltot =   0.00000     Cl'tot =   0.00000
```

```
 CYtot =   0.00000     Cmtot =  -0.01882
 CZtot =  -0.17418     Cntot =  -0.00000     Cn'tot =  -0.00000

 CLtot =   0.17323
 CDtot =   0.03008
 CDvis =   0.02826     CDind = 0.0018222
 CLff  =   0.17270     CDff  = 0.0018055    | Trefftz
 CYff  =   0.00000         e =    0.9774    | Plane

  elevator        =   0.00000
  aileron         =   0.00000

 ---------------------------------------------------------------

 Geometry-axis derivatives...

                   axial   vel. u     sideslip vel. v      normal  vel. w
                 ----------------    ----------------    ----------------
 x force CX  |    CXu =  -0.056945    CXv =   0.000000    CXw =   0.206393
 y force CY  |    CYu =   0.000000    CYv =  -0.179212    CYw =  -0.000000
 z force CZ  |    CZu =  -0.210759    CZv =   0.000000    CZw =  -3.939855
 x mom.  Cl  |    Clu =   0.000000    Clv =  -0.080213    Clw =  -0.000000
 y mom.  Cm  |    Cmu =  -0.016276    Cmv =  -0.000000    Cmw =  -0.610943
 z mom.  Cn  |    Cnu =  -0.000000    Cnv =   0.010944    Cnw =   0.000000

                      roll rate  p       pitch rate  q         yaw rate  r
                 ----------------    ----------------    ----------------
 x force CX  |    CXp =   0.000000    CXq =   0.076129    CXr =  -0.000000
 y force CY  |    CYp =  -0.002513    CYq =  -0.000000    CYr =   0.058209
 z force CZ  |    CZp =  -0.000000    CZq =  -4.975927    CZr =  -0.000000
 x mom.  Cl  |    Clp =  -0.363938    Clq =  -0.000000    Clr =   0.054415
 y mom.  Cm  |    Cmp =  -0.000000    Cmq =  -1.890816    Cmr =   0.000000
 z mom.  Cn  |    Cnp =  -0.021754    Cnq =  -0.000000    Cnr =  -0.008444

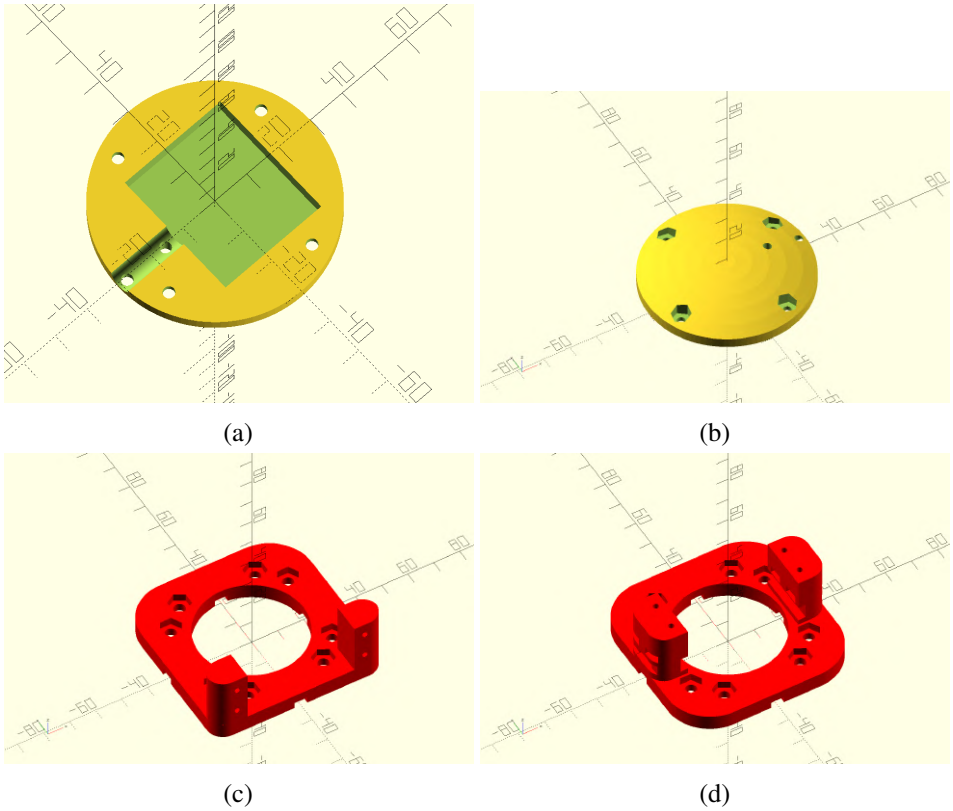
                 elevator     d1     aileron      d2
                 ----------------    ----------------
```

```
x force CX  |   CXd1 =   0.000029   CXd2 =   0.000000
y force CY  |   CYd1 =  -0.000000   CYd2 =  -0.000116
z force CZ  |   CZd1 =  -0.020476   CZd2 =   0.000000
x mom.  Cl  |   Cld1 =   0.000000   Cld2 =  -0.004051
y mom.  Cm  |   Cmd1 =  -0.009363   Cmd2 =  -0.000000
z mom.  Cn  |   Cnd1 =  -0.000000   Cnd2 =   0.000044
```

Appendix B

Articulated Mass Mechanism

The components of the articulated mass mechanism designed in openSCAD are shown in Figure B.1 below. Note that the dimensions are in cm.



(a) (b)

(c) (d)

Figure B.1: Articulated mass mechanism components in openSCAD: (**a**) First half of the bob mass. (**b**) Second half of the bob mass. (**c**) Mechanism for mounting mass longitudinally. (**d**) Mechanism for mounting mass laterally.

.

Appendix C

Leg Movement in Hoverfly Flight

So far, the focus of this thesis has been the effects of appendage motions in forward flight. This appendix considers the flight of the hoverfly, and the role that observed leg motions might play in their flight control system. The first section of the chapter introduces the hoverfly, its mode of flight and anatomy with particular comparison to dragonflies. Subsequently, the study discusses what is known about their leg movements, and introduces preliminary observations. The hoverfly basic dynamics parameters including the wing system, legs and body are estimated, and a simple model of their longitudinal dynamics is derived. Finally the research demonstrates how the angle of the legs could be used to control speed. The intent of the study is to generate a foundation for subsequent behavioural studies of hoverfly by ensuring that the hypothesis that hoverfly leg movements could meaningfully control flight is valid. It will also allow modelling of the effect of leg movements, thus informing statistical modelling of flight path to leg movement comparisons in subsequent studies.

C.1 Introduction

Biomimetics offers inspiration for new technological solutions by applying biological observations to design. There is also a hope that insights from biology lead to enhanced insight into the problem, that may in turn deepen understanding of biology. Here, the observation of appendage movements in insects such as dragonflies, and the theoretical flight dynamics framework produced in the body of this thesis is used to reveal the extent to which hoverfly leg movements might be a new moving mass control strategy. The technique raises inspiration for hover trim control of electric vertical take-off and landing aircraft using retractable undercarriage, for example.

Hoverflies are insects of the order Diptera. Anatomically this means that they have a single wing pair, rather than two [259]. Diptera hindwings have evolved into halteres, small drum stick shaped organs that have been shown to perform an inertial sensing role analogous to an oscillating gyroscope that was observed [260] long before it was understood [261]. Insects of the obscure order Strepsiptera, that are generally night flying endoparasites of other insects, have also developed halteres, however, in their case the hindwings remained wings and the front wings evolved to the drumstick form [262].

Diptera include many of the most prominent insects in the human experience. Members include house flies (*Musca domestica*), midges (*Chironomidae*), gnats (*Chloropidae*), mosquitoes (*Culicidae*) and horse flies (*Tabanidae*). Many of these insects include species that feed on human blood (mosquitoes, horse flies, midges and gnats), human refuse and wounds (house flies and blow flies), or have unpleasant behaviours such as attraction to eyes (for example eye gnats [263]). Many of them also transmit disease to humans, such as malaria, the rabies-like Chandipura virus, West Nile fever, yellow fever, encephalitis, and food borne illness. In this company, hoverflies are notably benign to humans, acting as predators on pest insects such as aphids, pollinating flowers, with larvae eating decaying vegetable matter or pest insect larvae.

A *Melangyna viridiceps* "Australian common hover fly" in flight is shown in Figure C.1. In appearance, hoverflies generally look like bees or wasps with black and yellow stripes which is a case of Batesian mimicry [264], although the degree or quality of mimicry is poor enough to have become a topic as to why it is poor [265]. They have a relatively large head and eyes, particularly in small species. They are often observed hovering, apparently almost perfectly still, near flowers, then moving sideways or forwards suddenly, and hovering again. They also engage in intra-species pursuit [266] with territorial or reproductive motives. Unlike the dragonfly abdomen, the legs of a hoverfly are comparatively slender and close to the body. However, like dragonflies, hoverflies when hovering, use an inclined stroke plane where the body is approximately horizontal.

Furthermore, the argument that has been demonstrated thus far has been that dragonflies use their abdomen in forward flight, hover has not been considered. There also appear to be questions about why a hoverfly might use legs rather than wings to generate subtle control during hover, since the wings would appear to be the more responsive system. Hence, observing hoverflies was a logical choice for hover related flight behaviours relating to possible appendage motions for control. The author observed hoverflies holding station near flowers. Leg movements were noted on occasion, usually after the



(a) (b)

Figure C.1: Individual hoverfly of the the species *Melangyna viridiceps*: (a) in flight. (b) at rest.

hover position was disrupted by gusts of wind. The movements were slow, over the order of 250 to 1000 millseconds. In isolation, no convincing hypothesis for the behaviour may have been formulated. However, the study from previous chapters on dragonfly abdomen articulation allowed a preliminary hypothesis that the leg movement might be part of flight control. There are technological precedents for moving mass control in hovering aircraft as discussed in Section 2.2. It is likely that these aircraft types share some of the problems faced by hoverflies in achieving controlled hover. Some analysis of feasibility is required to establish whether it is possible that flight control by this means is achievable, prior to a full observational study on hoverflies.

C.2 Observation Methods

The hoverfly is a difficult videography subject since the species in question, the Australian common hover fly *Melangyna viridiceps* are small, with body length of under 10 mm and wing span of 15 mm–20 mm. Initial observations were made in 2021 by humans without cameras, followed by incidental mobile telephone capture, which revealed how difficult high quality videography would be. The small size of the subject, hovering against a cluttered background leads to automatic focus limitations with normal camera equipment. The conditions under which they are seen is usually full sunlight, creating additional problems for operator use of cameras aimed using screens while taking video.

Despite the difficulties, a number of videos were created using a Samsung Galaxy S5 smartphone which captures 1080 pixels at 30 frames per second. The videos showed clear leg movements, apparently correlated with arresting backwards motion. Previous study by Collett and Land [267] reported pursuit manoeuvres of hoverflies ranging from 0.2 s to 0.5 s. Excerpts are included in Figures C.2 and C.3, both spanning 0.5 s which is sufficient to observe a manoeuvre. Although the video is not of high quality, the presence of the output of the leg motion reflex is clear. The input that induces the leg motion is not clear without a much larger sample, however, an initial research hypothesis is that the legs could be part of the hover control system. It is worth mentioning that the leg lowering in Figure C.3 is partial, and sustained, perhaps indicative that it is a controlled and variable response rather than a stereotypical behaviour.



Figure C.2: First sequence extracted from mobile telephone video of hoverfly leg lowering and raising in flight.

A Nikon 200 mm f/4 ED-IF AF Micro-NIKKOR was obtained to allow macro photography at intermediate distance, with aspirations to achieve videography in future. The relatively small f/4 maximum aperture of the lens combined with the dynamic nature of the subjects limits photographic scenarios to bright sunlight. Fortunately, hoverflies primarily operate in bright conditions. Although it was possible to capture some still images (Figure C.1a–b), a more controlled environment is required to achieve a high quality ethological study.

Having observed the behaviour, the intent was to establish feasibility of the flight control mechanism given estimates of hoverfly mass properties.



Figure C.3: Second sequence extracted from mobile telephone video of hoverfly leg lowering and raising in flight.

C.3 Mass Estimation

The morphological parameters required for analysis are the masses and cg locations of the major anatomical parts of the insect. The components of the hoverfly were taken as point masses. Since the focus of the study is leg movements, the components are the head, thorax, wings and abdomen combination, taken as the central body B, the combined properties of the legs, taken as the second body L. Another body C was defined to include the total mass m of the hoverfly. Using the outlines of scanned images (Figure C.4) of an actual hoverfly from a study by Mou et al. [268], the method used to estimate those morphological parameters follows. It must be stressed that this is an approximation for establishing feasibility and more accuracy would be required for a definitive ethological study. The central body's cross-section was considered to be an assembly of ellipses of uniform density. The combined mass of the legs was obtained by approximating each leg as a cylinder of uniform density. The underlying assumption was that the density of the body does not vary between segments. The parts were assumed to have the density of water (1.0 g/cm^3) as an approximation and to standardise across body parts.

C.4 Feasibility of Balance Based Hover Control

Segments of videos that contained distinct and clearly visible flight behaviour were selected for analysis. The essence of the analysis was to assess the potential impact of this change of combined cg on the

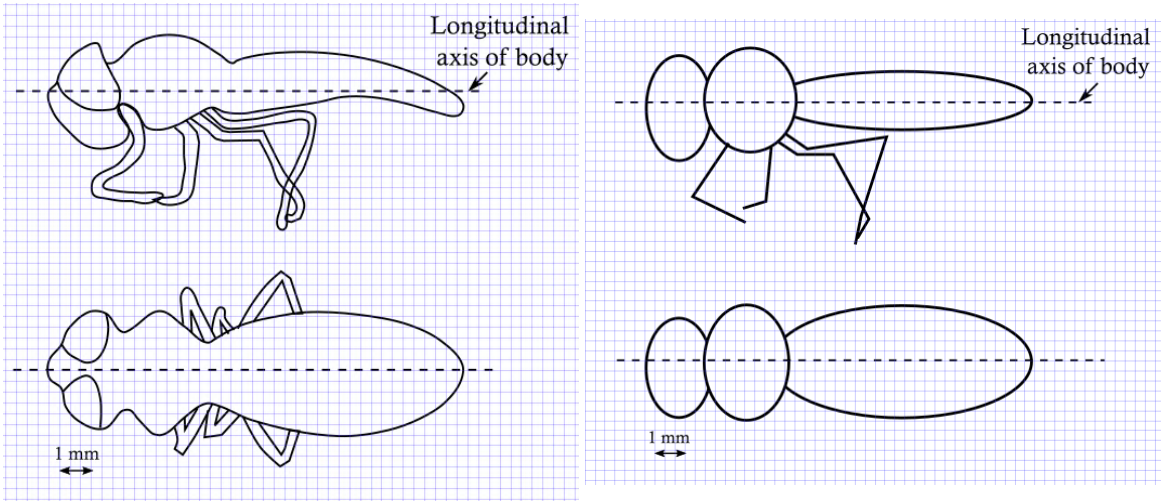


Figure C.4: Outlines of dorsal and lateral views of a hoverfly: (a) scanned outline [268]. (b) approximated outline.

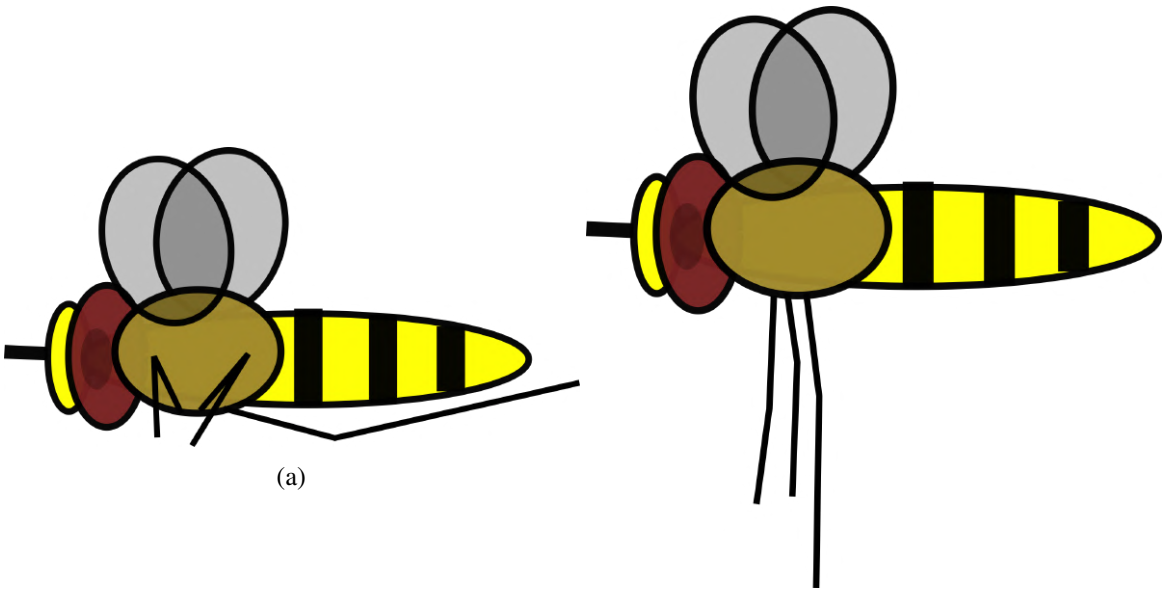
manoeuvring of these insects in longitudinal flight.

This study requires an understanding of the forces involved and the likely accelerations they will cause on the x_B-axis of the hoverfly. A clear line diagram of the observed configuration of the hoverfly in hover is shown in Figure C.5.

The geometry of the animal is such that the rear pair of legs are long. In normal flight they are held flat against the rear of the body, shown in Figure C.6a and are then rotated down so as to be approximately orthogonal to the body, creating a longitudinal shift in mass, but also a vertical shift compared to where the upward force of the hovering wings is generated. This creates a pendular system as illustrated in Figure C.6b.

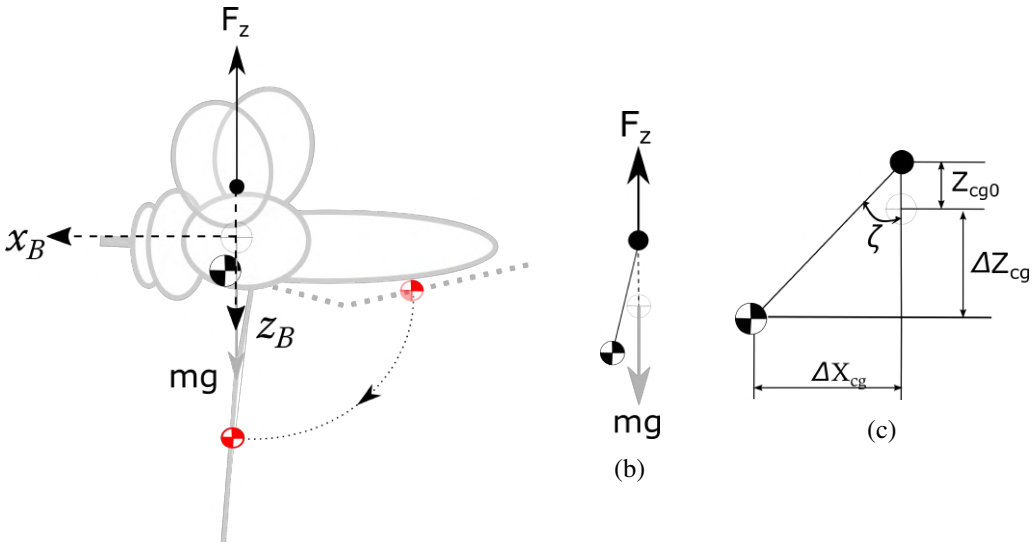
Since an assumption was made that the hoverfly is balanced before the legs rotate, the changed mass distribution will cause the hoverfly to experience a forward pitching torque, that is opposed by a torque pitching back caused by the projection of the legs onto the gravity vector. In a static situation this would reach an equilibrium angle.

A simplified model of the shift in combined centre of gravity Δcg relative to the centre of lift is illustrated in Figure C.6. The equilibrium angle with legs extended is simply the angle between the



(a) (b)

Figure C.5: The configuration of a hoverfly in flight: (a) with raised legs, cg to rear. (b) with lowered legs, cg to front.



(a) (b) (c)

Figure C.6: (a) Centre of gravity shift geometry when legs are lowered. (b) abstraction of forces (c) abstraction of angles

Note: ◔ represents the cg position of the legs.
● represents the centre of lift, and
⊕ and ◔ represent the initial and final overall cg positions, respectively.

centre of lift and the new centre of mass. The mass of the insect is conserved, the magnitude of F_z will change to maintain height, although the vertical component will remain constant to do so.

Based on Figure C.1, the wings appear to emerge about 30% of the thorax depth below the dorsal surface of the thorax. Symmetrical flapping is assumed, and the flapping cycle averaged force F_z is implied [269]. In addition, we assumed the mean aerodynamic centre of pressure point cop, was located at $\approx$ 60% along the line connecting the tip of the wing from its root, a value that is representative for typical insect wings [270], [271]. The diagrams of the hoverfly in Figure C.5 show the general configuration of the legs in the raised position based on many photographs of hoverflies in flight. Once lowered, the forward two leg pairs probably contribute very little to change in horizontal cg location, but will contribute to vertical shift. The hindlegs will contribute to both vertical and horizontal shift in cg.

Assuming that the initial combined cg (body and legs) position was immediately under the centre of lift, at vertical distance Z_{cg_0} below the centre of lift, the initial equilibrium angle ζ of the system is 0°, relative to the gravity vector. After the change in centre of gravity induced by the legs lowering, using the small angle approximation, the angle relationship between centre of lift and new centre of gravity is $\frac{\Delta X_{cg}}{Z_{cg_0}+\Delta Z_{cg}}$, where ΔX_{cg} and ΔZ_{cg} are the change in horizontal and vertical displacement of the centre of gravity respectively, relative to the initial cg location (see Figure C.6c). The direction of weight now contains a horizontal component relative to gravity. The cosine governing the vertical component of lift is small for small angles, whereas the sine of the horizontal component is proportional to the angle. Using the small angle approximation, the acceleration $\dot{u}$ that must be generated to cancel the horizontal component of the cg shift is $\frac{g\Delta X_{cg}}{Z_{cg_0}+\Delta Z_{cg}}$, so the fraction of gravity of the cg shift.

A 5% shift, would result in around $0.5ms^{-2}$ acceleration, a 1% shift in around $0.1ms^{-2}$. Intuitively, 50–250 mm in one second seems a very useful amount of motion for manoeuvre in close quarters, for a short nervous system with rapid reactions.

To quantify these expressions, we use the estimated values of the hoverfly presented in Figure C.4. The estimated mass of the central body was $\approx$ 40 mg and $\approx$ 2.88 mg for the legs, making the legs 6% of the total body mass. Therefore, the cg positions of each component were chosen such that the overall cg position of the insect in initial hover configuration (Figure C.1a) was directly below the centre of vertical lift F_v of the wing at a distance Z_{cg_0}. Additionally, the overall cg was assumed to lie along the x_B axis (see Figure C.6).

With reference to Figure C.7, the morphological parameter ratios were taken from [268] to be $\frac{l_{cg}}{l_B} = 0.42$

and $\frac{h_r}{l_B} = 0.06$. The length of the hoverfly wing was also taken from [268] as 9.7 mm. The definition of coordinate system for the legs with respect to the central body is the same as that defined in Figure 4.4 in Chapter 4.

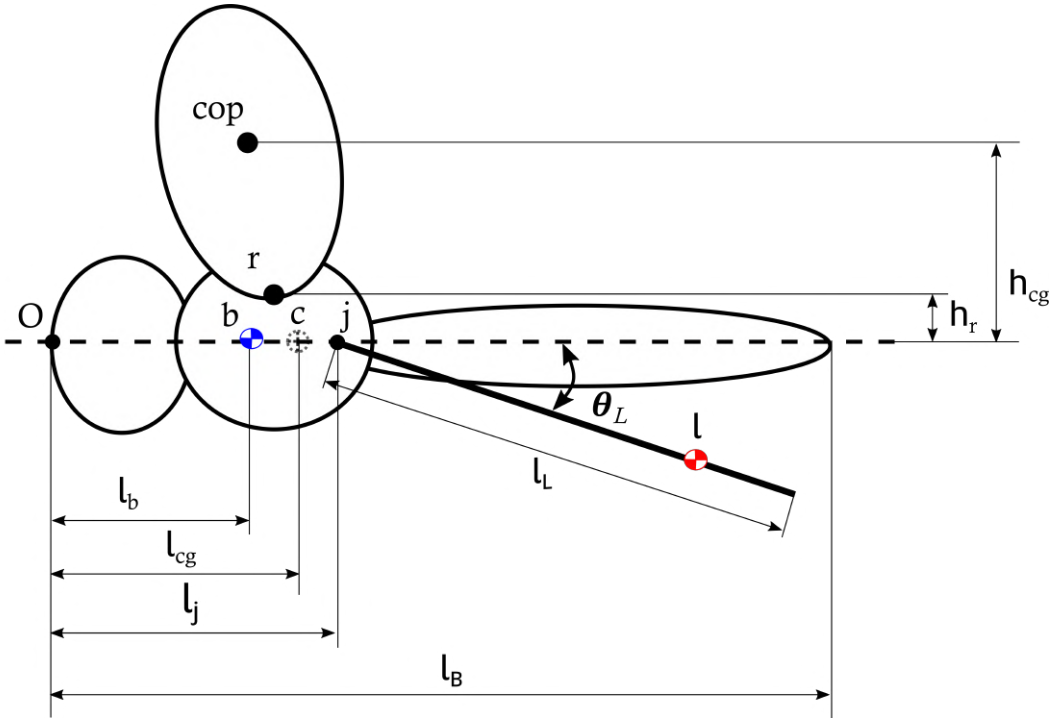


Figure C.7: Morphological parameters definition.

Note: O, b, c, j, l, r and cop are the respective points representing the tip of the head, central body point mass, overall point mass, joint of the legs to the central body, point mass of the legs, wing root and aerodynamic centre of pressure.
l_b, l_{cg}, and l_j are the respective horizontal distances of points b, c, and j from point O.
l_l and l_B are the respective representative lengths of all the legs and the body of the hoverfly from point O.
h_r is the vertical distance of points r from the horizontal axis.
represents the location of the point mass of the central body B.
represents the cg position of the legs.

The hoverfly parameters used are listed in Table C.1. Note that s_{Ob}, s_{jb}, and s_{lj}, are relative the displacements between the points as per Figure C.7, and the pitch angle of the legs, θ_L, is given relative to the x_B axis of the body.

Table C.1: Hoverfly parameters.

Parameter	**Value**	**Parameter**	**Value**
l_L	7 mm	l_B	12 mm
m^B	40 mg	m^L	2.88 mg
$[s_{Ob}]^B$	[4.54;6.00] mm	$[s_{jb}]^B$	[2;6.54] mm
$[s_{lj}]^L$	[5;6.54] mm	θ_L	10°

The combined cg (body and legs) locations at the initial hover condition are given in Table C.2

Table C.2: Initial centre of gravity locations in hover.

	Centre of gravity
X_{cg_0}	5.04 mm
Z_{cg_0}	6.54 mm

The new cg position is obtained using

$$cg = s_{Ob} + \frac{m^L}{m}[R]^{BL}[s_{lj}]^T + s_{jb}] \tag{C.1}$$

where the transformation matrix from legs to body frame, $[R]^{BL}$, is given by

$$[R]^{BL} = \begin{bmatrix} cos(\theta_L) & -sin(\theta_L) \\ sin(\theta_L) & cos(\theta_L) \end{bmatrix} \tag{C.2}$$

The new centre of gravity given an increase in the pitch angle of the legs from ($\theta_L = 10°$) to ($\theta_L = 90°$) results in $cg = [4.69; 6.84]$. Therefore, the change in cg induced by the movement of the legs is ($\Delta cg = cg - cg_0$).

Considering x_B axis, the acceleration $\dot{u}$ that must be generated to cancel the horizontal component resulting from a change in the angle of the legs,

$$g\frac{\Delta X_{cg}}{Z_{cg_0} + \Delta Z_{cg}} = -0.052g \tag{C.3}$$

The vertical force created by the hoverfly is assumed to be in a feedback loop to maintain height. For this application there is no requirement to model the wing beat, or the dynamics, since the study is considering small variations of horizontal forces around trimmed hover.

C.5 Discussion

From the analysis in Section C.4, a small horizontal acceleration of around 5.2% of the acceleration due to gravity was created by the leg movements. This is enough for manoeuvre, although it does not

prove that the behaviour is used for this purpose, or that any movement seen when the legs are moved is actually caused by balance induced rotation and not opposed or dominated by the thrust vector of the wings. Determining causation and correlation is an important research question for a following study.

The subtle forces involved in the leg movements also raise question of why the legs might be used, and not the powerful and direct forces of the flight system. A working hypothesis that might be testable is that the wing control system has significant hysteresis or inertia. It may be the case that subtle changes to the hover trim condition are not rapid or even possible. The indirect innervation of the flight motor of Diptera might play a role in this. Experimentation to test this might be quite complex and involve strain gauge tethers, and might require the animal to be induced to hover in an artificial environment.

Such apparatus have been built in specialised laboratories for measuring forces and torques produced by living Diptera [272]. There is a question of whether just the observation and feasibility shown in this chapter are enough to contribute to the body of knowledge. This same question is associated with ensuring hypotheses are pursued that are well enough connected to meaningful lines of enquiry about neuroscience, vision and flight.

The purpose of this study was to establish if the leg movements would produce forces that could be used for flight control, and consistent with the movements observed. The calculations show that this is the case. This might justify an experiment to determine whether the forces are actually in use, and then to establish why the legs might be used in concert with the wings.

It is also possible the the purpose of the leg movements is not related to flight control at all. Possible purposes could include drag brakes or preparation for forced landing. Regardless of other uses, the motion of the legs is apparent, repeated and an inescapable physical phenomenon that will modify balance in flight.

C.6 Summary

This chapter has established that hoverfly leg movements will induce longitudinal accelerations suitable for manoeuvre due to centre of gravity shift. This finding allows the formulation of observational studies to test hypotheses about whether it is actually being used as an adjunct to the wing complex,

and particularly the reason that it might be necessary or desirable. This finding was based on research questions informed by a deeper understanding of how insect body movements might be useful for biomimetic aircraft.

Bibliography

[1] M. H. Sadraey, *Design of Unmanned Aerial Systems*. John Wiley & Sons, 2020.

[2] K. P. Valavanis and G. J. Vachtsevanos, *Handbook of unmanned aerial vehicles*. Springer, 2015, vol. 2077.

[3] M. Khamsi, "Design and analysis of an unmanned aerial vehicle capable of carrying the camera," 2019.

[4] L. A. Doan *et al.*, "Micro air vehicle to nano air vehicle: Theoretical and experimental studies of an artificial flapping insect," Ph.D. dissertation, Nanotechnology Department, Universite Polytechnique, Valenciennes France, 2019.

[5] P. Ramesh and M. L. Jeyan, "Mini unmanned aerial systems (uav)-a review of the parameters for classification of a mini uav.," *International Journal of Aviation, Aeronautics, and Aerospace*, vol. 7, no. 3, p. 5, 2020.

[6] M. Arjomandi, S. Agostino, M. Mammone, M. Nelson, and T. Zhou, "Classification of unmanned aerial vehicles," *Report for Mechanical Engineering class, University of Adelaide, Adelaide, Australia*, 2006.

[7] G. Singhal, B. Bansod, and L. Mathew, "Unmanned aerial vehicle classification, applications and challenges: A review," 2018.

[8] N. Elmeseiry, N. Alshaer, and T. Ismail, "A detailed survey and future directions of unmanned aerial vehicles (uavs) with potential applications," *Aerospace*, vol. 8, no. 12, p. 363, 2021.

[9] J. M. McMichael, "Micro air vehicles-toward a new dimension in flight," *http://www.arpa.gov/tto/MAV/m*
auvsi.html, 1997.

[10] R. E. Cory, "Supermaneuverable perching," Ph.D. dissertation, Massachusetts Institute of Technology, 2010.

[11] S. Armanini, J. Caetano, C. De Visser, M. Pavel, G. De Croon, and M. Mulder, "Modelling wing wake and tail aerodynamics of a flapping-wing micro aerial vehicle," *International Journal of Micro Air Vehicles*, vol. 11, p. 1 756 829 319 833 674, 2019.

[12] J. Chahl, N. Chitsaz, B. McIvor, T. Ogunwa, J.-M. Kok, T. McIntyre, and E. Abdullah, "Biomimetic drones inspired by dragonflies will require a systems based approach and insights from biology," *Drones*, vol. 5, no. 2, p. 24, 2021.

[13] T. A. Lenau, A.-L. Metze, and T. Hesselberg, "Paradigms for biologically inspired design," in *Bioinspiration, Biomimetics, and Bioreplication VIII*, International Society for Optics and Photonics, vol. 10593, 2018, p. 1 059 302.

[14] R. Berthé and F.-O. Lehmann, "Body appendages fine-tune posture and moments in freely manoeuvring fruit flies," *Journal of Experimental Biology*, vol. 218, no. 20, pp. 3295–3307, 2015.

[15] M. Sridhar, C.-K. Kang, and T. Lee, "Geometric formulation for the dynamics of monarch butterfly with the effects of abdomen undulation," in *AIAA Scitech 2020 Forum*, 2020, p. 1962.

[16] G. Rüppell, D. Hilfert-Rüppell, B. Schneider, and H. Dedenbach, "On the firing line–interactions between hunting frogs and odonata," *International Journal of Odonatology*, pp. 1–19, 2020.

[17] C. P. Ellington, "The aerodynamics of hovering insect flight. iv. aerodynamic mechanisms," *Philosophical Transactions of the Royal Society of London. B, Biological Sciences*, vol. 305, no. 1122, pp. 79–113, 1984.

[18] C. P. Ellington, "The aerodynamics of hovering insect flight. vi. lift and power requirements," *Philosophical Transactions of the Royal Society of London. B, Biological Sciences*, vol. 305, no. 1122, pp. 145–181, 1984.

[19] C. J. Pennycuick, "A wind-tunnel study of gliding flight in the pigeon columba livia," *Journal of experimental Biology*, vol. 49, no. 3, pp. 509–526, 1968.

[20] C. J. Pennycuick, "Control of gliding angle in ruppell's griffon vulture gyps ruppellii," *Journal of Experimental Biology*, vol. 55, no. 1, pp. 39–46, 1971.

[21] M. Cook and M. Spottiswoode, "Modelling the flight dynamics of the hang glider," *The Aeronautical Journal*, vol. 109, no. 1102, pp. I–XX, 2005.

[22] T. Libby, T. Y. Moore, E. Chang-Siu, D. Li, D. J. Cohen, A. Jusufi, and R. J. Full, "Tail-assisted pitch control in lizards, robots and dinosaurs," *Nature*, vol. 481, no. 7380, p. 181, 2012.

[23] C. T. Orlowski, "Flapping wing micro air vehicles: An analysis of the importance of the mass of the wings to flight dynamics, stability, and control," Ph.D. dissertation, University of Michigan, 2011.

[24] A. M. Hassan and H. E. Taha, "Aerodynamic-dynamic interactions and multi-body formulation of flapping wing dynamics: Part i modeling," in *AIAA Guidance, Navigation, and Control Conference*, 2017, p. 1274.

[25] K. M. Kajak, M. Karasek, Q. P. Chu, and G. De Croon, "A minimal longitudinal dynamic model of a tailless flapping wing robot for control design," *Bioinspiration & biomimetics*, vol. 14, no. 4, p. 046 008, 2019.

[26] J. Choi, D. Gong, J. Lee, C. Kim, and S. Shin, "Simulation of the flapping wing aerial vehicle using flexible multibody dynamics," *International Journal of Micro Air Vehicles*, vol. 13, p. 17 568 293 211 043 305, 2021.

[27] K. Bakhshaei, H. MoradiMaryamnegari, S. SalavatiDezfouli, A. M. Khoshnood, and M. Fathali, "Multi-physics simulation of an insect with flapping wings," *Proceedings of the Institution of Mechanical Engineers, Part G: Journal of Aerospace Engineering*, vol. 235, no. 10, pp. 1318–1339, 2021.

[28] J. Pei, G. Bassett, J. Grisham, P. Finch, M. Toniolo, L. Miller, and P. Bandu, "Generic control allocation toolbox for preliminary vehicle design," in *2018 Modeling and Simulation Technologies Conference*, 2018, p. 3894.

[29] J. Anderson, *Aircraft performance and design*. WCB/McGraw-Hill,Boston, MA, 1999.

[30] D. Anderson and S. Eberhardt, "A physical description of flight," *Fermi National Accelerator Laboratory Seattle, WA*, 2004.

[31] F. L. Janssens and J. C. van der Ha, "Stability of spinning satellite under axial thrust, internal mass motion, and damping," *Journal of Guidance, Control, and Dynamics*, vol. 38, no. 4, pp. 761–771, 2015.

[32] F. L. Chernousko, L. D. Akulenko, and D. D. Leshchenko, *Evolution of motions of a rigid body about its center of mass*. Springer, 2017.

[33] J. Han and G. Hong, "Modeling of aircraft with time-varying inertia properties," in *AIAA Modeling and Simulation Technologies Conference*, 2015, p. 1133.

[34] O. Chanute, *Progress in flying machines*. Courier Corporation, 1997.

[35] H. S. Wolko and J. Anderson, *The wright flyer: An engineering perspective*, 1983.

[36] L. Qin and M. Yang, "Moving mass attitude law based on neural networks," in *2007 International Conference on Machine Learning and Cybernetics*, IEEE, vol. 5, 2007, pp. 2791–2795.

[37] J. Rogers and M. Costello, "A variable stability projectile using an internal moving mass," *Proceedings of the Institution of Mechanical Engineers, Part G: Journal of Aerospace Engineering*, vol. 223, no. 7, pp. 927–938, 2009.

[38] J. Rogers, *Applications of internal translating mass technologies to smart weapons systems*. Georgia Institute of Technology, 2009.

[39] J. Rogers and M. Costello, "Control authority of a projectile equipped with a controllable internal translating mass," *Journal of Guidance, Control, and Dynamics*, vol. 31, no. 5, pp. 1323–1333, 2008.

[40] S. Wang, M. Yang, and Z. Wang, "Moving-mass trim control system design for spinning vehicles," in *2006 6th World Congress on Intelligent Control and Automation*, IEEE, vol. 1, 2006, pp. 1034–1038.

[41] L. Chen, G. Zhou, X. Yan, and D. Duan, "Composite control of stratospheric airships with moving masses," *Journal of aircraft*, vol. 49, no. 3, pp. 794–801, 2012.

[42] S. A. Erturk, "Performance analysis, dynamic simulation and control of mass-actuated airplane," Ph.D. dissertation, University of Texas at Arlington, 2016.

[43] S. R. Vengate, S. A. Erturk, and A. Dogan, "Development and flight test of moving-mass actuated unmanned aerial vehicle," in *AIAA Atmospheric Flight Mechanics Conference*, 2016, p. 3713.

[44] T. Haus, M. Orsag, and S. Bogdan, "Mathematical modelling and control of an unmanned aerial vehicle with moving mass control concept," *Journal of Intelligent & Robotic Systems*, vol. 88, no. 2-4, p. 219, 2017.

[45] T. Haus, M. Orsag, and S. Bogdan, "Design considerations for a large quadrotor with moving mass control," in *2016 International Conference on Unmanned Aircraft Systems (ICUAS)*, IEEE, 2016, pp. 1327–1334.

[46] S. Bouabdallah, R. Siegwart, and G. Caprari, "Design and control of an indoor coaxial helicopter," in *2006 IEEE/RSJ International Conference on Intelligent Robots and Systems*, IEEE, 2006, pp. 2930–2935.

[47] C. Bermes, S. Leutenegger, S. Bouabdallah, D. Schafroth, and R. Siegwart, "New design of the steering mechanism for a mini coaxial helicopter," in *2008 IEEE/RSJ International Conference on Intelligent Robots and Systems*, IEEE, 2008, pp. 1236–1241.

[48] D. Childs, *An investigation of a movable mass-attitude stabilization system for artificial-g space*, 1972.

[49] D. W. Childs and T. L. Hardison, "A movable-mass attitude stabilization system for cable-connected artificial space stations," *Journal of Spacecraft and Rockets*, vol. 11, no. 3, pp. 165–172, 1974.

[50] D. W. Childs, "A movable-mass attitude-stabilization system for artificial-g space stations," *Journal of Spacecraft and Rockets*, vol. 8, no. 8, pp. 829–834, 1971.

[51] T. L. Edwards and M. H. Kaplan, "Automatic spacecraft detumbling by internal mass motion," *AIAA Journal*, vol. 12, no. 4, pp. 496–502, 1974.

[52] Q. Zheng and Z. Zhou, "Stability of moving mass control spinning missiles with angular rate loops," *Mathematical Problems in Engineering*, vol. 2019, 2019.

[53] J. Li, C. Gao, C. Li, and W. Jing, "A survey on moving mass control technology," *Aerospace Science and Technology*, vol. 82, pp. 594–606, 2018.

[54] C. Gao, W. Jing, and P. Wei, "Research on application of single moving mass in the reentry warhead maneuver," *Aerospace Science and Technology*, vol. 30, no. 1, pp. 108–118, 2013.

[55] X.-L. Su, J.-Q. Yu, Y.-F. Wang, and L.-l. Wang, "Moving mass actuated reentry vehicle control based on trajectory linearization," *International Journal of Aeronautical and Space Sciences*, vol. 14, no. 3, pp. 247–255, 2013.

[56] S. Candel, "Concorde and the future of supersonic transport," *Journal of propulsion and power*, vol. 20, no. 1, pp. 59–68, 2004.

[57] H. Turner, "Fuel management for concorde: A brief account of the fuel system and the fuel pumps developed for the aircraft," *Aircraft Engineering and Aerospace Technology*, 1971.

[58] D. Collard, "Concorde airframe design and development," *SAE transactions*, pp. 2620–2641, 1991.

[59] R. C. Nelson *et al.*, *Flight stability and automatic control*. WCB/McGraw Hill New York, 1998.

[60] L. Chrif and Z. M. Kadda, "Aircraft control system using lqg and lqr controller with optimal estimation-kalman filter design," *Procedia Engineering*, vol. 80, pp. 245–257, 2014.

[61] J. Shaji and R. Aswin, "Pitch control of flight system using dynamic inversion and pid controller," *Int. J. of Engineering Research & Technology*, pp. 1–5, 2015.

[62] R. Lungu, M. Lungu, and L. T. Grigorie, "Automatic control of aircraft in longitudinal plane during landing," *IEEE Transactions on Aerospace and Electronic Systems*, vol. 49, no. 2, pp. 1338–1350, 2013.

[63] M. T. Islam, M. S. Alam, M. A. R. Laskar, and A. Garg, "Modeling and simulation of longitudinal autopilot for general aviation aircraft," in *2016 5th International Conference on Informatics, Electronics and Vision (ICIEV)*, IEEE, 2016, pp. 490–495.

[64] N. Wahid and N. Hassan, "Self-tuning fuzzy pid controller design for aircraft pitch control," in *2012 Third International Conference on Intelligent Systems Modelling and Simulation*, IEEE, 2012, pp. 19–24.

[65] J. Ohri *et al.*, "Ga tuned lqr and pid controller for aircraft pitch control," in *2014 IEEE 6th India International Conference on Power Electronics (IICPE)*, IEEE, 2014, pp. 1–6.

[66] I. Ibrahim and M. Al Akkad, "Exploiting an intelligent fuzzy-pid system in nonlinear aircraft pitch control," in *2016 International Siberian Conference on Control and Communications (SIBCON)*, IEEE, 2016, pp. 1–7.

[67] M. Babar, S. Ali, M. Shah, R. Samar, A. Bhatti, and W. Afzal, "Robust control of uavs using h∞ control paradigm," in *2013 IEEE 9th International Conference on Emerging Technologies (ICET)*, IEEE, 2013, pp. 1–5.

[68] J. López, R. Dormido, S. Dormido, and J. Gómez, "A robust controller for an uav flight control system," *The Scientific World Journal*, vol. 2015, 2015.

[69] J. Doyle, K. Glover, P. KhgaoeSar, and B. Francis, "Statespace solutions to standard hi aid control problems," *IEEE Trans. oc Ant Control*, vol. 34, no. 8, 1989.

[70] M. Polas and A. Fekih, "A multi-gain sliding mode based controller for the pitch angle control of a civil aircraft," in *2010 42nd Southeastern Symposium on System Theory (SSST)*, IEEE, 2010, pp. 96–101.

[71] E. Promtun and S. Seshagiri, "Sliding mode control of pitch-rate of an f-16 aircraft," *IFAC Proceedings Volumes*, vol. 41, no. 2, pp. 1099–1104, 2008.

[72] X. Cheng, H. Liu, and W. Lu, "Chattering-suppressed sliding mode control for flexible-joint robot manipulators," in *Actuators*, Multidisciplinary Digital Publishing Institute, vol. 10, 2021, p. 288.

[73] W. MacKunis, P. M. Patre, M. K. Kaiser, and W. E. Dixon, "Asymptotic tracking for aircraft via robust and adaptive dynamic inversion methods," *IEEE Transactions on Control Systems Technology*, vol. 18, no. 6, pp. 1448–1456, 2010.

[74] N. Wahid and M. F. Rahmat, "Pitch control system using lqr and fuzzy logic controller," in *2010 IEEE Symposium on Industrial Electronics and Applications (ISIEA)*, IEEE, 2010, pp. 389–394.

[75] G. Călugăru and E.-A. Dănişor, "Improved aircraft attitude control using generalized predictive control method," in *2016 17th International Carpathian Control Conference (ICCC)*, IEEE, 2016, pp. 101–106.

[76] O. Härkegård, "Backstepping and control allocation with applications to flight control," Ph.D. dissertation, Linköpings universitet, 2003.

[77] O. Härkegård, "Quadratic programming control allocation toolbox(qcat)," `http://research.harkegard.se/qcat`, 2004.

[78] Y. Luo, A. Serrani, S. Yurkovich, M. W. Oppenheimer, and D. B. Doman, "Model-predictive dynamic control allocation scheme for reentry vehicles," *Journal of Guidance, Control, and Dynamics*, vol. 30, no. 1, pp. 100–113, 2007.

[79] M. A. Bolender and D. B. Doman, "Nonlinear control allocation using piecewise linear functions: A linear programming approach," *Journal of Guidance, Control, and Dynamics*, vol. 28, no. 3, pp. 558–562, 2005.

[80] W. Durham, K. A. Bordignon, and R. Beck, *Aircraft control allocation*. John Wiley & Sons, 2017.

[81] J. M. Buffington and D. F. Enns, "Lyapunov stability analysis of daisy chain control allocation," *Journal of Guidance, Control, and Dynamics*, vol. 19, no. 6, pp. 1226–1230, 1996.

[82] A. Rupp, "Control allocation for over-actuated road vehicles," *University of Graz*, pp. 13–26, 2013.

[83] M. W. Oppenheimer, D. B. Doman, and M. A. Bolender, "Control allocation for over-actuated systems," in *2006 14th Mediterranean Conference on Control and Automation*, IEEE, 2006, pp. 1–6.

[84] C. Badrya, "Cfd/quasi-steady coupled trim analysis of diptera-type flapping wing mav in steady flight," Ph.D. dissertation, University of Maryland, College Park, 2016.

[85] J. A. V. Caetano, "Model identification of a flapping wing micro aerial vehicle," 2016.

[86] W. Hoff, "Der flug der insekten und der vögel," *Naturwissenschaften*, vol. 7, no. 10, pp. 159–162, 1919.

[87] G. T. Walker, "The flapping flight of birds," *The Aeronautical Journal*, vol. 29, no. 179, pp. 590–594, 1925.

[88] J. M. V. Rayner, "A vortex theory of animal flight. part 1. the vortex wake of a hovering animal," *Journal of Fluid Mechanics*, vol. 91, no. 4, pp. 697–730, 1979.

[89] C. P. Ellington, "The aerodynamics of hovering insect flight. i. the quasi-steady analysis," *Philosophical Transactions of the Royal Society of London. B, Biological Sciences*, vol. 305, no. 1122, pp. 1–15, 1984.

[90] C. P. Ellington, "The aerodynamics of hovering insect flight. v. a vortex theory," *Philosophical Transactions of the Royal Society of London. B, Biological Sciences*, vol. 305, no. 1122, pp. 115–144, 1984.

[91] M. Osborne, "Aerodynamics of flapping flight with application to insects," *Journal of Experimental Biology*, vol. 28, no. 2, pp. 221–245, 1951.

[92] T. Theodorsen, "General theory of aerodynamic instability and the mechanism of flutter," *NACA Technical Report*, vol. 496, 1935.

[93] I. Garrick, *Propulsion of a flapping and oscillating airfoil*, 1937.

[94] T. Von Karman, "General aerodynamic theory-perfect fluids," *Aerodynamic theory*, vol. 2, pp. 346–349, 1935.

[95] A. Willmott and C. Ellington, "The mechanics of flight in the hawkmoth manduca sexta. i. kinematics of hovering and forward flight," *Journal of experimental Biology. The Company of Biologists Ltd*, vol. 200, no. 21, pp. 2705–2722, 1997.

[96] R. Zbikowski, "On aerodynamic modelling of an insect-like flapping wing in hover for micro air vehicles," *Philosophical Transactions of the Royal Society of London. Series A: Mathematical, Physical and Engineering Sciences*, vol. 360, no. 1791, pp. 273–290, 2002.

[97] C. B. Pedersen, "An indicial-polhamus model of aerodynamics of insect-like flapping wings in hover," 2003.

[98] F. Minotti, "Unsteady two-dimensional theory of a flapping wing," *Physical Review E. APS*, vol. 66, no. 5, p. 51 907, 2002.

[99] S. Ansari, *A nonlinear, unsteady aerodynamic model for insect-like flapping wings in the hover with micro air vehicle applications*. Cranfield University, 2004.

[100] D. Prosser, *Flapping wing design for a dragonfly-like micro air vehicle*, 2011.

[101] T. Weis-Fogh, "Quick estimates of flight fitness in hovering animals, including novel mechanisms for lift production," *Journal of experimental Biology. The Company of Biologists Ltd*, vol. 59, no. 1, pp. 169–230, 1973.

[102] S. Sane, "The aerodynamics of insect flight," *Journal of experimental biology. The Company of Biologists Ltd*, vol. 206, no. 23, pp. 4191–4208, 2003.

[103] S. Sane and M. Dickinson, "The control of flight force by a flapping wing: Lift and drag production," *Journal of experimental biology. The Company of Biologists Ltd*, vol. 204, no. 15, pp. 2607–2626, 2001.

[104] S. Sane and M. Dickinson, "The aerodynamic effects of wing rotation and a revised quasi-steady model of flapping flight," *Journal of experimental biology. The Company of Biologists Ltd*, vol. 205, no. 8, pp. 1087–1096, 2002.

[105] D. Lentink and M. Dickinson, "Rotational accelerations stabilize leading edge vortices on revolving fly wings," *Journal of Experimental Biology. The Company of Biologists Ltd*, vol. 212, no. 16, pp. 2705–2719, 2009.

[106] H. Nagai and K. Isogai, "Effects of flapping wing kinematics on hovering and forward flight aerodynamics'," *AIAA journal*, vol. 49, no. 8, pp. 1750–1762, 2011.

[107] H. Ren, Y. Wu, and P. Huang, "Visualization and characterization of near-wake flow fields of a flapping-wing micro air vehicle using piv," *Journal of visualization. Springer*, vol. 16, no. 1, pp. 75–83, 2013.

[108] G. C. Lewin and H. Haj-Hariri, "Modelling thrust generation of a two-dimensional heaving airfoil in a viscous flow," *Journal of Fluid Mechanics*, vol. 492, p. 339, 2003.

[109] M. Jones and N. K. Yamaleev, "Adjoint-based optimization of three-dimensional flapping-wing flows," *AIAA Journal*, vol. 53, no. 4, pp. 934–947, 2015.

[110] J.-S. Han, J. W. Chang, and J.-H. Han, "An aerodynamic model for insect flapping wings in forward flight," *Bioinspiration & biomimetics*, vol. 12, no. 3, p. 036 004, 2017.

[111] Y. Liu and M. Sun, "Wing kinematics measurement and aerodynamics of hovering droneflies," *Journal of Experimental Biology. The Company of Biologists Ltd*, vol. 211, no. 13, pp. 2014–2025, 2008.

[112] M. Sun and J. Tang, "Unsteady aerodynamic force generation by a model fruit fly wing in flapping motion," *Journal of experimental biology. The Company of Biologists Ltd*, vol. 205, no. 1, pp. 55–70, 2002.

[113] H. Liu and K. Kawachi, "Leading-edge vortices of flapping and rotary wings at low reynolds number, fixed and flapping wing aerodynamics for micro air vehicle applications," *AIAA Reston, VA*, vol. 195, pp. 275–285, 2001.

[114] J. Wu, Y. Zhang, and M. Sun, "Hovering of model insects: Simulation by coupling equations of motion with navier–stokes equations," *Journal of Experimental Biology. The Company of Biologists Ltd*, vol. 212, no. 20, pp. 3313–3329, 2009.

[115] Y. Lee, K.-B. Lua, T. Lim, and K. Yeo, "A quasi-steady aerodynamic model for flapping flight with improved adaptability," *Bioinspiration & biomimetics*, vol. 11, no. 3, p. 036 005, 2016.

[116] S. Ansari, R. Zbikowski, and K. Knowles, "Aerodynamic modelling of insect-like flapping flight for micro air vehicles," *Progress in aerospace sciences*, vol. 42, no. 2, pp. 129–172, 2006.

[117] H. Taha, M. Hajj, and A. Nayfeh, "Flight dynamics and control of flapping-wing mavs: A review," *Nonlinear Dynamics. Springer*, vol. 70, no. 2, pp. 907–939, 2012.

[118] D. D. Chin and D. Lentink, "Flapping wing aerodynamics: From insects to vertebrates," *Journal of Experimental Biology*, vol. 219, no. 7, pp. 920–932, 2016.

[119] H. Xuan, J. Hu, Y. Yu, and J. Zhang, "Recent progress in aerodynamic modeling methods for flapping flight," *AIP Advances*, vol. 10, no. 2, p. 020 701, 2020.

[120] R. M. Alexander, *Principles of animal locomotion*. Princeton University Press, 2013.

[121] K. G. Gotz, B. Hengstenberg, and R. Biesinger, "Optomotor control of wing beat and body posture in drosophila," *Biological Cybernetics*, vol. 35, no. 2, pp. 101–112, 1979.

[122] J. Zanker, "On the mechanism of speed and altitude control in drosophila melanogaster," *Physiological entomology*, vol. 13, no. 3, pp. 351–361, 1988.

[123] J. M. Zanker, M. Egelhaaf, and A.-K. Warzecha, "On the coordination of motor output during visual flight control of flies," *Journal of Comparative Physiology A*, vol. 169, no. 2, pp. 127–134, 1991.

[124] S. A. Combes and R. Dudley, "Turbulence-driven instabilities limit insect flight performance," *Proceedings of the National Academy of Sciences*, vol. 106, no. 22, pp. 9105–9108, 2009.

[125] B. Cheng, X. Deng, and T. L. Hedrick, "The mechanics and control of pitching manoeuvres in a freely flying hawkmoth (manduca sexta)," *Journal of Experimental Biology*, vol. 214, no. 24, pp. 4092–4106, 2011.

[126] T. L. Hedrick and T. L. Daniel, "Flight control in the hawkmoth manduca sexta: The inverse problem of hovering," *Journal of Experimental Biology*, vol. 209, no. 16, pp. 3114–3130, 2006.

[127] T. Luu, A. Cheung, D. Ball, and M. V. Srinivasan, "Honeybee flight: A novel 'streamlining' response," *Journal of Experimental Biology*, vol. 214, no. 13, pp. 2215–2225, 2011.

[128] A. T. Bode-Oke, S. Zeyghami, and H. Dong, "Flying in reverse: Kinematics and aerodynamics of a dragonfly in backward free flight," *Journal of The Royal Society Interface*, vol. 15, no. 143, p. 20 180 102, 2018.

[129] J. M. Zanker, "How does lateral abdomen deflection contribute to flight control of drosophila melanogaster?" *Journal of Comparative Physiology A*, vol. 162, no. 5, pp. 581–588, 1988.

[130] J. P. Dyhr, K. A. Morgansen, T. L. Daniel, and N. J. Cowan, "Flexible strategies for flight control: An active role for the abdomen," *Journal of Experimental Biology*, vol. 216, no. 9, pp. 1523–1536, 2013.

[131] A. J. Hinterwirth and T. L. Daniel, "Antennae in the hawkmoth manduca sexta (lepidoptera, sphingidae) mediate abdominal flexion in response to mechanical stimuli," *Journal of Comparative Physiology A*, vol. 196, no. 12, pp. 947–956, 2010.

[132] M. A. Frye, "Effects of stretch receptor ablation on the optomotor control of lift in the hawkmoth manduca sexta," *Journal of Experimental Biology*, vol. 204, no. 21, pp. 3683–3691, 2001.

[133] J. P. Dyhr, N. J. Cowan, D. J. Colmenares, K. A. Morgansen, and T. L. Daniel, "Autostabilizing airframe articulation: Animal inspired air vehicle control," in *2012 IEEE 51st IEEE Conference on Decision and Control (CDC)*, IEEE, 2012, pp. 3715–3720.

[134] E. A. Arbas, "Control of hindlimb posture by wind-sensitive hairs and antennae during locust flight," *Journal of Comparative Physiology A*, vol. 159, no. 6, pp. 849–857, 1986.

[135] J. M. Camhi, "Sensory control of abdomen posture in flying locusts," *Journal of Experimental Biology*, vol. 52, no. 3, pp. 533–537, 1970.

[136] J. M. Camhi, "Yaw-correcting postural changes in locusts," *Journal of Experimental Biology*, vol. 52, no. 3, pp. 519–531, 1970.

[137] K. Tejaswi, C.-K. Kang, and T. Lee, "Dynamics and control of a flapping wing uav with abdomen undulation inspired by monarch butterfly," in *2021 American Control Conference (ACC)*, IEEE, 2021, pp. 66–71.

[138] K. Tejaswi, M. K. Sridhar, C.-k. Kang, and T. Lee, "Effects of abdomen undulation in energy consumption and stability for monarch butterfly," *Bioinspiration & Biomimetics*, vol. 16, no. 4, p. 046 003, 2021.

[139] S. Agrawal, R. Madangopal, and Z. Khan, "Biologically inspired design of small flapping wing air vehicles using four-bar mechanisms and quasi-steady aerodynamics," *Journal of Mechanical Design*, vol. 127, p. 809, 2005.

[140] G. Gebert, P. Gallmeier, and J. Evers, "Equations of motion for flapping flight," in *AIAA Atmospheric Flight Mechanics Conference and Exhibit*, 2002, p. 4872.

[141] M. Sun, J. Wang, and Y. Xiong, "Dynamic flight stability of hovering insects," *Acta Mechanica Sinica. Springer*, 2007.

[142] X. Deng, "Flapping flight for biomimetic robotic insects: Part i-system modeling'," *IEEE Transactions on Robotics. IEEE*, vol. 22, no. 4, pp. 776–788, 2006.

[143] X. Deng, L. Schenato, and S. S. Sastry, "Flapping flight for biomimetic robotic insects: Part ii-flight control design," *IEEE Transactions on Robotics*, vol. 22, no. 4, pp. 789–803, 2006.

[144] A. A. Shabana, *Dynamics of multibody systems*. Cambridge university press, 2020.

[145] R. M. M. Orsino, "A contribution on modeling methodologies for multibody systems.," Ph.D. dissertation, University of São Paulo, Brazil, 2016.

[146] D. Sgarioto, "Non-linear dynamic modelling and optimal control of aerial tethers for remote delivery and capture of payloads," Ph.D. dissertation, RMIT University, 2006.

[147] M. Jammer, *Concepts of force*. Courier Corporation, 2012.

[148] L. Wang, *Multibody dynamics using conservation of momentum with application to compliant offshore floating wind turbines*. Texas A&M University, 2012.

[149] L. Haixu, Q. Xiangju, and W. Weijun, "Multi-body motion modeling and simulation for tilt rotor aircraft," *Chinese Journal of Aeronautics*, vol. 23, no. 4, pp. 415–422, 2010.

[150] A. Sakhaei, "Dynamic modelling and predictive control for insect-like flapping wing aerial micro robots," Ph.D. dissertation, Ryerson University, 2010.

[151] J. Grauer, E. Ulrich, J. Hubbard, D. Pines, and J. Humbert, "System identification of an ornithopter aerodynamics model," in *AIAA Atmospheric Flight Mechanics Conference*, 2010, p. 7632.

[152] J. Grauer, E. Ulrich, J. Hubbard Jr, D. Pines, and J. S. Humbert, "Testing and system identification of an ornithopter in longitudinal flight," *Journal of Aircraft*, vol. 48, no. 2, pp. 660–667, 2011.

[153] C. Orlowski, A. Girard, and W. Shyy, "Open loop pitch control of a flapping wing micro-air vehicle using a tail and control mass," in *Proceedings of the 2010 American Control Conference*, IEEE, 2010, pp. 536–541.

[154] J. Caetano, M. Weehuizen, C. De Visser, G. De Croon, C. De Wagter, B. Remes, and M. Mulder, "Rigid vs. flapping: The effects of kinematic formulations in force determination of a free flying flapping wing micro air vehicle," in *2014 International Conference on Unmanned Aircraft Systems (ICUAS)*, IEEE, 2014, pp. 949–959.

[155] M. Bolender, "Rigid multi-body equations-of-motion for flapping wing mavs using kane's equations," in *AIAA Guidance, Navigation, and Control Conference*, 2009, p. 6158.

[156] J. Su, C. Su, S. Xu, and X. Yang, "A multibody model of tilt-rotor aircraft based on kane's method," *International Journal of Aerospace Engineering*, vol. 2019, 2019.

[157] M. Lasek and K. Sibilski, "Modelling and simulation of flapping wing control for a micromechanical flying insect (entomopter)," in *AIAA Modeling and Simulation Technologies Conference and Exhibit*, 2002, p. 4973.

[158] J. Jackson, R. Bhattacharya, and T. Strganac, "Modelling and suboptimal trajectory generation for a symmetric flapping wing vehicle," in *AIAA Guidance, Navigation and Control Conference and Exhibit*, 2008, p. 6465.

[159] A. A. Paranjape, S.-J. Chung, and M. S. Selig, "Flight mechanics of a tailless articulated wing aircraft," *Bioinspiration & biomimetics*, vol. 6, no. 2, p. 026 005, 2011.

[160] C. Du, J. Xu, and Y. Zheng, "Modeling and control of a dragonfly-like micro aerial vehicle," *Adv Robot Autom S*, vol. 2, p. 2, 2015.

[161] E. Torenbeek and H. Wittenberg, *Flight physics: essentials of aeronautical disciplines and technology, with historical notes*. Springer Science & Business Media, 2009.

[162] P. A. Kuchment, *Floquet theory for partial differential equations*. Birkhuser, 2012, vol. 60.

[163] G. Taylor and A. Thomas, "Dynamic flight stability in the desert locust schistocerca gregaria," *Journal of Experimental Biology. The Company of Biologists Ltd*, vol. 206, no. 16, pp. 2803–2829, 2003.

[164] G. K. Taylor and R. Żbikowski, "Nonlinear time-periodic models of the longitudinal flight dynamics of desert locusts schistocerca gregaria," *Journal of the Royal Society Interface*, vol. 2, no. 3, pp. 197–221, 2005.

[165] M. Sun and Y. Xiong, "Dynamic flight stability of a hovering bumblebee," *Journal of experimental biology. The Company of Biologists Ltd*, vol. 208, no. 3, pp. 447–459, 2005.

[166] M. Sun and J. Wang, "Flight stabilization control of a hovering model insect," *Journal of Experimental Biology. The Company of Biologists Ltd*, vol. 210, no. 15, pp. 2714–2722, 2007.

[167] Y. Zhang and M. Sun, "Dynamic flight stability of a hovering model insect: Lateral motion'," da, *Acta Mechanica Sinica. Springer*, vol. 26, no. 2, pp. 175–190, 2010.

[168] I. Faruque and J. Humbert, "Dipteran insect flight dynamics. part 1 longitudinal motion about hover," *Journal of theoretical biology. Elsevier*, vol. 264, no. 2, pp. 538–552, 2010.

[169] I. Faruque and J. Humbert, "Dipteran insect flight dynamics. part 2: Lateral–directional motion about hover," *Journal of theoretical biology. Elsevier*, vol. 265, no. 3, pp. 306–313, 2010.

[170] N. Gao, H. Aono, and H. Liu, "A numerical analysis of dynamic flight stability of hawkmoth hovering," *Journal of Biomechanical Science and Engineering. The Japan Society of Mechanical Engineers*, vol. 4, no. 1, pp. 105–116, 2009.

[171] M. Bolender, "Open-loop stability of flapping flight in hover," in *AIAA Guidance, Navigation, and Control Conference*, 2010, p. 7552.

[172] K. Nguyen, L. T. K. Au, H.-V. Phan, and H. C. Park, "Comparative dynamic flight stability of insect-inspired flapping-wing micro air vehicles in hover: Longitudinal and lateral motions," *Aerospace Science and Technology*, vol. 119, p. 107 085, 2021.

[173] A. M. Hassan and H. E. Taha, "Aerodynamic-dynamic interactions and multi-body formulation of flapping wing dynamics: Part ii trim and stability analysis," in *AIAA Guidance, Navigation, and Control Conference*, 2017, p. 1275.

[174] D. Doman, M. Oppenheimer, and D. Sigthorsson, "Dynamics and control of a minimally actuated biomimetic vehicle: Part i-aerodynamic model," in *AIAA Guidance, Navigation, and Control Conference*, 2009, p. 6160.

[175] R. Wood, "The first takeoff of a biologically inspired at-scale robotic insect," *IEEE transactions on robotics. IEEE*, vol. 24, no. 2, pp. 341–347, 2008.

[176] A. Serrani, "Robust hovering control of a single-dof flapping wing mav," in *American Control Conference (ACC*, IEEE, 2010, pp. 1302–1307.

[177] H. Minglang, "Control of insect-like flapping wing micro air vehicles i: Control mechanic," in *Control Conference, 2007. CCC 2007. Chinese. IEEE*, 2007, pp. 643–648.

[178] H. Minglang, W. Ruixuan, and C. Xiaofeng, "Control of insect-like flapping wing micro air vehicles ii: Control parameter," in *Control Conference, 2007. CCC 2007. Chinese. IEEE*, 2007, pp. 649–653.

[179] Y. Xiong and M. Sun, "Stabilization control of a bumblebee in hovering and forward flight," *Acta Mechanica Sinica. Springer*, vol. 25, no. 1, pp. 13–21, 2009.

[180] J. Geder, "Modeling and control design for a flapping-wing nano air vehicle," in *AIAA Guidance, Navigation, and Control Conference*, 2010, p. 7556.

[181] Q. Guo, "Hovering control based on fuzzy neural networks for biomimetic flying robotic," in *Information and Automation, 2008. ICIA 2008. International Conference on. IEEE*, 2008, pp. 504–508.

[182] M. Hu, "Controllability issues for insect like flapping wing micro-air vehicle," in *Intelligent Control and Automation, 2008. WCICA 2008. 7th World Congress on. IEEE*, 2008, pp. 6365–6368.

[183] B. Cheng and X. Deng, "Near-hover dynamics and attitude stabilization of an insect model'," in *American Control Conference (ACC*, IEEE, 2010, pp. 39–44.

[184] H. Rifai, N. Marchand, and G. Poulin, "Bounded control of a flapping wing micro drone in three dimensions," in *Robotics and Automation, 2008. ICRA 2008. IEEE International Conference on. IEEE*, 2008, pp. 164–169.

[185] R. J. Full and D. E. Koditschek, "Templates and anchors: Neuromechanical hypotheses of legged locomotion on land," *Journal of experimental biology*, vol. 202, no. 23, pp. 3325–3332, 1999.

[186] J. Lee, S. N. Sponberg, O. Y. Loh, A. G. Lamperski, R. J. Full, and N. J. Cowan, "Templates and anchors for antenna-based wall following in cockroaches and robots," *IEEE Transactions on Robotics*, vol. 24, no. 1, pp. 130–143, 2008.

[187] A. Nel, J. Prokop, M. Pecharová, M. S. Engel, and R. Garrouste, "Palaeozoic giant dragonflies were hawker predators," *Scientific reports*, vol. 8, no. 1, p. 12 141, 2018.

[188] M. L. May, "A critical overview of progress in studies of migration of dragonflies (odonata: Anisoptera), with emphasis on north america," *Journal of Insect Conservation*, 2013.

[189] A. Azuma and T. Watanabe, "Flight performance of a dragonfly," *Journal of experimental biology*, vol. 137, no. 1, pp. 221–252, 1988.

[190] J. Wakeling and C. Ellington, "Dragonfly flight. i. gliding flight and steady-state aerodynamic forces.," *Journal of Experimental Biology*, vol. 200, no. 3, pp. 543–556, 1997, ISSN: 0022-0949.

[191] B. Newman, "Model test on a wing section of a dragonfly," *Scale effects in animal locomotion*, pp. 445–477, 1977.

[192] B. Heinrich and T. M. Casey, "Heat transfer in dragonflies:'fliers' and 'perchers'," *Journal of Experimental Biology*, vol. 74, no. 1, pp. 17–36, 1978.

[193] R. Scorer, "The nature of convection as revealed by soaring birds and dragonflies," *Quarterly Journal of the Royal Meteorological Society*, vol. 80, no. 343, pp. 68–77, 1954.

[194] M. L. May, "Thermoregulation and adaptation to temperature in dragonflies (odonata: Anisoptera)," *Ecological Monographs*, vol. 46, no. 1, pp. 1–32, 1976.

[195] M. May, "Dependence of flight behavior and heat production on air temperature in the green darner dragonfly anax junius (odonata: Aeshnidae)," *Journal of Experimental Biology*, vol. 198, no. 11, pp. 2385–2392, 1995.

[196] P. H. Zipfel, *Modeling and simulation of aerospace vehicle dynamics*. American Institute of Aeronautics and Astronautics, 2007.

[197] M. Drela and H. Youngren, "Athena vortex lattice (avl)," *Computer software. AVL*, vol. 4, 2017.

[198] M. Drela and H. Youngren, *Xfoil manual*, 2001.

[199] A. Deperrois, "Analysis of foils and wings operating at low reynolds numbers," *Guidelines for XFLR5*, vol. 4, 2009.

[200] T. A. Sims, "Design and control considerations for a skid-to-turn unmanned aerial vehicle," 2009.

[201] K. Budziak, *Aerodynamic Analysis with Athena Vortex Lattice (AVL)*. Hamburg: Aircraft Design and Systems Group (AERO), Department of Automotive, 2015.

[202] M. Drela and H. Youngren, "Avl overview," *online product brochure], http://web. mit. edu/drela/Public/web/avl/[retrieved 12 Jun. 2020]*, 2014.

[203] O. Dantsker and M. Vahora, "Comparison of aerodynamic characterization methods for design of unmanned aerial vehicles," in *2018 AIAA Aerospace Sciences Meeting*, 2018, p. 0272.

[204] A. Deperrois, *Xflr5*, `http://www.xflr5.tech/xflr5.htm`, (Accessed on 03/08/2020).

[205] A. Deperrois, "Xflr5 analysis of foils and wings operating at low reynolds numbers," *Guidelines for XFLR5*, vol. 142, 2009.

[206] S. F. Hoerner, "Fluid-dynamic drag," *Hoerner fluid dynamics*, 1965.

[207] I. Abdulrahman, "Matlab-based programs for power system dynamic analysis," *IEEE Open Access Journal of Power and Energy*, vol. 7, pp. 59–69, 2019.

[208] MATLAB, *MATLAB version 9.7.0.1190202 (R2019b)*. Natick, Massachusetts: The MathWorks Inc., 2019.

[209] E. T. Falangas, *Performance evaluation and design of flight vehicle control systems*. John Wiley & Sons, 2015.

[210] A. A. Paranjape and N. Ananthkrishnan, "Combat aircraft agility metrics-a review," *Journal of Aerospace Sciences and Technologies*, vol. 58, no. 2, pp. 143–154, 2006.

[211] R. A. Bunge, A. E. Alkurdi, E. Alfaris, and I. Kroo, "In-flight measurement of wing surface pressures on a small-scale uav during stall/spin maneuvers," in *AIAA flight testing conference*, 2016, p. 3652.

[212] M. Oborne, *Mission planner open-source ground station software, version 1.3.75*, `https://ardupilot.org/planner/`, Accessed: 2021-12-13, 2015.

[213] A. Sobron, *Design and testing of a flight control system for unstable subscale aircraft*, 2015.

[214] J. Alwood, *Dragonflies in super slomo: Narrated*, `https://www.youtube.com/watch?v=7eNERCQW41I`, (Accessed on 10/08/2022), 2021.

[215] Slate, *Epic footage of dragonflies hunting - youtube*, https://www.youtube.com/watch?v=XWROwMxepoM, (Accessed on 10/08/2022), 2013.

[216] H. H. M. Institute, *Dragonfly prey capture, leonardo lab, hhmi/janelia research campus - youtube*, https://www.youtube.com/watch?v=IAoTAl8FuZc&t=3s, (Accessed on 02/24/2023), Jun. 2018.

[217] R. C. Wrede, *Introduction to vector and tensor analysis*. Wiley, New York, 1963.

[218] J. Verbeke and J. D. Schutter, "Experimental maneuverability and agility quantification for rotary unmanned aerial vehicle," *International Journal of Micro Air Vehicles*, vol. 10, no. 1, pp. 3–11, 2018.

[219] J. Silsby, *Dragonflies of the World*. CSIRO Publishing, 2001, ISBN: 9780643065123.

[220] R. W. Beard and T. W. McLain, *Small unmanned aircraft: Theory and practice*. Princeton university press, 2012.

[221] H. S. Mohammad, *Aircraft design: A systems engineering approach*, 2012.

[222] M. Okamoto, K. Yasuda, and A. Azuma, "Aerodynamic characteristics of the wings and body of a dragonfly," *Journal of experimental biology*, vol. 199, no. 2, pp. 281–294, 1996.

[223] N. Chitsaz, R. Marian, and J. Chahl, "Experimental method for 3d reconstruction of odonata wings (methodology and dataset)," *PloS one*, vol. 15, no. 4, e0232193, 2020.

[224] M. Tsagarakis, *Project solaris-analysis of airfoil for solar powered flying wing uav*, 2011.

[225] *Airfoil database for tailless and flying wings*, https://www.aerodesign.de/english/profile/profile_s.htm, Accessed: 2020-04-06.

[226] P. Wick, "Peter wick on planks. part 3: The good slope plank," *Radio Controlled Soaring Digest*, vol. 23, no. 3, pp. 7–11, 2006, Available at http://www.rcsoaring.com/rcsd/RCSD-2006-03.pdf.

[227] L. Song, H. Yang, Y. Zhang, H. Zhang, and J. Huang, "Dihedral influence on lateral-directional dynamic stability on large aspect ratio tailless flying wing aircraft," *Chinese Journal of Aeronautics*, vol. 27, no. 5, pp. 1149–1155, 2014.

[228] J. Loth, *Engineering approach to aerodynamics and aircraft performance*, 2007.

[229] P. Lin, N. Kham, and H. Tun, "Longitudinal and lateral dynamic system modeling of a fixed-wing uav," *vol*, vol. 6, pp. 171–174, 2017.

[230] E. Bøhn, E. M. Coates, S. Moe, and T. A. Johansen, "Deep reinforcement learning attitude control of fixed-wing uavs using proximal policy optimization," in *2019 International Conference on Unmanned Aircraft Systems (ICUAS)*, IEEE, 2019, pp. 523–533.

[231] H. V. de Castro, *The longitudinal static stability of tailless aircraft*, 2001.

[232] M. J. Abzug and E. E. Larrabee, *Airplane stability and control: a history of the technologies that made aviation possible*. Cambridge University Press, 2005, vol. 14.

[233] M. Borri and L. Trainelli, "Basic airplane equilibrium and stability revisited," in *International Conference on Aeronautical Science and Air Transportation (ICASAT) Tripoli*, vol. 23, 2007, p. 25.

[234] R. J. Bomphrey, T. Nakata, P. Henningsson, and H.-T. Lin, "Flight of the dragonflies and damselflies," *Philosophical Transactions of the Royal Society B: Biological Sciences*, vol. 371, no. 1704, p. 20 150 389, 2016.

[235] R. L. Shaw, "Fighter combat," *Tactics and maneuvering*, 1985.

[236] J. R. Boyd, T. P. Christie, and J. E. Gibson, "Energy-maneuverability," *Air Proving Ground Center Report (APGC-TR-66-4)*, vol. 1, 1966.

[237] A. Lambregts, "Automatic flight controls," *Federal Aviation Administration, Tech. Rep. KNVLPAP6*, 1998.

[238] G. R. Balmer, *Modelling and control of a fixed-wing uav for landings on mobile landing platforms*, 2015.

[239] J. K. Ly, "Angle of attack determination using inertial navigation system data from flight tests," Ph.D. dissertation, University of Tennessee, Knoxville, 2017.

[240] T. S. Clawson, S. Ferrari, E. Farrell Helbling, R. J. Wood, B. Fu, A. Ruina, and Z. J. Wang, "Full flight envelope and trim map of flapping-wing micro aerial vehicles," *Journal of Guidance, Control, and Dynamics*, vol. 43, no. 12, pp. 2218–2236, 2020.

[241] *Constrained nonlinear optimization algorithms - matlab & simulink - mathworks*, `https://au.mathworks.com/help/optim/ug/constrained-nonlinear-optimization-algorithms.html`, (Accessed on 09/16/2020).

[242] A. Bolsunovsky, N. Buzoverya, B. Gurevich, V. Denisov, A. Dunaevsky, L. Shkadov, O. Sonin, A. Udzhuhu, and J. Zhurihin, "Flying wing-problems and decisions," *Aircraft design*, vol. 4, no. 4, pp. 193–219, 2001.

[243] L. Song, H. Yang, X. Yan, C. Ma, and J. Huang, "A study of instability in a miniature flying-wing aircraft in high-speed taxi," *Chinese Journal of Aeronautics*, vol. 28, no. 3, pp. 749–756, 2015.

[244] B. D. Anderson and J. B. Moore, "Optimal control linear quadratic methods prentice hall international," *Inc. Englewood Cliffs NJ*, vol. 7632, 1989.

[245] P. Dorato, V. Cerone, and C. Abdallah, *Linear quadratic control: An introduction*, 2000.

[246] B. Bacon and I. Gregory, "General equations of motion for a damaged asymmetric aircraft," in *AIAA atmospheric flight mechanics conference and exhibit*, 2007, p. 6306.

[247] A. E. Bryson, *Control of spacecraft and aircraft*. Princeton university press Princeton, New Jersey, 1993, vol. 41.

[248] A. Hamada, A. Sultan, and M. Abdelrahman, "Design, build and fly a flying wing," *Athens Journal of Technology and Engineering*, vol. 5, no. 3, pp. 223–250, 2018.

[249] E. M. Coates and T. I. Fossen, "Geometric reduced-attitude control of fixed-wing uavs," *Applied Sciences*, vol. 11, no. 7, p. 3147, 2021.

[250] S. Markin, "Multiple simultaneous specification attitude control of a mini flying-wing unmanned aerial vehicle," Ph.D. dissertation, University of Toronto (Canada), 2010.

[251] D. Alexander, "Wind tunnel studies of turns by flying dragonflies," *Journal of Experimental Biology*, vol. 122, no. 1, pp. 81–98, 1986.

[252] M. Kintel and C. Wolf, "Openscad," *GNU General Public License, p GNU General Public License*, 2014.

[253] J. W. Adams, "Determining airspeed without a pitot-static system for use in a general aviation flight data recorder using an ardu-pilot," Ph.D. dissertation, Carleton University, 2017.

[254] J. Huber and J. Noyes, "A new genus and species of fairyfly, tinkerbella nana (hymenoptera, mymaridae), with comments on its sister genus kikiki, and discussion on small size limits in arthropods," *Journal of Hymenoptera Research*, vol. 32, pp. 17–44, 2013.

[255] A. Jusufi, Y. Zeng, R. J. Full, and R. Dudley, *Aerial righting reflexes in flightless animals*, 2011.

[256] C. Ellington, "Aerodynamics and the origin of insect flight," *Advances in insect physiology*, vol. 23, pp. 171–210, 1991.

[257] J. D. Anderson Jr, *Fundamentals of aerodynamics*. Tata McGraw-Hill Education, 2010.

[258] Z. H. Zhu, *Nonlinear elastodynamic analysis of low tension cable using a new beam element*. 2004.

[259] R. R. Gerhardt and L. J. Hribar, "Flies (diptera)," in *Medical and Veterinary Entomology*, Elsevier, 2019, pp. 171–190.

[260] J. C. Fabricius, *Philosophia entomologica sistens scientiae fundamenta adiectis definitionibus, exemplis, observationibus, adumbrationibus*. Impensis Carol. Ernest. Bohnii, 1778.

[261] G. Fraenkel and J. Pringle, "Biological sciences: Halteres of flies as gyroscopic organs of equilibrium," *Nature*, vol. 141, no. 3577, pp. 919–920, 1938.

[262] J. Kathirithamby, "Review of the order strepsiptera," *Systematic Entomology*, vol. 14, no. 1, pp. 41–92, 1989.

[263] B. Greenberg, *Flies and disease*. Princeton University Press, 2019.

[264] Y. Golding, R. Ennos, M. Sullivan, and M. Edmunds, "Hoverfly mimicry deceives humans," *Journal of Zoology*, vol. 266, no. 4, pp. 395–399, 2005.

[265] M. Edmunds, "Why are there good and poor mimics?" *Biological Journal of the Linnean Society*, vol. 70, no. 3, pp. 459–466, 2000.

[266] T. S. Collett and M. Land, "How hoverflies compute interception courses," *Journal of comparative physiology*, vol. 125, no. 3, pp. 191–204, 1978.

[267] M. Thyselius, Y. Ogawa, R. Leibbrandt, T. J. Wardill, P. T. Gonzalez-Bellido, and K. Nordstrom, "Male hoverflies (eristalis tenax) do not use heuristic rules based on retinal size and speed to initiate indoor pursuits of artificial targets," *bioRxiv*, 2022.

[268] X. L. Mou, Y. P. Liu, and M. Sun, "Wing motion measurement and aerodynamics of hovering true hoverflies," *Journal of Experimental Biology*, vol. 214, no. 17, pp. 2832–2844, 2011.

[269] H. V. Phan, Q.-T. Truong, and H.-C. Park, "Implementation of initial passive stability in insect-mimicking flapping-wing micro air vehicle," *International Journal of Intelligent Unmanned Systems*, 2015.

[270] J. Whitney, *Design and performance of insect-scale flapping-wing vehicles*, 2012.

[271] C. P. Ellington, "The aerodynamics of hovering insect flight. ii. morphological parameters," *Philosophical Transactions of the Royal Society of London. B, Biological Sciences*, vol. 305, no. 1122, pp. 17–40, 1984.

[272] J. Haag, W. Denk, and A. Borst, "Fly motion vision is based on reichardt detectors regardless of the signal-to-noise ratio," *Proceedings of the National Academy of Sciences*, vol. 101, no. 46, pp. 16 333–16 338, 2004.